EFFECT OF COMPOSITION AND PHASE EQUILIBRIA ON TRANSFORMATION AND PRECIPITATION CHARACTERISTICS IN NI–TI–HF HIGH TEMPERATURE SHAPE MEMORY ALLOYS

A Dissertation

by

TEJAS UMALE

Submitted to the Office of Graduate and Professional Studies of
Texas A&M University
in partial fulfillment of the requirements for the degree of

DOCTOR OF PHILOSOPHY

Chair of Committee,	Ibrahim Karaman
Committee Members,	Raymundo Arroyave
	Dimitris Lagoudas
	Patrick Shamberger
Head of Department,	Ibrahim Karaman

August 2020

Major Subject: Materials Science and Engineering

ABSTRACT

Shape memory alloys (SMAs) are a class of material that can “memorize” their original shape and recover it when stimulated with temperature or stress or both. For the increasing need of high temperature SMAs for advanced aerospace, transportation and energy applications, the NiTiHf alloys standout from its other NiTi-based competitors because of its economical and stable precipitation strengthening. The Ni-lean NiTiHf alloys possess high transformation temperatures (TTs) but suffer from high thermal and dimensional stability because of the presence of brittle $(Ti,Hf)_2Ni$ phases and low matrix strength which makes them vulnerable during practical applications. Whereas, the Ni-rich NiTiHf alloys despite possessing slightly lower TTs than Ni-lean counterparts, they depict high strength, high thermal and dimensional stability. The TTs and strength of the Ni-rich NiTiHf alloys can be enhanced further with H-phase precipitation. The Ni-rich NiTiHf alloys despite possessing such impressive properties the compositional space is not explored systematically. Also, despite notable enhancement of shape memory properties upon H-phase precipitation, the systematic thermodynamic and kinetic studies on the H-phase is still missing. The aforementioned studies once conducted, can aid in developing novel NiTiHf alloys with required transformation characteristics.

In the present study, efforts have been made to understand the compositional dependence of the NiTiHf alloys on the TTs. More than 42 NiTiHf alloys of different compositions in the Ni-lean, equiatomic and Ni-rich regimes were prepared by vacuum arc melting with highest accuracy and were tested for TTs. Also, the thermodynamics of

H-phase precipitation is explored by using the high throughput diffusion multiple experiments and the phase diagram for the Ni-Ti-Hf system was established along with H-phase equilibrium with other phases. The kinetic study of the H-phase precipitates was performed using the Small Angle X-ray Scattering, which enabled to understand the evolution of precipitate size and volume fraction with time at different heat treatment temperature. Also, a new machine learning based approach was implemented to explore the NiTiHf alloys with required TTs.

Therefore, by combining the chemistry, thermodynamics and kinetics based studies of the NiTiHf system, novel NiTiHf HTSMAs can be developed for required aerospace, energy, oil-gas industries and various other applications. Also, the machine learning based approach can be used to fill in the knowledge gaps and further assist in developing NiTiHf alloys for specific engineering applications.

DEDICATION

Dedicated to my beloved Guruji Sri Sri Paramhansa Yogananda, my mother Suchita Umale, my father Vinayak Umale, my brother Sudhanshu Umale and my wife Rasika Umale for their undying love, faith and believe in me.

ACKNOWLEDGEMENTS

The time here in College Station was very amazing and peaceful. I consider myself very fortunate that I had a chance to pursue doctoral degree at Texas A&M University. The process of PhD, as correctly said is a marathon and not a sprint race. Wining such a marathon is not possible without the support of caring and wonderful people who has stood there for me always.

Firstly, I would like to thank Dr. Ibrahim Karaman for accepting me as his student and entrusting me with his faith to carry out the research work here. He is my 'technical guru' and will hold a very important place in my life. Apart from technical knowledge he has also inspired me to be diligent towards my work and stay humble to other no matter at what position you stand. I am also thankful to him to extend his endless support and guidance throughout my PhD and helped to make this experience for me as smooth as possible. If in the world, I get a chance to do another PhD, I would still love to have Dr. Karaman as my advisor again.

I would also like to thank Dr. Raymundo Arroyave for being my second mentor and involving me in different projects which helped me to extend my learning horizons into machine learning and other computational materials science tools. Your guidance and discussion have always provided me with thought provoking insights into research has helped me to make the discoveries in my research. I would also like to acknowledge Dr. Anjana Talaptra for her support and collaboration work on CALPHAD studies of NiTiHf phase diagram, which bolstered my experimental results. I would also like to thank Dr.

Dimitris Lagoudas and Dr. Patrick Shamberger for serving on my dissertation committee and guiding my research towards completion.

I would also like to thank Shahin Boluki, Dr. Xiaoning Qian and Dr. Edward R. Dougherty for their collaboration on helping us with machine learning coding, which led us to discovery of novel NiTiHf SMAs. I would also like to thank Dr. Fan Zhang and Dr. Lyle Levine for their diligent efforts in conducting the X-ray scattering experiments for us, which has provided us with deep insights regarding the kinetics of H-phase precipitates.

I would like to thank Dr. Andrew Mott for helping me with Electron Microprobe and spending endless hours with me on the equipment. I will miss all that microprobe time Andrew. I would also like to thank Dr. Winson Kuo for his expertize in TEM and helping me with acquiring beautiful TEM images and successfully completing the TEM studies. I would also like to thank Dr. Anup Bandopadhay for conducting a number of DSC and TGA and XRD experiments for me as well as helping me in trouble-shooting other equipment's in the lab.

I would also like to thank Michael Eluverd, Robert Barber for helping me out with various equipment's in the machine shop and cutting endless number of samples for me. I would like to thank Michael Eluverd for helping me fix arc melter and various other equipment's in our lab essential for my research. I would also like to thank Michael Eluverd and his family for organizing and hosting my Bachelor's party at your ranch. Thanks for all the shooting experience as well, it was the bachelor's party I could have

thought of. I would also like to thank Murat Kaynak for his tremendous help during shifting of labs and witty jokes in coffee room.

Research acknowledgments cannot be completed without my very own MSEAM research group. I would like to thank Dr. Ankush Kothalkar, Dr. Ceylan Hayrettin, Dr. Taymaz Jozaghi, who graduated almost within a year or so after I joined but received me well in the group and made me comfortable with the lab working environment. I would like to specially thank Dr. Daniel Salas who became a very good friend a companion for grocery shopping. You are one of the humblest and kind person I have ever meet. Please keep it up. I would also like to thank Dr. Hande Ozcan, Dr. Kadri Atli Can, Dr. Omer Karakoc, Dr. Nick Barta, William Trehern, Benjamin Young, Sezer Picak, Woohyun Cho, Mathew Vaughan, Dominic Gehring, Olga Eliseeva, Raiyan Seede, Alex Demblon, Linda, Nathan Hite, Ryan Saucier for your support and scientific discussions and companionship. I would like to thank Wahaz Nazim for introducing me to K-pop and all the dinner's together watching trash youtube videos. I would also like to thank Lei Xue for being there for me always and bow-arrow and gun shooting events. Hope you find the lost arrow through the roof someday. I would also like to thank all my undergraduate students, Arber, Alex, Bradley, Carlos, Natalie, Nathan, Shengmin and entire CASMART team who gave me the opportunity to mentor them during their summer REU and other research projects. Hope I was a good mentor to you all and help you learn something

Life is always incomplete without good friends and I was fortunate to meet and have such people in my life. I would like to thank my lab-mate cum roommate Abhinav Srivastava for bearing with me over so many years. I would also like to thank my ex-

roommates Dr. Swanand Kadhe, Dr. Sneha Chawla, Dr. Shamik Basu for their support and being there for me always. I would also like to thank Janine Maier for being such a wonderful friend and travelling all the way to India for my wedding. All of my cousin's still miss you back there. I would also like to thank my very close friends Shubham Ingole and Pallavi Borkar for savoring the bond of lifelong friendship with me.

Lastly, I would like to thank my spiritual guru Sri Sri Paramhansa Yoganadaji for your unconditional love and silent blessings that has helped me to become self-aware.. Last but not the least, I would like to thank my family for standing with me through all life-situations and helping to endure hardships and bring the best out of me. All your love, care and dying support has helped me to become a better person.

It is because of you all, I am here.

CONTRIBUTORS AND FUNDING SOURCES

Contributors

The work was supervised by a dissertation committee consisting of Professor Ibrahim Karaman, Professor Raymundo Arroyave, Assistant Professor Patrick Shamberger of the Department of Materials Science and Engineering and Professor Dimitris Lagoudas of the Department of Aerospace Engineering.

The Small Angle X-ray Scattering was provided by Dr. Fan Zhang and Dr. Lyle Levine from the National Institute of Standards and Technology.

The machine learning predictions were provided by Shahin Boluki, Dr. Xiaoning Qian and Dr. Edward R. Dougherty from the Electrical and Computer Engineering department.

Funding Sources

My graduate study at Texas A&M Univeristy was made possible in part by National Science Foundation (NSF) - Designing Materials to Revolutionize and Engineer our Future (DMREF) under Grant no. 1534534. Its contents are solely the responsibility of the authors and do not necessarily represent the official views of the NSF.

NOMENCLATURE

A_f	Austenite Finish Temperature
A_p	Austenite Peak Temperature
A_s	Austenite Start Temperature
BCC	Body Centre Cubic
BSE	Back Scatter Electron
CC	Clausius–Clapeyron
σ_{SIM}	Critical Stress for Martensitic Transformation
DM	Diffusion Multiple
DSC	Differential Scanning Calorimetry
ECAE	Equal Channel Angular Extrusion
EPMA	Electron Microprobe Analyzer
HAADF	High Angle Annular Dark Field
HT	Heat Treatment
HTSMA	High Temperature Shape Memory Alloy
ε_{irr}	Irrecoverable strain
M_f	Martensite Finish Temperature
M_p	Martensite Peak Temperature
M_s	Martensite Start Temperature
MT	Martensitic Transformation
PPMS	Physical Property Measurement System

ε_{rec}	Recoverable strain
SEM	Scanning Electron Microscope
SIM	Stress Induced Martensite
SMAs	Shape Memory Alloy
SHT	Solution Heat Treatment
STEM	Scanning Transmission Electron Microscope
TGA	Thermogravimetric Analysis
TTs	Transformation Temperatures
TRIP	Transformation Inducted Plasticity
WQ	Water Quench
XRD`	X-ray Diffraction

TABLE OF CONTENTS

Page

LIST OF FIGURES

Page

LIST OF TABLES

Page

CHAPTER I

INTRODUCTION

This chapter emphasizes on the importance of choice of NiTiHf alloys as a novel high temperature shape memory alloy (HTSMA) candidate for actuation at high temperature applications. The main objective of the work is to explore the Ni-Ti-Hf system in order to design shape memory alloys (SMA) with specific targeted martensitic transformation characteristics, such as martensitic transformation temperatures, thermal hysteresis, transformation strain etc. The initial motivation for this work will be outlined, as to why Ni-Ti-Hf SMA systems is better, as compared to its other counterparts. Then, the objectives of this work will be outlined followed by a brief account of experimental and computational work planned in order to achieve the specific goals. Also, in the consecutive chapter an detailed background and literature review is also been provided in order to understand basic concepts related to martensitic transforming shape memory alloys and make the entire manuscript coherent for the readers.

1.1. Motivation

Shape memory alloys (SMAs) are a class of material that can “memorize” their original shape and recover it when stimulated with temperature, magnetic field and/or stress. This shape memory effect is a result of a reversible martensitic transformation (MT) between a high temperature, high symmetry austenite phase and a lower temperature, lower temperature martensite phase [1, 2]. A large amount of strains can be generated from the SMAs by utilizing the martensitic transformation. When the phase transition between austenite-martensite phases is carried out under a bias load, mechanical work output can be obtained [3], which is highly essential

in various aerospace, automobile and energy applications [4, 5]. Various SMA system has been widely explored and can be fairly classified as thermo- elastic or magneto strictive SMAs. The thermo-elastic SMAs converts the thermal energy to elastic energy, whereas the magneto strictive SMAs convert the electromagnetic energy to mechanical energy [6, 7]. The thermo-elastic SMAs are more robust and handier to operate than magneto strictive SMAs as it requires only an assembly of heating coils to generate temperature stimulus. On the other hand, magneto strictive SMAs possess lower strength and requires a complicated magnetic setup in order to induce the magnetic stimulus into the SMA. Hence despite of some magnetic SMAs produce larger strain as compared to the thermo-elastic SMAs, their applicability in intricate and critical applications such as aerospace, energy and transportation is limited because of the complicated machineries and setup required to operate it.

The shape memory alloys were discovered in early 1950s, as it was first observed in Au-Cd beta phase [8] and later in In-Tl system [9, 10] followed by the Ni-Ti phase in 1963 by Buehler et al [11]. Since then, NiTi system is the mostly widely studied SMA system because of its enhanced strength, transformation strain, corrosion resistance and biocompatibility [1, 2, 6]. Because of such extraordinary properties, the NiTi alloys have found applications from aerospace to biomedical industry [5, 12]. The transformation temperatures and thermal hysteresis of NiTi SMAs can also be tailored to the required values by changing the composition or short time aging heat treatments [13, 14]. Short term aging heat treatments tends to promote Ni_4Ti_3 intermetallic precipitation, which tends to increase the strength, transformation temperatures and provide cyclic stability to the alloy [15-19]. Despite of possessing such key properties, one of the major drawbacks or limitations of use of NiTi is that the transformation temperatures are limited below 100°C. Recent advanced aerospace applications of SMAs in aerospace, automobile and other fields

such as variable geometry chevrons, variable geometry nozzles etc., required the SMA component to undergo martensitic transformation at a temperature higher than 100°C and hence conventional NiTi SMAs cannot be used [20].

Such advanced aforementioned applications need a robust SMA which is thermally and mechanically stable at an operation temperature (>100°C) and can render solid state actuation at elevated temperatures without undergoing creep. Such SMAs that exhibit transformation above 100°C are termed as High Temperature Shape Memory Alloys (HTSMAs). Such alloys have a great deal of potential and are extensively studied recently because of their unique potential candidacy to replace complicated pneumatic actuators and thus offer lightweight solutions to many aerospace problems. There are a wide range of materials systems that can transform at higher transformation temperatures (TTs), such as U-Nb [21-23], Ru-Nb [9, 24-26], Ru-Ta [8, 27] systems but are highly unlikely to be used to commercial applications because of presence of radioactive elements. There are also several Co-based [28, 29], Cu-based [30-32], NiMn-based [7, 32-34] SMAs with TTs with high transformation temperatures, but due to their magnetic behavior or lower strength, they cannot be implemented into critical aerospace applications. One more effective way to increase the TTs is by ternary and quaternary alloying to the NiTi SMAs [35]. Elements like Ag, Pt, Pd, Zr, Hf are added in order to enhance the TTs. As Ag, Pt and Pd addition is very expensive and hence not suitable for commercializing purposes. Also, the precipitation in NiTiPd and NiTiPt systems is not stable and makes the system more complicated for use [36-38], as dynamic precipitation occurs at the operation temperature and hence the TTs, strength changes with consecutive number of transformation cycles. As precipitates tends to grow more and more with time, the strength of the material deteriorates in service. Apart from unstable precipitation related issues, the material also experiences very high transformation induced plasticity and creep

at high operating temperatures and thus increasing the possibility of failure exponentially [4, 39]. Though the NiTiPd and NiTiPt alloys possess high transformation temperatures and narrow hysteresis, its use is limited because of its cost, unstable precipitation, TRIP and creep associated failures. Therefore, the focus in last decade is highly diverted to NiTiHf and NiTiZr alloys, as they are relatively inexpensive, lightweight and exhibits stable precipitation as compared to NiTiPd, NiTiPd and NiTiAu alloys.

Among the NiTiHf/Zr alloys, addition of Zr is less preferable because of its poor thermal and dimensional stability [4, 40] as the transformation temperatures changes heavily with initial transformation cycles. Ma et al [4] compared Differential Scanning Calorimetry (DSC) data from various sources and showed that the TTs of NiTiHf alloy stabilize in the first 5 DSC cycles whereas that of the NiTiZr alloys do no stabilize even completely even after 100 DSC cycles. Apart from TTs, NiTiHf alloys are relatively stronger than NiTiZr alloys and hence exhibit very stable thermo-mechanical cycling under load. The NiTiHf alloys tends to show higher transformation recovery and exhibit very low irrecoverable strains and hence stands out to be the most eligible candidate for the high temperature actuation based applications in the aerospace, energy and transportation industry. Therefore, Hf addition is most economical and robust [41-43].

The NiTiHf alloy firstly discovered by AbuJodam et al [44], where the authors studied $Ni_{49}Ti_{51-x}Hf_x$ alloys with varying Hf from x= 0 at.% to Hf=30 at.% and found that with increasing the Hf content, the martensitic peak temperature (M_p) and the austenitic peak temperature (A_p) increases slightly up to Hf=10 at.% addition followed by a drastic increase upto Hf=30 at.%. AbuJodam et al, so showed that with increasing the Hf content, the hardness value increases drastically with initial increase in Hf content. The hardness variation with Hf content tends to follow a parabolic trend, where the parabola is symmetric along the X-axis. AbuJodam et al, also

studied the dependence of Hf content on the TTs by fabricating and testing various $Ni_xTi_{90-x}Hf_{10}$, with varying Ni content from x=40 at.% to x=51 at.% alloys in order to obtain the TTs. The authors observed that with increasing Ni content the TTs didn't change until 48.at% addition. Beyond Ni=48 at.% addition the TTs tend to increase slightly for Ni=49 at.% followed by a steep decrease until Ni=51 at.% . Similar studies were also performed by Angst et al [45], Olier et al [46], Thoma et al [47] and others [48-51] also conducted similar research on Ni-lean (Ni<50 at.%) NiTiHf alloys and observed similar trends. Besseghini et al [40] heat treated the Ni-lean NiTiHf alloys at 800°C for 1hr followed by water quenching (WQ) and reported that with increasing the Ni content, the amount of second phase i.e., $(Ti+Hf)_4Ni_2O_x$ decreases.

Much later in 1997 Han et al conducted aging heat treatment at 600°C for 150 hours on a Ni48.5TiHf15 alloy and conducted extensive Transmission Electron Microscopy (TEM) revealing the presence of a precipitate phase which possess an orthorhombic structure and belongs to the F 2/d 2/d 2/d space group [52]. Han named these precipitates as 'H-phase precipitates' after his name. Meng et al studied the H-phase precipitation in the Ni-rich (Ni>50 at.%) NiTiHf alloys and showed the precipitate phase tends to enhance the transformation temperatures and also improves the thermal stability of the material [53-55]. Evirgen et al revealed that by performing secondary aging precipitation heat treatments on $Ni_{50.3}TiHf_{15}$ alloy, the TTs can be changed over a span of 100˚C in the same starting composition [56, 57], as the aging heat treatments facilitate the growth of H-phase precipitates. Therefore, unlike in NiTi, TTs in NiTiHf can also be tailored over a wide range via compositional [35, 45-47, 58] and precipitation [53-55, 57] changes. Despite owning excellent tailorable transformation characteristics, the Ni-rich side of the NiTiHf system is not explored systematically. The studies conducted in early 1990's by aforementioned authors has only explored Ni-lean systems and in the last decade very specific compositions such as $Ni_{(50.3,51)}TiHf_{(15,20,25)}$

alloys. Also there is a lot of discrepancies among the available literature data so far regarding the mismatch between targeted composition and actual composition. Recently many studies have been based on $Ni_{50.3}Ti_{29.7}Hf_{20}$ alloy and the reported value of M_s temperature among them for solution heat treated (SHT) sample varies over a range of 150°C [58-63]. Therefore, a detailed study is needed to be done in order to understand the compositional dependence of transformation temperatures on NiTiHf alloys more accurately and reliably, especially in the Ni-rich side of the NiTiHf alloys. Knowledge of such compositional dependence on TTs will unable to aid us design alloys with required transformation characteristics.

Along with composition, as mentioned above, precipitation is also one of the common methods to tune the transformation characteristics in NiTi based systems. Upon performing short term aging heat treatments on the Ni-rich NiTi binary alloy, yields an intermetallic Ni_4Ti_3 like precipitates which strength the alloy, increases the TTs and decrease the irrecoverable strains when the material undergoes thermo-mechanical cycling under load [1, 2, 15-17, 19, 64-66]. As mentioned before, Han et al [52] discovered the H-phase precipitates in NiTiHf system and mentioned it to be orthorhombic, but he did not analyze the composition of the precipitates. Meng et al in early 2000's, mentioned that the H-phase precipitates are $Ni_4(Ti,Hf)_3$ like just similar to that found in the NiTi binary system [53, 55]. Recently in 2012, Santamarta et al [67] and Yang et al [68] in their indigenous work, found out that the H-phase precipitate has a composition of around Ni=51.7 to 53 at.% whereas Hf=27 to 33 at.% and found out that the H-phase precipitate has a unit cell of 192 atoms and possess a certain crystallographic relationship with the B2 austenite phase. Santamarta et al also conducted the precipitation studies on different compositions of NiTiHf alloys and revealed that the precipitation kinetics of the H-phase is increases with increasing Ni content of the material. The authors also revealed that the H-phase is a super-structure From

various literature survey's it can be observed that the measured composition of the H-phase precipitates varied with changing the initial starting composition of the material for the same heat treatment time and temperature [59, 67-69]. This signifies that the H-phase composition changes, unlike that of Ni_4Ti_3 precipitates, where the composition is fixed despite of the initial composition of the NiTi binary alloy. Therefore, based on such observations, I hypothesize that the H-phase precipitate is not a line compound as an intermetallic like but is a solid solution phase and occupies the region in the phase diagram. Knowledge of such equilibrium between the H-phase and the B2 Ni(Ti,Hf) martensitically transforming phase will aid in designing the novel NiTiHf SMAs with required transformation temperatures and develop precipitation models.

Importance of precipitation in NiTiHf system has been pointed out by various researchers, in regard of enhancing the strength, TTs and thermal and dimensional stability and decreases the plastic deformation arising from martensitic transformation [4, 34, 41, 42, 58, 63, 70-72]. All the aforementioned transformation characteristics results from the size, distribution, volume fraction and interparticle distance between the H-phase precipitates in the micro-structure. Evirgen et al have conducted a systematic study by heat treating the $Ni_{50.3}TiHf_{15}$ alloy at different temperatures ranging from 450°C to 600°C and different time ranging from 30 minutes to 48 hours [57]. Evirgen et al demonstrated that by employing different heat treatment parameters, the size and interparticle distance of the H-phase particles can be controlled. If the H-phase particles are small (5-10 nm), the B2 austenite phase matrix gets trapped within the tiny precipitates and the critical size of nucleation for martensite decreases and hence a higher degree of undercooling is required to convert the B2 austenite to B19' martensite and hence the M_s temperature decreases. When the precipitate size increases, the critical radius of nucleation for martensite increases as the matrix is depleted of Ni, the Ni content of the matrix decreases and the TT_s increase. Therefore, knowledge

of such H-phase precipitation kinetics can be used to control the size and interparticle distance of the H-phase precipitates and hence develop NiTiHf alloys with required transformation properties and also generate various micro-mechanical models to predict the TTs and transformations strains, etc.

Apart from the compositional and micro-structural aspects of the material science, an aspect of data-science known as 'machine learning' can also be implemented to design the NiTiHf alloys with required transformation properties. To date, most of the recent developments in HTSMAs are based on trial and error or intuition-guided experimental efforts based on the published literature. Some of the studies utilizes the measure of crystallographic compatibility (λ_2 value) between martensite and austenite phase and the combinatorial method suggests that the more compatible both the phases are, lower is the thermal hysteresis [73-76]. But Evirgen et al studied the λ_2 value dependence on hysteresis of Ni50.3TiHf20 alloy in SHT and aged condition, and revealed that the slope of λ_2 Vs hysteresis curve for NiTiHf system is much shallow and hence the crystallographic compatibility is not highly related to thermal hysteresis of the alloy [77]. Very less efforts have been made in the direction to explore the statistical or machine learning (ML) based approaches to design the SMAs with required TTs [78, 79]. These ML based studies utilized physical and chemical parameters such as atomic radii, electronegativity, composition, volume fraction etc, to generate a model or a set of mathematical equations which related the properties to TTs with certain associated uncertainties. Then this model is used to make predictions for the next best candidate alloy to meet the required TTs. Upon testing the predicted composition, obtained results are combined with initial database and again the model framework is executed to obtain another prediction. In such an iterative fashion, novel NiTiHf HTSMAs can be designed for required applications.

Therefore, as NiTiHf alloys stands out of the class of HTSMAs and hence a more systematic approach should be observed in order to address the above arising questions. One has to work along the outlined motivation in the current section, which will facilitate the development of novel NiTiHf HTSMAs as per aerospace, automobile and oil and gas industries. Therefore, a detailed compositional dependence of TTs study will be performed to understand their inter-relation. This TTs data can also be utilized as initial dataset in the machine learning model to design new NiTiHf alloys. The precipitation kinetics will be examined thoroughly with using small angle X-ray scattering experiments and the phase equilibrium will be analyzed using the diffusion multiple experiments. Once, the above data is obtained, the development of NiTiHf alloys will be highly enhanced and instead of trivial trial and error methods, a more guided, structured and systematic approach can be implemented. Fig. 1.1 shows the over arcing goal of the research, which shows different chemistry based, micro-structural based and data-science based approaches that can be implemented to design novel NiTiHf alloys with required transformation temperatures for specific applications. Such approach is very universal and can be implemented to any material system in order to optimize or discover material properties tailored to the specific applications.

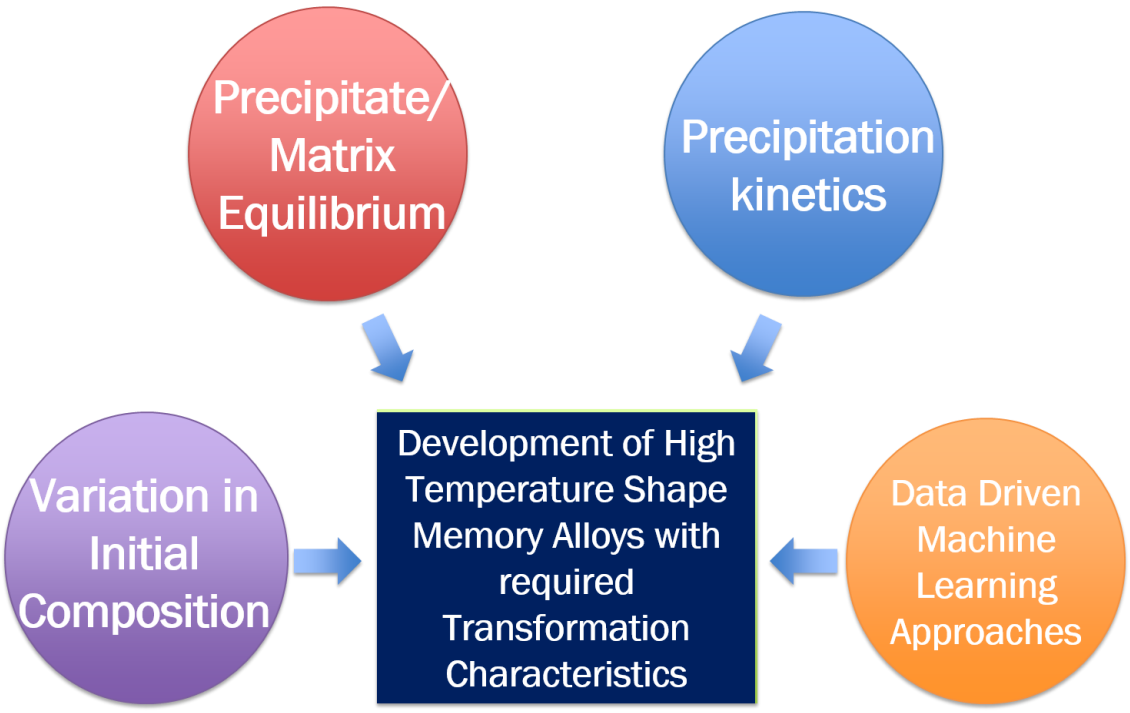

Figure 1.1 Overview of the research

1.2. Objective

To conquer the above mentioned feat in section 1.1, efforts were made with a goal to find out effective methodologies to develop and design novel NiTiHf HTSMAs with required transformation temperatures. The main objective of this work is to demonstrate that the aforementioned 4 different methods can be used to derive a guidance map or framework towards development of NiTiHf alloys which can then further extended to different material systems.

The compositional dependence on TTs study of NiTiHf alloys, firstly will help in exploring the Ni-rich compositional space for TTs thoroughly, as so far only Ni-lean systems has been explored in detail. As the data obtained under this study is from a very reliable methodology and hence the variation of actual composition from the targeted composition is negligible. Secondly, as this study will yield a composition Vs TTs map that will serve as a guideline or guide map for

all researchers who mass produce the alloy and as a result tend to deviate more from the targeted compositions. Comparing the TTs obtained from the composition Vs TTs map will help to find out the actual composition of the mass produced ingot.

The second aim of this study is to understand the thermodynamics of the H-phase in the Ni-Ti-Hf phase equilibria. The study aims to find if the H-phase is an equilibrium stable phase or a meta-stable phase. This work also aims to seek whether the H-phase is a solid solution equilibrium phase and occupies a region in the equilibrium phase diagram, unlike the Ni_4Ti_3 phase in NiTi which is an intermetallic phase. If the establishment of equilibrium between the H-phase precipitates and B2 martensitically transforming phase is confirmed, then the corresponding tie-lines connecting the two phases can be used as guidelines to design new NiTiHf alloys with required TTs and other shape memory properties.

The third aim of the work is to study the kinetics of the H-phase precipitation in the NiTiHf alloys at different heat treatment temperatures. The study of kinetics will utilize the advanced X-ray Diffraction experiments to analyze the in-situ evolution of the size and volume fraction of the H-phase precipitates. The resultant kinetic study will be used in association with the transformation strain results to understand the effect of differential H-phase kinetics on the shape memory strain of NiTiHf alloys. This work will give a great insight towards controlling the TTs and other transformation characteristics using the size and volume fraction of the precipitates.

Lastly, the study aims to utilize the artificial intelligence approach known as ‘machine learning’ to design new alloys with required transformation characteristics. The compositional dependence on TTs data obtained in this work will serve as an initial database that the machine learning needs in order to train the model. As the initial dataset is prepared in a highly clean atmosphere and hence the oxygen contamination is eliminated to a large extent. The post-melt

processing of the alloy is done with extreme care by the same person and hence the errors arising from external factors have been minimized. This helps in developing a highly accurate model to make the prediction, for the alloy needed to be designed for specific purposes.

In order to summarize, this study makes sincere efforts to explore the Ni-Ti-Hf system with respect to chemistry, thermodynamics and kinetics and understand their effect on the transformation characteristics. By exploring these traits, the study tries to establish a strong co-relation between the chemistry, thermodynamics and kinetics based parameters and the TTs, as well strive to present a framework which can be utilized to design novel NiTiHf HTSMAs for high temperature applications.

CHAPTER II

BACKGROUND AND MOTIVATION

In this chapter, a detailed background knowledge is provided in order to understand the concepts and terminologies used in the study and make the dissertation reading more coherent for the readers. Along with basic concepts, this chapter also includes literature review of all the research work performed on NiTiHf alloys so far, related to the study. Lastly, this chapter also highlights the current state of art research in all the four different aspects (mentioned in Fig, 1.1), that are utilized to design the NiTiHf alloys.

2.1 Martensitic Phase Transformation

A martensitic phase transformation is a solid to solid phase transformation associated between a high temperature, high crystallographic symmetry austenite phase to a low temperature, low symmetry martensite phase. The martensitic phase transformation can also be utilized this transformation between the two phases can result by a stimulus in temperature, pressure, magnetic field, or a mixture of them. A certain class of materials that undergoes martensitic transformation in such a way that they remember their pre-deformed shape and can regain it by reverse transformation. Such alloys who can memorize their pre-strained shape are called as ‘shape memory alloys’. Such a reversible martensitic phase transformation can be utilized as actuators, which upon stimulus can change shape and have potential to replace complex pneumatic hydraulic systems.

2.1.1 Mechanism of Martensitic Phase Transformation in SMAs

Shape Memory Alloys (SMAs) as mentioned are able to recall their pre-deformed shape as a result of solid to solid phase reversible martensitic transformation (MT) between the austenite and martensite phase. During the MT, the atoms in the crystal structure of the austenite phase moves or diffuses over a very short range with a coordinated shear, such that the near neighboring atoms remain the same, but the crystal structure is transformed to martensite. This transformation from austenite to martensite is termed as forwards MT and vice versa. Such a transformation is capable to introduce macroscopic strains within the material. During the forward MT, a large amount of local strain is generated within the material as a highly symmetric crystal stricture transforms to a less symmetric one. These local strains produced are so high that all of it cannot be accommodated elastically and hence in order to compensate the excess strain, a twinned martensite structure is formed as shown in Fig. 2.1.

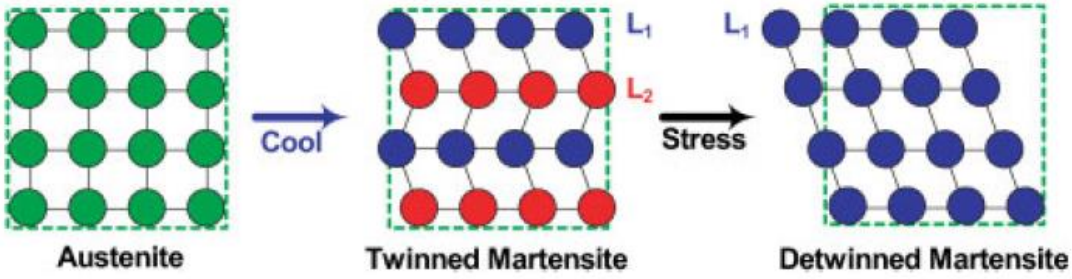

Figure 2.1 Schematic of martensitic phase transformation from a high symmetry austenite phase upon cooling transforms into a self-accommodating twin martensite structure. The twinned martensite structure formed consist of multiple lattice variants labeled as L1 and L2. Upon application of stress on twinned martensite one of the favorable variants grow at the expense of other and hence resulting in a detwinned single variant martensite [4].

For the MT to occur there are several different pathways by which the highly symmetric austenite can transform to a lower symmetry martensite structure. These different 'pathways' are related to the different number of ways in which the austenite unit cell can be deformed or distorted such that it transforms into a martensite unit cell. These different pathways are related to different sequences in which the bond length and bond angle in austenite unit cell will change and the move towards achieving the martensite unit cell. These different pathways are called as martensite lattice correspondence variants. For example, there are 12 different ways in which a body centered cubic (BCC) austenite can transform into a monoclinic martensite structure or in other words there are 12 lattice correspondence variants with which a monoclinic martensite can be formed from BCC austenite. Under stress free conditions all of the lattice correspondence variants individually are energetically equivalent to each other. But by forming twin related lattice correspondence variants, the system is able to accommodate a much large amount of strain upon MT as compared to that accommodated by adopting only one lattice correspondence variant. Fig. 2.1 depicts an example where under stress free condition upon cooling the austenite transforms to a martensitic structure formed by twinned lattice correspondence variants. These twin related lattice correspondence variants are referred to as habit plane variants. Therefore, during a forward MT, several such twinned lattice correspondence variants (or habit plane variants) can form which collectively contributes in accommodating the transformation strains and result is practically no evident macroscopic change in shape upon MT. Such a martensite structure which is the combination of several habit plane variants is called as a 'self-accommodating martensite'.

When an external load is applied to such a self-accommodated martensite structure, the habit plane variants that are favorable to grow in the direction of applied stress grows at the expense of others and thus resulting in a deformed single habit plane variant martensite. Also the

martensite variants can detwin upon application of stress and the lattice correspondence variant that is favorable or in other words capable to accommodate the desired strains will grow at the expense of other as shown in Fig. 2.1[4]. More detailed information regarding MT mechanics can be found in these references [2, 4, 6, 80-93].

2.1.2 Shape Memory and Superelasticity Effect

The martensitic transformation in an SMA can be introduced by either stress or temperature or both. Increase in temperature and decrease in applied stress makes the austenite phase more stable, whereas decrease in temperature and increase in applied stress drives the austenite → martensite reaction forward. Actually, the stress and temperature bear an intimate linear relationship, when it comes to MT. A linear relationship between them can be established using the thermodynamic principles for phase transformation, also called as the Clausius Clapeyron relationship. It states that the $d\sigma/dT$ = constant, i.e., the transformation temperatures is a straight line in the σ-T plane.

The MT by its very nature, does not happen all together at one single value of temperature or pressure, rather it transforms over a range. It is because as any SMA system is not ideal and the martensite has to nucleate first inside an austenite matrix. This point at which martensite nuclei are formed inside the material is termed as martensite start temperature (M_s). In order to make these martensite nuclei grow, an extra under-cooling is required to provide enough driving force. Therefore, as temperature decreases, the martensite grows more and the temperature at which the material completely transforms to 100% martensite is called as the Martensite Finish Temperature (M_f). Conversely, upon heating, the martensite plates start to collapse, and austenite start to form. The temperature at which martensite → austenite is called as Austenite Start Temperature (As),

i.e., onset of reverse transformation. He temperature at which the material completely transforms back to 100% austenite is called Austenite Finish Temperature (A_f). All of the above mentioned transformation temperatures follow the linear relationship σ-T plane, and represent as parallel lines for an ideal SMA, as shown in Fig 2.2. In practical application, as the SMA system is not ideal and there are various losses related to transformation and increased mobility of microstructural features (grain boundary, dislocations etc.) hence these TTs lines tend to deviate from their parallelism. In Fig. 2,2 it is clearly evident that temperature or stress or both can aid in MT. The region to the left of Mf line in Fig. 2.2 marks the stability of martensite phase whereas the region to the right of the Af line marks the regime of stability of austenite in the σ-T plane.

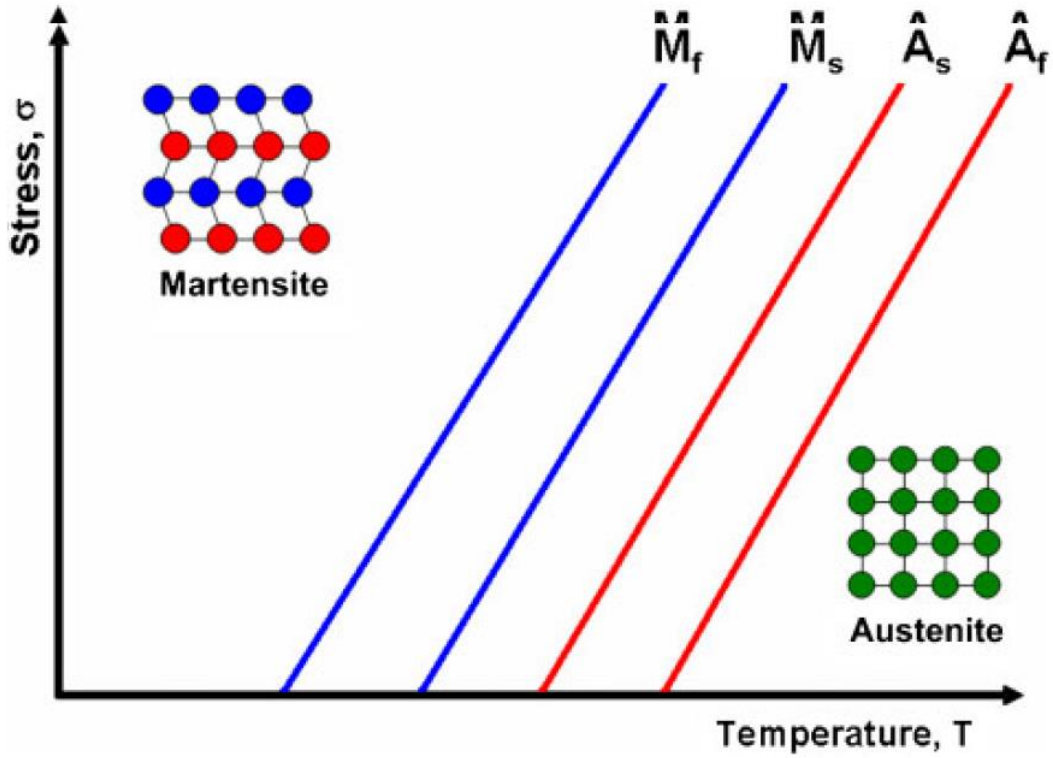

Figure 2.2 The Stress-Temperature pane behavior of the SMA undergoing martensitic transformation as a result of change in stress or temperature or both. The SMA is in complete martensite phase to the left of M_f line, whereas the SMA is in fully austenite state to the right of A_f line [4].

The phenomenon of recovering the pre-deformed shape is known as the shape memory effect. When a sample of an SMA is at lower temperature, it is in martensitic state or twinned martensite. Upon deforming the SMA sample the twinned martensite structure within the sample starts converting into a single lattice correspondence variant or detwinned martensite. When this deformed detwinned martensite sample is heated above and upon formation of austenite phase the sample regains its original pre-deformed shape, as shown in the strain-temperature plane of Fig. 2.3. Upon cooling back from austenite to martensite the sample maintains its original shape and all the strains from martensitic transformation are accommodated by forming twinned self-accommodating martensite. This phenomenon when carried out under no bias load or constant stress, then such a phenomenon is called as ‘shape memory effect’. When the same heat-cooling effect is carried out under external constant force, then it is called as ‘isobaric shape memory effect’, as shown in Fig. 2.3.

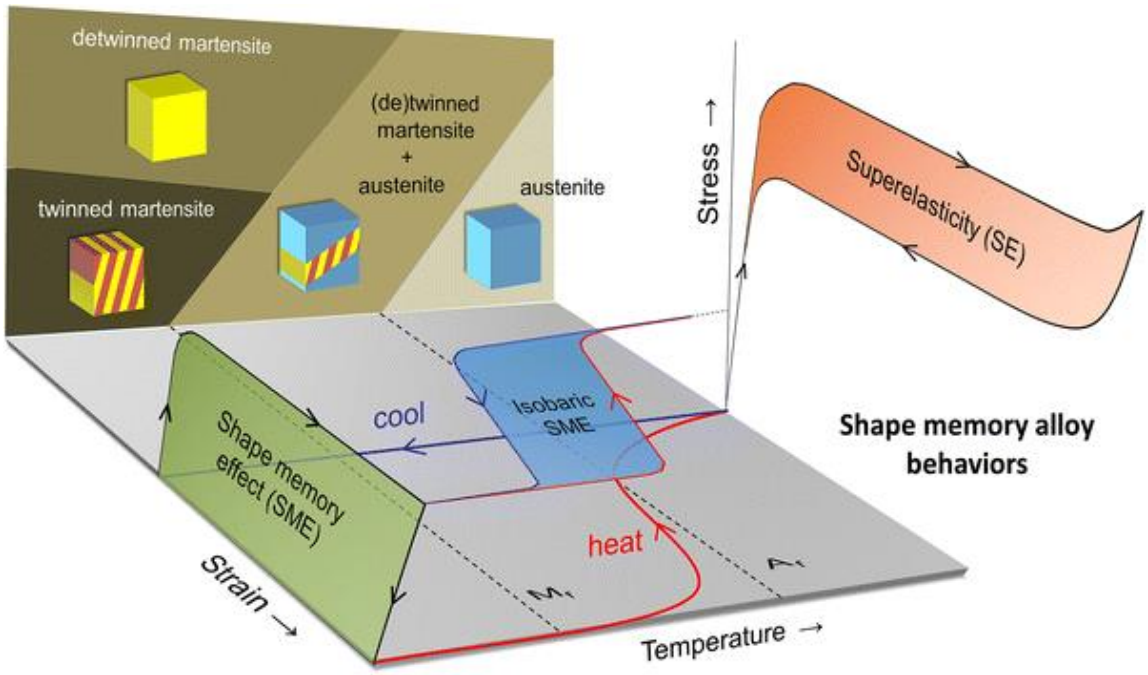

Figure 2.3 A three dimensional presentation of general three phenomenon (viz., shape memory effect, isobaric shape memory effect and superelasticity effect) occurring inside a shape memory alloy upon being used as an actuator. [94].

The superelasticity effect also called as the pseudo-elasticity effect is observed when the material is in complete austenite state and cycled by varying stress under constant isothermal conditions. When a stress is applied on the austenite phase, it initially undergoes an elastic deformation, which is depicted by a straight line in the stress-strain plane as shown in Fig. 2.3. As the applied stress is increased above a certain critical value, which is known as the critical stress for martensitic transformation (σ_{SIM}), the austenite starts to transform to martensite. This phenomenon of introduction of martensite above A_f temperature under applied stress is known as 'stress induced martensite' (SIM). Once the σ_{SIM} is reached, the austenite is transformed to martensite and the strain associated with this MT appears by a plateau in the stress-strain plot as shown in Fig. 2.3. Once the 100% martensite is stabilized and the stress is increased above σ_{SIM} then elastic deformation of martensite occurs. Upon release of this applied stress, the martensite

will undergo a reverse MT to austenite as the isothermal is still above A_f. This reverse MT is associated with the strain, which appears as a plateau in the reverse direction as shown in Fig. 2.3. Upon transforming to 100% austenite, all the strain from forward transformation is recovered during the reverse transformation by an ideal SMA and hence complete shape recovery has occurred. Such a phenomenon of complete recovery of strain via a forward and reverse MT is called as the superelasticity or pseudo-elasticity effect in SMAs.

2.1.3 Characterization of Shape Memory Properties

The SMAs undergoing a martensitic transformation can be characterized by different equipment's which can sense the energy of MT or phenomenon due to the change in crystal structure or from the strain arising as a result of MT. The DSC or thermogravimetric analysis (TGA) measurements as a function of change in temperature, can be used to analyze TTs based on their sensitivity to detect the exothermic/endothermic energies associated with MT. The electrical resistivity measurements as a function of temperature also helps in detecting the TTs as there is a change in crystal structure when the MT occurs. Usually a DSC cannot function with great accuracy below -120°C and hence one has to seek help of electrical resistivity measurements as a function of temperature using a Physical Property Measurement System in order to detect TTs below -120°C. As the DSC and TGA functions on the similar principle in order to compute the TTs, hence the working of DSC will be demonstrated here followed by electrical resistivity measurement. A typical DSC response from an SMA is shown in Fig. 2.4. When the sample is cooled from higher temperature phase austenite to a lower temperature phase, this forward MT is exothermic in nature, whereas the reverse MT is endothermic. The DSC or TGA is capable of detecting the energy liberated or absorbed during the respective MT and hence can be used to

analyze TTs.

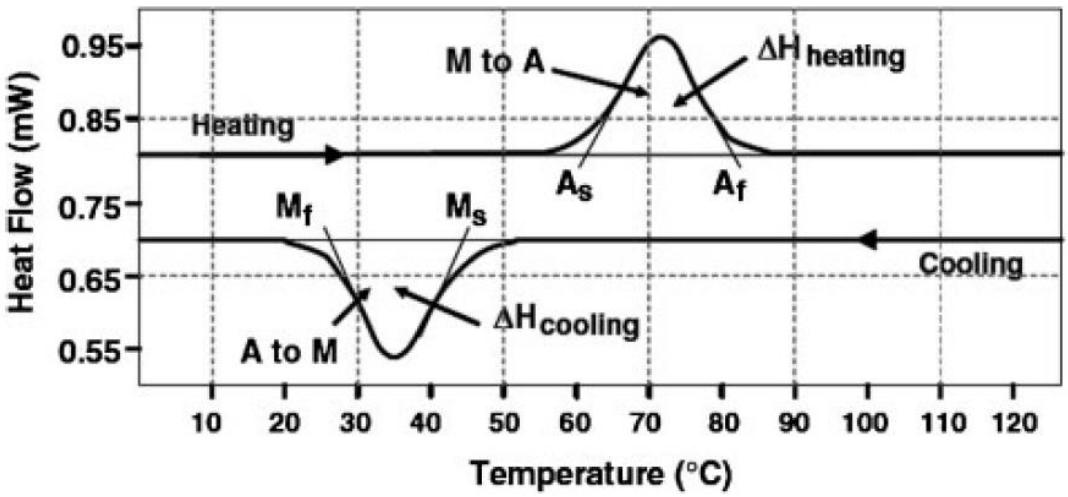

Figure 2.4 A schematic of DSC data which shows the martensitic transformation start and finish i.e., M_s, M_f, A_s, A_f. The thermal hysteresis of an SMA is defined by difference between the A_f and M_s (A_f - M_s) [4].

The measurement of electrical resistance as a function of temperature can also be used to analyze the TTs, based on a simple principle that change in crystal structure will yield a change in resistivity of the material. As seen from Fig. 2.5, it can be seen that upon cooling the austenite phase from room temperature, the resistivity of the material increases with decreasing temperature. Upon reaching a particular temperature, when the austenite starts to transform to martensite, the crystal structure starts to change which is reflected by inflection in the resistivity – temperature plot. This particular temperature is marked by M_s temperature in Fig. 2.5. When the MT is complete and now the sample contains only

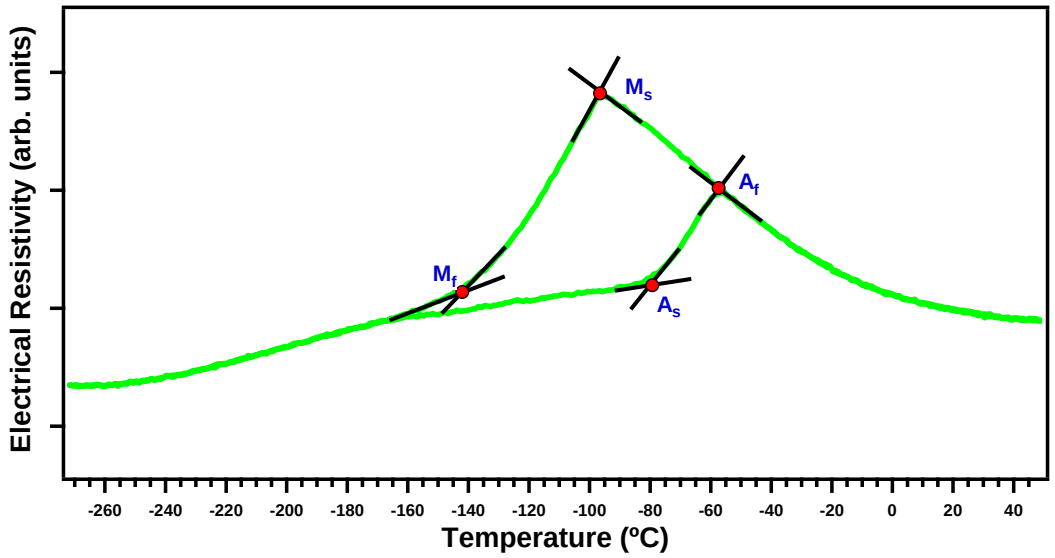

Figure 2.5 Schematic of a NiTi sample depicting the resistivity measurement as a function of temperature. Upon cooling the austenite starts transforming to martensite and as the crystal structure starts to change due to MT, the nature of resistivity dependence on temperature also changes, which can be marked by M_s temperature. Similarly, other TTs can also be marked.

100% martensite, the slope of the resistivity-temperature curve will show an inflection point as the crystal structure transition is complete, which is marked by M_f temperature in Fig. 2.5. In similar fashion, inflection points can be marked while heating the sample and A_s and A_f temperatures can me identified accordingly.

Along with stress free analysis of TTs, it is also important to analyze the TTs and transformation strain (ε_{tr}) that is arising from the occurrence of isobaric SME or superelasticity in stressed, as any SMA component in application will be under some form of stress. A standard procedure to test the isobaric SME of an SMA, a tension dog-bone

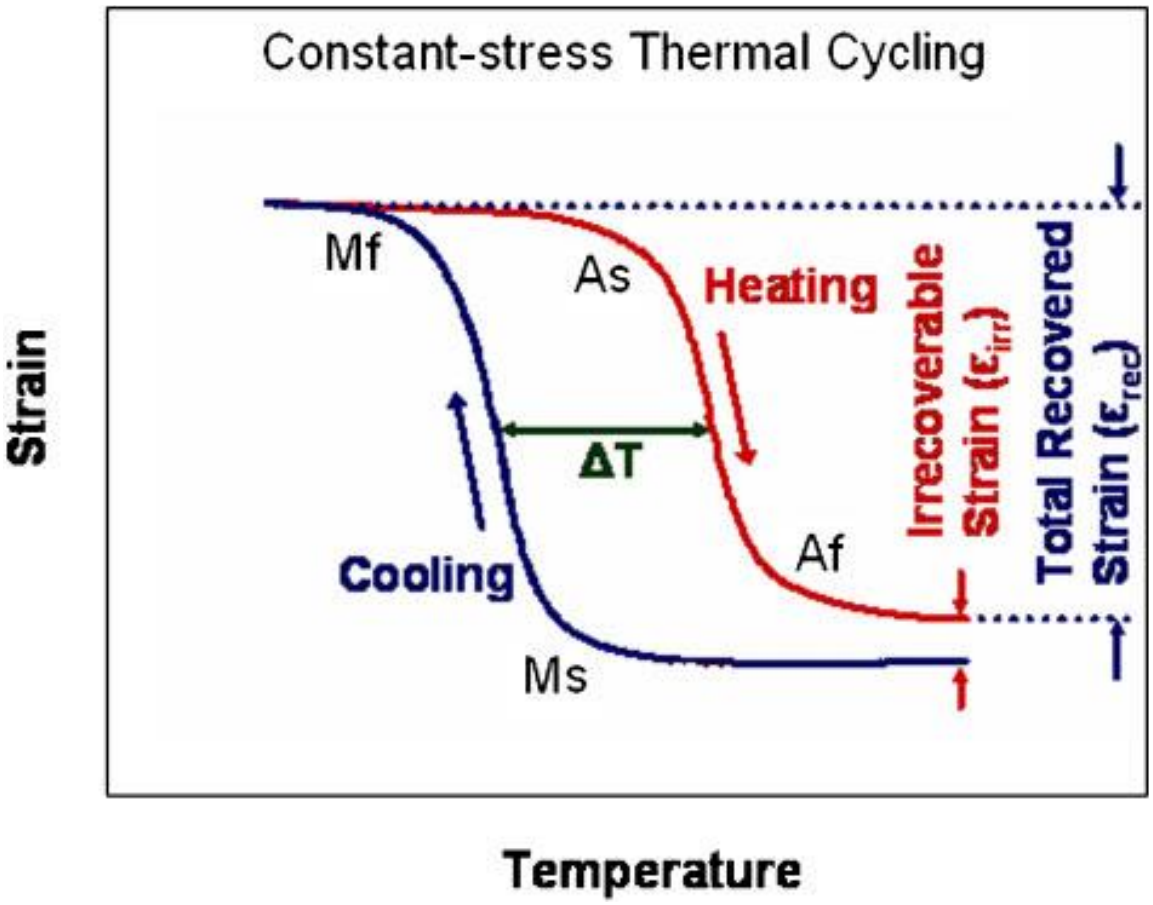

Figure 2.6 A schematic of an isobaric SME or constant-stress thermal cycling. Under stress the material undergoes MT at higher TTs as compared to the stress-free condition. The TTs is analyzed by change in strain associated with MT and the inflection points in strain-temperature plot is marked accordingly. On completion of 1 cycle, the amount of total strain that is recovered by the material upon reverse and forward MT is recoverable strain (ε_{rec}) whereas the plastic deformation incurred during the cycle is called as irrecoverable strain (ε_{irr}) [4].

sample is used. The sample is subjected to subsequent increasing stress and thermally cycled in order to obtain the MT response of the SMA. Starting in austenite, when the material is cooled under stress, upon advent of MT, the strain associated with the MT triggers in and the inflection point in strain-temperature plot. This first inflection point on cooling from austenite is the M_s temperature. As the MT is progressing, there is a continuous increase in strain until M_f is reached. Below M_f as the material is 100% martensite, no more significant change in strain is obtained upon

further cooling. Similarly, upon heating the martensite, upon start of austenite formation, the strain associated from reverse transformation arises and a steep decrease in strain is observed from A_s to A_f. The thermal hysteresis (ΔT) is expressed as the difference in temperature recorded during 50% completion of the forward and reverse transformation as shown in Fig. 2.6. Apart from TTs, it is also crucial to determine the strains associated with the MT. Upon completing one cycle of forward and reverse MT, the material returns back to austenite phase and the strain recovered during reverse MT is called as recoverable strain (ε_{rec}) and the difference between the strain experienced during forward MT and reverse MT is called as irrecoverable strain (ε_{irr}). Therefore, if strains experienced during forward and reverse MT is same, then the material will recover its original shape completely, i.e., $\varepsilon_{irr} = 0$. But usually at high stress level, all of the strains endured by the material during the forward MT is not equal to the amount of strain recovered during reverse MT and hence the material cannot recover its original shape completely i.e., $\varepsilon_{irr} \neq 0$, because of development of dislocations arising from incompatibilities at austenite-martensite transformation fronts and plastic deformation experienced due to high stress levels.

Similarly, during a superelastic test, where the material is loaded-unloaded at a constant temperature and such loading-unloading cycles are carried out at several temperatures. Usually the SMA exhibits the superelastic properties above A_f, but the larger the difference between the testing temperature, the larger is the driving force required by the SMA to undergo stress induced transformation. Therefore, higher stress values will be required to induce transformation and hence as the material will undergo plastic deformation at higher stress values the resultant super-elastic properties will be poor. Once the test temperature rises above a certain temperature called M_d, the stress induced MT is not the dominant deformation mode but instead the plastic deformation of austenite is. Fig. 2.7 shows a schematic of a superelastic test at a temperature above the A_f. Upon

application of stress, the austenite deforms elastically until σ_{SIM} is reached. At σ_{SIM} the stress induces forward MT, the sample starts to transform to martensite and a plateau is reached in the stress-strain plot. So the forward MT, occurs which is marked by the large amount of strain with a very slight change in stress. Upon further increase in stress the martensite starts to deform elastically. When this stress is released, the martensite starts to recover certain strain as a result of recovery due to elastic deformation (ε_{el}). When the applied stress decreases below σ_{SIM}, the material starts to transform back to martensite. This reverse transformation also shows a plateau and again a lot of strain is recovered with a very slight change in stress. This strain recovered because of reverse MT is called as superelastic strain (ε_{se}). The sum of elastic recovery and recovery due to reverse MT is the total recovered strain ($\varepsilon_{rec} = \varepsilon_{se} + \varepsilon_{el}$). Upon the completion of transformation, the material is back in austenitic state and when the stress reaches zero, the austenite seizes to deform. The amount of strain that is still not recovered is called as the irrecoverable strain (ε_{irr}). The recovered and irrecoverable strain tend to increase with the increasing applied strain value.

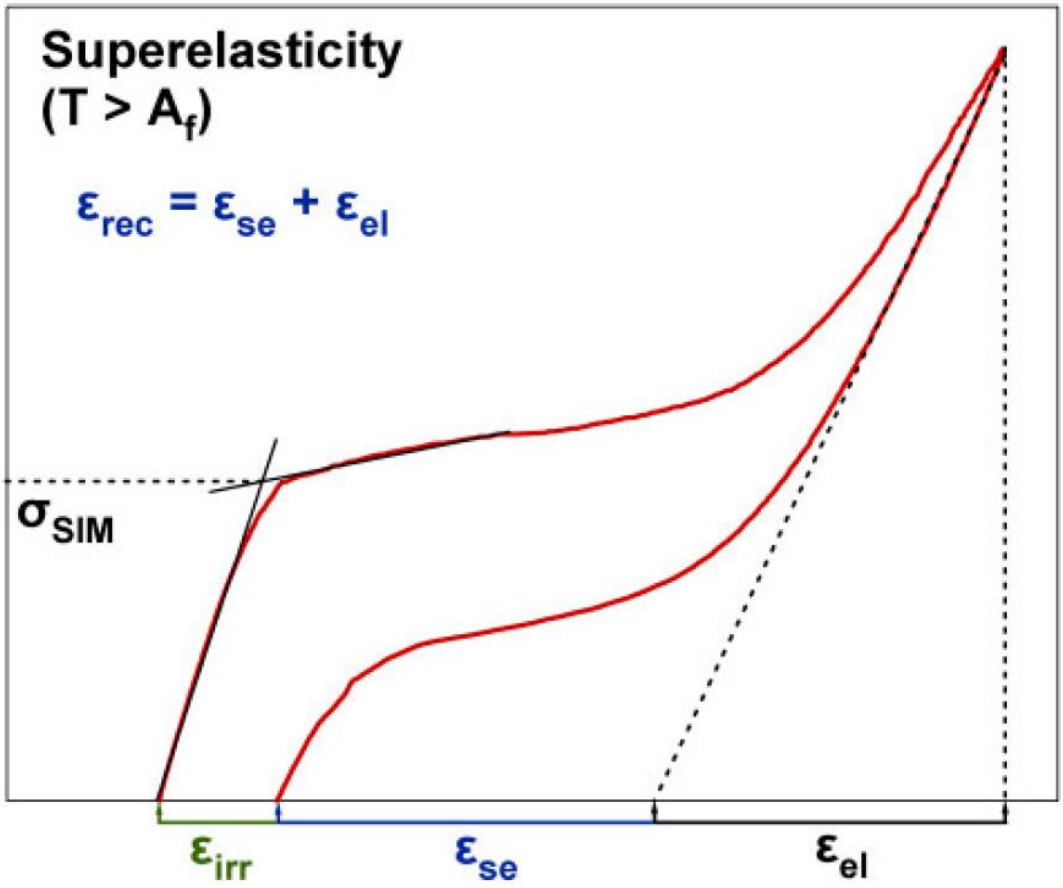

Figure 2.7 Schematic of superelastic response of SMA at a temperature above A_f. It shows after the austenite undergoes elastic at σ_{SIM} the SMA undergoes forward MT and the strain associated with it appears as a plateau. Similar plateau is found upon reverse MT. The ε_{el} is elastic strain recovery after release of applied stress. The ε_{se} is the strain recovered as a result of reverse MT whereas ε_{irr} is the irrecoverable strain [4].

2.2 High Temperature Shape Memory Alloys

As discussed in Chapter 1, that NiTi system possess properties such as high strength, tunable transformation temperatures, enhanced thermal and dimensional stability via Ni_4Ti_3 precipitation, relatively high transformation strains, good fatigue life, bio-compatible and good corrosion resistance. But despite of possessing such impressive properties, the limitation of the system is that the NiTi alloys cannot transform above 100°C. Recently advanced aerospace,

automobile, energy and transportation applications require SMAs that can operate above 200°C. The binary NiTi alloys cannot function at a temperature higher than 100°C. Therefore in order to increase the TTs of the NiTi system, the most efficient method is to increase the TTs beyond 100°C is by alloying the binary NiTi alloy with a ternary or quaternary element.

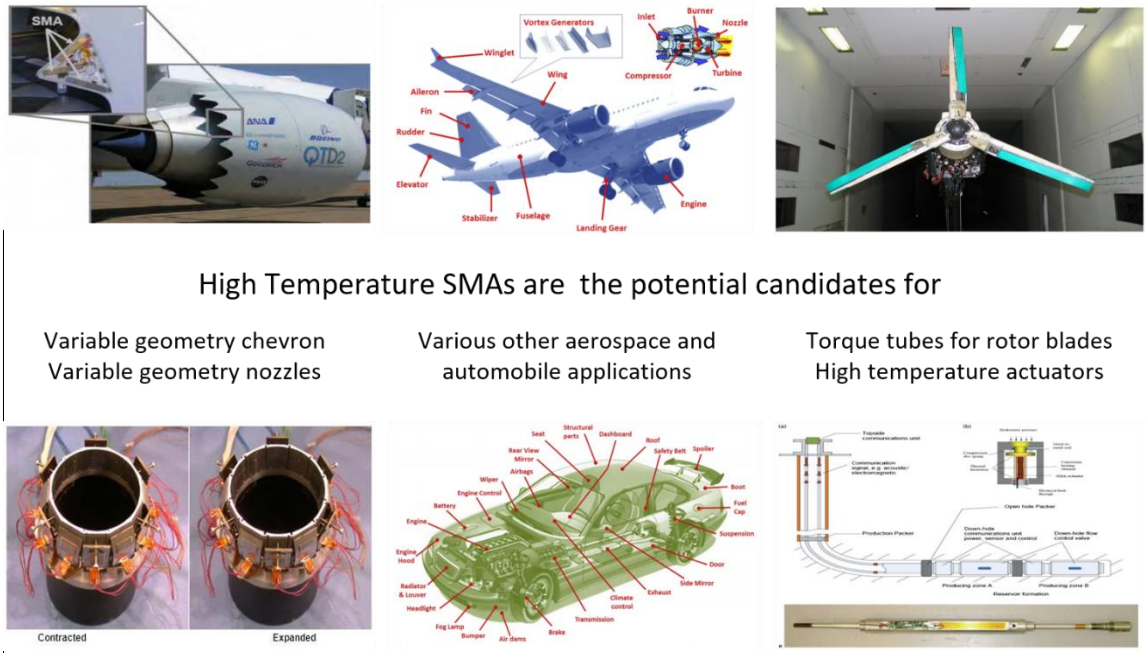

Figure 2.8 The modern day application of shape memory alloys which required them to operate at a temperature higher than 100°C [4, 5, 95, 96].

2.2.1 Ternary NiTi-based High Temperature Shape Memory Alloys

The ternary element addition to NiTi has shown a significant potential to increase the TTs by either replacing Ni or Ti. Among the ternary elements Pt, Pd, Au, Zr and Hf can be used to increase the TTs drastically. [4, 35, 97]. Among the viable ternary elements, Pt, Pd and Au increases the TTs drastically by replacing Ni in the equiatomic binary composition. As seen in Fig. 2.9, NiTiPt alloys have the potential to produce the HTSMAs with highest TTs among its other

competitors. Fig. 2.10 shows the relative TTs and transformation strain of individual material systems. It can be seen that the NiTiPt alloys shows that the highest range of TTs can be achieved but the amount of transformation strain that can be achieved is limited. Similarly, NiTiPd and NiTiAu alloys also shows that quite a wide range of TTs can be achieved with enhanced range of transformation strains as compared to the NiTiPt system. But a huge drawback that is associated with the Pt, Pd and Au addition is very expensive and hence not suitable for commercializing purposes. Also, the precipitation in NiTiPd and NiTiPt systems is not stable and makes the system more complicated for use [36-38]. Therefore, when such HTSMAs are put into application, the shape memory properties can change over time because of their ability to undergo dynamic precipitation with consecutive thermal cycling. From Fig. 2.10, it can be seen that Zr addition to binary NiTi will still produce HTSMAs, but their TTs and transformation strains are relatively less as compared to NiTiHf system. Moreover, the NiTiZr high temperature SMAs (HTSMAs) suffer from poor thermal and dimensional stability making Hf the most viable one to increase the TTs [40, 42, 57, 72, 98-100]. Also, from Fig. 2.11 it can be seen that NiTiHf alloys are capable to produce high work output and simultaneously operate at high transforming temperatures as compared to any other of its NiTi-based ternary alloys and hence makes it the best candidate for HTSMA applications. NiTiHf HTSMAs have recently gained interest because of their wide range of TTs, which can be controlled by varying compositions or secondary heat treatments [42, 44, 45, 56, 57, 61, 71, 101, 102].

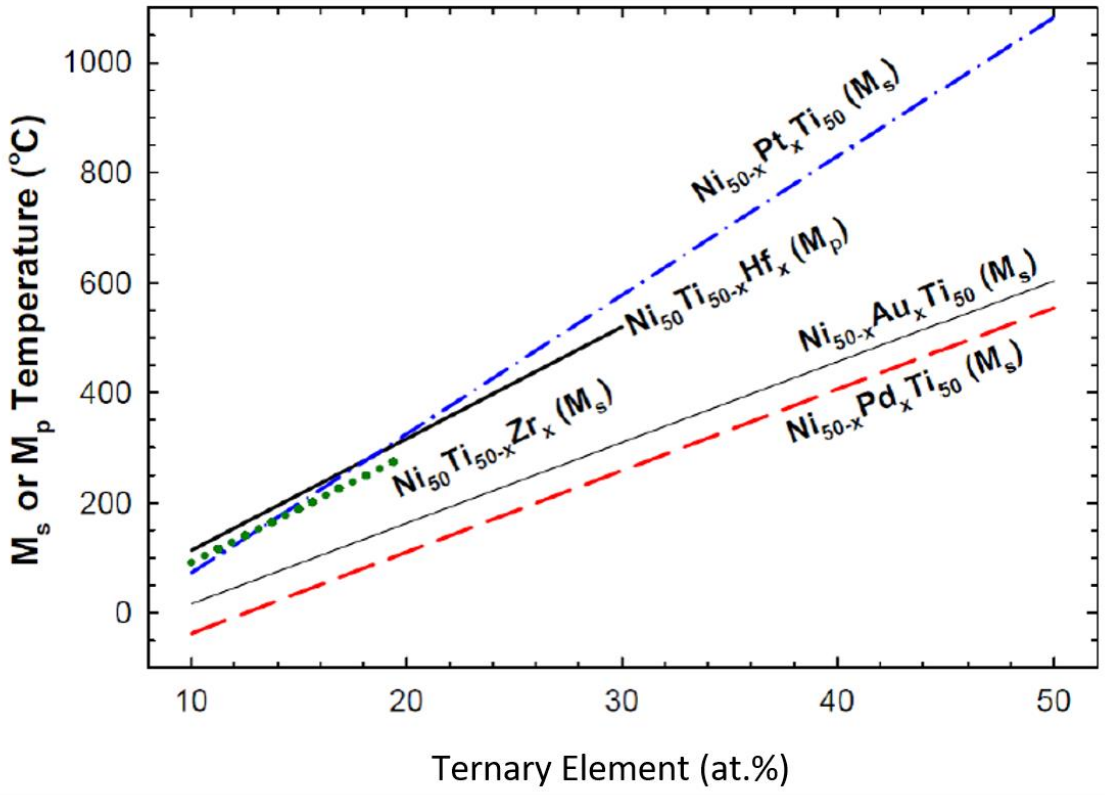

Figure 2.9 Effect of ternary element addition to the NiTi binary system [97].

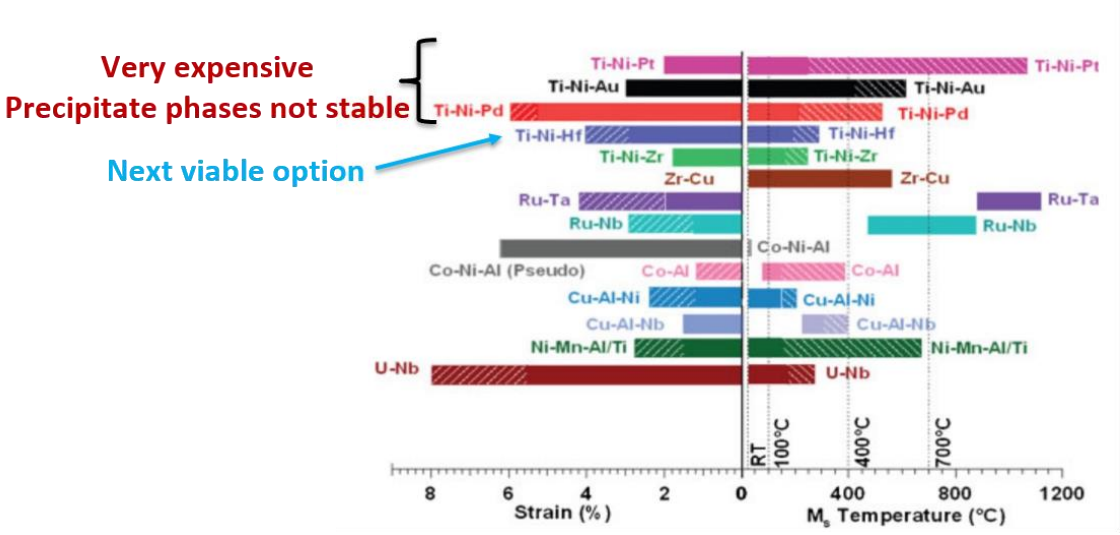

NiTiHf possess relatively high transformation temperatures and high transformation strains

Figure 2.10 A comparison of transformation temperature and transformation strains of various high temperature shape memory alloy systems [4].

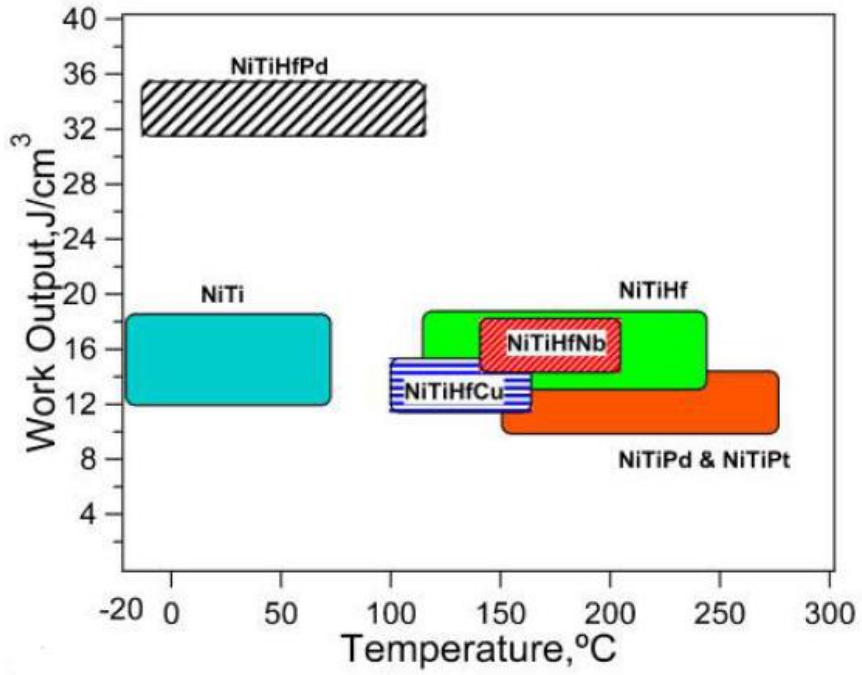

Figure 2.11 Work output Vs transforming temperature range for various NiTi-based HTSMAs. The NiTiHf system possess the high work output with a high range of operating temperature [41].

2.2.2 NiTiHf High Temperature Shape Memory Alloys

As shown in section 2.2.1, the NiTiHf system is emerging as a highly probable candidate for high temperature actuation based applications. Recently the Ni-rich NiTiHf torque tubes were used to create actuation and successful test flights of unmanned prototype folding wings aircraft, where the winglets were able to rotate over 160° rotation [103]. Researchers also demonstrated that that torque tubes can be used to actuate an F18 wing over a span of 90° rotation [104]. Fig. 2.12 shows images from prototype folding wing and torque tube setup assembly used to actuate F18 wing. Despite of such profound candidacy, the NiTiHf alloy material system as such has not been completely explored in regard to its transformation characteristics such as compositional dependence of TTs, transformation strain etc. Shape memory characteristics of NiTiHf SMAs are highly composition dependent. In the past, a very few studies have been conducted which mostly focused on Ni-lean NiTiHf systems. When Ni≤50at%, NiTiHf alloys tend to have higher TTs, as compared to the Ni-rich counterparts, with comparatively lower strength, higher transformation hysteresis, and worse cyclic stability [4, 100, 105] . High strength, lower transformation hysteresis, and impressive cyclic stability in Ni-rich NiTiHf SMAs make them suitable for aerospace applications [43, 58, 61, 67, 70, 71]. However, there is limited data available in literature which systematically presents the compositional dependence of MT characteristics of NiTiHf SMAs [35, 44, 45, 60]. Previous works have only focused on narrow composition ranges (e.g. $Ni_{50.3}Ti_{49.7-X}Hf_X$ where X=15, 20 or 25 or Ni≤50at% compositions). The following sections will recapitulate the amount of work done towards exploring the NiTiHf system with respect to composition dependence, precipitation and the any other potential approach that can be implemented to explore the NiTiHf system or design novel NiTiHf alloys.

Figure 2.12 Recent NiTiHf SMA breakthrough's with NASA's PTERA prototype folding wings and NASA's F18 folding wing.

2.3 Compositional Dependence of NiTiHf on Transformation Temperatures

2.3.1 Ni-lean or Equiatomic NiTiHf alloys (1992-2006)

The initial idea of NiTiHf alloys started by AbuJodam et al [44] who conducted a series of experiments and made attempts to systematically explore the NiTiHf system by studying several alloys with varying Hf composition and fixating the Ni content to 49 at.%. By systematically varying the Hf content from 0 at.% to 25 at.% and holding the Ni content at 49 at.%, AbuJodam et al observed that the M_p temperature doesn't change much with initial Hf addition of upto 10 at.%. Upon increasing the Hf content above 10 at.% the M_p temperature increased drastically. Similar results were also obtained for all the other martensitic associated TTs. Other studies conducted by Angst et al [45], Olier et al [46], Besseghini et al [40] and other researchers conducted similar research and found similar compositional dependence. The combined effort made towards studying compositional dependence of Hf on TTs is combined by Ma et al [4] as shown in Fig. 2.13, where data from all different studies follow the trend as outlined by AbuJodam

et al. The similar trend of Hf compositional dependence was also observed on TTs for $Ni_{50}Ti_{50-x}Hf_x$ alloys.

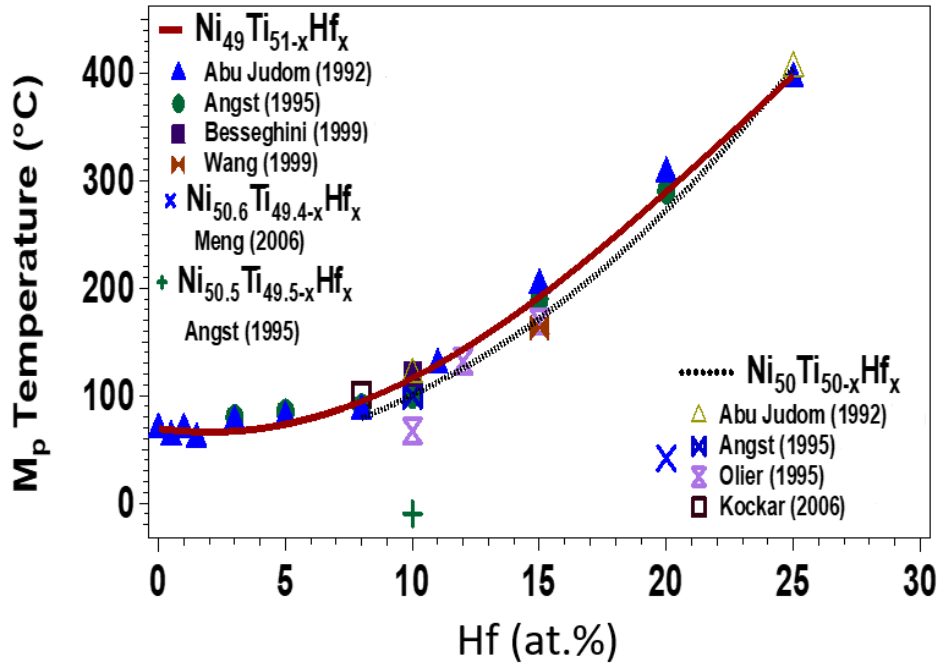

Figure 2.13 Compositional dependence of martensitic peak temperature Mp on the Hf content in the NiTiHf alloys [4].

AbuJodam et al [44] also made attempts to understand the compositional dependence of Ni content in the NiTiHf alloys by fixating the Hf content to 10 at.% and varying Ni from 40 at.% to 51 at.%. They revealed that the M_p temperature doesn't change until Ni=50 at.%, but beyond 50 at.% the M_p temperature drops drastically. Fig. 2.14a shows the dependence of Ni content on the M_p temperature as plotted by Ma et al [4]. The thermal hysteresis defined as A_p-M_p of the Ni-lean $Ni_{49}TiHf_x$ alloys shows that the hysteresis increases from Hf=0 at.% to Hf=8 at.%, followed

by a decrease until Hf=20 at.% and then increases further until Hf=30 at.% [44]. Similar results were also reported by Angst et al[45] as shown in Fig. 2.14b.

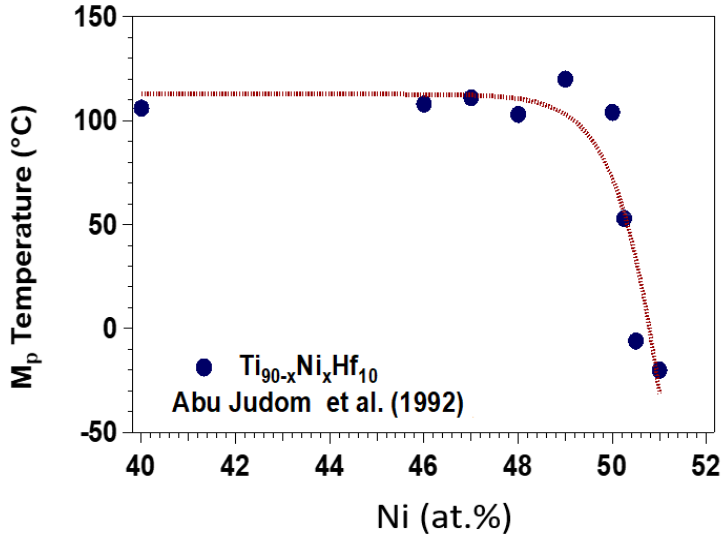

Figure 2.14 Shows the compositional dependence of martensitic peak temperature Mp on the Hf content in the NiTiHf alloys [4].

Therefore, until 2006 only Ni-lean systems were explored systematically to understand Hf dependence on TTs. Also a significant amount work was also done in this time-frame in order to understand the micro-structure and shape memory response of the Ni-lean (Ni > 50 at.%) or equiatomic (Ni = 50 at.%) NiTiHf systems, whereas efforts were made to increase their shape memory response especially by thermo-mechanical deformation [100] to improve the transformation characteristics. Various high and low temperature heat treatment were also conducted in order to analyze precipitation phenomenon in Ni-lean or equiatomic NiTiHf systems.

In order to analyze thermal cyclic stability of the Ni-lean NiTiHf alloys, Besseghini et al [40] showed that with increasing consecutive DSC cycles, the Ms temperature seems to drop significantly from the 1st cycle to 10th cycle, but the Ms doesn't change until the 60th cycle. On the

other hand the A_f temperature is not that stable and doesn't stabilize even until 60th DSC cycle. Similarly as A_f is not stable the thermal hysteresis (A_f-M_s) keeps changing.

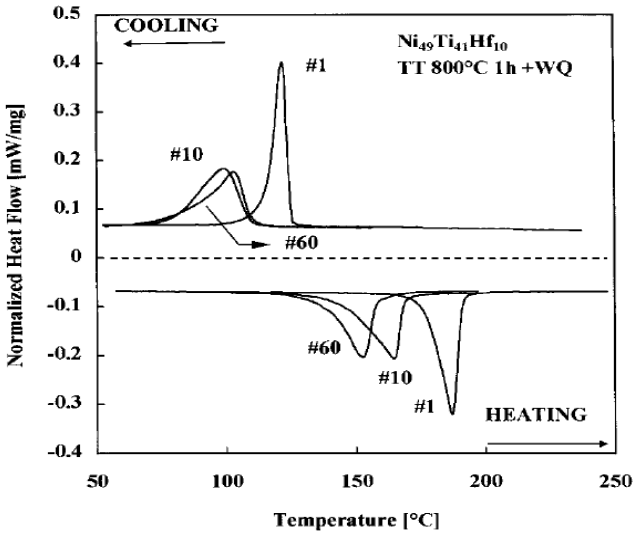

Figure 2.15 Cyclic stability of a $Ni_{49}Ti_{41}Hf_{10}$ sample heat treated at 800°C for 1 hour followed by water quenching [40].

Similarly the dimensional stability of the Ni-lean systems was also analyzed during which shows that Ni-lean NiTiHf systems shows high accumulation of plastic strain during isobaric thermal cycling in homogenized conditions [100]. Kockar et al conducted a detailed study on $Ni_{49.8}Ti_{42.2}Hf_8$ alloy and demonstrated that homogenized alloy exhibited poor transformation strains and accumulation of high amount of plastic strain. When the same alloy is subjected to Equal Channel Angular Extrusion (ECAE), the transformation strain and induced plasticity is decreased substantially. After ECAE, annealing the alloy at 400°C for short time will help getting rid of less stable forest dislocation, which will induce a highly stable and refined grain microstructure and help stabilizing the dimensional stability immensely [100], as shown in Fig. 2.16. Apart from poor isobaric thermal cycling properties, the Ni-lean NiTiHf alloys also exhibit

poor or no superelasticity. Meng et al studied $Ni_{49}Ti_{36}Hf_{15}$ alloys above their A_f temperatures and observed highly poor superelasticity [106], as shown in Fig. 2.17.

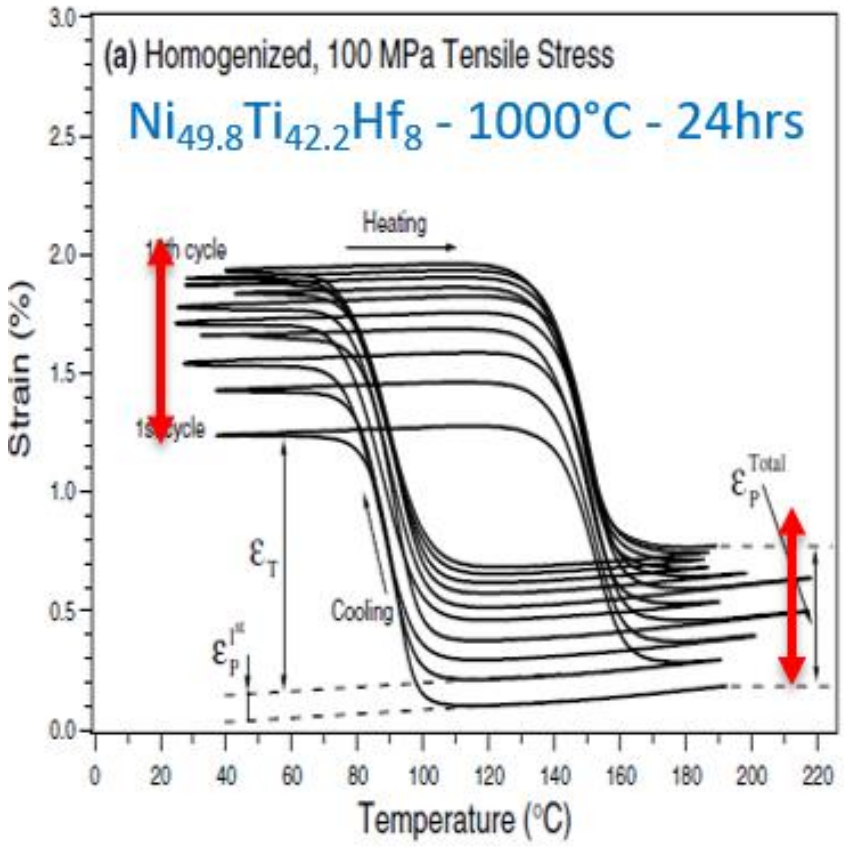

Figure 2.16 A Ni-lean $Ni_{49.8}Ti_{42.2}Hf_8$ alloy showing poor isobaric shape memory effect as indicated by red arrows, which shows the enhanced plasticity with increasing number of cycling [100].

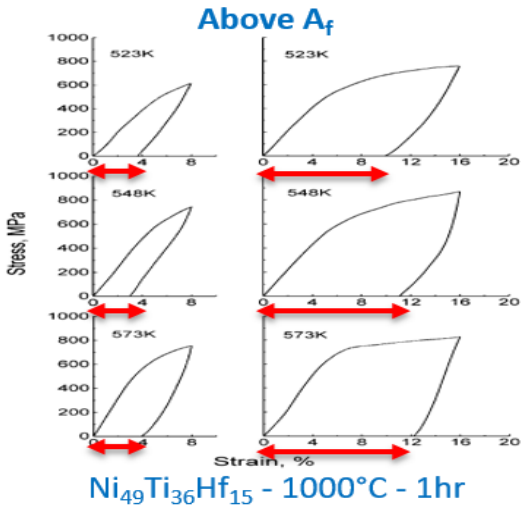

Figure 2.17 A Ni-lean Ni49Ti36Hf15 alloy showed poor signs of superelasticity as very less recovery is been observed after straining the alloy in austenite phase and let it cool down to martensitic phase [106].

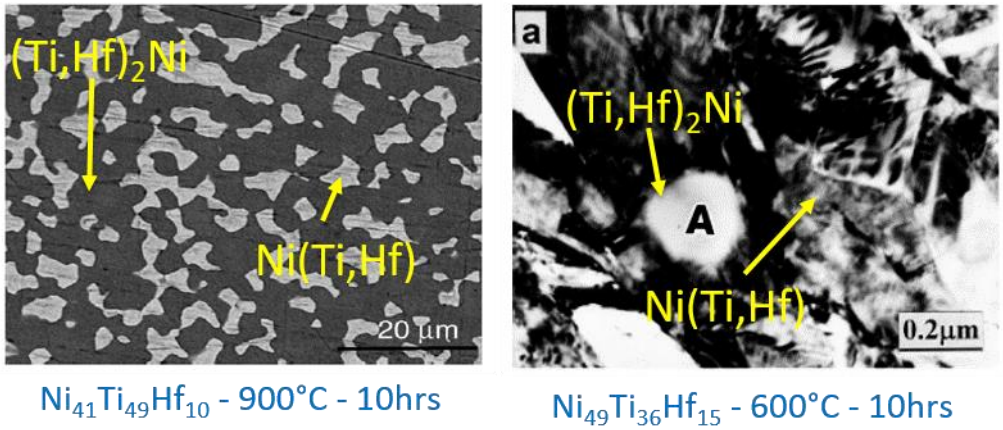

Figure 2.18 Microstructure of Ni-lean alloy showing a martensitic matrix with brittle $(Ti,Hf)_2Ni$ particles [49, 106].

Micro-structural investigations of Ni-lean NiTiHf systems revealed that the reason for such deteriorating isobaric SME and superelasticity properties is because of the presence of brittle $(Ti,Hf)_2Ni$ or $(Ti,Hf)_4Ni_2O_x$ particles as second phases, as shown in Fig. 2.18. These second phases are large in size and are high incompatible with the matrix and hence impart enhanced brittleness

and poor mechanical properties [46, 49, 106]. Hence, the Ni-lean NiTiHf alloys though shows high TTs but suffer from poor mechanical, isobaric SME and superelasticity properties.

2.3.2 Ni-rich NiTiHf alloys (2006-2016)

In 2006, there was a dawn of an era of Ni-rich NiTiHf alloys when Meng et al investigated a series of Ni-rich $Ni_xTi_{80-x}Hf_{20}$ (x = 50.4, 50.6, 50.8, 51) alloys and demonstrated that these alloys exhibits excellent thermal stability even in SHT condition. The thermal stability can be further enhanced by performing low temperature small term aging heat treatment and introducing the H-phase precipitates. Fig. 2.19 a and b shows the

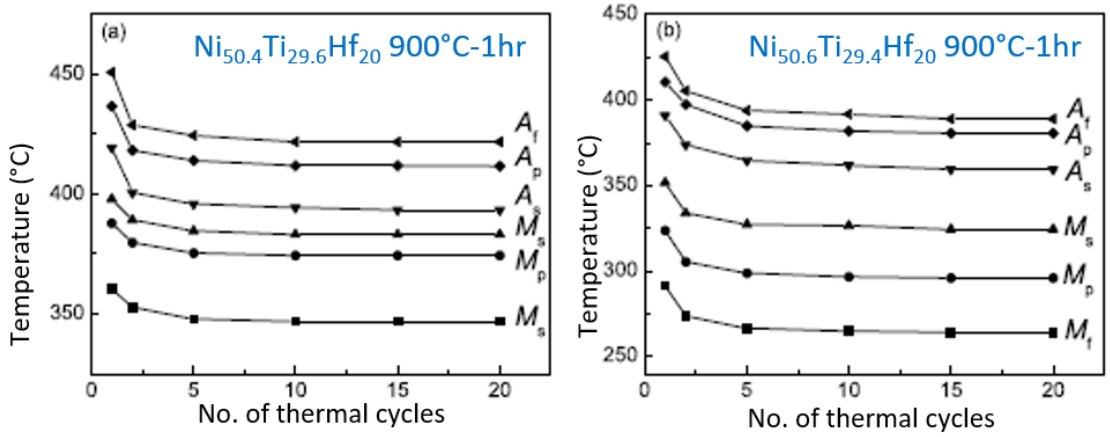

Figure 2.19 Thermal stability of SHT $Ni_{50.4}Ti_{29.6}Hf_{20}$ and $Ni_{50.6}Ti_{29.4}Hf_{20}$ depicting that thermal stability is enhanced for Ni-rich SHT alloys as compared to its SHT Ni-lean counterparts. [107].

thermal stability of the Ni-rich $Ni_{50.4}Ti_{29.6}Hf_{20}$ and $Ni_{50.6}Ti_{29.4}Hf_{20}$ alloys in SHT condition, which shows that the thermal stability of Ni-rich alloys is much better as compared to the Ni-lean NiTiHf alloys as shown in Fig. 2.15. Apart from thermal stability, the dimensional stability of the Ni-rich systems is also enhanced drastically. The Ni-rich alloys exhibit superelasticity effect with high

recovery strains and negligible irrecoverable or plastic strain as compared to the Ni-lean systems. Fig. 2.20 shows the superelastic response from a Ni-rich $Ni_{50.3}Ti_{29.7}Hf_{20}$ alloy without precipitation, which exhibits complete recovery when strained to lower strain values. Upon straining to a large strain value, the alloy still shows a large ε_{rec} and very low ε_{irr} as compared to Ni-lean systems [108].

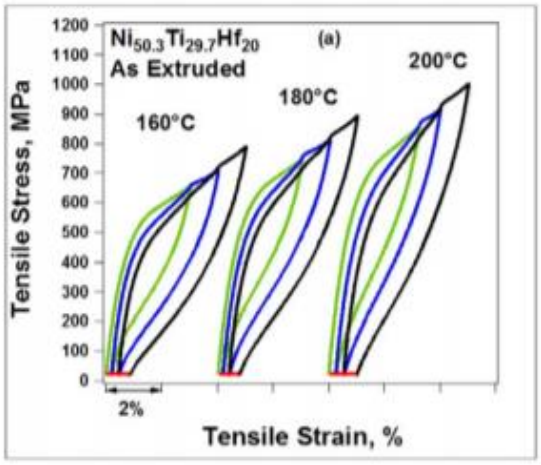

Figure 2.20 Superelasticity response of a Ni-rich $Ni_{50.3}Ti_{29.7}Hf_{20}$ alloy after extrusion [108].

Despite the Ni-rich NiTiHf alloys possess impressive thermal and dimensional stability, the Ni-rich regime of the Ni-Ti-Hf HTSMA system haven't been explored systematically to understand the compositional dependence on the transformation temperatures. Such a compositional dependence knowledge can be helpful in designing new alloys with required TTs, serve as a map to identify composition of unknown NiTiHf alloys with given TTs and can also be used to calibrate the micro-mechanical model, which can be further used to make predictions of shape memory response of NiTiHf SMAs. Fig. 2.21 gives a flowchart representation current knowledge about the NiTiHf system and the motivation or emphasis that should be given towards exploring the Ni-rich regime of the NiTiHf HTSMAs.

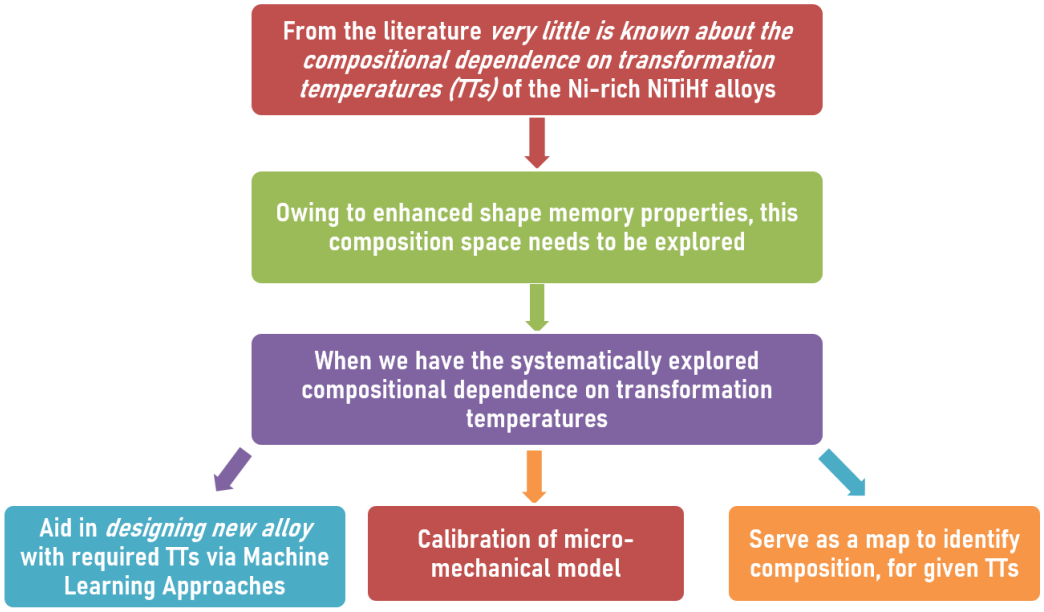

Figure 2.21 Flowchart to understand the present knowledge about the compositional dependence on TTs of NiTiHf alloys and the motivation to explore the Ni rich regime of the Ni-Ti-Hf alloy system.

2.4 Precipitation in NiTiHf HTSMAs

The Ni-lean NiTiHf systems tend to possess $(Ti,Hf)_2Ni$ brittle particles of tens of microns in size and exhibit poor H-phase precipitation kinetics as compared to its Ni-rich counterparts[52, 106, 109]. The Ni-rich NiTiHf microstructure also is free from the brittle $(Ti,Hf)_2Ni$ which makes them ideal candidates for use after precipitation strengthening. Fig. 2.22 shows the microstructure of a Ni-rich NiTiHf alloy, which shows uniform distribution of H-phase precipitates with no signs of (Ti,Hf)2Ni phases. Fig 2.22a shows the micro-structure of the as-extruded $Ni_{50.3}Ti_{29.7}Hf_{20}$ alloy which shows martensite variants and no H-phase precipitates. Fig 2.22b shows the micro-structure of same alloy after HT at 550°C-3hrs, which depicts a fine distribution of nano-sized H-phase precipitates with a very small inter-particle distance. On the other hand, Fig. 2.22c shows the

micro-structure of the $Ni_{50.3}Ti_{29.7}Hf_{20}$ alloy HT at 650°C-3hrs, depicting coarse H-phase precipitates with large interparticle distance [42].

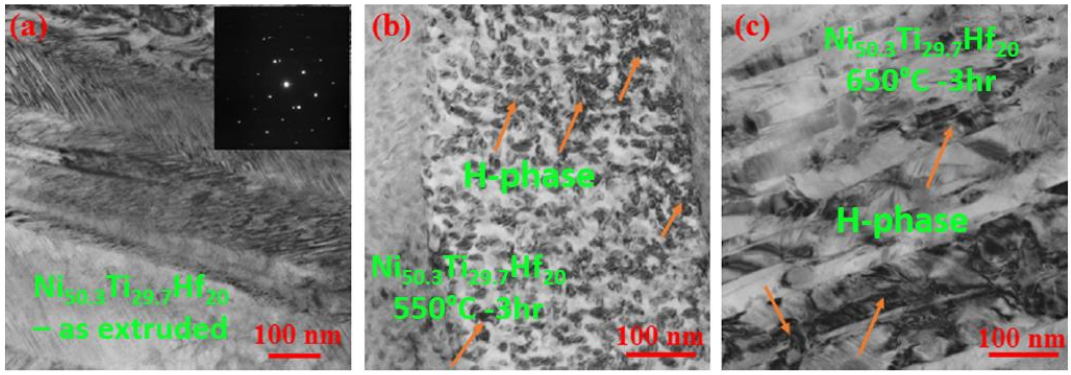

Figure 2.22 Microstructure of Ni50.3Ti29.7Hf20 in (a) as extruded condition without precipitates (b) HT at 550°C-3hrs which shows uniform distribution of nano-sized precipitates with very small inter-particle distance and (c) HT at 650°C-3hrs shows the coarse H-phase precipitates with large inter-particle distance [42].

2.4.1 Phase Equilibrium of the H-phase precipitates

Precipitation in NiTi and NiTiHf SMA systems is one of the governing micro-structural factors along with grain size, second phases, dislocation density, texture etc., which not only strengthens the material but also enhances the transformation strain and reduces the thermal hysteresis and irrecoverable strains [14-17, 42, 69, 110-112]. The precipitate in binary NiTi system are Ni_4Ti_3 intermetallic which appear as a line compound at 57.14 at.% Ni in the binary NiTi phase diagram and has a rhombohedral crystal structure. On the other hand in NiTiHf system, the precipitate phase was very firstly observed by Han et al in $Ni_{48.5}Ti_{36.5}Hf_{15}$ alloy after heat treating it at 600˚C-150 hours [52]. Han et al conducted extensive TEM analysis on the precipitate phase and concluded that it possesses an orthorhombic structure (space group #70 F 2/d 2/d 2/d) and has a chemical compositional form of $(Ti_{0.6}Hf_{0.4})Ni$. Later, Meng et al also conducted precipitation

studies on Ni-rich NiTiHf compositions and concluded that the precipitates are of $(Ti,Hf)_3Ni_4$ form, similar to that in NiTi system [53-55]. Meng et al claimed the precipitates in $Ni_{50.6}TiHf_{20}$ to be $(Ti,Hf)_3Ni_4$ like, based on the 1/7<321> characteristic diffraction spots. However, work by Meng et al [53-55] are the only ones who report the precipitates in NiTiHf system to be $(Ti,Hf)_3Ni_4$ like. However, Han et al [52] and more recent extensive TEM studies performed by Santamarta et al [67], Coughlin et al [101] and Yang et al [68], showed no evidence of 1/7<321> diffraction spots as reported by Meng et al. Also, Meng et al did not provide any EDX compositional measurements to bolster the existence of $(Ti,Hf)_3Ni_4$ like precipitates in NiTiHf system. In 2009, Zarinejad et al, also conducted aging heat treatments on equi-atomic and Ni-rich NiTiHf alloys and suggested the precipitated are of the form of $Ni_4(Ti_{0.85}Hf_{0.15})_3$ using X-ray diffraction [113].

In 2012, extensive TEM studies conducted by Santamarta et al [67], Coughlin et al [101] and Yang et al [68], show that the H-phase precipitates are not $(Ti,Hf)_3Ni_4$ like and have a Ni content ranging from 52-54 at.%. Also, both the works, indigenously confirmed that additional satellite diffraction spots along with the principle diffractions spots in 1/3<110> direction are the unique characteristics associated with the H-phase precipitates. Santamarta et al [67] also revealed by their EDX studies that the composition of the H-phase precipitates changes with change in initial starting composition of the material, heat treatment temperature etc., unlike in case in NiTi where the composition of the precipitate is always Ni=57 at.% and Ti=43at.% irrespective of the composition of the starting material and heat treatment temperature. This led us to hypothesize that the H-phase in Ni-Ti-Hf equilibrium phase diagram must not be a line compound but should occupy a region in the phase diagram. Knowledge of the phase equilibria between the B2 phase and H-phase precipitates will enable us to design new alloys with required transformation temperatures. It will also enable us to design alloys with desired volume fraction of H-phase

precipitates which will further allow in enhanced control of transformation strains, strength of alloy, etc.

In both NiTi and NiTiHf systems precipitation phenomenon is similar in the sense of Ni and Ti diffusion during precipitation. The precipitates in both NiTi and NiTiHf systems are formed by depleting the Ni from the martensitically transforming phase, making the matrix Ni-lean than that before precipitation, while the Ti diffuses out of the precipitate making the matrix Ti-rich as compared to the non-precipitated composition. In NiTiHf, the H-phase precipitates are also Hf-rich and hence it can be said that along with Ni, Hf also diffuses into the precipitate making the matrix more Hf-lean as compared to the starting composition. Apart from both the precipitates being Ni-rich, the precipitation phenomenon differs in the sense of kinetics of formation of these precipitates. In NiTi system, the Ni_4Ti_3 precipitates are formed directly upon aging at temperatures below 600˚C [15]. There are no transient or intermediate precipitate phase formed before the appearance of Ni_4Ti_3 precipitates in the NiTi microstructure. On the other hand, in NiTiHf system, during initiation of precipitation, an intermediate H'-phase is formed, which acts as a precursor to the H-phase precipitates. The H'-phase is found to be Hf-rich as compared to the matrix, but the Ni content is same as that of the neighboring phase [69].

Therefore, as H-phase precipitation with correct size and in order to understand volume fraction can yield to novel NiTiHf SMAs, the system is barely thermodynamically explored in order to understand the phase equilibrium between various phases and especially one concerning with H-phase precipitates and the B2 martensitically transforming phase. Semeova et al conducted a detailed study in order to explore the solidus and liquidus temperatures in the Ti–TiNi–HfNi–Hf system using differential thermogravimetric analysis and also presented a phase map with respective equilibrium phase reactions occurring between them [114, 115]. Recent work by Liu at

al [116], studied the NiTiHf phase equilibrium at 800˚C and 900˚C using the diffusion multiple approach, but didn't find any evidence of H-phase region at that temperatures. Knowledge of the existence of H-phase region in the phase diagram, will enable us to design numerous NiTiHf HTSMAs with desired transformation temperatures and transformation strain by using the precipitation and micro-mechanical models [65, 117, 118], and hence in the present study we have studied the Ni-Ti-Hf system at 600˚C in order to determine the H-phase equilibrium region in the phase diagram. Zhao et al introduced a unique inter-diffusion experimental approach to determine the stable equilibrium phases present in a ternary and quaternary system [119-121]. Compositional analysis of such inter-diffused tri-junctions can be used to generate equilibrium ternary phase diagram isotherms.

2.4.2 H-Phase Precipitation Kinetics

For metallic materials, understanding of the formation kinetics of nanoscopic precipitates is often critical to comprehend the solid state transformation and the alloy's age hardening behavior. Precipitates, by impeding the movement of dislocations, can effectively increase yield strength of a variety of alloys, including aluminum alloys, titanium alloys, steels, and superalloys. Controlling and optimizing the size distribution, spatial distribution, and number density of the precipitates also governs alloys properties such as ductility and corrosion resistance. Detailed and quantitative information about the precipitates has significant implication in determining the optimal heat treatment procedure for the desired final microstructure. While no experimental technique can provide all-around information regarding these precipitations, including structural

(phase), chemical (composition), and morphological (size and shape) information, a combination of complementary techniques can provide a comprehensive picture.

Despite of such detailed studies, the precipitation kinetics or the evolution of volume fraction (v_f) of H-phase precipitates with increasing heat treatment time is not clearly understood yet. Hornbuckle et al [122, 123], used atom probe tomography (APT) to estimate the volume fraction of the H-phase precipitates at 550°C for varying HT time and reported an increase in v_f with increasing aging time. As APT is not an *in-situ* measurement technique and hence can analyze v_f for samples aged for specific heat treatment time. Moreover, APT estimation of v_f is based on assumption of an iso-concentration surface, and hence in-correct choice of element for iso-concentration surface analysis can lead to higher degree of error in compositional characterization and v_f estimation. In addition, with increasing HT temperature and time, the composition of the matrix and precipitate is evolving continuously [42, 67, 123], hence the same iso-concentration surface cannot accurately estimate the volume fraction of precipitates for different HT time and temperatures. Other ex-situ technique such as transmission electron microscopy (TEM) has been utilized to study the morphology, size, crystallography of H-phase precipitates for different compositions and HT time and temperatures [42, 58, 67, 68, 124]. Various in-direct methods such as differential scanning calorimetry (DSC), shape memory and superelasticity effect tests, hardness testing, etc are also employed to understand the effect of precipitation characteristics in NiTiHf alloys [41, 60, 69, 101]. Yet, an *in-situ* study, which would help in improving the understanding of dynamic evolution of H-phase precipitates over relevant length scales, is missing.

Small angle X-ray scattering (SAXS) is a powerful technique that can resolve the structure heterogeneity at the nanometer and micrometer scale [125]. Comparing with other techniques such as electron microscopy or atomic force microscopy that can also characterize nanoscale structures,

SAXS has two clear advantages. (1) SAXS data are often acquired from a large sample volume (often $10^{7\text{-}8}$ μm^3 and above), hence the structure information acquired from SAXS is typically statistically representative. (2) SAXS data collection can be conducted in situ, especially when experiments are conducted at a synchrotron beamline, which provides a unique opportunity to peer into the structure evolution or transformation of the features of interest.

SAXS, as a global technique that provide average information on a large population of precipitates, was originally developed over 60 years ago to quantify the microstructure of precipitates. However, for most of the period since its discovery, SAXS analysis of precipitates was not ideal due to the ex situ nature of the measurements and complexity of scattering data from metallic systems. Recent development of robust numerical analysis methods and in situ SAXS techniques, as well as other analytical techniques that can provide a priori information for SAXS modeling, have greatly enabled the advance of SAXS in metals research [126]. For this reason, we performed rigorous SAXS experiments at a synchrotron source to understand the precipitation behavior and its kinetics in a NiTiHf alloy.

In order to analyze the precipitate kinetics synchrotron-based *in-situ* small angle x-ray scattering (SAXS) is a technique which is capable of quantifying microstructural feature size over a range of 0.5°A to 30 μm [127]. SAXS as a scattering technique involves, examination of clusters, precipitates or any in-homogeneity originating inside the material at atomic length scales or above [128-132]. SAXS, as a technique is governed by conventional laws of diffraction. When a beam of high energy x-rays is incident on a material, the transmitted x-rays will scatter/diffract at different angles '2θ', depending on their electronic interaction with the material, as shown in schematic Fig. 2.23. These scattered/diffracted spherical waves interfere and form concentric-rings like diffraction pattern. The phase difference between these interfering waves at

scattering/diffracting angle 2θ can be defined by a scattering wave vector '$\vec{q}$' which is the difference between the incident wave vector '$\vec{\imath}$' and scattered wave vector '$\vec{s}$' and its magnitude is $q=4\pi*\sin(\theta)/\lambda$, where θ is one-half of the scattering/diffraction angle 2θ, and λ is the monochromatic X-ray wavelength. During *in-situ* SAXS experiments, as precipitate nucleation and growth occurs, the incident electrons tend to scatter/diffract more because of the changing matrix/precipitate composition as a result of enhanced electronic interactions between electrons and material. Thus, a wide range of q provides a larger window to examine the nucleation and growth kinetics of precipitates, accurate to angstrom length scales. In the present work, we combined USAXS, SAXS and XRD techniques to provide a continuous q range between 1×10^{-4} $Å^{-1}$ and 6 $Å^{-1}$.

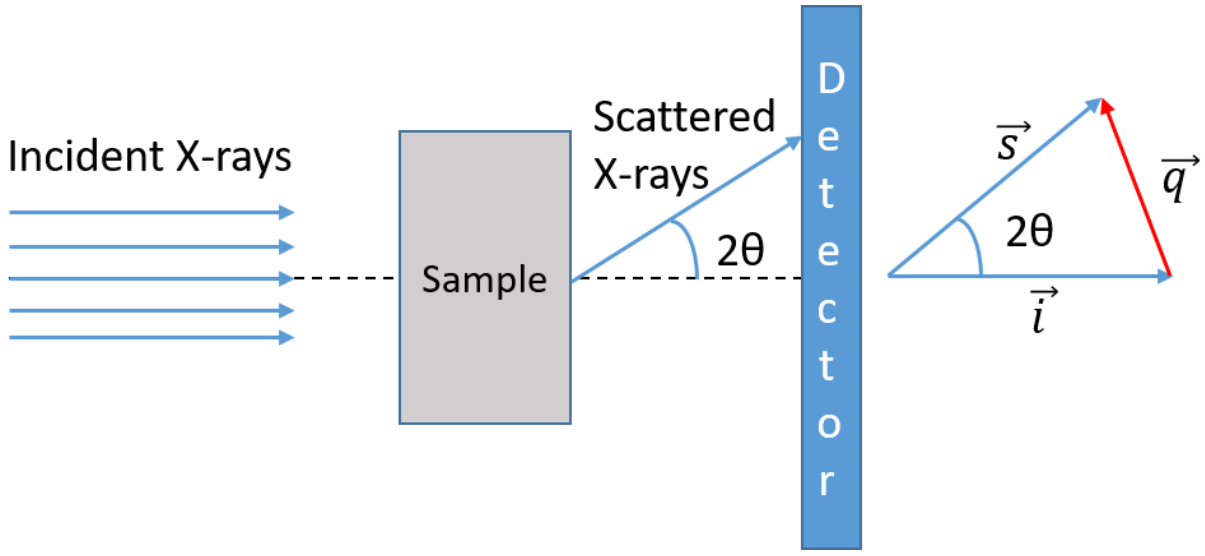

Figure 2.23 Schematic of X-ray diffraction during Small Angle X-ray Scattering (SAXS) along with depiction of the interfering electron waves after diffracting from the sample. The phase difference between these interfering waves at scattering/diffracting angle 2θ can be defined by a scattering wave vector '$\vec{\boldsymbol{q}}$' which is the difference between the incident wave vector '$\vec{\boldsymbol{\imath}}$' and scattered wave vector '$\vec{\boldsymbol{s}}$' and its magnitude is $q=4\pi*\sin(\theta)/\lambda$, where θ is one-half of the scattering/diffraction angle 2θ, and λ is the monochromatic X-ray wavelength.

Recent investigations though limited, have revealed the utility of SAXS on SMAs. Huang et al, conducted *in-situ* SAXS experiments on $Ni_{51.3}Ti_{48.7}$ alloy at 250°C and reported that for first 0 to 5 hours, the disk/plate like Ni_4Ti_3 precipitates grow with simultaneous dissolution of Ni-rich nano-domains followed by coarsening of Ni_4Ti_3 precipitates with further increase in time [133]. Prasher et. al conducted *ex-situ* SAXS measurements on heat treated $Ni_{50.3}Ti_{29.7}Hf_{20}$ alloy, revealing that the volume fraction and surface to volume ratio of H-phase precipitates tends to decrease with an increase in heat treatment temperature from 550°C-3hrs to 650°C-3hrs [59]. They attributed this decrease in volume fraction to coarsening of H-phase precipitates with increase in heat treatment temperature. Therefore, to simultaneously monitor the changes in the v_f, morphology and size of H-phase precipitates during an isothermal heat treatment of NiTiHf alloy, we conducted *in-situ* synchrotron ultra-small angle X-ray scattering (USAXS), small-angle X-ray scattering (SAXS), and X-ray Diffraction (XRD) experiments at the USAXS facility of the Advanced Photon Source, Argonne National Laboratory [134]. Fig. 2.23 shows a flowchart depiction of the importance of the thermodynamic and kinetic studies of H-phase precipitate will help in designing novel NiTiHf alloys with required shape memory properties. The knowledge of thermodynamics and kinetics together will help is selecting the correct initial composition of the alloy and the heat treatment temperature and time in order to produce precise matrix composition and volume fraction of H-phase precipitates which will in return control the martensitic phase transformation behavior of the alloy.

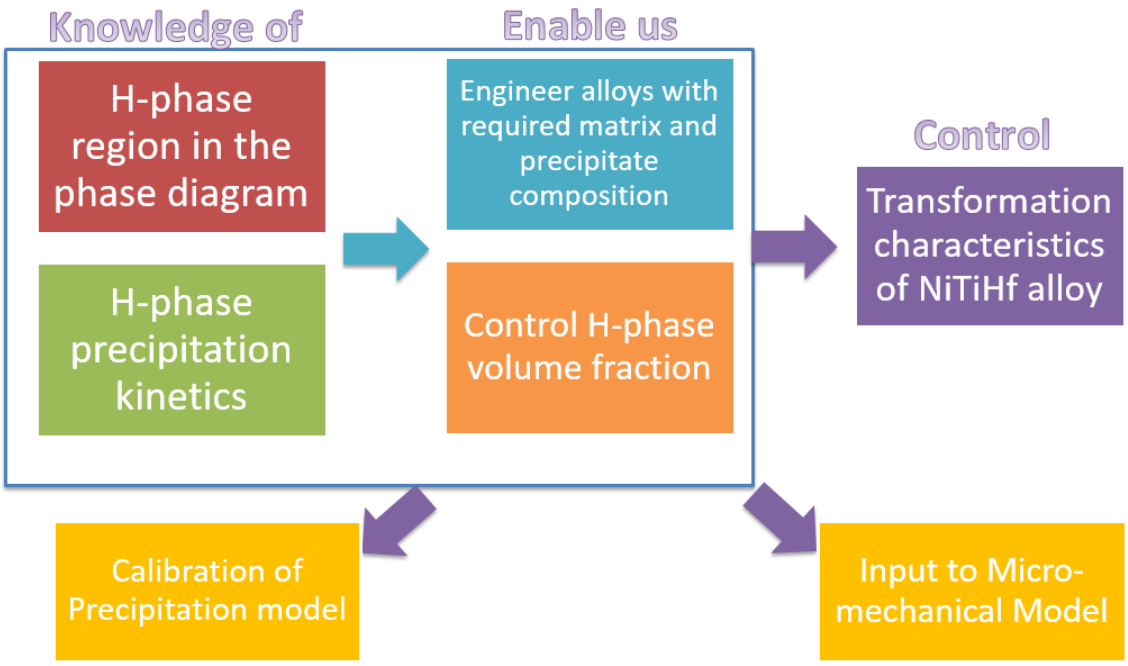

Figure 2.24 Flowchart representation of thermodynamic and kinetic studies of H-phase precipitate enabling to design novel NiTiHf HTSMAs.

2.5 Machine Learning Enabled Alloy Designing

Artificial Intelligence is a new branch of data science, which has recently gained huge amount of attention and is widely used to explore various material systems and optimize their material properties. For HTSMAs, in many such applications, the target operating temperature is usually between 100°C - 400°C, requiring SMAs with relatively high transformation temperatures to avoid uncontrollable actuation due to normal changes in operating conditions. At the same time, in many applications increased efficiencies demand small hysteresis. The transformation temperatures and other transformation characteristics of shape memory alloys can be precisely tailored by varying composition as well as microstructure through carefully controlled thermo-mechanical processing [4, 13, 35, 57, 99, 135-137]. Intuition-guided studies of such SMA systems

have led to the discovery and exploration of a limited region in the potential SMA compositional space, since a blind exploration of the entire available space, all the way from manufacturing, processing, testing and characterization is very time and resource-intensive. By implementing statistics and machine learning-based approaches, the composition and processing space for these alloys can be sampled and explored in such a way that we can design a novel material and achieve targeted required property with a minimal number of experiments.

The implementation of multi-objective Bayesian experimental design, also known as Bayesian Optimization (BO) can be implemented for discovering novel high temperature shape memory alloys (HTSMAs) with required transformation temperatures (TTs) and thermal hysteresis. More specifically, Bayesian experimental design with constraints based on the concept of Mean Objective Cost of Uncertainty (MOCU) [138, 139] is developed for the HTSMA design problem under study. We note that while many other works [140, 141] have deployed BO-based approaches to carry out the optimal exploration of materials design spaces, no work to date has been reported on such exploration subject to (probabilistic) performance constraints. This is an important improvement over existing optimal approaches to materials discovery as constraints in target performance are essential in alloy/materials development for two reasons: (i) often times it is not practical to set materials discovery as merely an optimization problem; (ii) ignoring constraints can make the search problem intractable due to the enormity of the materials composition-processing space, even when using Bayesian optimal approaches to explore them.

To date, most of the recent developments in HTSMAs are based on trial and error or intuition-guided experimental efforts based on the published literature. A few studies tend to utilize combinatorial approaches based on the geometrically non-linear theory of martensite to design SMAs with the least possible hysteresis [73-76]. The theory considers the difference between the

crystal structure of the martensite and the austenite to predict the geometrical incompatibilities at the martensite and austenite phase. According to this theory, when the second eigenvalue (λ_2) of the transformation stretch tensor is closer to 1, austenite and martensite tend to be elastically compatible which in turn results in a lower hysteresis. The current compatibility-based design paradigm suggests that deviations of λ_2 from 1 generally result in large increases in hysteresis. The compatibility theory has helped rationalize the outcome of the open-loop combinatorial designs mentioned above but we must point out that such compatibility measure is impossible to predict *a priori*, thus precluding its use in the actual search of the alloy space. Moreover, Evirgen at al [77] recently showed that depending on the ternary element addition to a base NiTi alloy, the hysteresis dependence on λ_2 can adopt either a steep or a shallow slope. In other words, hysteresis in alloys like NiTiCu, NiTiPd, NiTiAu etc. is very highly dependent on λ_2 value, whereas hysteresis in alloys like NiTi, NiTiHf, NiTiZr is not highly dependent on λ_2 value and hence this compatibility metric cannot be used to identify potential SMAs with low hysteresis.

To date, a few number of works have used statistical [142] and/or machine learning [143, 144] approaches to design SMAs. Xue et al [78] has demonstrated that the search of new SMAs with very low thermal hysteresis can be expedited by implementing an adaptive design approach coupled with experiments. Another study by Xue et al [145], utilizes a statistical learning approach over material descriptors related to composition, atomic bonding and atomic radii in order to predict the transformation temperatures. In both the studies Xue et al, predicted compositions for new SMA for certain objective functionality using an adaptive design framework which offered a tradeoff between exploration and exploitation of new alloys with respect to the initial training dataset. Using an iterative approach towards materials discovery Xue and collaborators were able

to identify alloy compositions with minimal hysteresis, although with relatively low transformation temperatures, thus limiting the practical impact of such alloy discovery.

Any experiment design problem has the goal of identifying a material with the desired property, usually in terms of optimizing one (or multiple) objective function(s). Without loss of generality, we assume minimization of an objective as $x^* = argmin_{x \in X} f(x)$, where X denotes the design space. In materials discovery, the true objective function f is unknown, but can be approximated by a surrogate model, which models the relationship between the inputs and outputs, i.e. maps the degrees of freedom for an experiment (such as composition) to the output property that is the target of the exploration over the materials design space. This approximation is updated with the new results, as they become available. In the so-called Bayesian Optimization (BO) or Bayesian experiment design (BED) [138, 139, 146, 147] context, the prior model is sequentially updated after each experiment. The surrogate model used for BO/BED provides information about the output prediction as well as uncertainties. In BO, the common choice for the surrogate model is a nonparametric model, such as a Gaussian process regression (GPR) [148] or Support Vector Regression [149, 150]. With the only prior beliefs about the experimental space being continuity and smoothness, GPRs are flexible models that can asymptotically converge to the true objective function, provided a sufficient number of observations is available. BO-based approaches have recently been adopted for guiding the efficient exploration of the materials design space [118, 141, 151-153], although the focus of the majority of the works published thus far has been on single objectives without the imposition of design constraints.

A key element in any BO/BED approach is the acquisition function use to judge the utility of making a specific observation of the available, unexplored design space. After constructing a probabilistic approximation to the objective function based on the available data at each iteration,

the next experiment that maximizes a pre-specified acquisition function is selected. The acquisition function is itself dependent on the modeling of the objective function and is designed to balance the trade-off between exploitation based on the current state of the model and exploration of the regions with high model uncertainty. Different acquisition functions can emphasize more on exploitation or exploration, i.e. putting more trust in the model or trying to improve the model by querying uncertain regions of the design space. Some of the most widely used acquisition functions in the literature are Probability of Improvement (PI), Expected Improvement (EI) used in the Efficient Global Optimization (EGO) [154], Knowledge Gradient [155], and Mean Objective Cost of Uncertainty (MOCU) [138, 139]. For the connection of MOCU with KG and EGO the reader can refer to [138].

Seko et al [141, 149] used models based on SVR and GPR with PI as the acquisition function to discover unary and binary crystals with the highest melting point. In [141], the authors employed a GPR model and PI acquisition to discover low thermal conductivity compounds. Balachandran et al [79] used EI for materials discovery for the first time in the design of MAX phases with maximum elastic moduli as predicted via DFT calculations. In [78] using EGO and KG, and different models including GPR and SVR with bootstrap uncertainty estimates, physical experiments have been leveraged to accelerate the discovery of NiTi-based SMAs with low thermal hysteresis. The authors in [156] have employed a Bayesian linear regression model with truncated Gaussian prior and pure exploitation (greedy approach) to expedite discovery of BaTiO3-based piezo-electrics with vertical phase boundary using physical experiments. In [153], MOCU-based BED was applied to a computational problem for SMA design with desired stress-strain profiles for a particular dopant at a given concentration utilizing time-dependent Ginzburg-Landau theory (SMA design with the lowest energy dissipation at a specific temperature).

Solomou et al and Talapatra et al, [118, 152] are among the few works that have studied multi-objective experiment design for materials discovery, with both utilizing computational experiments during iterations of the experiment design process. Solomou et al [118] investigated multi-objective experiment design with GPR models and Expected Hyper-Volume Improvement (EHVI) [157] acquisition function to discover precipitation strengthened NiTi SMAs for selected target properties. Talapatra et al [152] combined Bayesian model averaging (BMA) with BO to explore the design space efficiently under model uncertainty. They adopted EI and EHVI acquisition functions for one and two objective problems for the MAX ternary carbide/nitride phase's space. To the best of our knowledge, none of the previous works has studied experiment design problems with constraints on the target properties as additional objectives. More specifically, here our experiment design problem is formulated as $x^* = \arg min_{x \in X} f(x)$ subject to $c(g(x))$, where $g(x)$ is a set of properties of the material and $c(\cdot)$ is a set of inequality constraints.

In order to implement the multi-objective iterative design framework, an initial reliable NiTiHf dataset of more than 42 different compositions was constructed, within the composition range of interest. Predictions were made based on this initial dataset using machine-learning models, and new alloys were selected based on the designed acquisition functions and fabricated. From here on in the manuscript, 'a model' will be referred to as a statistical/machine learning surrogate model for the functional relationship between the inputs and outputs, co-relating the physical properties of the alloy such as composition, atomic radius, electronegativity etc., to a measured property of the alloy, such as yield strength, bulk modulus, transformation temperatures in this case etc. Results from the 1st iteration were then incorporated along with initial dataset to train the model and make new predictions and select the next experiments.

After the 4th iteration, the improvement in the objective seemed to saturate and hence no further iterations were performed because of cost considerations. Fig. 2.24 shows a general framework or steps implemented in alloy designing by data driven machine learning approach.

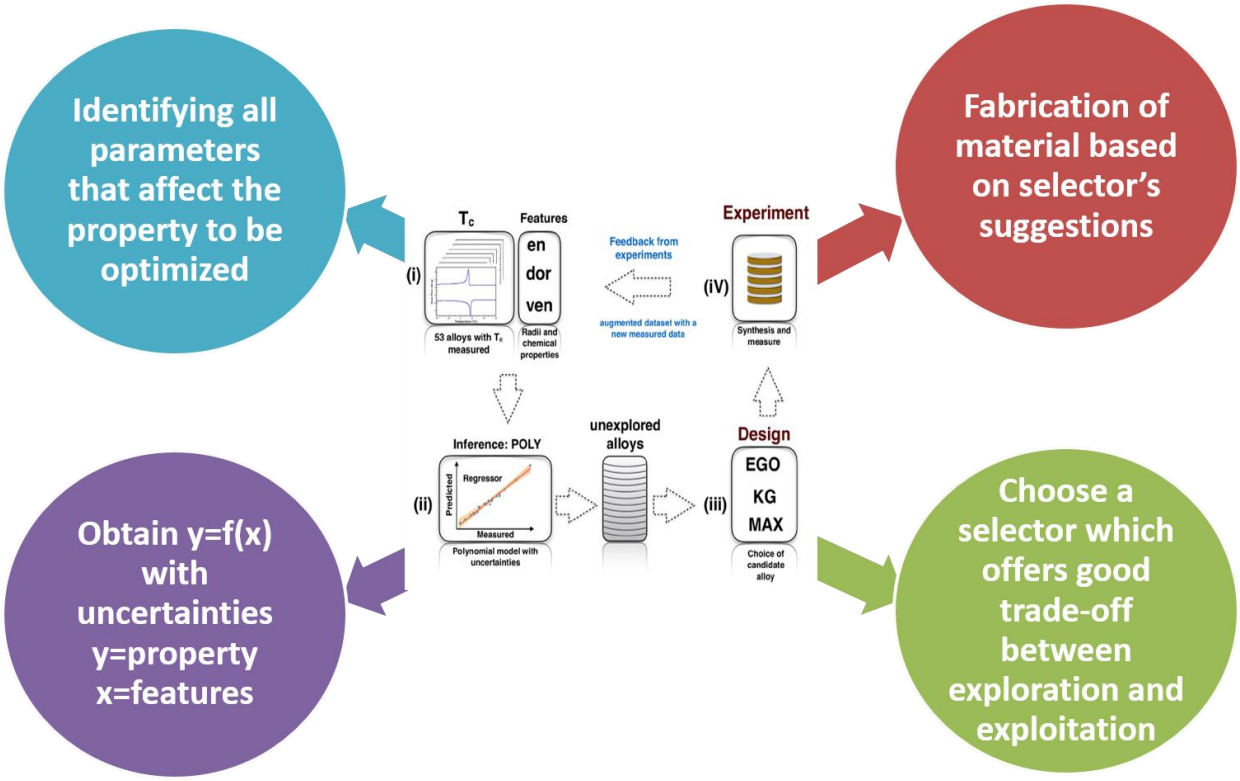

Figure 2.25 A general Data Driven Machine Learning Approach for alloy design

To sum up this chapter, the aforementioned methods can be made the basis and can be utilized to its full potential to explore the Ni-Ti-Hf system in terms of chemistry, thermodynamics and kinetics. The chapter also gives methodologies with suitable examples that can be used to develop a framework to design and develop new NiTiHf alloys with required transformation characteristics.

CHAPTER III

EXPERIMENTAL PROCEDURE

This chapter summarizes the detailed experimental procedure adopted to study the NiTiHf alloys in order to explore the system. The chapter describes about various fabricating methods to cast alloys to understand compositional dependence and generate diffusion assembly to study the phase equilibrium in NiTiHf system. The chapter also details out the procedures that were used to conduct mechanical, micro-structural and diffraction characterization of the NiTiHf alloys.

3.1 Compositional Dependence on Transformation Characteristics

$Ni_XTi_{100-X-Y}Hf_Y$ alloy buttons (Ni_XTiHf_Y in what follows) were fabricated through vacuum arc melting of 10 g of 99.98% Ni, 99.99% Ti and 99.9% Hf (with b1%Zr) elements under high purity argon. The arc melting chamber was first pumped down to a pressure of 5×10^{-5} Torr or less, and then backfilled with ultra-high purity argon. This was repeated three times. The buttons were then re-melted six times to reduce compositional heterogeneity. After the re-melting steps, the weight loss was measured to be b0.10% in all cases that were selected for further characterization. The buttons were wrapped in tantalum foils, sealed in quartz tubes under high purity argon, and solution heat treated (SHT) at 1050 °C for 2 h followed by water quenching. The TTs of the SHT buttons were determined using Differential Scanning Calorimetry (DSC) and Thermogravimetric Analysis (TGA), with a heating-cooling rate of 10 °C/min. For TTs less than −100 °C, the temperatures were determined from the temperature-dependence of the electrical resistivity, measured down to −263 °C, using a Quantum Design Physical Property Measurement System (PPMS), with a heating-cooling rate of 2 °C/min. Hardness measurements were conducted using a Vickers Micro-

hardness with a load of 500 grams at room temperature. For better statistics, 10 to 12 reading were obtained from each sample across the length of the sample and the average with standard deviation was reported in HV units. Scanning Electron Microscopy (SEM) was performed to observe the microstructure and search for possible second phases, compositions of which were analyzed, using a Cameca SXFive Electron Microprobe Analyzer (EPMA) using wavelength dispersive spectroscopy (WDS), operated at 15 KeV and 20 mA. The microstructure and diffraction patterns of the selected samples were obtained using an FEI Technai G2-F20 Transmission Electron Microscopy (TEM) operated at 200 kV. For TEM investigations, 3 mm diameter discs with 100 μm thickness were twin-jet electro polished using a 30%HNO3 + 70% methanol solution at −20°C under 10–12 V. The crystallographic compatibility was assessed by computing the middle second eigen value (λ_2), using a laboratory based X-ray Diffraction (XRD) system with heating enabled stage. The XRD pattern was acquired at room temperature to analyze the martensite lattice parameters, whereas the sample was heating above A_f temperature and XRD pattern was acquired from 3 different temperature above A_f temperature. While cooling back, the sample was again held at 2 temperatures above Ms temperature to gather XRD pattern to analyze the austenite lattice parameters. After analyzing the austenite lattice parameters at higher temperatures, the value of austenite lattice parameter was extrapolated to room temperature. Using romm temperature martensite and austente lattice paraemeters the λ_2 values were computed.

3.2 Matrix/Precipitate Phase Equilibrium – Diffusion Multiples

3.2.1 Bulk $Ni_{50.3}Ti_{29.7}Hf_{20}$ alloy

A $Ni_{50.3}Ti_{29.7}Hf_{20}$ alloy was prepared by vacuum induction melting followed by homogenization heat treatment at 1050˚C for 72 hours followed by air cooling. The ingot was the hot forged to an R ratio of 2.35:1 followed by cooling in the air. After receiving the ingot 3 mm diameter and 1 mm thick cylindrical disc samples were cut to perform Differential Scanning Calorimetry (DSC). The 3mm disc samples were then solution heat treated (SHT) at 900˚C for 1 hour followed by water quenching. DSC was performed on the SHT sample by cycling the sample between a temperature range of 0˚C to 300˚C at the rate of 10 ˚C/minute. Other SHT samples was then subjected to further aging heat treatment at 600˚C (from here on referred as HT600) and 650 ˚C (from here on referred as HT650) for 10 hours followed by water quenching and subsequently DSC was performed on them. In order to analyze the precipitate size and morphology, the samples were high resolution transmission electron microscopy (TEM) was performed using a spherical aberration corrected Titan Themis 300 Scanning TEM (STEM) at 300kV. The TEM samples were grinded and polished down to thickness of around 70 µm and then subjected to twin-jet polishing using a 30% HNO_3 and 70% ethanol solution, operating at 12V and -30˚C. Energy Dispersive X-ray (EDX) Spectroscopy was also performed to obtain X-ray compositional maps which was further analyzed to obtain the composition of the matrix and H-phase precipitates.

3.2.2 Diffusion Multiple Assembly

In order to generate the Ni-Ti-Hf isotherm, the ternary NiTiHf diffusion multiple assemblies were created using highly pure Ni, Ti and Hf. The highly pure Ni was received in the form of a cylindrical rod with a diameter of 25.4 mm and the Ti and Hf was received in the form of

cylindrical rod with a diameter of 12.7 mm. The Ni cylinder was then machined such that we created a square cavity of 11*11 mm using an Electro Discharge Machining (EDM) in the center of the cylinder. The Ti and Hf cylinders were also machined to the dimensions of 25.4*11*5.5 mm using an EDM so that they can press fit directly inside the square cavity created inside the Ni cylinder as shown in Fig. 3.1. Before inserting the Ti and Hf pieces in places the re-cast layers from all the EDM cut surface was removed and cleaned using the ultra- sonic cleaner for 15 minutes. After having the Ni, Ti and Hf pieces in a compactly packed setting, the entire assembly was then again press fitted inside a hollow Grade II Ti cylinder (inner diameter = 25.4 mm; outer diameter = 31.75 mm) with a Ta foil inserted in between them as shown in Fig 1. The Grade II Ti cylinder was used as a sacrificial material to encase and protect the Ni-Ti-Hf assembly from oxidation during the prolonged heat treatment. The Grade II Ti lids with a diameter of 31.75 mm and thickness of 3 mm were electron beam (e-beam) welding unto the top and bottom of the Grade II Ti press fitted assembly under a high vacuum atmosphere of 3*E-7 torr. The e-beam welded assembly was then subjected to Hot Iso-static Pressing (HIPing), with a applied pressure of 200 MPa at 900˚C for 4 hours followed by air cooling. The HIPing is very essential as it helps to establish a close contact with all elements and closes any air pockets or pores present during machining processes. The oxide layer formed on the Grade II Ti can was removed using a 400 grit size paper and then it was wrapped with Ta foil once again and then sealed inside a quartz tube in ultra-high purity Ar atmosphere. A piece of yttrium wrapped in Ta foil was also sealed along with the assembly, which also acts as an oxygen getter. This sealed quartz tube was then subjected to a prolonged heat treatment at 600˚C for 5000 hours followed by water quenching to room temperature. The HIPed assembly was then cut perpendicular to the length and the cross sectional area was polished to mirror finish surface and the Ni-Ti-Hf tri-junction was then analyzed using

the Electron Microprobe Analyzer (EPMA) using the Wavelength Dispersive Spectroscopy (WDS) technique. The WDS is one of the most accurate technique to perform the compositional quantitative analysis and hence was employed it to perform compositional line-scans across the phases and the data was employed to plot the single phase regions in the Ni-Ti-Hf ternary isotherm. Along with acquiring compositional line-scans, the EPMA equipment is also equipped with an Electron Dispersive Spectroscopy (EDS) setup. The EDS setup was also employed to acquire EDS X-ray maps from the entire tri-junctional diffusion zone and specific phases in particular H-phase region, in order to determine the compositional span of respective phases and access the diffusion profile of individual elements in them.

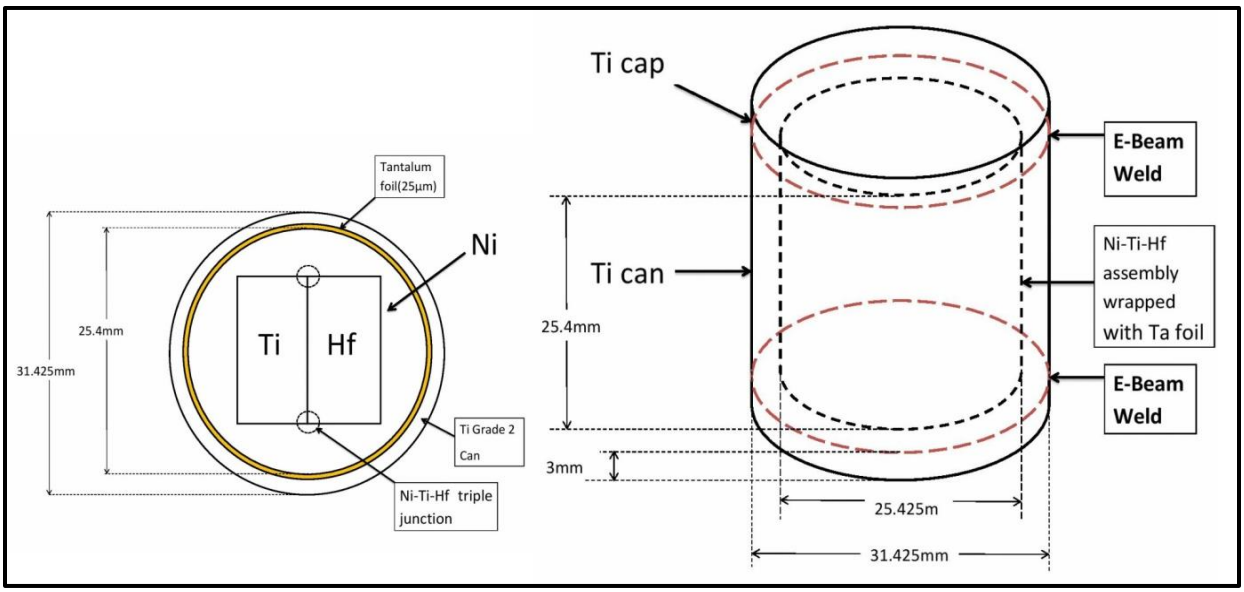

Figure 3.1 Schematic design of Ni-Ti-Hf diffusion multiple assembly.

Diffusion Multiple Sample name	Diffusion Multiple Annealing Temperature (°C)	Diffusion Multiple Annealing Time (hours)	HIPing Temperature (°C)
DM600	600	5000	900
DM700	700	1500	700
DM800	800	1000	800
DM900	900	1000	900

Table 3.1 Diffusion Multiple heat treatment and HIPing parameters.

3.3 H-Phase Precipitation Kinetics

A nominal $Ni_{50.3}Ti_{29.7}Hf_{20}$ alloy was vacuum induction melted and homogenized at 1050°C for 72 hours followed by air cooling and hot forging. 3mm diameter round samples and square samples with 25.4mm*25.4mm*1mm were cut for Differential Scanning Calorimetry (DSC) and SAXS using electro-discharge machine (EDM). The samples was then encapsulated in quartz tubes in Ar atmosphere and solution HT (from hereby referred as SHT) at 900°C for 1 hour followed by water quenching to room temperature. After SHT, a DSC sample was heat treated at 550°C, 600°C and 650°C for 10 hours followed by water quenching (from hereby referred as HT550°C, HT600°C and HT650°C respectively). DSC measurements were conducted on the samples by cycling them between 0°C to 400°C, with a heating and cooling rate of 10°C/min. Three thermal cycles were performed on each sample. TTs were calculated using tangent method and reported from 2nd DSC thermal cycle in order to avoid 1st cycle effect. Thermal stability of the material is reported as the difference of martensite start temperature (Ms) between the 1st and 3rd DSC thermal cycles. TEM on HT550°C samples was conducted using a FEI Technai G2-F20 TEM operated at

200kV. 3mm diameter discs with ~100 μm thickness were twin-jet electro-polished using a 30%HNO_3+70%methanol solution at -35°C under 11V. For the *in-situ* SAXS experiments, X-rays energy was 21 keV (λ = 0.5904 Å), and the X-ray flux density was ≈ 10^{13} photons/s/mm^2. The beam size for USAXS, SAXS, and XRD was 0.8 mm × 0.8 mm, 0.8 mm × 0.2 mm, and 0.8 mm × 0.2 mm, respectively. SAXS and XRD cameras were calibrated using AgBe and NIST standard reference 660a (lanthanum hexaboride), respectively with calibrated intensity range exceeding 10^{10}. The SHT sample was mechanically polished to 52 μm to ensure X-ray transmission. The heat-treatment was conducted using a Linkam 1500 thermal stage (Linkam Scientific Instruments Ltd., Tadworth, UK). The thermal stage was calibrated using a 99.999% purity Pt foil sample, with temperature uncertainty estimated at 1 °C. The SHT sample was heated to desired temperatures at a heating rate of 200°C/minute. Data was acquired in a repeated sequence of USAXS, SAXS, and XRD, with individual scan time set at 90sec, 30sec, and 60sec, respectively.

3.4 Data Driven Machine Learning Approach for Designing Novel SMAs

Alloys were manufactured with similar procedure as reported in Section 4.1. The initial dataset served as the training data for various machine learning models, and then the approaches predict compositions for the defined objective of 200°C<Ms<300°C with minimum hysteresis (A_f-M_s). Obtained machine learning compositions were again fabricated using procedure from section 4.1.

CHAPTER IV

THE EFFECTS OF WIDE RANGE OF COMPOSITIONAL CHANGES ON THE MARTENSITIC TRANSFORMATION CHARACTERISTICS OF NITIHF SHAPE MEMORY ALLOYS

4.1 Micro-structural Characterization*

Microstructural characterization results of selected NiTiHf alloys are shown from Fig. 4.1 to Fig. 4.4. The Fig. 4.1 displays the backscattered secondary electron (BSE) image of SHT $Ni_{49.8}TiHf_{10}$ showing martensite matrix and $(Ti,Hf)_4Ni_2O_x$ [46] particles marked with red circles. Fig.4.2 displays the BSE image of SHT $Ni_{50.3}TiHf_{25}$ with martensite and HfO_2 inclusions marked with red circles. The results of these investigations performed on all samples are presented in the form of a phase map in Fig. 4.3 as a function of Ni and Hf contents. The map shows which other phases are observed in addition to austenite and martensite. The map was generated using the SEM microstructures, and hence is accurate down to micron scale. Fig. 4.4 presents representative DSC and resistivity responses for $Ni_{51}TiHf_{20}$ and $Ni_{51}TiHf_{1.5}$ alloys, respectively, across MT during single cooling-heating cycles, demonstrating how the TTs are determined using these two methods.

---

* "Section 4.1 and 4.2 of this chapter are Reprinted from Scripta Materialia, 161, Tejas Umale, Daniel Salas, Bradley Tomes, Raymundo Arroyave, Ibrahim Karaman, The effects of wide range of compositional changes on the martensitic transformation characteristics of NiTiHf shape memory alloys, Copyright 2018, with permission from Elsevier"

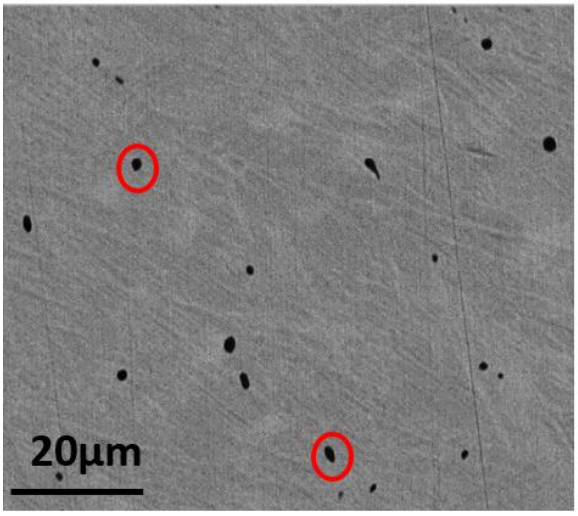

Figure 4.1 $Ni_{49.8}Ti_{40.2}Hf_{10}$ showing $(Ti,Hf)_4Ni_2O_x$ particles marked with red circles in the martensite matrix.

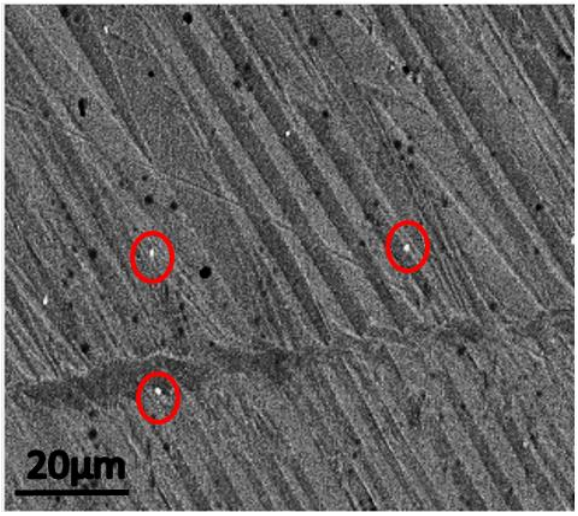

Figure 4.2 $Ni_{50.3}Ti_{24.7}Hf_{25}$ showing HfO_2 inclusions marked with red circles, again in martensite matrix. The black spots are surface contamination, which was also seen as bright spots in secondary electron image mode.

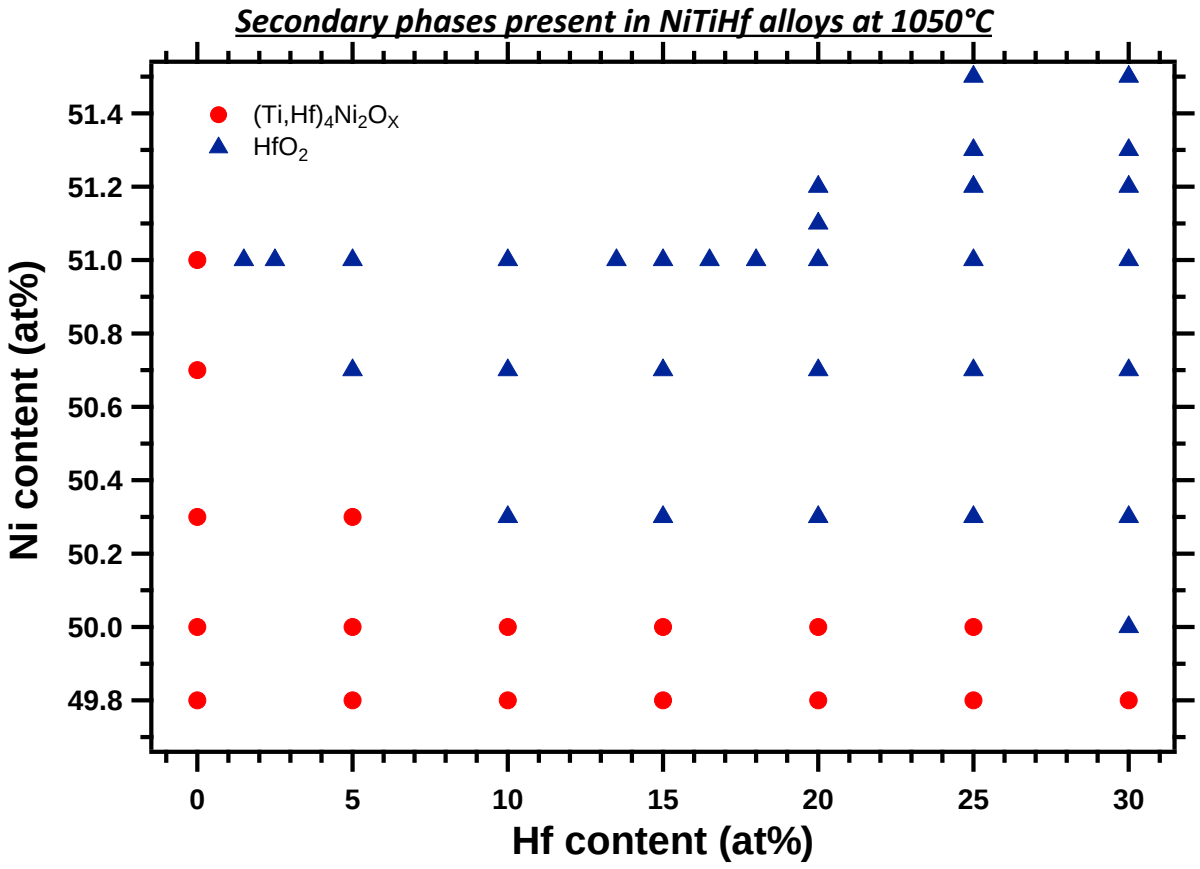

Figure 4.3 Phase map indicating the presence of B2 (austenite) or B19' (martensite) matrix phase along with second phases observed in SEM, accurate down to micron scale.

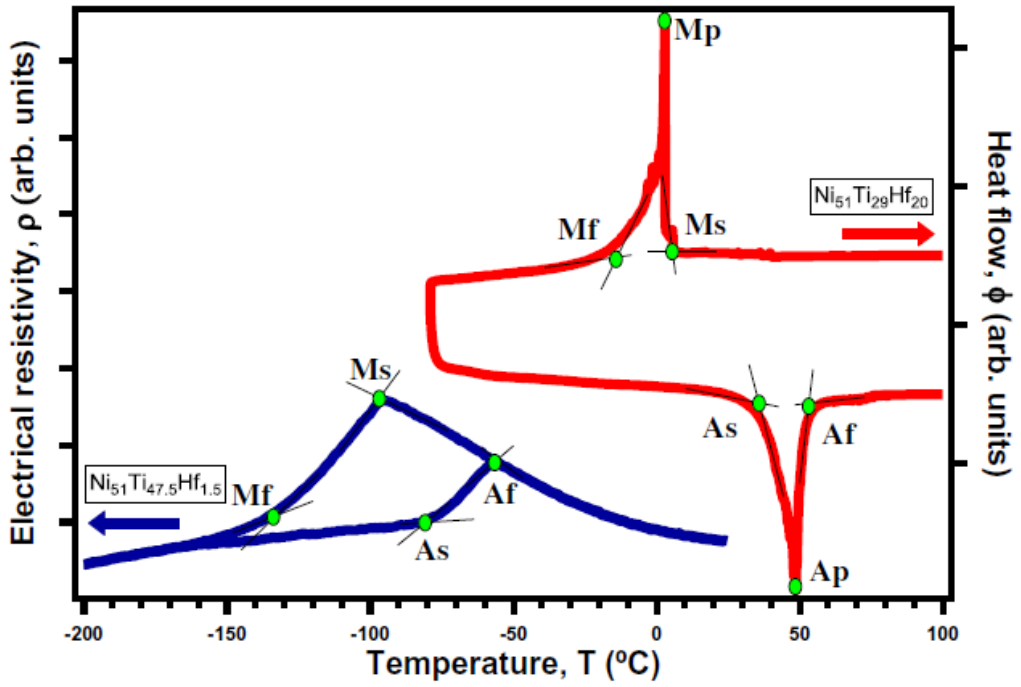

Figure 4.4 Shows representative DSC and PPMS plots for $Ni_{51}Ti_{29}Hf_{20}$ and $Ni_{51}Ti_{47.5}Hf_{1.5}$ alloys, respectively, depicting how the transformation temperatures were determined using two different methods.

4.2 Compositional dependence of Martensitic Transformation Temperatures*

TTs in NiTiHf alloys demonstrate a significant compositional dependence. Fig.4.5 presents the Hf dependence of Ms for different Ni contents. For Ni-lean, Ni=50 and 50.3at% compositions, M_s almost stays constant up to 5 to 10%Hf addition and increases drastically beyond 10% Hf. Previous reports on the Ni-lean compositions [35, 45, 158] present similar trends in Hf dependence of M_s. For Ni-rich compositions, M_s tends to initially decrease with increasing Hf, attaining a minimum, and then increase continuously. For Ni=50.7at% (Ni50.7), the M_s sharply decreased from 6°C for 0%Hf to -66°C for 10%Hf, where the minimum was attained. With further increase in Hf, M_s was found to increase. The DSC response of $Ni_{50.7}TiHf_{10}$ showed avalanche-like transformation behavior [159, 160], while all other $Ni_{50.7}Ti_{49.3-Y}Hf_Y$ showed a single peak

B2→B19' MT. For Ni=51at%, initial drop in M_s with Hf content was more pronounced than Ni50.7 alloys, from -22°C for 0%Hf to -96°C for 1.5at%Hf. However, $Ni_{51}TiHf_5$, $Ni_{51}TiHf_{10}$, and $Ni_{51}TiHf_{15}$ didn't undergo MT down to -260˚C and this is indicated in Fig.4.5 asb a dashed line disappearing at the bottom of the figure. To guide the readers, the solid lines connect compositions which show full transformation, while dashed lines link transforming and non-transforming compositions.

To better reveal the compositional boundary for the full suppression of MT in Ni51 alloys, $Ni_{51}TiHf_{2.5}$, $Ni_{51}TiHf_{16.5}$ and $Ni_{51}TiHf_{18}$ alloys were also prepared. PPMS measurements for $Ni_{51}TiHf_{2.5}$ and $Ni_{51}TiHf_{16.5}$ demonstrate no MT. The DSC result of $Ni_{51}TiHf_{18}$ exhibits many sharp, discrete transformation peaks, indicating avalanche-like transformation bursts [159]. MT can occur in the form of avalanches, if there are barriers to MT which tend to pin down the transformation front. With the higher degree of undercooling/overheating, when the system has enough driving force to overcome the barriers, the transformation can proceed until obstructed again by new barriers, and hence advancing in the form of bursts. For Ni51.2 alloys, in addition to $Ni_{51.2}TiHf_0$, 3 other compositions were fabricated with Hf contents ranging from 20% to 30at%, where the samples are expected to transform. Firstly, the M_s increases with Hf content similar to the previous cases within this high Hf range. Secondly, when MT occurred at low temperatures in $Ni_{51.2}TiHf_{20}$ and $Ni_{51.2}TiHf_{25}$ alloys, the transformations displayed avalanche-like transformation features in DSC, whereas $Ni_{51.2}TiHf_{30}$ alloy experienced a single peak MT.

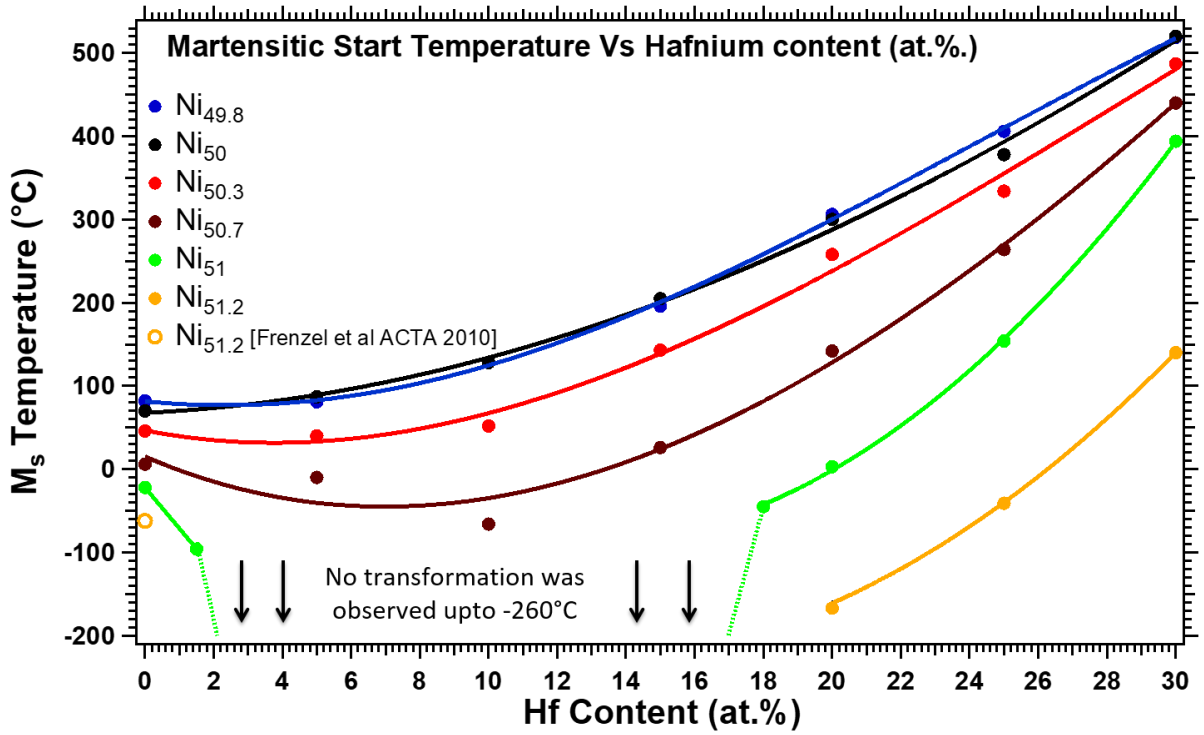

Figure 4.5 Variation of M_s temperatures with hafnium content for various NiTiHf alloys for selected Ni contents.

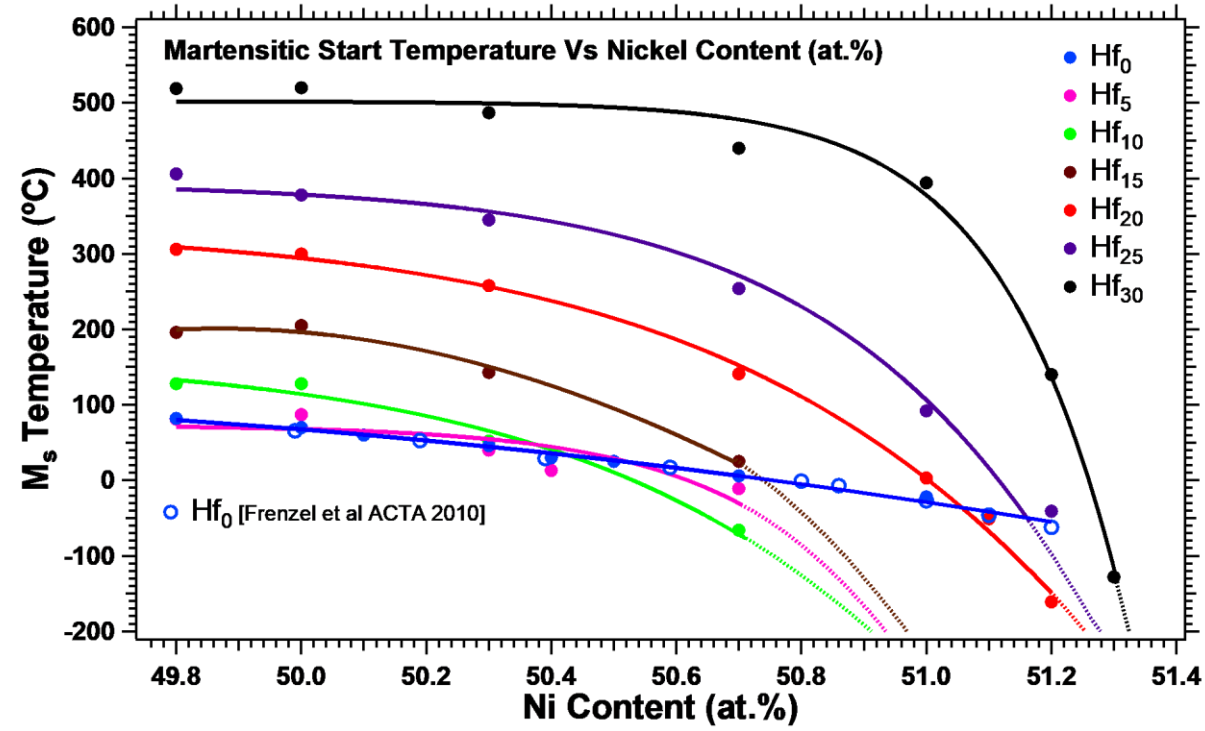

Figure 4.6 Variation of M_s temperatures with nickel content for constant Hf contents

To better understand the effect of Ni on TTs and compare the Ni dependence of NiTiHf alloys to that of binary NiTi, Fig.4.6 is constructed as a function of Ni using constant Hf curves. For Hf≤25% curves, M_s is roughly independent of Ni-content for Ni≤50%. However, above 50% Ni, M_s exhibits a non-linear negative dependence on Ni which becomes steeper with increasing Ni beyond 51%. This trend is similar to binary NiTi [13] and initial compositional studies performed by AbuJodam *et al.* which also depicted that the TTs didn't change with increase in Ni≤50at.% (attaining a plateau) followed by steep decrease in TTs for Ni≥50at.%. As alloys with Ni≥49.8at.% was melted for the present study, Fig. 4.6 shows the region of steep decrease in TTs. If the length scale on X-axis is changed to accommodate more Ni-lean compositions, then the trend lines in Fig. 4.6 would also show a plateau for Ni≤50at.% followed by steep decrease beyond Ni≥50at.%. For 30%Hf, no appreciable change in M_s was observed up to Ni=50.7%, but M_s started decreasing very rapidly beyond Ni=50.7%. Hence, the degree of the M_s dependence on the amount of excess Ni required to fully suppress MT depends on Hf content. For example, Ni=51% is sufficient to suppress MT for Hf=10% alloys, whereas Ni=51.5% is required to suppress MT for Hf=20,25 and 30%.

Fig. 4.7 presents the Hf dependence of the transformation hysteresis (A_f - M_s) for different nickel contents, exhibiting a strongly non-monotonic behavior. With increasing Hf, the hysteresis tends to increase and attain a maximum around Hf=8-11%, (which coincides with the M_s minimum), and then a minimum around Hf=20%. Beyond Hf=20%, MT hysteresis increases again, however it displays stronger Ni dependence and larger scattering as compared to the lower Hf contents. Nevertheless, the results indicate that Ni-rich compositions exhibit larger hysteresis than Ni-lean compositions for Hf≥20%.

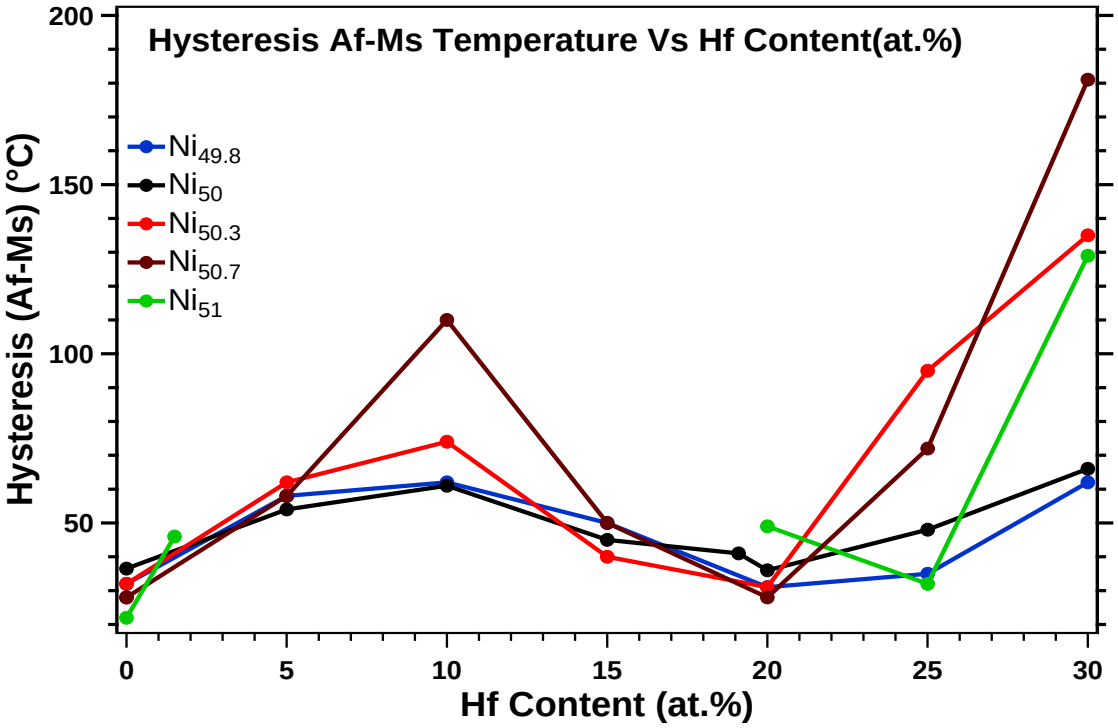

Figure 4.7 Variation of transformation hysteresis (A_f - M_s) vs. Hf content for varying Ni contents.

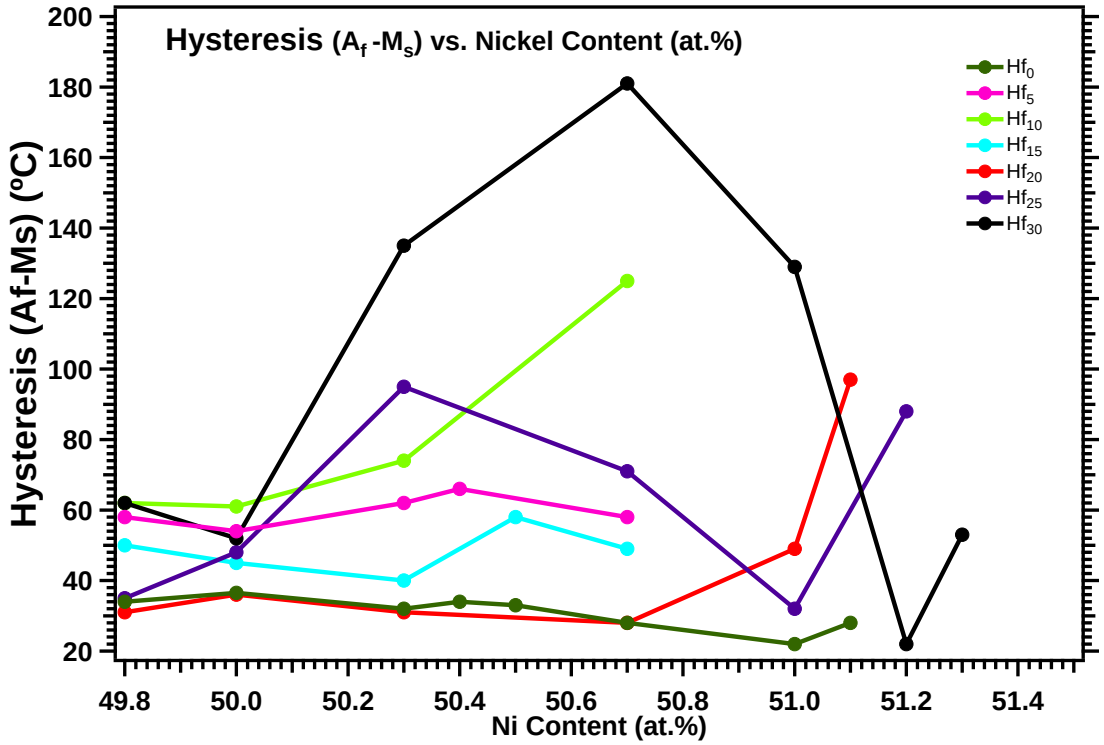

Figure 4.8 Variation of transformation hysteresis (A_f - M_s) vs. Ni content for varying Hf contents.

Fig. 4.8 shows the dependence of thermal hysteresis (Af-Ms) with Ni content for different fixed Hf contents. There is no common monotonic or non-monotonic trend of hysteresis with respect to Ni content for different Hf contents. Usually the hysteresis tends to decrease with increasing Ni content, for the binary NiTi alloys [1, 13, 14, 35, 161]. Similar results were observed in the present study. For a fixed Hf content of 5 at.% and 15 at.%, the hysteresis doesn't bear a fixed relationship with Ni content. The hysteresis values more or less remain unchanged and vary within a range of 30°C. For Hf=10 at.%, it is seen that the hysteresis tends to increase continuously from Ni=49.8 at.% to Ni=50.7 at.%, with no martensitic transformation observed for Ni=51 at.% alloy until -260°C. One of the reasons for such monotonic increase can be because of the increased local lattice strains at Hf=10 at.%. From Fig. 4.7 and 4.8 it can be seen that the hysteresis has a local maximum is obtained for Hf=10 at.% and also for fixed Hf=10 at.%, the hysteresis increases with increasing Ni. This suggest that the lattice experience enhanced local lattice strain because of Ni-antisite atoms on the Ni-rich compositions and bulky Hf atoms, which makes it hard for the austenite atoms to undergo a relative shear and transform into martensite. A detailed explanation on enhanced local lattice strain effects will be elaborated in section 4.5. .For Hf=25 at.% the hysteresis tends to increase with increasing Ni content until Ni=50.3 at.% and achieves a local maximum. With further increase in Ni content, the hysteresis decreases until Ni=51 at.%, followed by further increase. For Hf=30at.%, it can be observed that the hysteresis values don't change much until Ni=50 at.%, but then increases drastically up to Ni=50.7 at.%. With further increase in Ni content the hysteresis values drop drastically until Ni=51.2 at.% followed by slight increase for Ni=51.3 at.%. The exact reason for such behavior is not known, but local lattice strains can be one of the reasons for such behavior. One more reason for such behavior might be because of presence of extremely small nano-sized H-phase precipitates for Ni-rich compositions, which might have

nucleated and sparingly grown during DSC cycling, as the Ni_xTiHf_{25} alloys tend to transform at a very high temperature and hence the DSC or TGA upper testing temperature has to be raised usually above 500°C. The Ni-richness with Hf content of 25 at.% imparts ideal conditions for high H-phase precipitation kinetics and hence some of the H-phase precipitates might be formed during high temperature DSC cycling.

Nominal Composition			Transformation temperatures							
Ni	Ti	Hf	Ms	Mf	As	Af	Mp	Ap	Af- Ms	Ap-Mp
49.8	50.2	0	82	54	85	116	68	106	34	38
49.8	45.2	5	81	45	93	139	70	132	58	62
49.8	40.2	10	128	98	151	190	120	181	62	61
49.8	35.2	15	196	175	222	246	188	236	50	48
49.8	30.2	20	306	286	327	337	296	333	31	37
49.8	25.2	25	406	378	425	441	399	435	35	36
49.8	20.2	30	519	485	541	581	509	566	62	57
50	50	0	70	54	82	106.5	66	97	36.5	31
50	45	5	88	52	107	142	77	135	54	58
50	40	10	128	104	170	189	120	180	61	60
50	35	15	205	174	230	250	194	241	45	47
50	30	20	298	244	312	334	291	330	36	39
50	25	25	378	246	408	426	331	420	48	89
50	20	30	516	498	543	568	513	560	52	47
50.3	49.7	0	46	30	54	78	35	72	32	37
50.3	44.7	5	41	2	48	103	26	82	62	56
50.3	39.7	10	52	22	68	126	46	101	74	55
50.3	34.7	15	144	105	158	184	128	177	40	49
50.3	29.7	20	258	238	274	289	250	282	31	32
50.3	24.7	25	345	265	333	440	340	416	95	76
50.3	19.7	30	487	413	583	622	453	610	135	157
50.4	49.6	0	30	2	32	64	22	50	34	28
50.4	44.6	5	14	-34	12	80	-4	40	66	44
50.5	49.5	0	25	10	29.5	58	19	44	33	25
50.7	49.3	0	4	-20	6	32	-1	26	28	27

Table 4.1 continued……

Nominal Composition			Transformation temperatures							
Ni	Ti	Hf	Ms	Mf	As	Af	Mp	Ap	Af- Ms	Ap-Mp
50.7	44.3	5	-10	-48	-4	48	-20	16	58	36
50.7	39.3	10	-85	-127	-19	40	-78	26	125	104
50.7	34.3	15	26	-18	41	76	22	66	50	44
50.7	29.3	20	142	98	133	170	128	153	28	25
50.7	24.3	25	263	214	274	334	248	310	71	62
50.7	19.3	30	439	357	565	620	441	601	181	160
51	49	0	-25	-51	-23	-3	-37	-13	22	24
51	47.5	1.5	-97	-134	-80	-51	-101		46	101
51	44	5	no transformation observed until -260°C							
51	39	10								
51	34	15								
51	29	20	3	-13	36	52	3	48	49	45
51	24	25	92	74	109	124	88	121	32	33
51	19	30	396	350	438	525	367	475	129	108
51.1	48.9	0	-65	-96	-58	-37	-79	-50	28	29
51.2	23.8	25	-40	-60	20	48	-42	30	88	72
51.2	18.8	30	140	106	136	162	130	152	22	22
51.3	18.7	30	-124	-159	-91	-71			53	

Table 4.1 Transformation Temperatures measured using DSC, TGA and PPMS for give NiTiHf compositions

TTs presented here are higher than the ones reported in literature for most commonly studied alloys such as $Ni_{50.3}TiHf_{20}$ and $Ni_{50.3}TiHf_{15}$ [57, 60]. This is because of the fact that only nominal compositions are reported in literature, and most of these alloys were manufactured in large quantities using vacuum induction or skull melting techniques. During melting with these methods, a considerable amount of Hf/ Ti is lost because of oxidation and/or carbide formation, hence, increasing the real nickel content of the alloy. The compositional measurements using the inductively coupled plasma atomic emission spectroscopy (ICP-AES) on some of these $Ni_{50.3}TiHf_x$ samples revealed Ni contents to range between 50.7 to 51.4at%. However, those measurements

consists of relatively large uncertainties from the ICP-AES measurements. Recent study conducted by Benafan *et al.* [60] showed that the degree of the scatter associated with ICP-AES measurements for Ni can range close to 1 at%, which could change TTs over 300°C depending on the Hf content. In the present study, since we only used the samples where the weight loss during melting was less than 0.10%, we believe the current results are reasonably accurate. Table 4.1 shows the detailed measured TTs for the compositions shown in Fig. 4.5, 4.6 and 4.7.

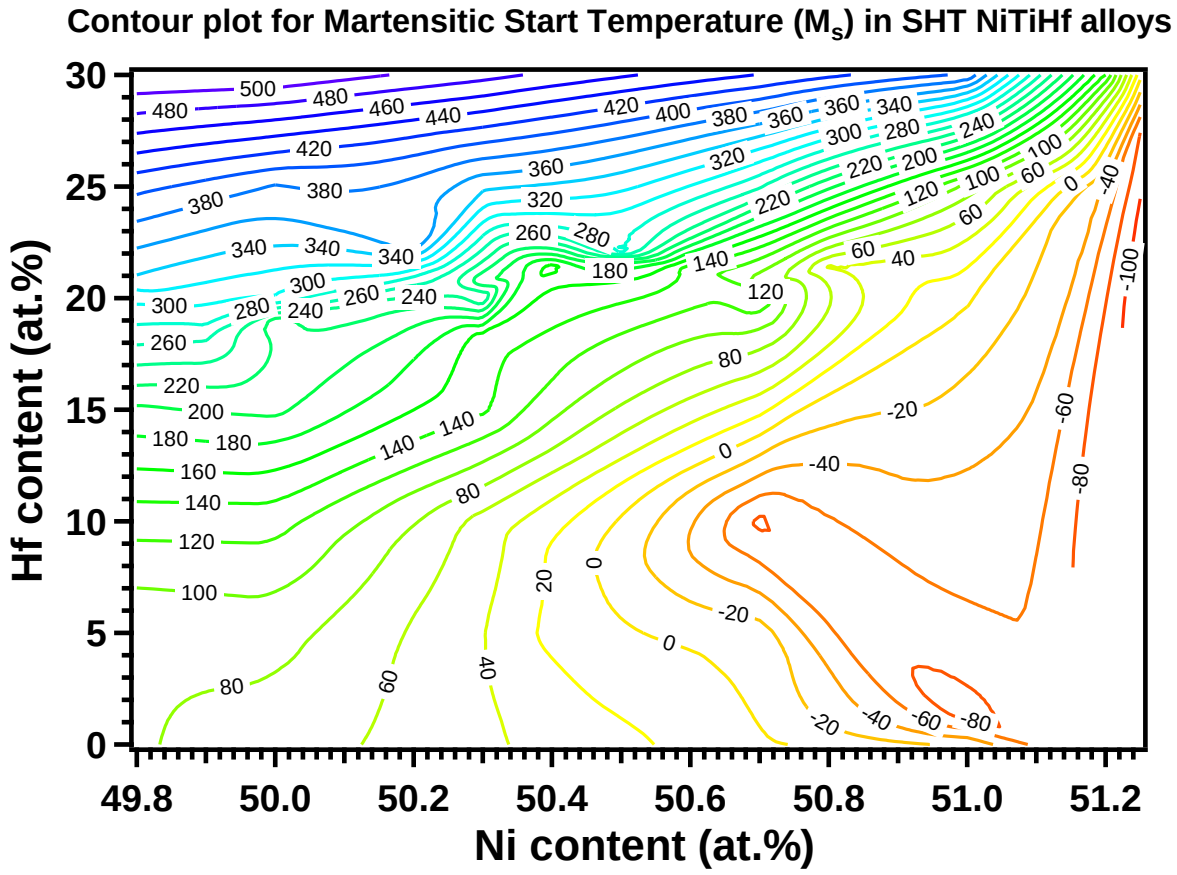

Figure 4.9 Contour plot of Martensitic Start Temperature (M_s) in the Ni and Hf space for SHT NiTiHf alloys.

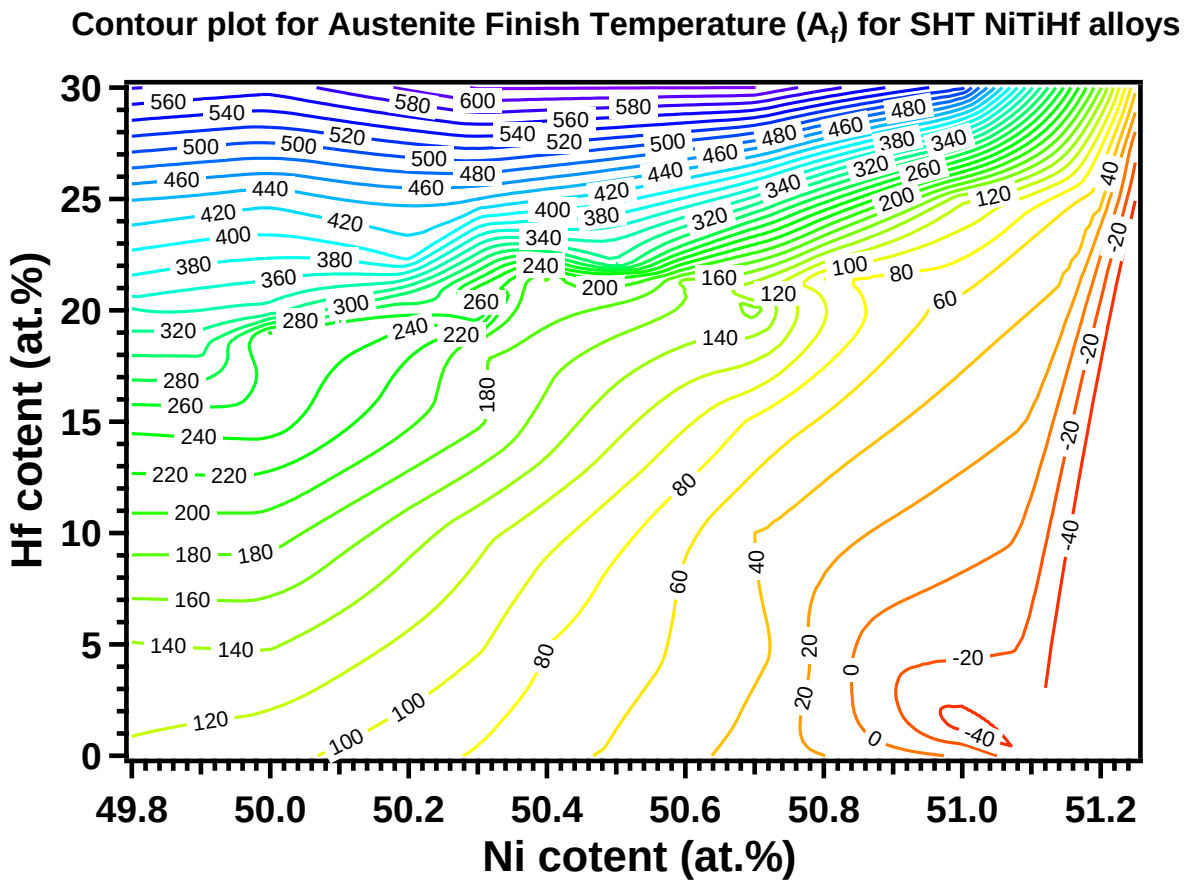

Figure 4.10 Contour plot of Austenite Finish Temperature (A_f) in the Ni and Hf space for SHT NiTiHf alloys.

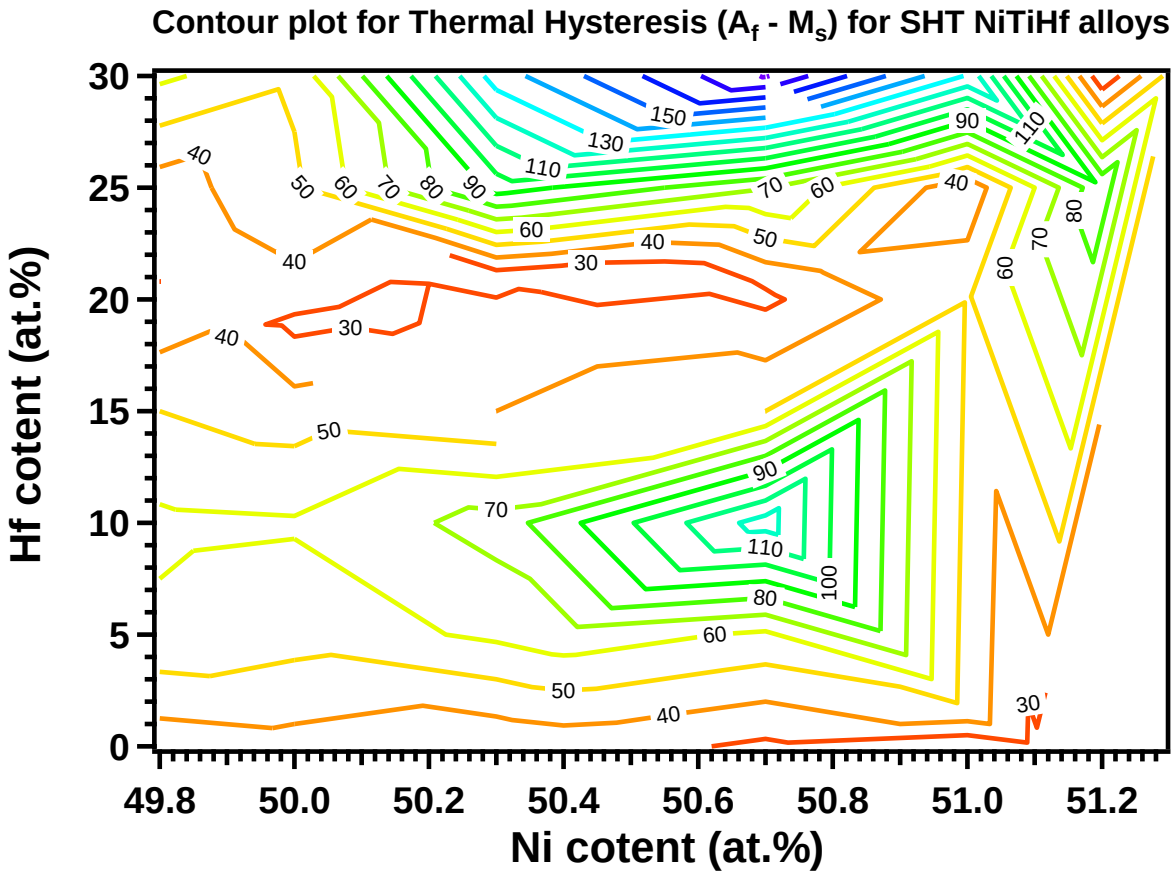

Figure 4.11 Contour plot of thermal hysteresis (A_f - M_s) in the Ni and Hf space for SHT NiTiHf alloys.

The above contour plots depict the variation of TTs and thermal hysteresis in the Ni – Hf composition space for SHT the NiTiHf alloys. Fig. 4.9 shows the contour plot for M_s temperature in the Ni-Hf compositional space. Fig. 4.10 shoes the plot for A_f temperature for various NiTiHf alloys. Whereas Fig. 4.11 shows the contour plot of thermal hysteresis (A_f – M_s) for various Ni and Hf content. The contour plot helps to give a big picture idea of the specific trends of the TTs and hysteresis much clearly. Also, such populated contour plots can also serve as composition maps and can be used to estimate the actual composition of an unknown NiTiHf alloy, provided the TTs are known in SHT condition.

4.3 Compositional dependence on Hardness

The hardness measurements were conducted on all the SHT samples by using a Vickers Micro-Hardness Tester with a load of 500 grams at room temperature. The results obtained from the hardness testing is shown in Fig. 4.12, where the hardness values in HV units are plotted against Hf content for respective Ni content. It can be seen that a general trend of hardness seems to increase with increasing Hf. As all the readings were recorded at room temperature, some of the alloys are in 100% martensitic state or 100% austenitic phase or a mixture of both. By the crystallographic nature of the austenite phase, since it's more regular and symmetrical in nature, possess higher hardness value than its corresponding martensite phase which is comparatively less symmetric. Therefore, alloys that are in austenitic phase at room temperature i.e., $Ni_{50.7}TiHf_{10}$ and $Ni_{51}TiHf_{(5,10,15)}$ shows an enhanced hardness and tend to deviate from the martensite trend line projection. The $Ni_{50.7}TiHf_{15}$ alloy shows a mixed micro-structure at the room temperature and hence its hardness values lie in between the austenite and martensite phase transition region. From the plot, it seems that the phase transformation from martensite to austenite offers a much enhanced hardness than by increase in Hf content of the alloy. In short, the martensitic phase transformation has a pre-dominant effect on hardness than the compositional component.

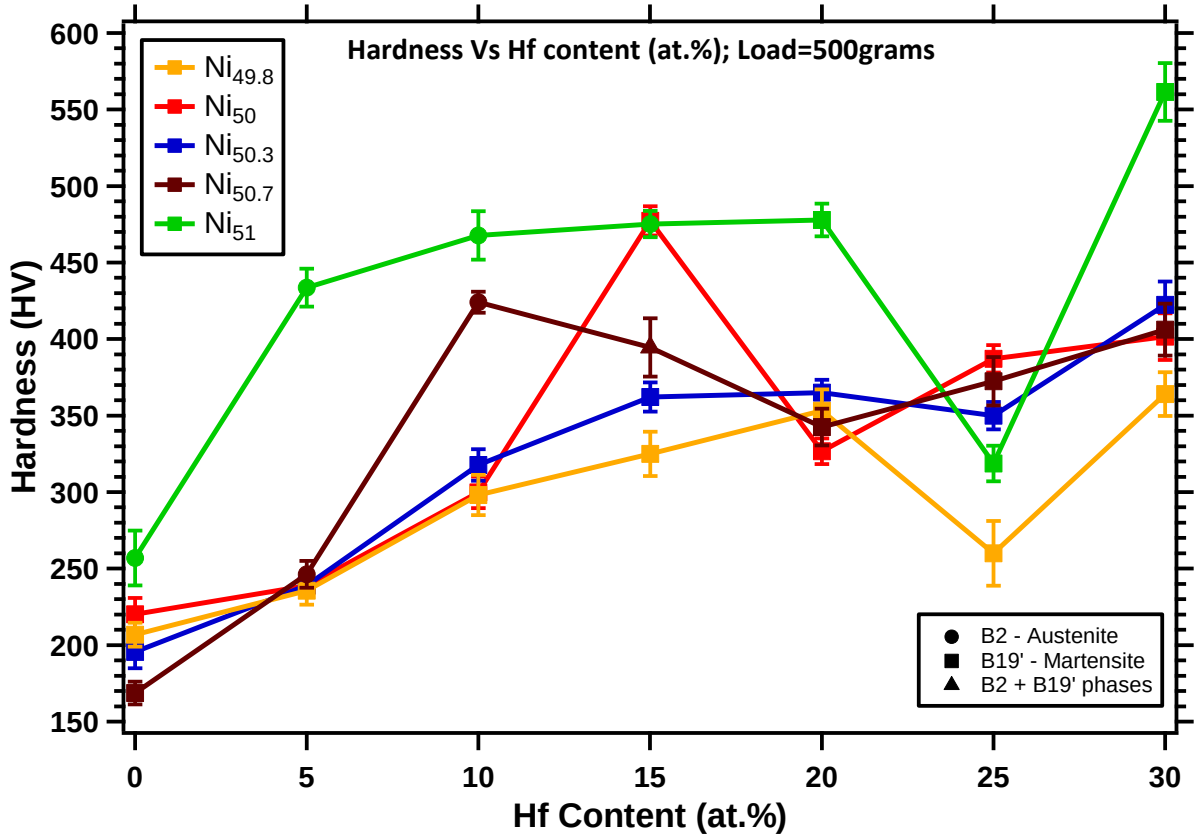

Figure 4.12 Hardness Vs Hf content plot of the SHT NiTiHf alloy conducted at room temperature. The general trend is hardness increases with Hf content.

4.4 Enthalpy of MT Co-relation to Composition and Thermal Hysteresis

The enthalpy of martensitic transformation is usually defined the energy dissipated during the MT. The enthalpy of MT can be measured using the DSC curve from a particular SMA, which is defined as the area under the transformation curve in the heat flow Vs temperature plot. The Fig. 4.13 shows such forward MT Enthalpy vs Hf composition plot for various NiTiHf alloys. A general trend observed is that for $Ni_{49.8}TiHf_x$ and $Ni_{50}TiHf_x$ alloys, is that the enthalpy tends to decrease initially with increasing Hf content upto 5 at.% followed by a continuous increase until 25 at.% Hf for $Ni_{49.8}TiHf_x$ and until 20 at.% Hf for $Ni_{50}TiHf_x$ alloys. With further increase in Hf content beyond the aforementioned limits the enthalpy values decrease for Ni-lean and equi-atomic NiTiHf

compositions. One reason for such decrease in the enthalpy values can be because of formation of H-phase precipitates during cooling, as the Hf content is so high.

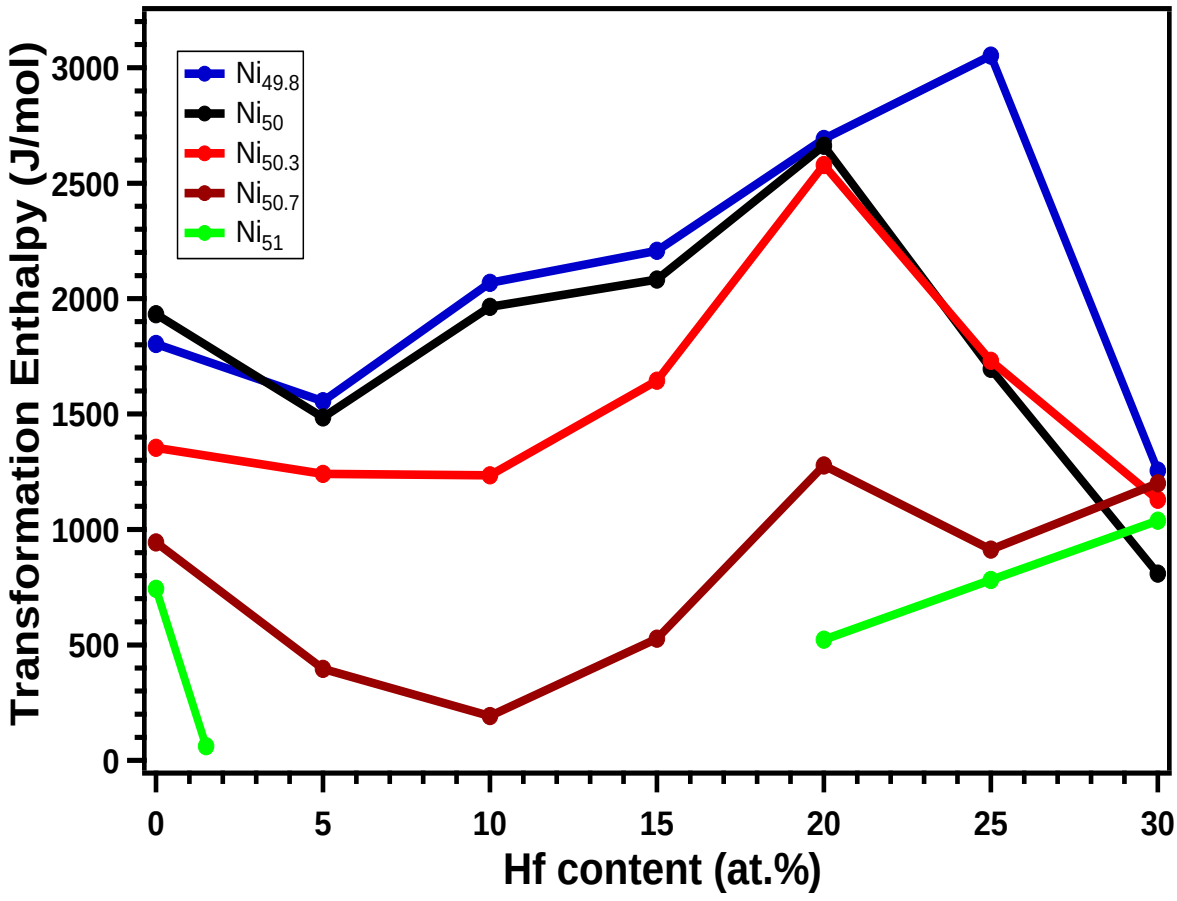

Figure 4.13 Martensitic Transformation Enthalpy (forward MT) Vs Hf content of varying Ni content

Similarly, for $Ni_{50.3}TiHf_x$ and $Ni_{50.7}TiHf_x$ alloys, it can be seen that the enthalpy value decreases slightly for Ni=50.3 at.% alloys and for Ni=50.7 at.% alloys the enthalpy tends to decrease drastically until 10 at.% Hf addition. With further increase in Hf content, above 10 at.%Hf addition, the enthalpy values tend to increase with increasing Hf content until 20 at.% for $Ni_{50.3}TiHf_x$ and $Ni_{50.7}TiHf_x$ alloys . Beyond Hf=20 at.%, the enthalpy tends to decrease drastically

with increasing Hf content for Ni=50.3 at.% compositions, whereas decreases slightly for the Ni=50.7 at.% compositions. For Ni=51 at.%, it can be seen that enthalpy decreases drastically with increase in Hf = 0 at.% to Hf=1.5 at.%. The martensitic transformation is completely suppressed for Hf=5 at.% to 15 at.%. With further increase in Hf content from Hf= 20 at.% to 30 at.%, the enthalpy increases monotonically. In Ni-rich NiTiHf compositions, the solution effect is enhanced as with bulky Hf atoms , the Ni atoms substituting the Ti atoms in Ni-rich NiTiHf compositions tends to enhance the local lattice strains, provides the difficulty for the movement of martensitic transformation fronts and hence the amount of austenite undergoing transformation to martensite is decreasing with increase in lattice strains and therefore the enthalpy value decrease. Beyond 10%Hf addition, as the overall lattice parameter of the unit cell expands the local lattice strains reduce and the normal MT is resumed.

The behavior of enthalpy with respect to Ni content is much clear and shows a monotonic decrease with increasing Ni content as seen in Fig. 4.14. For any Hf content, all of the alloys shows a general decrease trend with increasing Ni content with a negligible amount of scatter. These results are similar to those found by Frenzel et al in the binary NiTi system [13, 35]. With the increasing Ni content, the lattice strains associated with the Ni anti-site defects also increases and thus providing resistance to the MT. For Hf=30 at.% alloys, the enthalpy doesn't change significantly with increasing Ni content as compared for other constant Hf content curves. Also, for Hf=30 at.% alloys, the enthalpy tends to decrease slightly with increase in Ni content from 49.8 at.% to 50 at.%, followed by a slight increase for Ni=50.3 at.%. Beyond Ni=50.3 at.% the enthalpy doesn't vary much. Such unusual behavior of the Ni_xTiHf_{30} alloy can be because of the presence of H-phase precipitates formed during the cooling. As the Ni and Hf content is so high, the H-

phase kinetics is very high and hence during cooling nano-sized H-phase particles can be formed instantaneously.

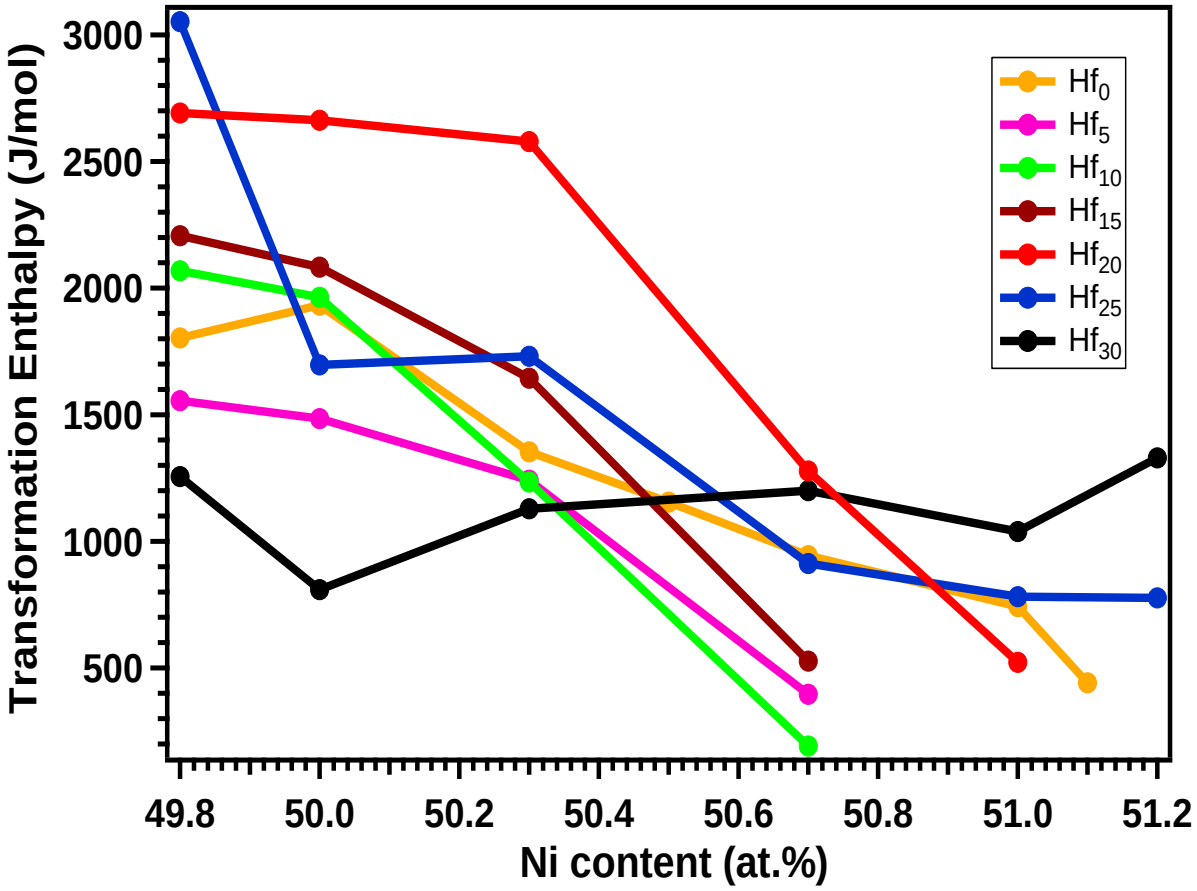

Figure 4.14 Martensitic Transformation Enthalpy (forward MT) Vs Ni content of varying Hf content

4.5 Crystallographic Computability Dependence on Composition

In order to understand the basic dependence of thermal hysteresis on the composition, the crystallographic compatibility was analyzed by computing the middle eigen value (λ_2) of the martensitic stretch transformation matrix. Based on crystallographic theory of martensitic transformation, researchers have developed a frame of equations to compute the eigen values of

the transformations stretch matrix for a monoclinic martensite transition to body centered cubic austenite [162, 163]. The theory suggests that closer the det U =1 and $\lambda_2 = 1$, the greater is the crystallographic compatibility between the two phases, where U is the transformation stretch matrix and det U = $\lambda_{1*}\ \lambda_{2*}\ \lambda_3$. Therefore, the Hf dependence on hysteresis shown in Fig. 4.7 was studied under the light of crystallographic theory of MT. Compositions with a fixed Ni content of 50.3 at.% and with varying Hf content from 0 at.% to 25 at.% were considered and was analyzed using XRD to obtain the middle eigenvalue (λ_2).

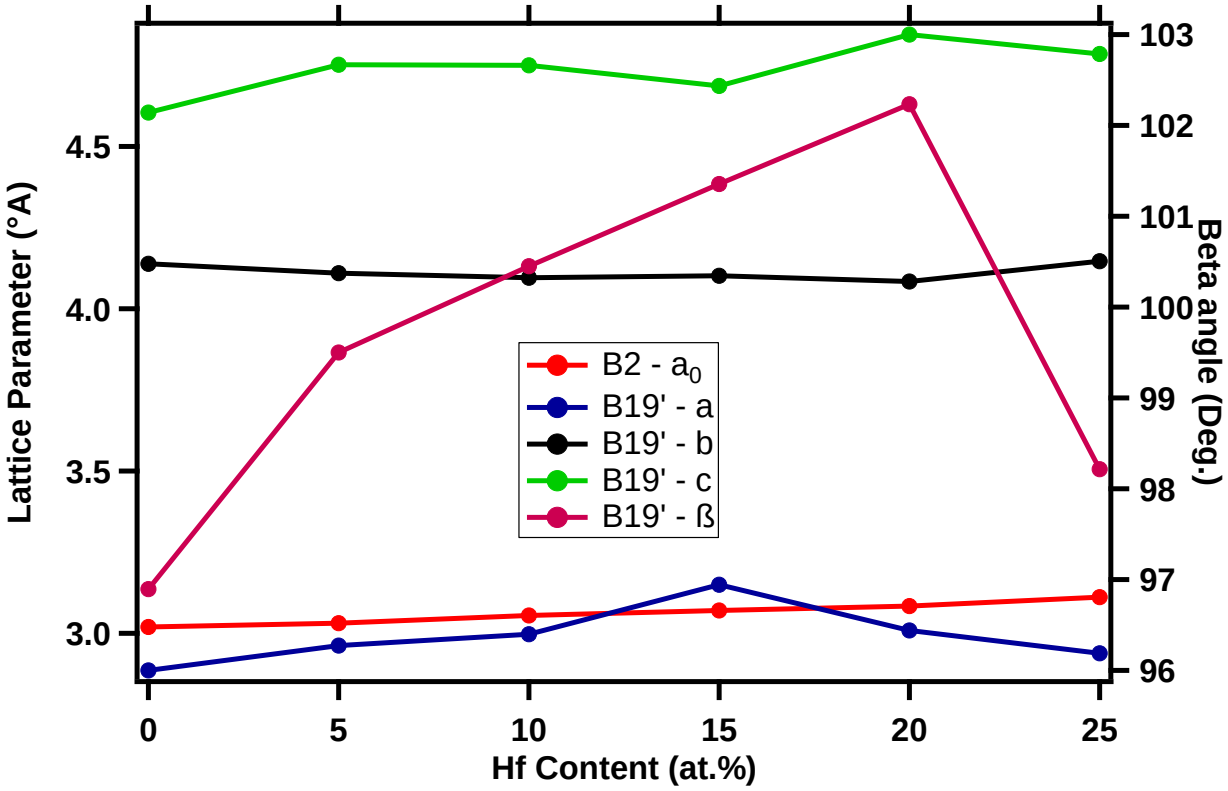

Figure 4.15 Lattice parameters of B19' martensite and B2 austenite phase as a function of Hf content for $Ni_{50.3}TiHf_{(x)}$ alloys. The lattice parameter of the cubic B2 cell seems to increase with increasing the Hf content.

Fig. 4.15 shows the variation of lattice parameters of B19' martensite and B2 austenite phases Vs hafnium content. The martensite lattice parameters were calculated at room temperature, whereas,

the austenite lattice parameter was calculated at several temperatures for which the material was in austenitic phase e.g., A_f+20, A_f+40, A_f+60, M_s+60, M_s+40, M_s+20, and extrapolated to room temperature. From Fig. 4.15 it can be seen that the austenite phase lattice parameter increases monotonically with increasing Hf content. This indicates that the volume of the austenite unit cell increases with increasing Hf content. The middle eigenvalue (λ_2) were calculated by comparing room temperature martensite and extrapolated austenite lattice parameters. Fig. 4.16 shows that λ_2 values decreases away from 1 with increasing Hf content upto 20at.% Hf addition followed by increase for Hf=25at.%. As mentioned before, the closer the middle eigenvalue (λ_2) is to 1, lower is the value of thermal hysteresis. Therefore, as the middle eigenvalue (λ_2) deviates from 1, the hysteresis values increase and thus forming a 'V-shape' curve with its lower intersecting apex being centered at $\lambda_2 = 1$. As studied by Evirgen et al. [77], shows that alloys transforming from B2→B19' martensite, follow a V-curve in Hysteresis Vs λ_2 plot, with a much shallower slope than alloys transforming from B2→B19 martensite. Fig. 4.17 shows the data from the present work along with other binary NiTi and NiTi-based SMAs. It can be seen that the alloys such as NiTi(Pt,Pd,Au,Cu) which undergoes MT from the cubic B2→B19 orthorhombic martensite, show a very high dependence of middle eigenvalue (λ_2) on the thermal hysteresis. As mentioned in section 2.5 of chapter 2, that such dependence was used to design new HTSMAs with narrow hysteresis. On the other hand alloys like binary NiTi, and NiTi(Hf,Zr) which undergoes a MT from the cubic B2→B19' monoclinic martensite shows a shallower V-curve behavior as compared to alloys undergoing B2→B19 MT.

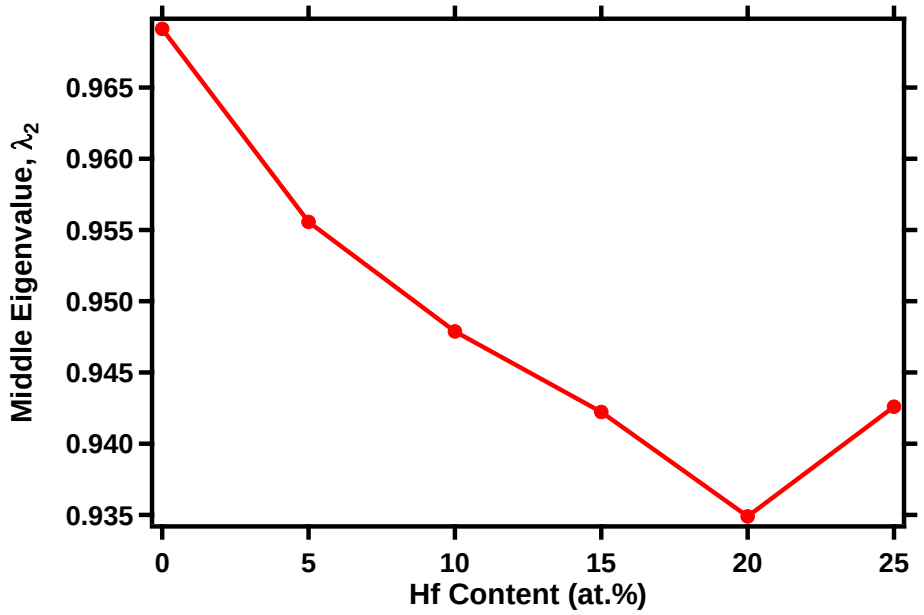

Figure 4.16 Middle eigenvalue (λ_2) Vs hafnium content for $Ni_{50.3}TiHf_{(x)}$ alloys.

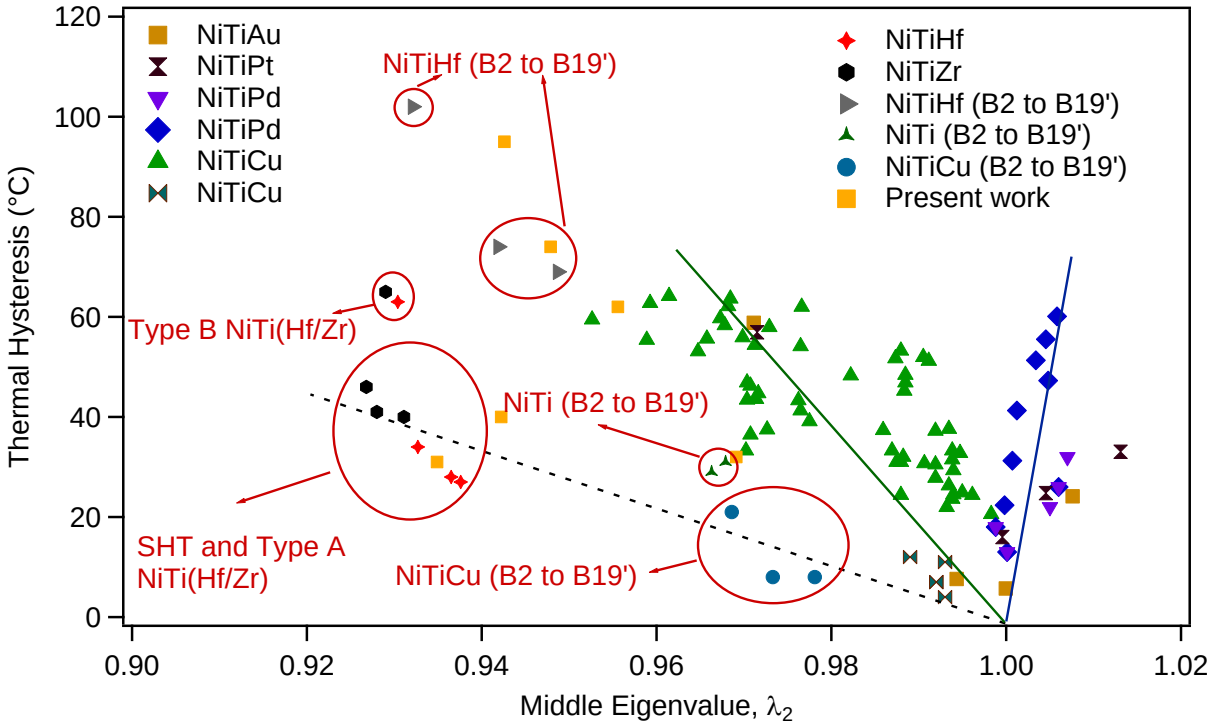

Figure 4.17 The thermal hysteresis Vs middle eigenvalue (λ_2) values for various NiTi and NiTi-based SMA compositions. For NiTi(Cu, Pd, Au) compositions showing steep dependence of hysteresis on λ_2 values as they undergo B2→B19 MT. Alloys like binary NiTi, NiTiHf and

NiTiZr follows the shallow V-curve and hysteresis is not highly dependent on λ_2 value as they undergo B2→B19' MT [77].

Along with literature data shown in Fig. 4.17, the middle eigenvalue (λ_2) of the present work is also plotted. It can be seen that the data from the current work fall closer to the shallow 'V-shape' curve or closer to NiTiHf data-points. So we can conclude that though the middle eigenvalue (λ_2) of transformation stretch matrix bears a relationship with composition, but still cannot answer the question of varying hysteresis as shown in Fog. 4.7 with increasing Hf content. Apart from middle eigenvalue (λ_2) value, the co-factor conditions can also be utilized to optimize the thermal hysteresis. The co-factor conditions address the compatibility between the austenite and martensite and corresponds to the degeneracies of the crystallographic theory of MT. If the second co-factor condition (CC2) approaches zero, then the thermal hysteresis also approaches zero or the minimum value. Therefore, instead of middle eigenvalue (λ_2), the co-factor conditions can provide more insight into the hysteresis dependence on composition in NiTiHf HTSMA systems.

4.6 Strain Glass and Precipitate Precursors

Analysis of the above results leads to the observation of few interesting phenomena related to the MT characteristics in NiTiHf alloys. Although it has been known that Hf, replacing Ti, increases the TTs of NiTi alloys [158], how off-stoichiometric Ni contents influence the change in TTs has not been systematically studied. It is clear from Fig. 4.6 that excess Ni leads to significant changes in TTs, yielding M_s variations as large as 500°C for a given Hf content, through a change in Ni from 50at% to 51.3at%. Such dependence of TTs in excess Ni in NiTiHf alloys are more

pronounced as compared to 83°C change in M_s with 1at% excess Ni in NiTi [13]. Secondly, the rapid reduction of TTs and complete suppression of MT with small Hf additions in Ni-rich NiTi alloys have not been reported before and are somewhat unexpected. These results indicate that, along with Ni anti-site defects in Ti sub-lattice, which lead to drop in TTs in binary NiTi [13, 35], bulky Hf atoms replacing Ti should contribute to the increase in local lattice distortions, and thus, the reduction in TTs in NiTiHf alloys. Density Functional Theory (DFT) calculations performed by Singh *et al.* [164] showed that Hf atoms will always prefer to go Ti sites only in a NiTi B2 lattice, and hence, to the best of our understanding, despite the amount of Hf added, it doesn't change the number of Ni anti-site atoms occupying Ti sites, but it does varies the degree of local lattice distortion produced by Hf atoms which might change the near neighbor configuration of atoms which might result in decrease in TTs [13, 35]. In addition, cumulative increase in local lattice distortions is likely to stabilize the quasi-dynamic strain nano-domains in austenite, similar to those reported by Zhang *et al.* [165] for Ni-rich NiTi. These defects tend to hinder MT, causing energy barriers to the nucleation and growth of martensite. As a consequence, amount of overcooling required for the onset of transformation increases, and hence M_s decreases. This hypothesis can be proven with electronic structure calculations, seeking for the role of Hf on the Fermi surface nesting responsible for MT, however, such calculations would be computationally expensive due to the size of the supercells needed to mimic the off-stoichiometric compositions.

Another effect of Ni and Hf substitutional defects on MT of NiTiHf alloys is that the degree of transformation arrest changes between alloys undergoing normal MTs and the ones showing no transformation, depending on the Ni and Hf concentrations. From Fig.4.5 and 4.6 it can be seen that TTs notably decrease for Hf-contents around 8-11% and with increase of excess Ni. The dependence of TTs and hysteresis on Hf is non-monotonic showing an M_s minimum and a

hysteresis maximum around these compositions. At the same time, Hf substitutions lead to an increase in the lattice parameter of the austenite, especially for Hf-contents beyond 10%, causing overall expansion of the unit cell. Therefore, the local lattice distortions caused by few Hf atoms start decreasing as a result of overall expansion of the unit cell at higher Hf contents [166]. Due to the reduction in the lattice distortions, barriers to B2→B19' transformation decrease and MT is recovered, causing increase in TTs and decrease in hysteresis. On the other hand, Fig. 4.7 depicts a minimum for MT hysteresis around Hf=20% for all Ni contents, and notable increase in the hysteresis beyond 20% Hf. The origin of this increase in the hysteresis with Hf beyond 20% is not clear.

Fig. 4.18 shows the room temperature selected area electron diffraction patterns (SAEDPs) of the NiTiHf alloys with fully suppressed MT. All SAEDPs exhibit characteristic primary reflections spots of the B2 austenite. Fig. 4.18a depicts the SAEDP from $Ni_{50.7}TiHf_{10}$ along $[75]_{B2}$ which shows diffuse scattering along <110> direction. Fig. 4.18b and 4.18c display the SAEDPs from $Ni_{51}TiHf_5$ and $Ni_{51}TiHf_{10}$ along $[001]_{B2}$, respectively, which feature similar intense diffuse scattering along<100> direction. Fig. 4.18d exhibits the SAEDP along $[1\bar{1}0]_{B2}$ from $Ni_{51}Ti_{34}Hf_{15}$,

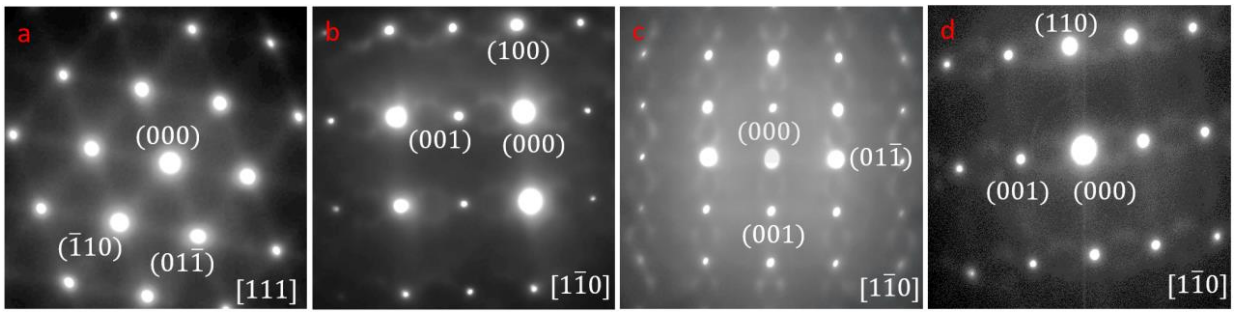

Figure 4.18 Selected area electron diffraction patterns (SAEDPs) obtained from (a) $Ni_{50.7}TiHf_{10}$ along $[111]_{B2}$ showing diffuse scattering along <110> directions; (b) $Ni_{51}TiHf_5$ and (c) $Ni_{51}TiHf_{10}$ along $\mathbf{[1\bar{1}0]_{B2}}$ showing diffuse scattering along <001> direction, while (d) $Ni_{51}TiHf_{15}$ along $\mathbf{[1\bar{1}0]_{B2}}$ which displays diffuse scattering along <001> and <110> directions. These diffuse scattering patterns are attributed to the short range ordering due to the redistribution between Ti and Hf atoms

with diffuse scattering along both <001> and <110> directions. Saghaian *et al.* [58] and Coughlin *et al.* [69] observed similar diffuse scattering in <001> and <$\bar{1}$10> SAEDPs in SHT $Ni_{51.2}Ti_{28.8}Hf_{20}$ and as extruded $Ni_{51}Ti_{28.8}Hf_{20}$, respectively. Sandu et al. [167, 168] conducted extensive TEM studies on $Ni_{52}TiZr_6$ and $Ni_{53}TiZr_6$ reporting that the diffuse scattering can be attributed to segregation and short range ordering (SRO) of Zr atoms (Hf in our case, NiTiZr system is similar to NiTiHf [67]). These diffuse streaks in diffraction patterns are attributed to the redistribution between Ti and Hf or Zr atoms, which can act as a precursor state to the formation of H-phase nano-precipitates, as proposed by Pérez-Sierra *et al.* [72]. Coughlin *et al.* [69] observed ~5nm sized high intensity areas showing characteristic n/4$(111)_{B2}$ superlattice spots in Fast Fourier Transformations (FFTs) obtained from high resolution TEM, which they defined as H' phase, precursor to the H-phase. It is believed that the SRO creates elastic barriers to the transformation, contributing to the reduction of TTs and suppression of MT in the present compositions. The compositions considered here were solutionized and water quenched without any additional heat treatment. This suggests that kinetics for the segregation of Ti and Hf atoms must be fast such that diffuse streaks in SAEDPs appear and MT is hindered. For Hf=10 %, the reduction in M_s is enhanced with increasing Ni-content, which indicates that higher the Ni-content is, higher the degree of SRO for Hf atoms might be. One possible reason for the increase in SRO with increasing Ni can be the excessive increase in local strains within the unit cell [35].

4.7 Summary

From the current chapter, it can be seen that transformation characteristics have a very high dependency on the transformation temperatures and other transformation characteristics of NiTiHf SMAs. The major findings of this chapter can be summarized as follows:

1. The TTs can be tailored in a wide range of temperatures ranging from -170°C up to 500°C by varying nickel (49.8 to 51.5 at%) and hafnium (0 to 30 at%). For Ni-lean and Ni=50 at% compositions, the TTs didn't increase much with Hf addition up to 10% followed by continuous increase of TTs beyond 10%. For Ni-rich compositions, TTs decreased with initial Hf addition attaining a minimum followed by continuous increase.
2. This initial drop of TTs can be attributed to the local lattice distortions created by nickel anti-site and hafnium substitutional defects which tend to stabilize austenite and cause frozen strain nano-domains in B2 austenite. One more contributing factor for lowering of TTs can be the short range ordering between Ti and Hf atoms in the Ti sub-lattice which can act as a precursor to H-phase nano-precipitates.
3. The hardness tends to increase with increasing the hafnium content of the samples for a fixed nickel content.
4. For enthalpy of MT is not highly dependent on Hf content for Ni-lean and equi-atomic compositions and shows a random behavior. One possible reason for the fluctuations in behavior might be the presence of different volume fraction of $(Ti,Hf)_2Ni$ second phase, which can alter the composition of the martensitically transforming phase
5. For Ni-rich Ni=50.3 and 50.7 at.% which is a single phase region and shows a specific behavior which is in contrast with the hysteresis dependence on composition. With

increasing Hf content, it can be seen that the enthalpy values decreases with initial increase in Hf content from 0 at.% to 10 at.% followed by an increase until Hf = 20 at.%. With further increase in Hf content beyond 20 at.% enthalpy value decreases drastically for Ni=50.3 at.% and decreases slightly for Ni=50.7 at.%. For Ni=51 at.%, the enthalpy initially decreases until MT disappears completely followed by increase with increasing Hf content.

6. The enthalpy of MT shows a decreasing trend with increasing Ni content for all fixed Hf values, except Hf = 30 at.%. For Hf = 30 at.%, the enthalpy more or less remain the same and doesn't change much with increasing Ni content.
7. The hysteresis dependence on Hf content was studied in the light of crystallographic theory of MT by computing the middle eigenvalue (λ_2) value. The current study shows that though that the λ_2 value has dependence on Hf content but the hysteresis is not highly dependent on λ_2 values.
8. Dynamic mechanical analysis and high resolution TEM need to be conducted on the specimens to gather additional evidences for the strain-glass or H-phase precursor aforementioned phenomena.

CHAPTER V

EXPERIMENTAL INVESTIGATION OF EQUILIBRIUM BETWEEN THE H-PHASE PRECIPITATES AND B2/B19' MARTENSITICALLY TRANSFORMING PHASE IN NiTiHf HIGH TEMPERATURE SHAPE MEMORY ALLOYS

This chapter is concerned towards exploring the thermodynamic equilibrium between the H-phase and the B2 martensitically transforming phase, which is talked so much about in the previous chapter. As seen in chapter 2 that the H-phase precipitates impart high strength and thermal and dimensional stability to the SMA, but the thermodynamic equilibrium between the two phases has not been yet explored. This chapter thus focuses on highlighting the importance of H-phase precipitation, followed by a detailed study of thermodynamics of H-phase precipitate and a methodology through which thermodynamics can be used to design NiTiHf alloys with tailored TTs.

5.1 Differential Scanning Calorimetry

Fig. 5.1 shows the DSC plot for the SHT and thermally aged $Ni_{50.3}TiHf_{20}$ alloy samples. It is very clearly evident that aging heat treatment increases the transformation temperatures drastically. The martensitic start (Ms) temperature tends to increase from 91˚C for SHT sample to 159˚C and 161˚C for samples aged at 600˚C-10hrs and 650˚C-10hrs, respectively. In order to exclude the 1st cycle effect from DSC, all the comparison and reporting of transformation temperature data is done from the 2nd DSC cycle. Also the austenite finish temperature (A_f) also increases with aging heat treatments. The Af was found to increase from 124˚C for SHT sample to 200 ˚C and 208 ˚C for HT600 and HT650 sample, respectively. Apart from M_s and A_f, all the

other transformation temperatures are also observed to increase in similar proportions. The thermal hysteresis computed as A_f-M_s was found to increase slightly upon aging at chosen heat treatment temperatures. The thermal hysteresis was observed to increase from 33˚C for SHT sample to 41˚C and 47˚C for HT600 and HT650 sample, respectively. As the thermal hysteresis are highly influenced by aging heat treatment temperatures [57], for a given $Ni_{50.3}TiHf_{20}$ alloy heat treated at 600 ˚C and above the precipitates are large enough to cause an increase in thermal hysteresis [42, 63, 169]. Along with elevated TTs, precipitation also enhances the cyclic stability of the martensitic transformation behavior with consecutive DSC cycles. Fig. 5.1 shows three DSC cycles for each sample and we have determined the cyclic stability by defining it as the difference between the M_s value from the 3rd DSC cycle and M_s value from 1st DSC cycle (M_s^3-M_s^1). The value of M_s^3-M_s^1 is 11˚C, 4˚C, 5˚C for SHT, HT600 and HT650 samples, respectively. Similar results were observed by Karaca et al [42] and Evirgen et al [56].

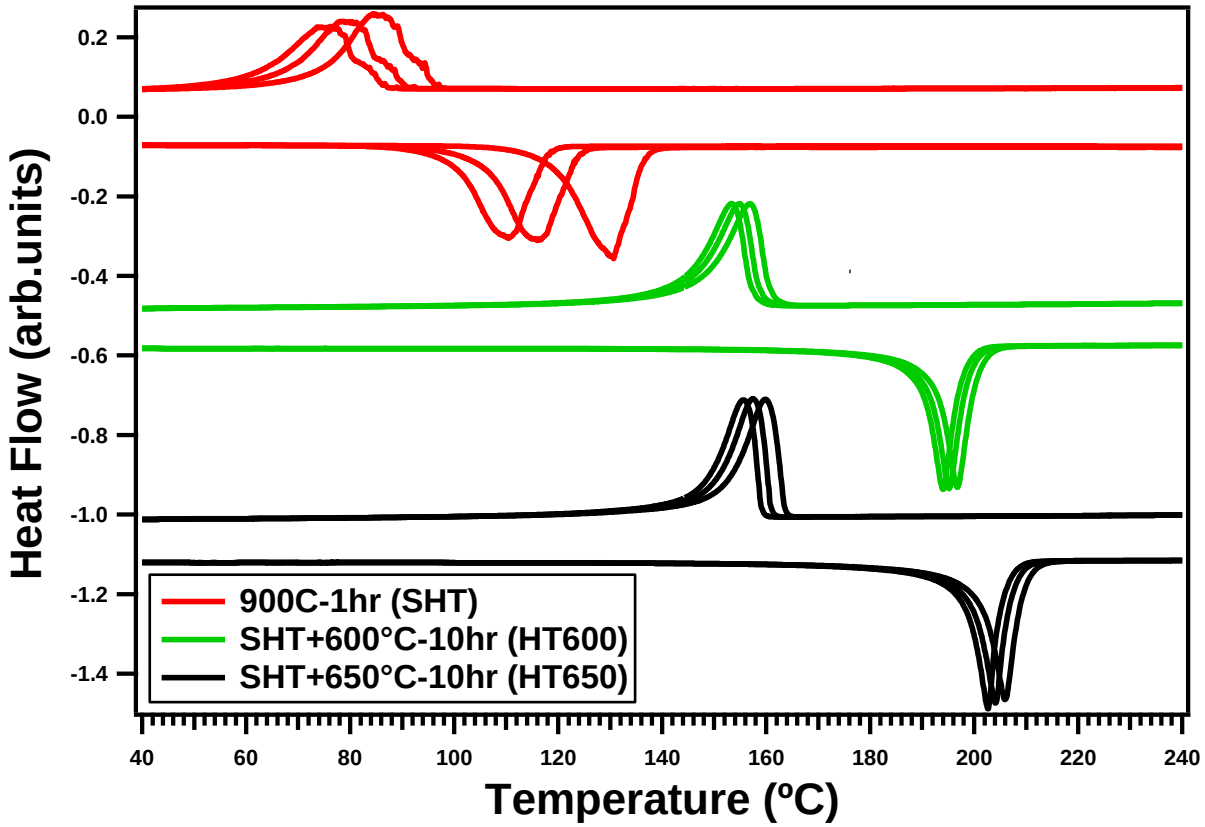

Figure 5.1 DSC results from the $Ni_{50.3}Ti_{29.7}Hf_{20}$ alloy after solution heat treatment at 900°C – 1hr and secondary aging heat treatment at 600°C - 10hours and 650°C - 10hours followed by water quenching. The DSC results show the aged samples HT600 and HT650 show higher transformation temperatures and higher thermal stability as compared to the SHT sample.

5.2 Micro-structural and Compositional analysis of H-phase precipitates

In order to determine the equilibrium H-phase precipitate region in the Ni-Ti-Hf ternary phase diagram, it is very essential to analyze the compositional characteristics of the H-phase precipitates. A detailed knowledge of the compositional distinction between the H-phase precipitate and the B2 martensitically transforming phase will give a better insight in analyzing the H-phase region in the diffusion multiple sample. Fig. 5.2a shows the high-angle annular dark field (HAADF) STEM image of HT600 sample with a uniform distribution of H-phase precipitates with average length of 36.2±9.4 nm and average width of 16.7±3.1 nm. Fig. 5.2b shows the

HAADF STEM image of HT650 sample with an average length and width of 91.2±18.0 nm and 30.8±10.3nm, respectively.

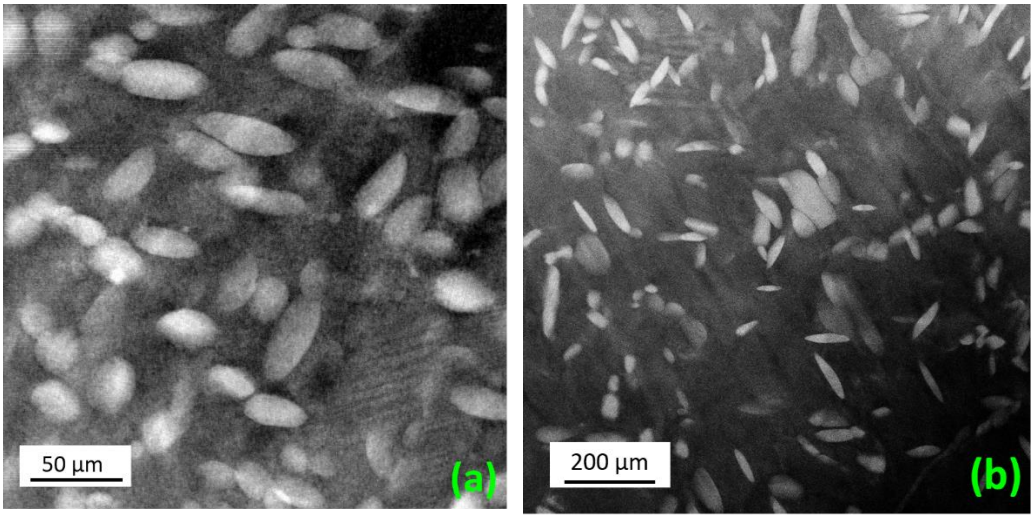

Figure 5.2 Shows a STEM-HAADF image of the $Ni_{50.3}Ti_{29.7}Hf_{20}$ alloy after aging heat treatment at (a) 600°C – 10 hrs i.e., HT600 sample with an average length of 36.2± 9.4nm and width of 16.7 ± 3.1 nm of H-phase precipitates, and (b) 650°C – 10 hrs i.e., HT650 sample with an average length of 91.2± 18.0 nm and width of 30.8± 10.3nm of H-phase precipitates.

After acquiring images from the respective samples, an area from the thin cross section of the sample was selected which had isolated H-phase precipitates, separated away from each other in a way that they don't seem to be overlap. EDX compositional maps were acquired from such an area in order to obtain the matrix and H-phase precipitate compositions. Fig. 5a shows the HAADF bright field image of the HT650 sample from where the EDX map was acquired. Fig. 5b, c and d show the individual elemental EDX scans of Ni, Ti and Hf, respectively and it is evident that the H-phase precipitate is rich in Ni and Hf, whereas lean in Ti. After acquiring the EDX maps, the average composition of the H-phase precipitate and B2 matrix phase is reported in Table 1. Similar EDX measurements were also performed on the HT600 sample and the results obtained from the EDX analysis are reported in Table 1. The average Ni content of the B2 matrix phase for

the HT600 and HT650 sample after aging is 49.93 and 48.36 at.% respectively. As mentioned in section 3.1 the increase the TTs for aged HT600 and HT650 sample is due to the drop in Ni content of the matrix as compared to the SHT samples. It is also very clearly evident from the Fig. 5.3, that the H-phase precipitates are large enough to restrict the growth of martensitic variants in between them. As the precipitate is considerably large, the increase in the number of invariant boundaries during the martensitic growth is confined to limited space between the large H-phase precipitate particles tends to increase the energy of dissipation during the martensitic transformation and thus resulting in higher hysteresis. Similar phenomenon of increase in thermal hysteresis after aging heat treatment have been observed in other recent studies as well [31, 56, 77].

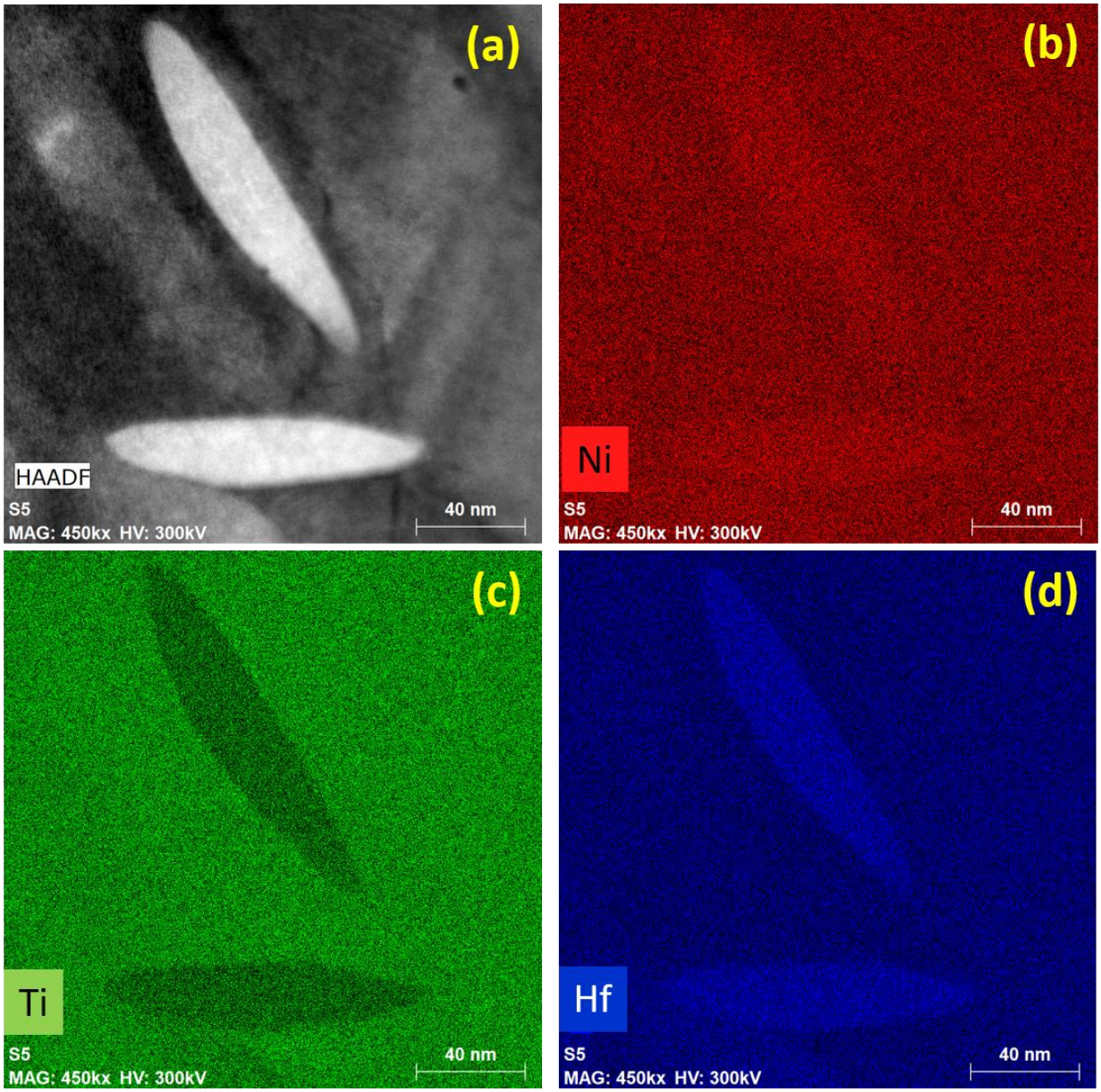

Figure 5.3 Shows the EDX maps of the precipitate and surrounding matrix of $Ni_{50.3}Ti_{29.7}Hf_{20}$ alloy heat treated at 650°C-10 hours-WQ in which (a) shows the HAADF bright field image and EDX X-ray maps of (b) Ni, (c) Ti and (d) Hf elements

The EDX X-ray maps obtained in Fig. 5.3 were also utilized to analyze the B2 matrix and H-phase precipitate composition as mentioned in Table. 1. For the HT600 sample, the Ni content of the H-phase precipitates is found to be 51.13 at.% whereas that for Hf is 27.16 at.%. On the

other hand, the Ni content of the H-phase precipitate composition for the HT650 sample is found to be 51.74 at.%, whereas the Hf content is around 30.79 at.%. It can be observed that, even when starting with the same alloy (nominal $Ni_{50.3}TiHf_{20}$, in our case), merely by varying the heat treatment temperature by 50˚C (i.e., from 600˚C for HT600 sample to 650˚C for HT650 sample in our case) the Ni and Hf content of the precipitate phase varies significantly. This is complete contrast as compared to the NiTi system as aging heat treatment would yield to form Ni_4Ti_3 intermetallic phases, as mentioned in section 1. Even if the heat treatment temperature is maintained constant and the initial starting alloy composition is changed, the resulting H-phase precipitates formed during the aging heat treatment varies in their composition as well, unlike in the case of NiTi system, in which despite of the initial starting composition the precipitates formed are intermetallic Ni_4Ti_3 phase [1, 14, 15]. Santamarta et al [67] conducted aging heat treatment on two different NiTiHf compositions at 600˚C for 10 hours and measured the composition of the matrix and the H-phase precipitates respectively as shown in Table 1. The authors reveal that, for $Ni_{50.3}TiHf_{15}$ alloy the measured composition for H-phase precipitates was Ni=52.5±0.8 at.%; Ti=21.2±0.8 at.% and Hf=26.3±0.8 at.%, whereas for Ni50.1TiHf25 alloy the H-phase measured composition was Ni=51.7±0.8 at.%; Ti=14.9±0.8 at.% and Hf=33.4±0.8 at.%. Similarly, Yang et al [68] also aged a Ni50.3TiHf20 alloy at 600˚C for 815 hours ad measured the H-phase composition to be Ni=53.62 at.%; Ti=20.03 at.% and Hf=26.35 at.%, as mentioned in Table 1. Also the corresponding measured matrix composition for all of the above are also notably different from each other as seen from Table. 1. By comparing all the above data (and of-course keeping in mind the error associated with EDX composition measurement) , it can be observed that as the Ni content of the initial alloy increases, the Ni content of the H-phase precipitate also increases. Similarly, with increase in Hf content of the initial alloy also tends to increase Hf content of the

H-phase precipitates. Hence, these observations tends to establish grounding proof to our hypothesis that the H-phase is not an intermetallic as suggested by Meng et al [54, 55] and Zarinejad et al [113] but occupies a region in the phase diagram.

5.3 Ni-Ti-Hf Diffusion Multiple

5.3.1 Diffusion Multiple at 600°C

5.3.1.1 Equilibrium Phase regions

The Ni-Ti-Hf tri-junction shown in Fig. 3.1 which had only pure metals after undergoing inter-diffusion at 600˚C for 5000 hours forms a series of inter-metallic and solid solution phases. Fig. 5.4a shows the Back Scatter Electron (BSE) image of the Ni-Ti-Hf tri-junction after inter-diffusion. Along with pure Ni, Ti, Hf, a series of phases are formed in-between them as seen by different contrast regions. Along with BSE, X-ray maps for the individual Ti, Ni and Hf elements were also obtained using EPMA as shown in Fig. 5.4 b, c and d respectively, in order to access their inter-diffusion patterns. Comparing all the three X-ray maps from Fig. 5.4 b,c and d, it is clearly evident that Ni diffuses the fastest and furthest as compared to Ti and Hf. The Ni diffuses more than 300 microns away from the pure Ni element and forms intermediate phases in between the pure Hf and Ti phases. Also from Fig. 5.4 d, it can be observed that Hf diffuses to a considerable extent in the Ni-Ti side, which reflects that Hf is going to have considerable solubility in all the individual phases that exist in the Ni-Ti equilibrium phase diagram. On the contrary, Ti does not diffuses on the Ni-Hf side as seen in Fig. 5.4c, which suggests that Ti is not going to have any significant solubility in the individual phases present in the Ni-Hf equilibrium phase diagram. Hence, in order to summarize the diffusion kinetics in the Ni-Ti-Hf system, it can be said that the Ni diffuses the fastest among all the three elements, followed by Hf and then Ti. These diffusion

results seems to be counter intuitive, as Hf is the bulkiest atom and hence should diffuse the slowest. Similar intuition based claims were also made in previous precipitation based studies of NiTiHf HTSMA system [54, 170] with the aging temperature considered in these studies was in between 400°C to 550°C. But based on diffusion multiple experiments from the present work and by Liu et al [116], Hf appears to dominate diffusion over Ti from a temperature range of 600°C and above.

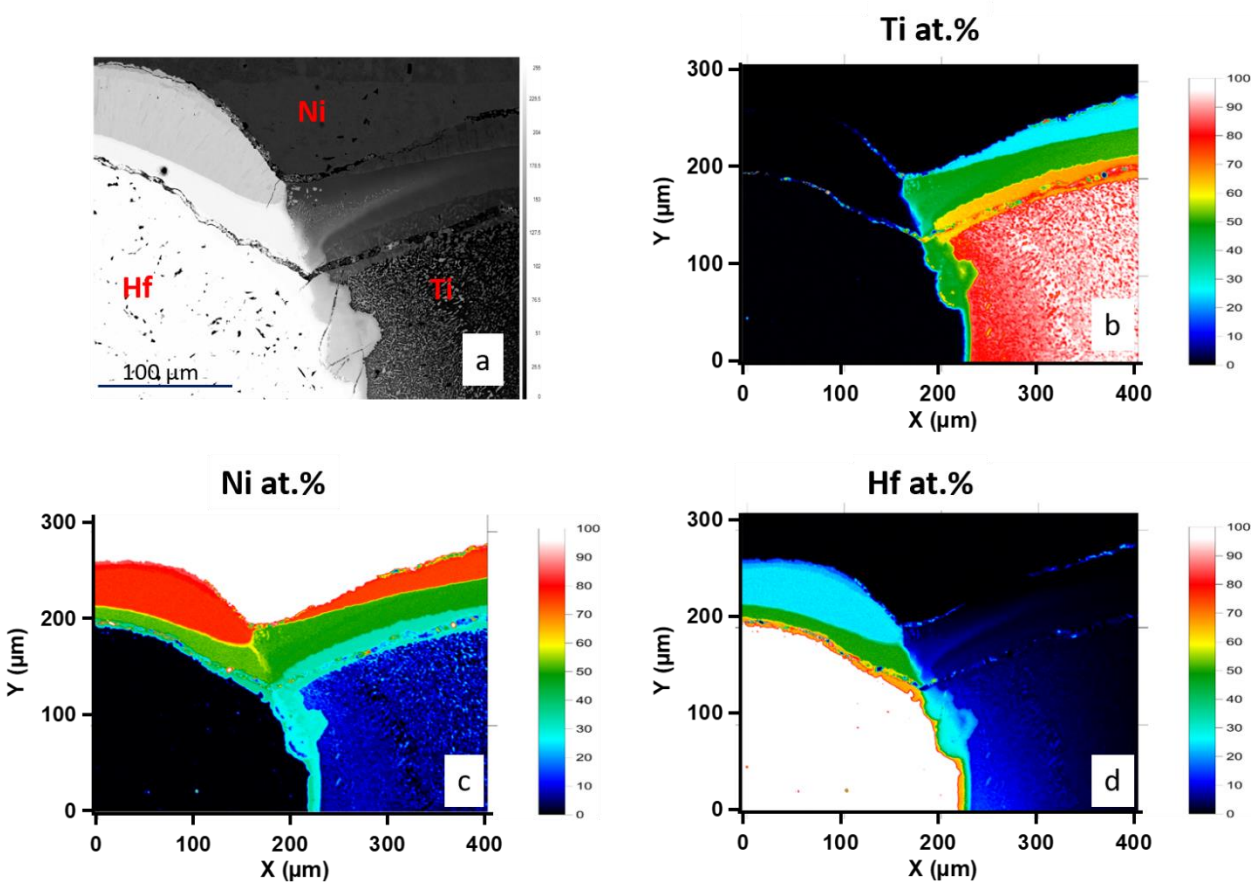

Figure 5.4 (a) Back Scatter Electron (BSE) image of the Ni-Ti-Hf tri-junctional diffusion multiple assembly after heat treatment at 600°C – 5000 hours, with individual elements at the terminal position and the equilibrium phases between them. Also shown is the X-ray maps of individual elements from the same diffusion multiple tri-junctional area shown in above. (b) shows the diffusion of Ti in the tri-junction diffusion zone. As seen Ti does not diffuse in the Ni-Hf side of the diffusion zone. (c) shows the diffusion of Ni in the diffusion zone. The Ni diffuses very fast and is present in huge amount (22 – 25 at.%) even 200 to 250 microns away from the pure Ni

region. (d) shows the diffusion of Hf across the diffusion multiple. The Hf diffuses on the Ni-Ti side and shows considerable solubility in all Ni-Ti binary phases.

Therefore, to identify all the phases, present in the Ni-Ti-Hf tri-junctional diffusion zone, EPMA was used to conduct compositional line-scans across all the phases and phase boundaries. An example of such a composition measurement line-scan is shown in Fig. 5.5a. The line 1 marked in Fig. 5.5a depicts the line-scan along which the composition was measured on the Ni-Ti side of the diffusion multiple far from the Ni-Ti-Hf tri-junction. Fig. 5.5b shows the measured Ni, Ti and Hf composition along the line-scan 1 on the Y-axis number for corresponding point on the X-axis. Plotting the measured compositions as shown in Fig. 5.5b gives a very clear picture about the phases present, the compositional span of the phase and the transition compositions from one phase to another. By comparing the measured compositions for individual elements from Fig. 5.5b to the binary Ni-Ti phase diagram, we can identify the phases as viz, Ni, Ni_3Ti, NiTi, $NiTi_2$, Ti [1]. It is also observed that all the phases that are present in the binary Ni-Ti phase diagram are present in the diffusion multiple along with some solubility of Hf in it. Hence, by analyzing individual line-scans and comparing them with the respective binaries [171, 172], the phases present in the diffusion multiple zone can be distinguished. Fig. 5.6 shows the tri-junction diffusion zone with all the phases labelled as observed by analyzing the compositional line-scans. The phase boundaries in Fig. 5.6 are drawn based on EPMA line-scan data, X-ray maps and phase contrast present between them and hence the phase boundary carved are accurate within a few microns distance. Also, there exist a diffusion zone in between phases (especially solid solution phases) as shown by data point # 41 and 42 in Fig. 5.5b, which is a transient diffusion layer between the two phases and hence can also contribute to the slight error in placement of the phase boundaries. As mentioned before all the phases present in the Ni-Ti binary phase diagrams were observed on the

Ni-Ti side of the tri-junction. Similarly all the phases present in the Ni-Hf binary phase diagram viz, Ni, Ni_5Hf, Ni_7Hf_2, Ni_3Hf, $Ni_{10}Hf_7$, NiHf, $NiHf_2$, Hf [171] were also observed on the Ni-Hf side of the tri-junction,

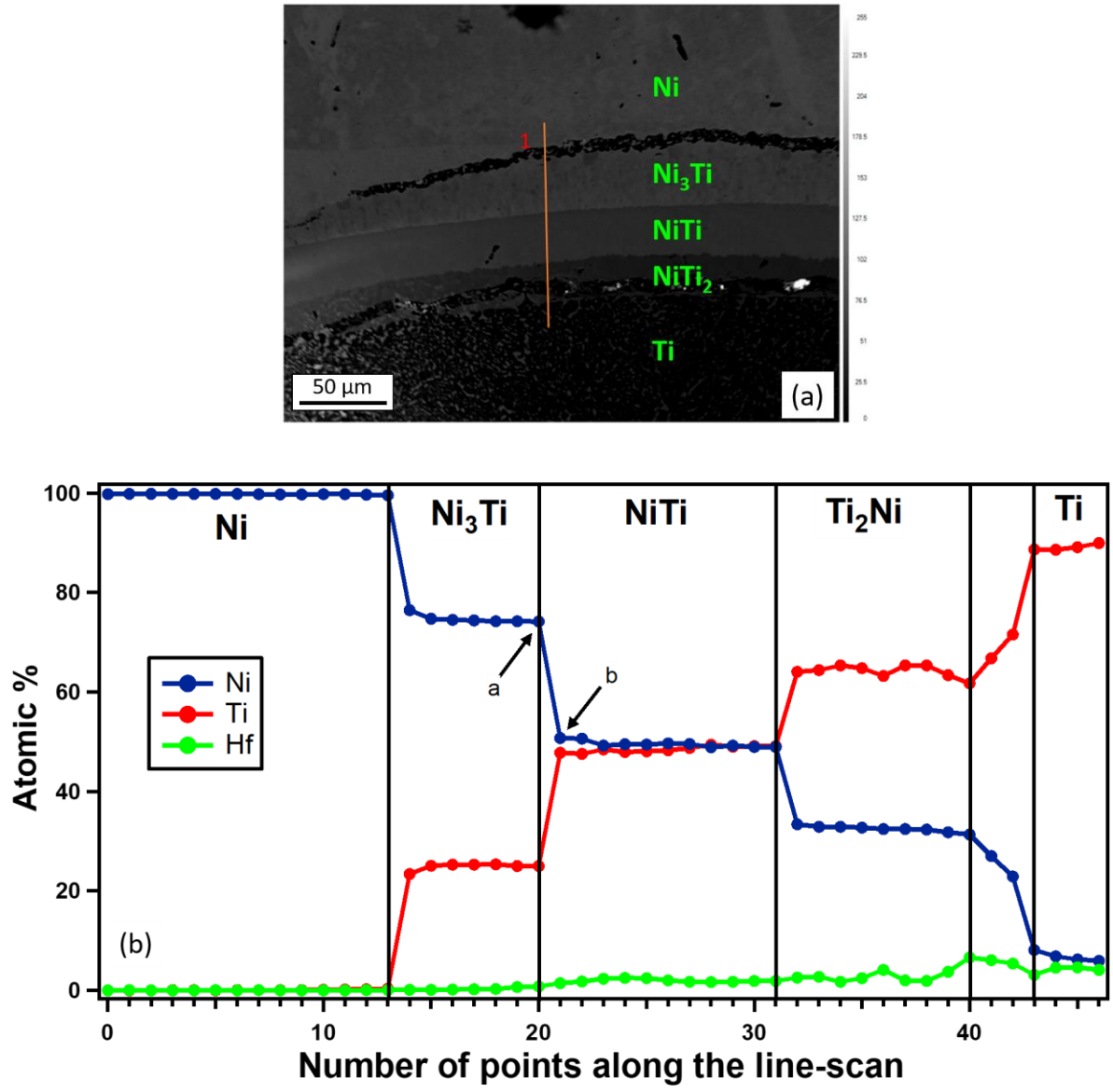

Figure 5.5 Shows (a) Line 1 depicts the line-scan along which composition was measured over the phases present in between Ni and Ti phases on the Ni-Ti side far from the Ni-Ti-Hf tri-junction. (b) the corresponding measured composition of the individual elements along the line-scan, which clearly shows the compositional span of each phase and helps to identify the boundary compositions. Identification of such boundary compositions help in identifying tie lines and generate ternary isotherms.

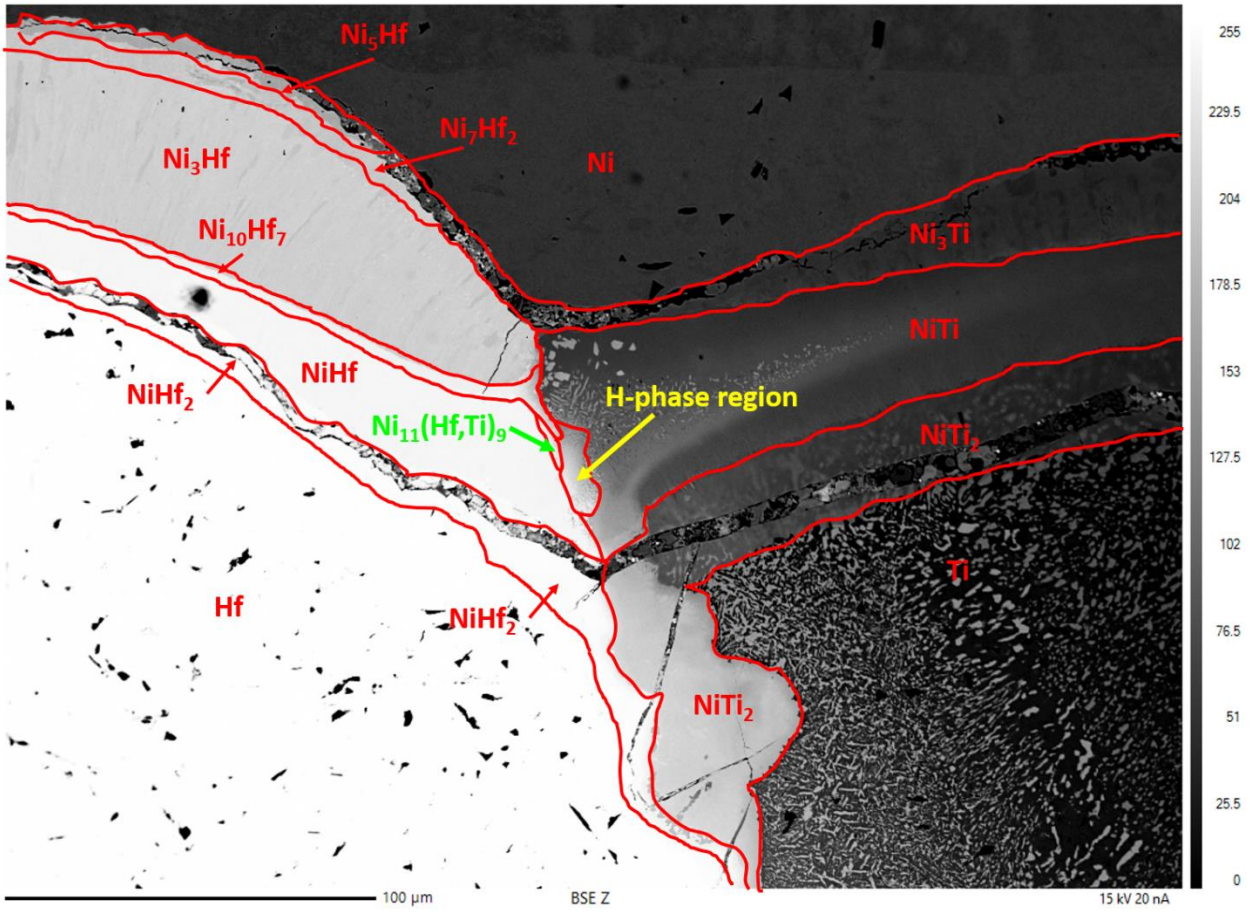

Figure 5.6 Back scatter image of the Ni-Ti-Hf triple junction after heat treating the diffusion multiple assembly at 600°C for 5000 hours followed by water quenching, with individual phases labelled within their respective phases boundaries. Along with the binary phases present in the respective binaries, a new phase which is not present in the binary phase diagram is found which is labelled as the H-phase. The H-phase is a very pre-dominant phase found during precipitation in Ni-rich NiTiHf alloys.

except the $Ni_{11}Hf_9$ intermetallic phase. One reason for the absence of $Ni_{11}Hf_9$ phase can possibly be that the phase is formed, but it is too small to be observed using the EPMA compositional analysis. The $Ni_{11}Hf_9$ phase on the Ni-Hf side of the tri-junction diffusion zone can also happen to exist over a very narrow range of composition and is sandwiched between NiHf and $Ni_{10}Hf_7$ and hence not detectable by EPMA. Another reason for absence of $Ni_{11}Hf_9$ phase, can also be that as the heat treatment temperature is lower than half of the homologous melting temperature of the

compound and thus the system might not have enough driving force to form it [121]. Similar behavior was also observed in Ti-Al system, where when a diffusion couple was formed between pure Ti and Al blocks, only $TiAl_3$ phase is formed. But when the diffusion couple is created in between pure Ti and $TiAl_3$ phase, then after heat treatment all the other phases are visible [173, 174]. However, the exact reason for absence one of the phases in the equilibrium phase diagram is not known. Later, it will be shown that the $Ni_{11}H_9$ is observed at the intersection of the tri-junctional diffusion zone with a certain solubility of Ti, thus making it $Ni_{11}(Hf,Ti)_9$. On the Ti-Hf side of the of the tri-junctional diffusion zone interestingly Ni diffuses much faster and forms the Ti_2Ni with certain solubility of Hf and also forms Hf_2Ni along with certain solubility of Ti. Several microns away from both the Ni-Ti-Hf tri-junction, at the geometrical center of the entire diffusion multiple assembly, which happens to be an interface between Ti and Hf only, no Ni was present. As known from the Ti-Hf binary phase diagram, both the elements tend to form a solid solution over the entire range of composition [172]. At the geometric of the diffusion multiple sample, similar phase organization was observed. The pure Ti phase was followed by a diffusion layer with a constant gradient of Hf and finally reaching to the highly pure Hf phase. No traces of Ni were observed at such a far distance from the tri-junctional diffusion zone. Among the measured data, the terminal compositions of each phase are of high interest, i.e., the last measured composition in previous phase and the first measured composition in the consecutive following phase, right across the phase boundary. The link between these two terminal compositions of the two phases across the phase boundary serves as the 'tie lines' between the two equilibrium phases and plotting these tie-lines on a ternary isotherm will help us to construct the equilibrium phase diagram. For example, as shown in Fig. 5.5b, point #20 which is marked as point 'a' using an arrow on the blue line (i.e., measured Ni data) marks the last terminal position or the last measured point in Ni_3Ti

region, whereas point #21, which is marked as point ‘b’ on the blue line indicates the first terminal measured composition in NiTi phase. In the remainder to of the manuscript, this is the definition for terminal compositions used to explain different aspects regarding construction of phase diagram. Using the aforementioned method, all the compositional line-scans acquired from the diffusion multiple was analyzed and used to obtain tie lines. More details regarding the use of combinatorial approach to map the phase diagrams for ternary and quaternary systems is provided by Zhao et al [119-121, 175]. Hence along with identification of individual phases present, the data presented in Fig. 5.5b can also be utilized to construct the ternary Ni-Ti-Hf phase diagram isotherm at 600˚C. All the phases labelled in Fig. 5.6 are marked by comparing their compositions with binary phases present in respective binary phase diagrams, but there are certain phases which tend to extend in the ternary phase diagram from their binary roots and some new phases are also formed which do not exist in any of the binary phase diagrams.

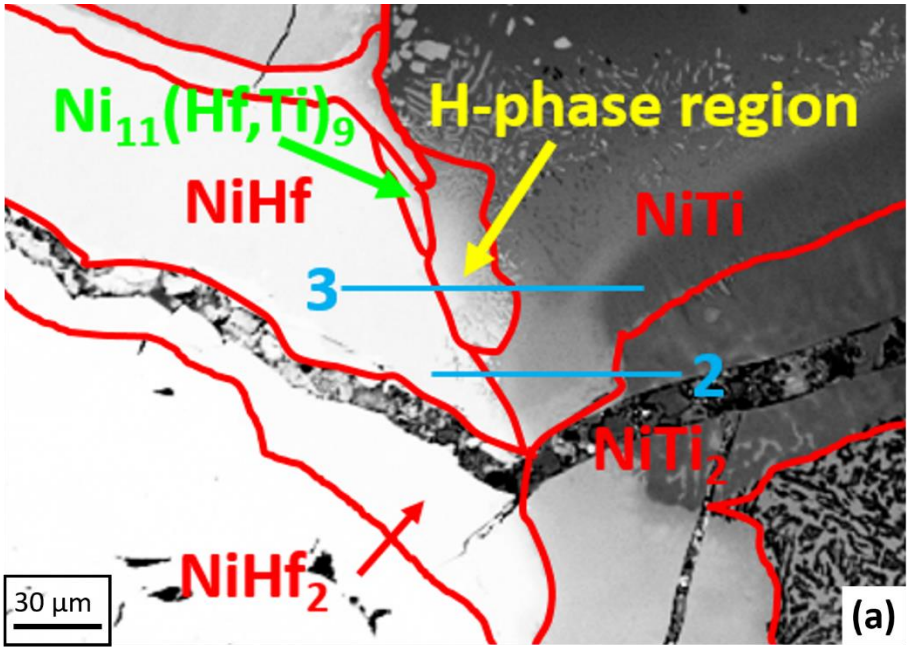

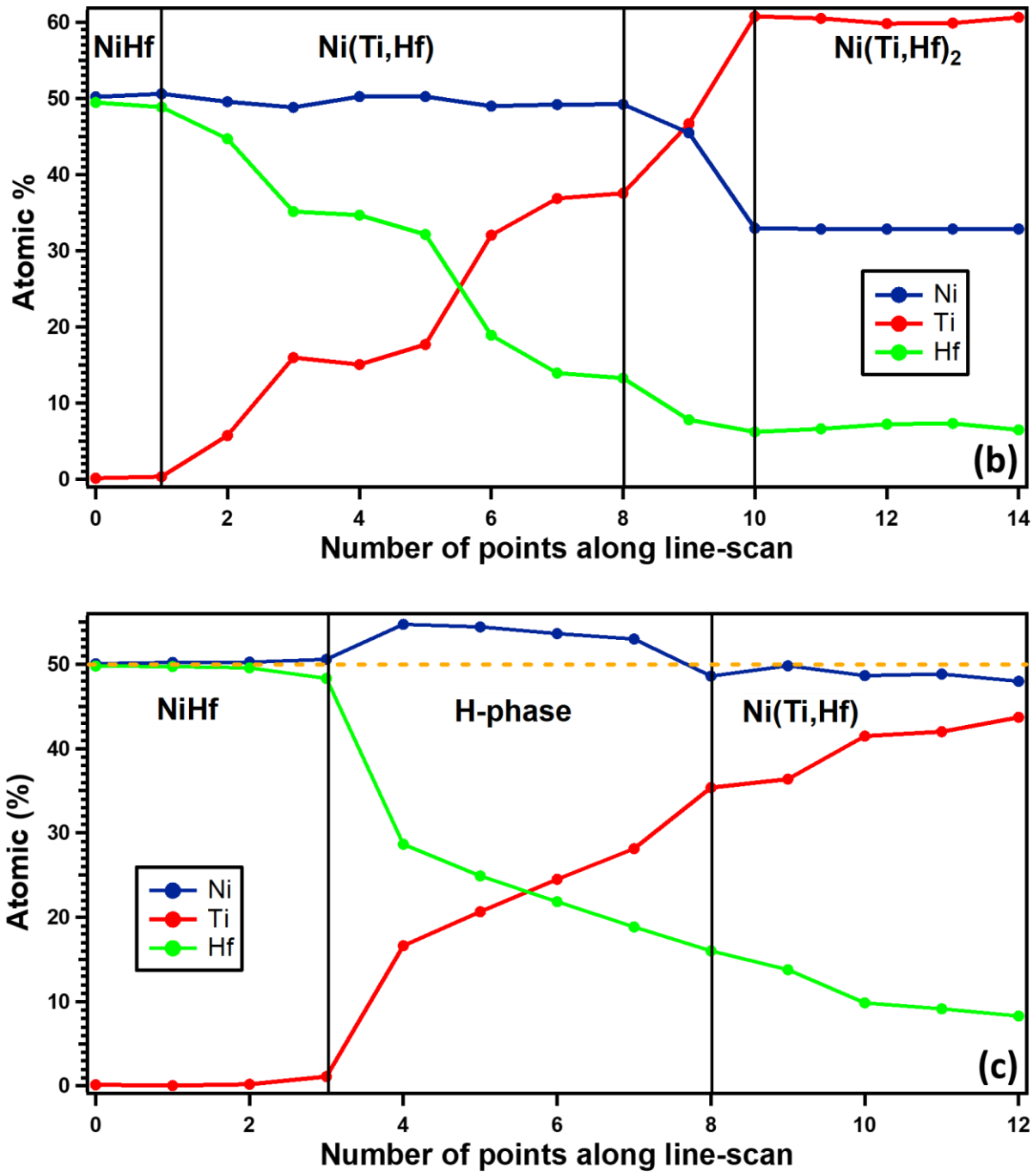

Figure 5.7 (a) Shows a close-up section of the tri-junction diffusion zone shown in Fig. 5.6 centered around the H-phase region with all the phases marked. Also two line-scans are acquired passing through different phases which are labelled as '2' and '3' respectively. The measured composition of individual elements from the line-scans acquired in the (a) are plotted in (b) for line-scan '2' and in (c) for line-scan '3'.

Such an example is shown in Fig. 5.7, where Fig. 5.7a shows the BSE image of a zoom in section of the tri-junction diffusion zone with two compositional line-scans shown by solid blue lines and labelled as '2' and '3' respectively. The composition measurement from line-scan 2 is shown in Fig. 5.7b in order to demonstrate how the phases that exist in the binary phase diagrams (e.g., Ni-Ti binary phase diagram) tends to extend inside the ternary phase diagram by exhibiting solid solubility with respect to the third element (e.g., Hf). Fig. 5.7b shows the composition measurement of respective elements obtained from the line-scan 2. It can be noted that the line-scan originates in the NiHf phases, as the composition of the first 2 data points measure Ni and Hf approximately around 50 at.% and the concentration of Ti is still around 0 at.%. Now as the line-scan 2 transitions from the NiHf phase to the NiTi phase, it can be seen that the Ni concentration does not change much (varies in a range of 50 ± 1.2 at.%), but the concentration of Hf starts to decrease rapidly and conversely the concentration of Ti increases rapidly. This shows that the Ti doesn't not show any appreciable solubility in the NiHf phase, but Hf shows a very high solid solubility in the NiTi phase and hence diffuses to a much larger distance inside the NiTi phase, from the binary phase diagram. Such contrasting solubility's of Ti and Hf into respective NiHf and NiTi phases suggests that the NiHf phase will not extend much inside the ternary Ni-Ti-Hf phase diagram, but the NiTi phase will extend inside the ternary phase diagram to a greater extend and will occupy a relatively larger phase region as compared to NiHf phase. As the line-scan 2 progresses more into the NiTi phase, the Ti concentration keeps increasing and Hf concentration keeps decreasing until it enters into the adjacent $(Ti,Hf)_2Ni$ phase. Upon entering the $(Ti,Hf)_2Ni$ phase, the concentration of all the three elements doesn't change much increase with acquisition of data-points. For the $(Ti,Hf)_2Ni$ phase, the Ni content is approximately around 33 at.% (varies in a range of 33 ± 0.2 at.%) , whereas the composition of Ti and Hf add up to approximately 67

at.%. In Fig. 5.7b, data-point # 8 was the last data-point acquired in the NiTi phase, point #9 was acquired at the phase boundary and hence shows the transitioning composition between the two phases and point #10 is the first data-point acquired in the $(Ti,Hf)_2Ni$ phase. Hence, upon plotting the composition data from point#8 and point#10 of Fig. 5.7b on a ternary isotherm, will indicate one of the equilibrium tie-lines between the NiTi and Ti_2Ni phase. Hence, all the individual line-scans obtained across various phases and phase boundaries can be plotted as shown in Fig. 5.7b and can be interpreted as mentioned above and thus the solubility of the elements in their corresponding binary phases can be obtained.

Conversely, the line-scan marked as '3' in Fig. 5.7a passes through a new phase which is not found initially in any of the binary phase diagrams. The measured compositions from various phases corresponding to line-scan 3 is shown in Fig. 5.7c. From Fig. 5.7c, it can be seen that it originates in the NiHf region, where the composition of Ni and Hf are approximately around 50 at.% and that of Ti is around 0 at.%. Point #3 in Fig. 5.7c is the last point in the NiHf phase, whereas measured data from point #4 to point #7 indicates presence of a new phase which is Ni-rich as compared to NiHf phase. Also, the Ti content increases and the Hf content decreases as the line-scan progresses from point #4 to point #7. From the knowledge of the Ni-Ti and Ni-Hf system, no intermetallic phase has composition in the aforementioned range of Ni content. At point #8, the Ni content drops drastically below 50 at.% and remains more or less the for the remaining the same, whereas the Ti content keeps increasing and the Hf content keeps decreasing. From Fig. 5.7a the phase beyond point #8 is the NiTi or can be called as Ni(Ti,Hf) phase, as it exhibits high Hf solubility. Hence the new phase observed here, is Ni-rich, Hf-rich and Ti-lean compared to the adjacent NiTi phase. This new phase resembles to the H-phase precipitates as observed in Fig. 5.3, where the H-phase precipitate is Ni-rich, Hf-rich and Ti-lean as compared to the B2 matrix which

is the Ni(Ti,Hf) phase. Also, by comparing the EDX data from Table. 1 and available studies concerning the precipitation studies in NiTiHf system [42, 59, 67, 68], the composition of H-phase precipitates lies in the range of 51.13 at.% to 54 at.%, whereas the Hf content lies approximately in the range of 21 at.% to 34 at.%. The measured Ni and Hf composition shown in line-scan 3 also lies in the aforementioned range of composition of H-phase precipitates. Such multiple line-scans across the newly founded phases yielded similar compositional relationship with neighboring phases. Hence, based on qualitative and quantitative compositional measurements, we can conclude that the new phase observed is the novel H-phase, which precipitates out during aging heat treatment in the NiTiHf systems. So for all the compositional line-scans performed from the NiHf to the NiTi region, which showed the presence of a Ni-rich phase (as demarcated by the orange dashed line in Fig. 5.7c) in between them was considered to be the H-phase and the span of the H-phase in the tri-junctional diffusion zone has been shown accordingly by the solid yellow arrow as shown in Fig. 5.6 and Fig. 5.7a.

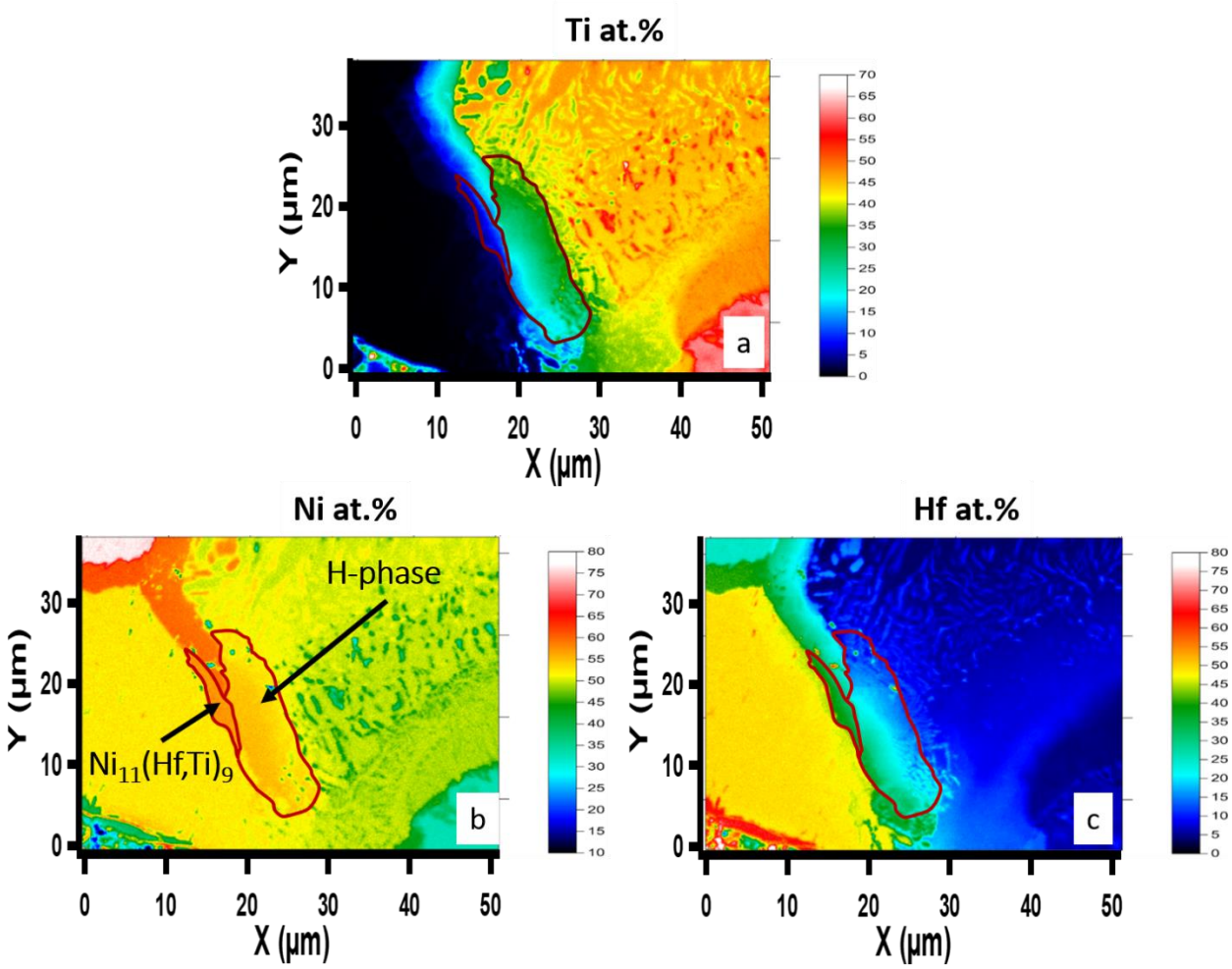

Figure 5.8 Shows the X-ray map acquired from the H-phase region of the diffusion multiple with respect to the individual elements (a) Ti, (b) Ni and (c) Hf. From the acquired X-ray maps it can be seen that the H-phase precipitates span approximately from 51 to 55 at.% Ni, 15 to 35 at.% Ti and 17at.% to 40 at.%. Hf.

In order to understand the spread and compositional boundaries of the H-phase in the NiTiHf equilibrium phase diagram, an EDS-X-ray map was acquired from the H-phase and other neighboring phases as shown in Fig. 5.8. As the X-ray map in Fig. 5.8 was acquired from a very small area (51µm*38µm) as compared to the one acquired in Fig. 5.6 (300µm*400µm), the compositional contrast is much higher and hence phases with a very small composition difference (≤ 1 or 2 at.%) can be differentiated fairly easily. Fig. 5.8a shows the BSE image of the area from

where the X-ray map was acquired, whereas Fig. 5.8b, c and d shows the corresponding EDS X-ray maps from the same region. As we intent to analyze the H-phase, the area selected for analyses was the diffusion phases formed between the NiTi and NiHf phase. At the tri-junctional diffusion zone, as there is a heavy inter-diffusion of Hf to the Ni-Ti phase, there exist a very steady gradient of Hf as we move from NiHf to NiTi phase. Conversely, there is also a steady flux of Ti as we move from the NiTi region to the diffusion phases formed. Hence, the only element that can be used to discern the different phases at the tri-junction, especially the H-phase is Ni. Also, as the H-phase region is Ni-rich as compared to the NiTi and NiHf phases, it is much wiser and accurate to distinguish phases based on Ni content. Hence, based on Ni-richness criteria, the H-phase is distinguished and marked in Fig. 5.8c. By referring to Fig 10c, the exact same area marked as H-phase was used to mark the H-phase region in Fig. 5.8b and d. Based on the EDS X-ray map analysis and by comparing the region's color contrast with the respective compositional scale bar (which is in at.%), it can be seen that the Ni content for the H-phase lies in between 51 at.% to 55 at.%, whereas Ti lies approximately in between 15 to 35 at.% and Hf lies approximately in between 17at.% to 40 at.%. The estimated compositional range for the H-phase by EDS mapping is fairly close to that measured by the WDS technique within an understandable amount of error (±2at.%) associated with EDS measurements. The aforementioned range of individual elements, is again a very fair range of compositions in which single phase H-phase exist at 600°C.

Once all the compositional line-scan data was plotted as shown in Fig. 5.5b, Fig. 5.7b and Fig. 5.7c, the terminal compositions across the phase boundaries are extracted. As mentioned before, when these terminal composition pairs are plotted on a ternary isotherm and connected using a line, such a line is called as a 'tie-line'. Hence by plotting all such tie-lines observed across phase boundaries, helps to generate the ternary isotherm or the phase diagram at a particular

temperature. Therefore, by plotting all the tie-lines extracted from line-scans across various phase shown in Fig. 5.6, a ternary isotherm or the ternary phase diagram of Ni-Ti-Hf system was generated at 600˚C as shown in Fig. 5.9. As it can be clearly observed that all the phases present in the individual binary phase diagrams exist in the ternary phase diagram. Also, most of the binary phases also exhibit solubility and extend inside the ternary phase diagrams, except for Ni_5Hf and Ni_7Hf_2 where appreciable solubility of Ti was not observed. Also, the $Ni_{11}Hf_9$ phase was not observed on the Ni-Hf side of the diffusion multiple sample but is present in the ternary diffusion region (as marked by green arrow in Fig. 5.6) with a maximum solubility of 11.15 at.% Ti as shown in Fig. 5.9. There are certain phases such as Ni_3Ti, Ni_3Hf, NiHf and $NiHf_2$ which extends inside the ternary phase diagram but shows a limited solubility of 10 at.% with respect to the corresponding ternary element and hence occupies relatively smaller area. On the other hand, phases like $Ni_{10}Hf_7$, NiTi and $NiTi_2$ exhibits a large solubility with respect to the corresponding ternary element and hence claim a relatively larger area in the phase diagram. Also, along with all the respective binary phases extending into the ternary, the H-phase was also successfully mapped in the phase diagram as shown in Fig. 5.9. It is clearly evident that the H-phase occupies a region in the phase diagram and spans from a minimum of Hf=7.11 at.% to a maximum of Hf=33.28 at.% in terms of Hf content, with Ni spanning from a minimum of Ni=51 at.% to a maximum of Ni=53.8 at.%. Finding this region in the phase diagram, confirms the hypothesis of the manuscript, that the H-phase precipitate is not a line compound of inter-metallic like phase, but is a solid solution phase and occupies a region in the aforementioned composition ranges, in the Ni-Ti-Hf phase diagram. From the observed tie-lines it can also be concluded that, the composition of H-phase is dependent on the initial starting compositions of the alloy. Knowledge of such equilibrium relations between the H-phase and the martensitically transforming Ni(Ti,Hf) phase, can be efficiently utilized to

design alloys with required transformation characteristics. The designing of alloys using the ternary phase diagrams will be discussed at length in section 4.

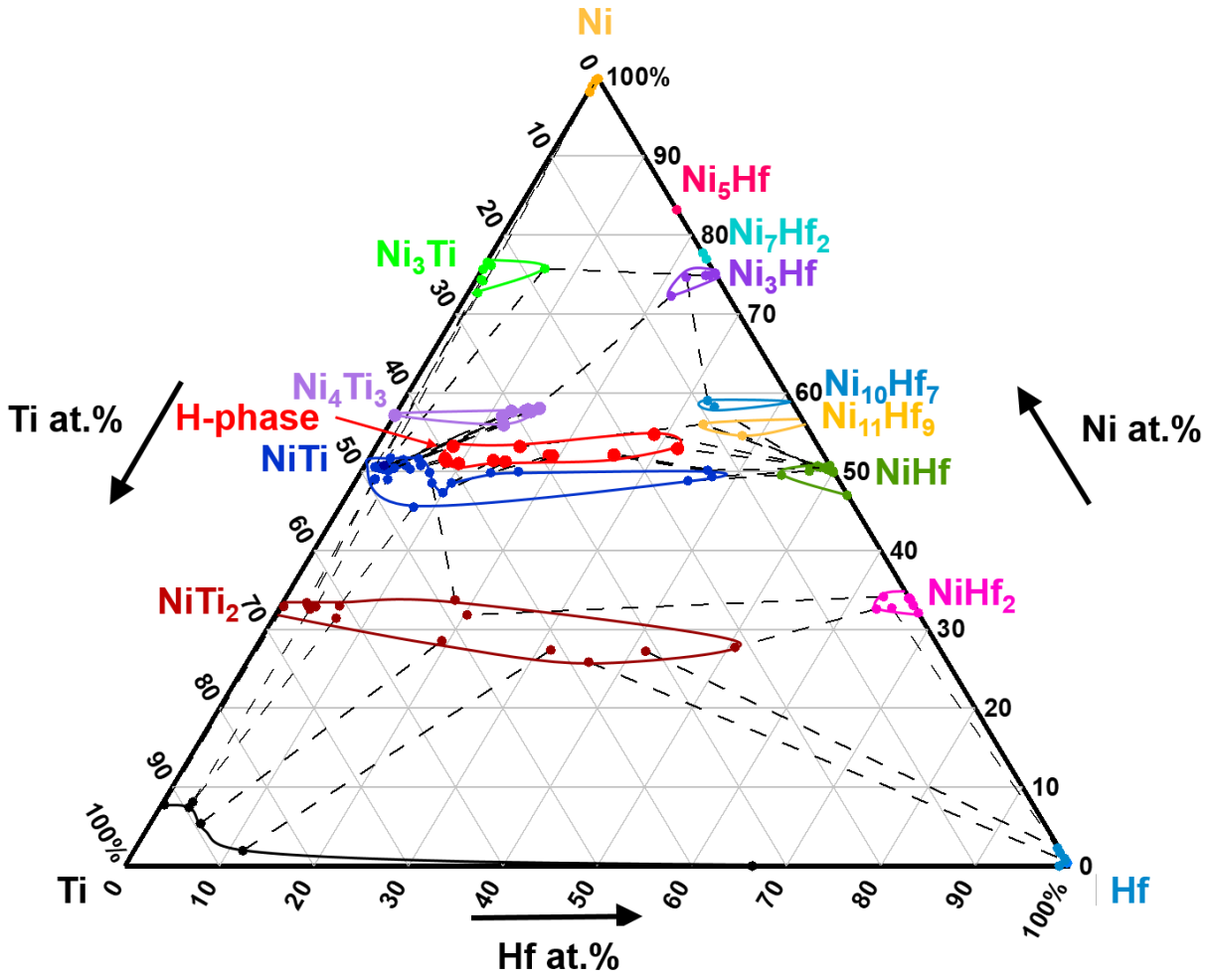

Figure 5.9 The ternary Ni-Ti-Hf phase isotherm at 600°C with all the phases and tie-lines marked accordingly. Along with the respective binary phases extending into the ternary phase diagram, the precipitate phases, i.e., Ni_4Ti_3 and the H-phase precipitates are also marked inside the ternary isotherm.

5.3.1.2 Second Phase Particles Inside Equilibrium Phase Regions

Due to prolonged heat treatment of the diffusion multiple assembly at 600˚C, along with single phase regions, a few two phase regions are also observed, where particles of second phase was found to be embedded in the primary phase. This is very similar to as a two phase micro-structure with the matrix as primary phase and a second phase present in the forms of particles. Such an example is shown in Fig. 5.10, where the BSE image shows the region in the NiTi phase of the diffusion multiple, where numerous second phase particles are embedded into it. In order to analyze these second phases an X-ray map was acquired from that region and diffusion profile for each individual element was revealed as shown in Fig. 5.10. The difference in compositional contrast based on Ti-content from Fig. 5.10a clearly differentiates the between the particle phase that is encapsulated in the NiTi phase. Upon performing compositional line-scan analysis with a small beam size and small step size, it was revealed that the particles inside the NiTi phase region have a Ni composition in the range of 56 to 58 at.%, whereas Ti and Hf was in the range of 27 to 31.5 and 11.5 to 16.8 at.% respectively from Fig. 5.10 b and c. Comparing with the Ni content, on possibility can be that the particles are very similar to $Ni_{10}Hf_7$ (i.e., Ni=58.8 at.%) like, with a very high solubility of Ti of 31.5 at.% being the highest, i.e., namely $Ni_{10}(Ti,Hf)_7$. Another possibility of such embedded particles can be the Ni_4Ti_3 like (i.e., Ni=57.14 at.%). Based on the measured composition, the embedded particles appear to be Ni_4Ti_3 like, but the solubility of Hf and Ti can alter the Ni content far from its respective binary phase composition. Therefore, it cannot be denied initially that it is equally possible that the particles embedded inside the NiTi phase can be either one of the two options mentioned above. Conducting a diffraction study on the embedded particles is very difficult as they are a few micron size and upon focusing the X-ray Diffraction

beam on this area will yield a very complex data, as the beam will encompass several neighboring phases and the diffraction pattern obtained will be highly complicated at analyze.

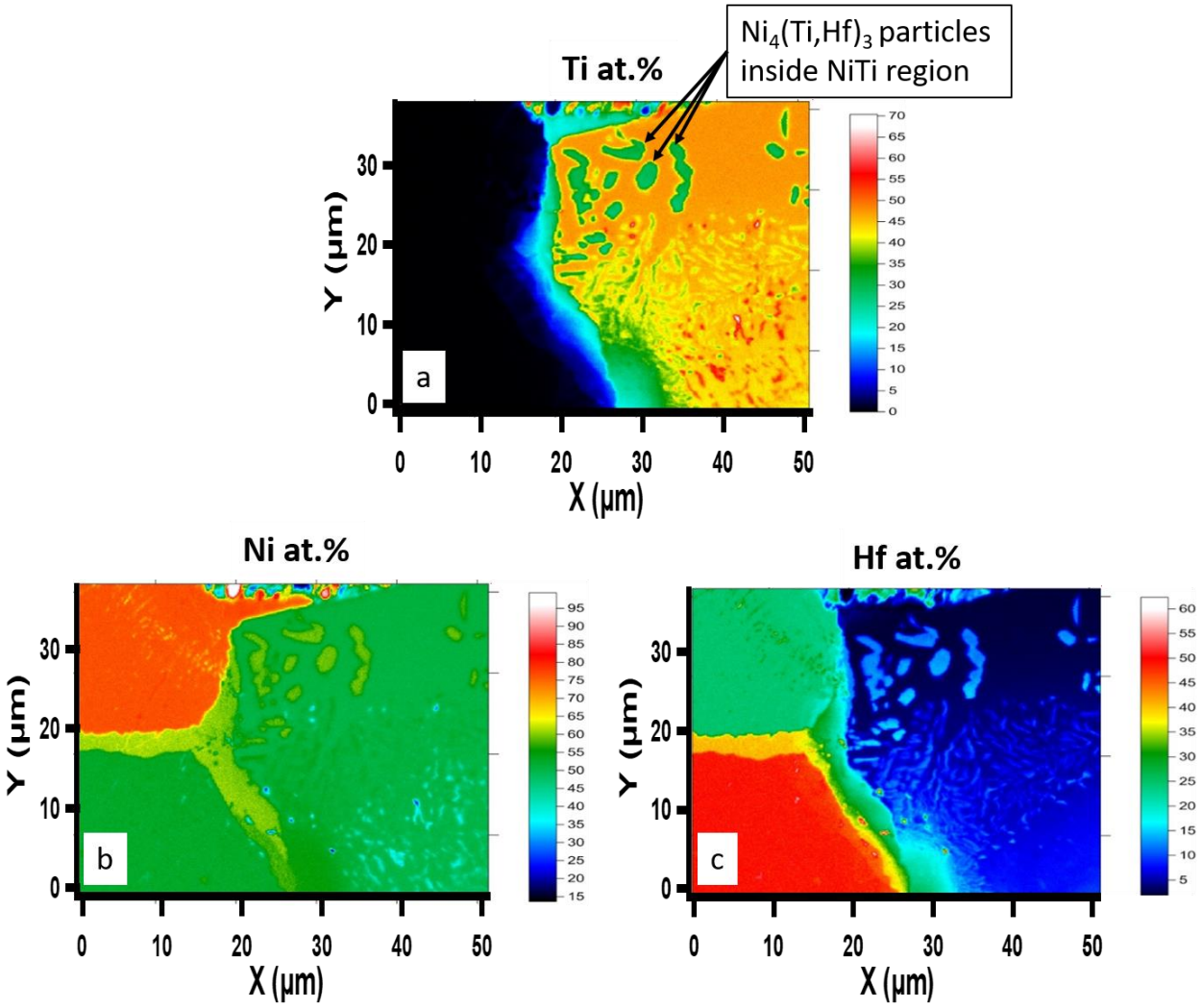

Figure 5.10 The X-ray maps of second phase particles found embedded inside the NiTi layer of the diffusion multiple zone. Upon performing line-scan and point composition analysis of the second phase, it was revealed that it was the Ni_4Ti_3 phase precipitates with certain Hf solubility.

Based on the literature knowledge, it is known that the Ni_4Ti_3 precipitates nucleate inside the super-saturated solid solution of NiTi phase [15, 16]. Also a study by Hornbuckle et al, showed that upon aging the $Ni_{54}Ti_{45}Hf_1$ and $Ni_{56}Ti_{40}Hf_4$ alloy at a temperature of 400°C for 24 hours and 300 hours respectively, yields a three phase micro-structure with Ni_4Ti_3 and H-phase precipitates

inside a B2 austenitic matrix [170]. Authors didn't perform any compositional analysis on the two precipitated phase, in order to determine if there is any Hf solubility in the Ni_4Ti_3 phase, but assured the presence of three phase region for Ni-rich and dilute Hf additions to binary NiTi. From various literature sources it is confirmed that the Ni_4Ti_3 and the H-phase precipitates are well stable in the range of 300°C to 650°C and therefore the precipitation stability at 600°C should be similar to that at 400°C, but of-course with enhanced thermal kinetics [19, 41, 42]. Therefore, extending the knowledge of presence of three phase regions (viz., B2 austenite, Ni_4Ti_3 and H-phase precipitates) at 400°C from Hornbuckle et al, can be extended to the presence of these three phases at 600°C as well, based on respective precipitate phases stability ranges. On the other hand, upon aging the much Hf-rich NiTiHf compositions (Hf > 15 at.%, Ni-lean or Ni-rich both) at 600°C, authors find only two major phases present, i.e., the H-phase precipitates inside a B2 austenite or B19' martensite matrix depending on the TTs [34, 52, 57, 67]. Therefore, from the above discussion, it can be said that there is a threshold Hf content required to suppress the Ni_4Ti_3 precipitation in NiTiHf system. In other words, below a critical value of Hf content, Ni_4Ti_3 phase is present along with H-phase and B2 austenite, whereas above this critical value only H-phase and B2 austenite phases are present. This critical value of Hf content may vary with varying heat treatment temperature as well as Ni content of the alloy.

Recent diffusion multiple studies by Liu et al on the Ni-Ti-Hf system has shown that at 800°C, the $Ni_{10}Hf_7$ phase has a maximum Ti solubility of approximately 26 at.% [116]. There upon decrease in temperature of heat treatment below 800°C, the solubility of Ti should decrease below 26 at.%. From the basic knowledge of thermodynamics of phase diagrams, it is known that the length of tie-line between the two phases increases as the solubility of the respective phases at a lower temperature tends to decrease. Therefore, from the above analogy, the maximum Ti

solubility of the $Ni_{10}Hf_7$ phase at 600°C will be less than its maximum solubility at 800°C, i.e., 26 at.%. The measured Ti content of the embedded particles are in the range of 27 to 31.5 at.% as mentioned before and hence these particles are not the $Ni_{10}Hf_7$ like. Also as the particles are formed inside the NiTi parent phase, with Ti being the second majority element in it. With fair amount of proof presented above it can be hypothesized that the particles embedded inside the NiTi phase region are of $Ni_4(Ti,Hf)_3$ like. Apart from larger particles, very fine needle shaped precipitate particles also appear to be formed in the NiTi region. As the needle shaped precipitates are super fine in size, EPMA analysis cannot be conducted on them because of lack of beam resolution required for quantitative analysis. These needle like precipitates also seem to be extending out of the neighboring H-phase region. Therefore, based on visual perception, the needle shaped precipitates can be H-phase precipitates, but as no compositional analysis can be performed on them in EPMA, it is just a speculation.

5.3.2 Diffusion Multiple at 800°C

As mentioned in Table 3.1, long term annealing of Ni-Ti-Hf diffusion multiple assembly was also carried out at 800°C for 1000 hours followed by water quenching. Upon dissecting the DM assembly at 800°C, a range of phases were found in the BSE image as shown in Fig. 5.11. Similar EPMA line-scan analysis was performed across various phase boundaries and phase inter-sections in order to determine tie-lines to construct the phase diagram. Based on the obtained line-scan analysis data, different phases were marked in the BSE image. Almost all the phases that appear in the individual binaries are also reflected here in the ternary phase equilibrium with respective solubility towards third element.

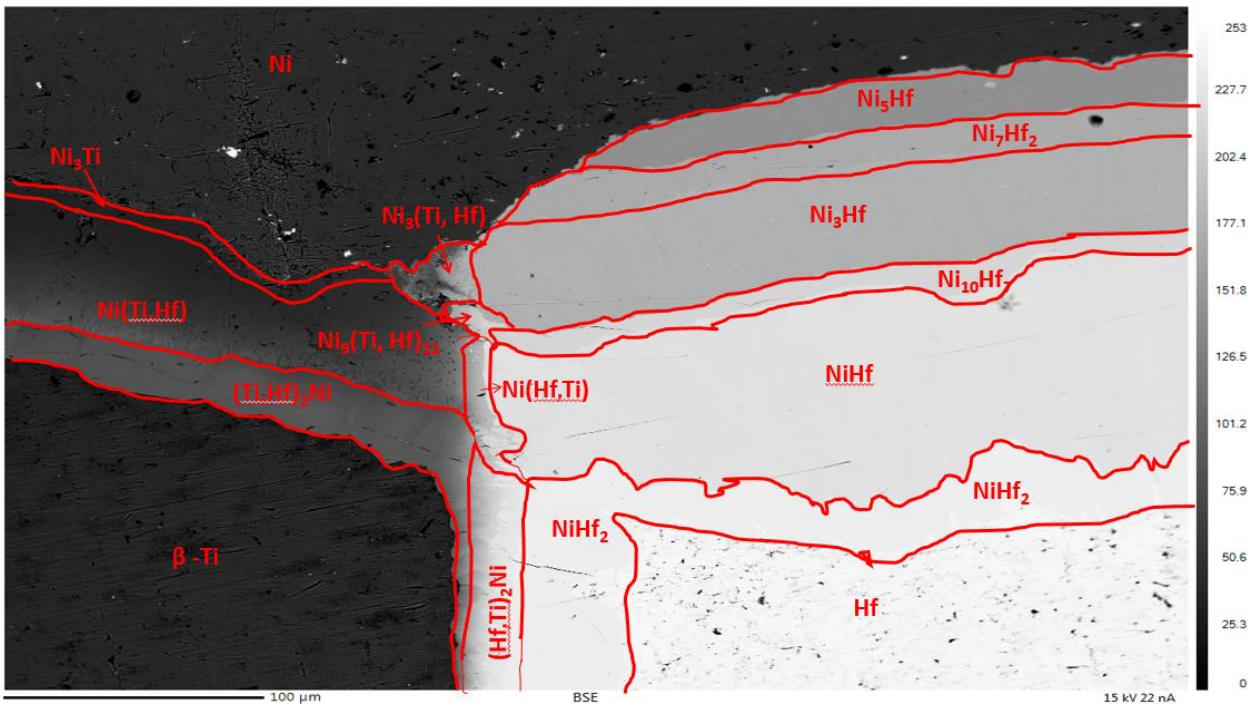

Figure 5.11 BSE image of the DM after heat treating at 800°C for 1000 hours followed by water quenching.

Though the starting material was pure elements with more than 99.9 at.% purity, it was interesting to observe that after heat treating at 800°C for 1000 hours, the highly pure Ti phase is replaced by β-Ti phase which has solubility of Ni and Hf upto 7-9 at.% in total with rest of Ti. On comparing Fig. 5.11 to Fig. 5.6, it can be seen that the H-phase region that was present at 600°C, is not present at 800°C. This is also in accordance with literature data, which suggests that H-phase Precipitates are not present when the material is heat treated at 650°C or above [41]. The X-ray maps from the BSE image in Fig. 5.11 was obtained in order to understand the diffusion profile of individual elements as shown in Fig. 5.12. From Fig. 5.12 it can be seen that the Ni diffuses that fastest among the three elements, as we can see considerable Ni present at the bottom of the DM assembly in between the pure Hf and Ti regions. Also Hf diffuses in a considerable amount in the

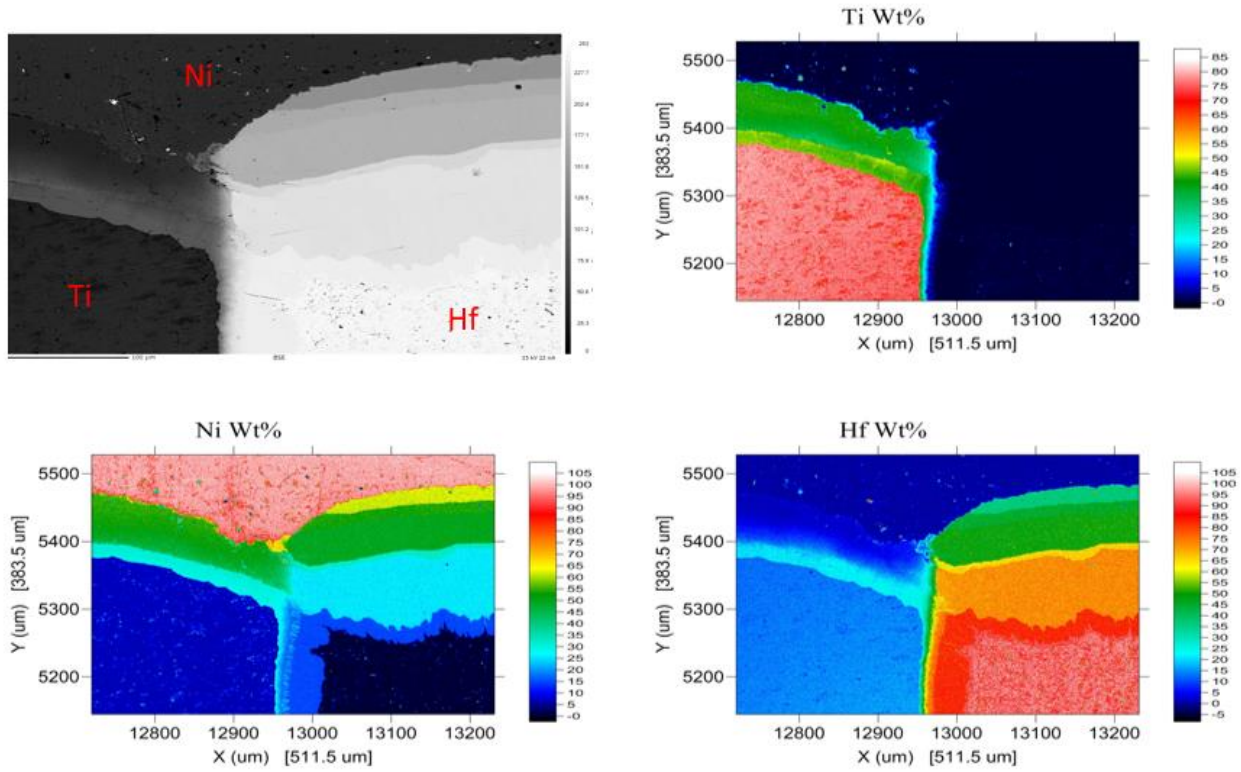

Figure 5.12 X-ray maps of individual elements obtained from the EPMA equipment in order to access the diffusion profile of individual elements.

Ni-Ti side of the DM, and exhibits higher solubility in the respective binary NiTi phases. On the other hand, Ti does not diffuse in the Ni-Hf side of the binary phase diagram and hence Ti shows very less solubility in the respective Ni-Hf binary phases. This indicates that the Ni-Ti binary phases will extend to a larger extend in the ternary phase diagram, because of the higher Hf solubility in them, whereas the Ni-Hf binary phases will extend to a lesser extent and occupy much smaller area in the ternary isotherm because of low Ti solubility.

Therefore, upon utilizing the various line-scan data and interpreting the tie-lines of various phases and plotting them on a ternary isotherm yields the Ni-Ti-Hf phase diagram at 800° as shown in Fig. 5.13. Along with respective binary phases extending inside the ternary phase diagram, no

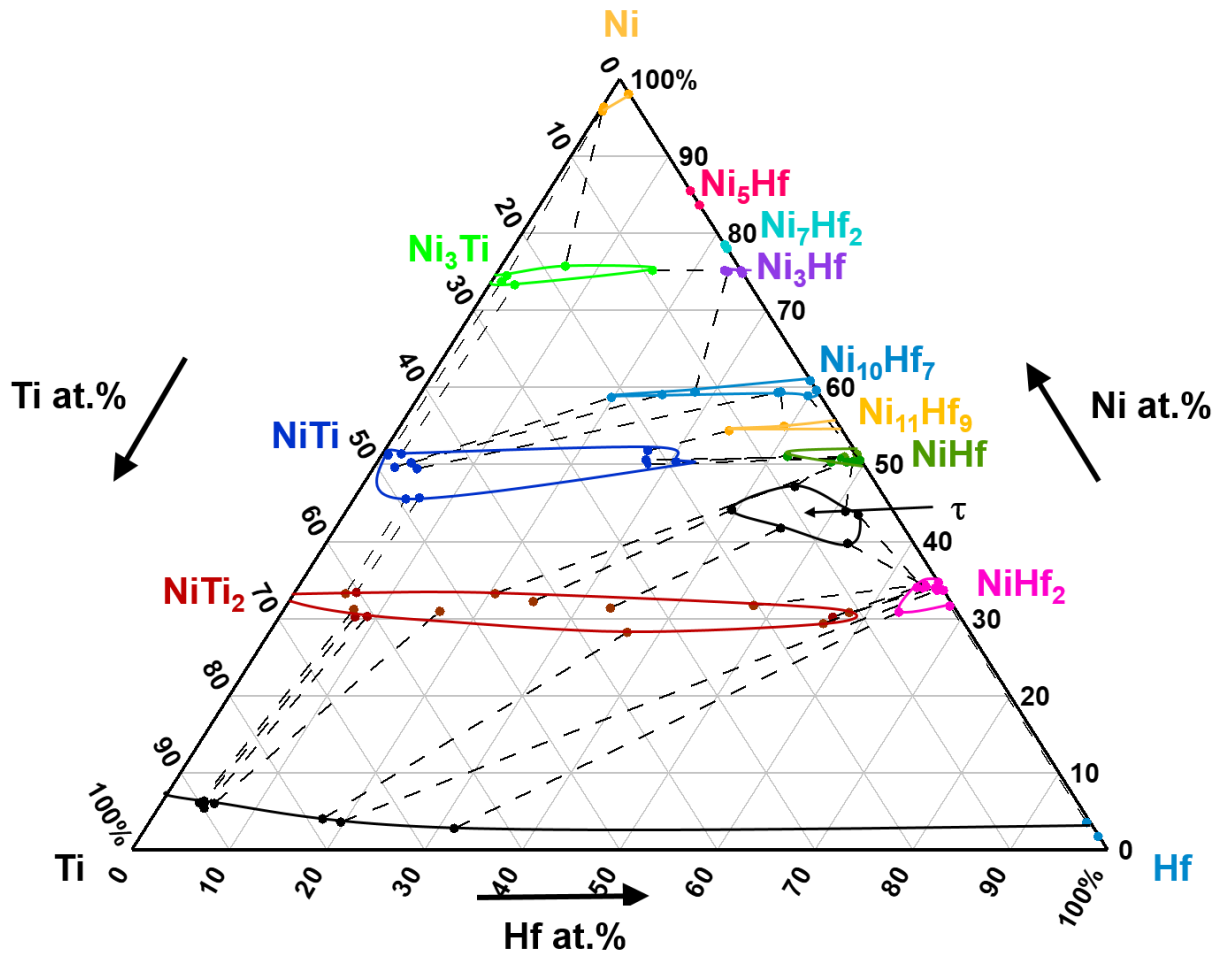

Figure 5.13 The ternary Ni-Ti-Hf phase isotherm at 600°C with all the phases and tie-lines marked accordingly. No evidence of Ni_4Ti_3 or H-phase precipitates was found in the phase diagram,

evidence of H-phase or Ni_4Ti_3 precipitate phases were found in the DM at 800°C. Apart from the individual binary phases, a new phase which is not present in the binary diagrams is observed to be present in between NiHf and $NiHf_2$ phase known as the τ phase. Similar existence of the τ phase was also reported by Liu et al [116]. Upon analyzing the DM assembly at 700°C and 900°C, phase diagram was found to be similar to the one at 800°C as shown in Fig. 5.13, with distinct phase solubility's and distinct spread in the phase diagram.

5.4. Alloy Design using Equilibrium Phase Diagram

As mentioned before, knowledge of the phase equilibria between the H-phase precipitates and B2 martensitically transforming phase can help us design novel NiTiHf shape memory alloys with required transformation characteristics. Most of the NiTiHf alloys have been designed so far based on trivial trial and error and intuition based method from the existing literature knowledge. Recently, some of the studies showed the potential of combinatorial approaches based on non-linear theory of martensitic transformation to design SMAs with very low hysteresis [74, 75]. The approach based on theory of martensitic transformation of designing new alloys, emphasizes on the geometric structural incompatibilities between the high symmetry austenite structure and low symmetry martensite structure. The theory suggests that when the second eigenvalue (λ_2) of the transformation stretch matrix is closer to 1, the higher is the austenite and martensite crystal structures are compatible with each other and hence lower is the thermal hysteresis and vice versa. But this approach is limited to only those SMA system who show a very significant dependence of thermal hysteresis on the λ_2 value [77] such as NiTiPd, NiTiAu, whereas systems like NiTiHf and NiTiZr show a very less dependence of hysteresis on λ_2 value. Also there is no significant evidence of strong dependence of λ_2 on Ms temperatures and thus λ_2 cannot be utilized to design alloys with specific transformation temperatures. There are also a few number of studies that utilized machine learning approaches to design novel SMAs. Recent studies have demonstrated a iterative framework can be implemented to predict the SMA manufacturing and processing recipe for a required need of transformation characteristics, with the help of a mathematical model which is based on the material's physical and chemical properties such as composition, atomic distance, electronegativity, etc [76, 79, 156]. However, the approach to design new alloys based on equilibrium is one of the most reliable among all other theoretical model based work, as the phase

diagram gives out composition of the transforming matrix with a higher certainty as compared to the other predicting models and hence the resultant alloy will have a higher chance to possess the chosen predicted transformation properties as compared to other methods.

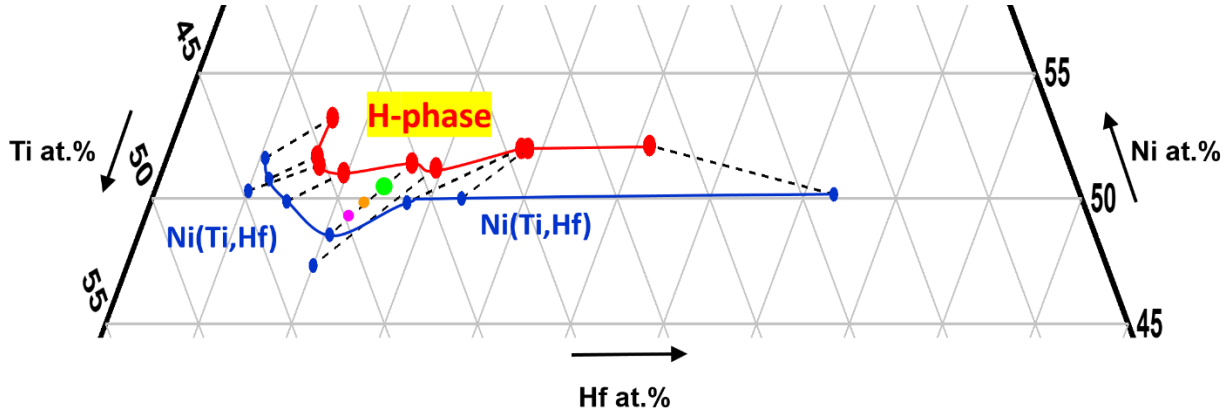

Figure 5.14 Shows a close-up view of the ternary phase isotherm shown in Fig. 5.9, with Ni extending from approximately 45 at.% to 60 at.% with focus being on the tie lines extending from the H-phase region to the B2 Ni(Ti,Hf) phase region. The red markers indicate the boundary compositions of the H-phase whereas the blue markers indicate the corresponding compositions in the Ni(Ti,Hf) region. The green, orange and pink markers are used to explain the change in composition of matrix occurs across a fixed path towards the equilibrium composition.

In order to elaborate on the idea of designing alloys by using phase diagrams, consider Fig. 5.11 which shows a part of the ternary isotherm from Fig. 5.9 with emphasizing on the tie-lines (marked by black dotted lines) present between the H-phase and the Ni(Ti,Hf) B2 martensitically transforming phase. The area between the H-phase who's boundary is marked by the red curve and the Ni(Ti,Hf) phase who's boundary is marked by the blue curve and the area between the two curves is called a two phase region in the ternary phase diagram. This two phase region between the red and blue curve in Fig. 5.11 comprises of the H-phase and the Ni(Ti,Hf) phase present together, as per the basic thermodynamic phase rule, i.e., there is always a two phase region present in between two single phase regions. The tie-lines as seen in Fig. 5.11 are connecting a specific

composition from the H-phase region to a specific composition in the Ni(Ti,Hf) phase region. Therefore, there exist a number of such unique tie-lines which connect a unique composition from the H-phase region to the unique composition in the Ni(Ti,Hf) phase region.

Now, consider a Ni-rich NiTiHf alloy which is manufactured using arc melting followed by solution heat treatment and water quenching possess a single phase microstructure, i.e., the Ni(Ti,Hf) phase [176]. Of course certain Ni-rich NiTiHf alloys that are fabricated using the vacuum indication melting tends to possess Hf-carbide particles embedded as impurities in the B2 Ni(Ti,Hf) phase [57]. But as the carbides are imparted into the micro-structure because of the use of graphite crucible during vacuum induction melting and as it is not the essential part of the material system, such carbide based micro-structures would be neglected. Based on SHT temperature for NiTiHf alloys which is usually at or above 900°C, the green circular as shown in Fig. 5.11 would represent the Ni-rich NiTiHf alloy composition that lies in a single phase region of Ni(Ti,Hf) phase, as the super-saturated Ni(Ti,Hf) solid solution phase is stable. As the alloy is heat treated at 600°C, H-phase starts to precipitate out of the super-saturated solid solution and the green circular transitions from the single phase region (i.e., after SHT at 900°C or above) into a two phase region. As soon as the alloy starts to precipitate out H-phase precipitates, the alloy establishes a tie-lines which extend to a unique composition in the H-phase precipitates that just precipitated-out in one direction and the other end extends to the composition of the modified Ni(Ti,Hf) phase region, as shown in Fig. 5.11. In the embryonic or nucleation stage of precipitation, very few of nanometer sized precipitates are formed and has a much lower volume fraction as compared to the matrix. As the time of aging heat treatment progresses, the H-phase precipitates grows in size and the volume fraction of the precipitates increases. During the growth stage of the H-precipitates as some precipitates grows at the expense of others, the composition of

the H-phase is still the same as that in nucleation stage, only the volume fraction of the precipitates increases drastically. While coarsening though the precipitate volume fraction increases, the matrix is been depleted from Ni and Hf. So as the precipitation progresses through its different stages, the volume fraction of the Ni-rich and Hf-rich H-phase precipitates increases continuously by depleting the matrix with Ni and Hf, thus making the matrix more Ni and Hf poor. As the aging heat treatment continues for infinite time, the initial super saturated solid solution will precipitate out all the H-phase and a chemical equilibrium will be established between the two phases.

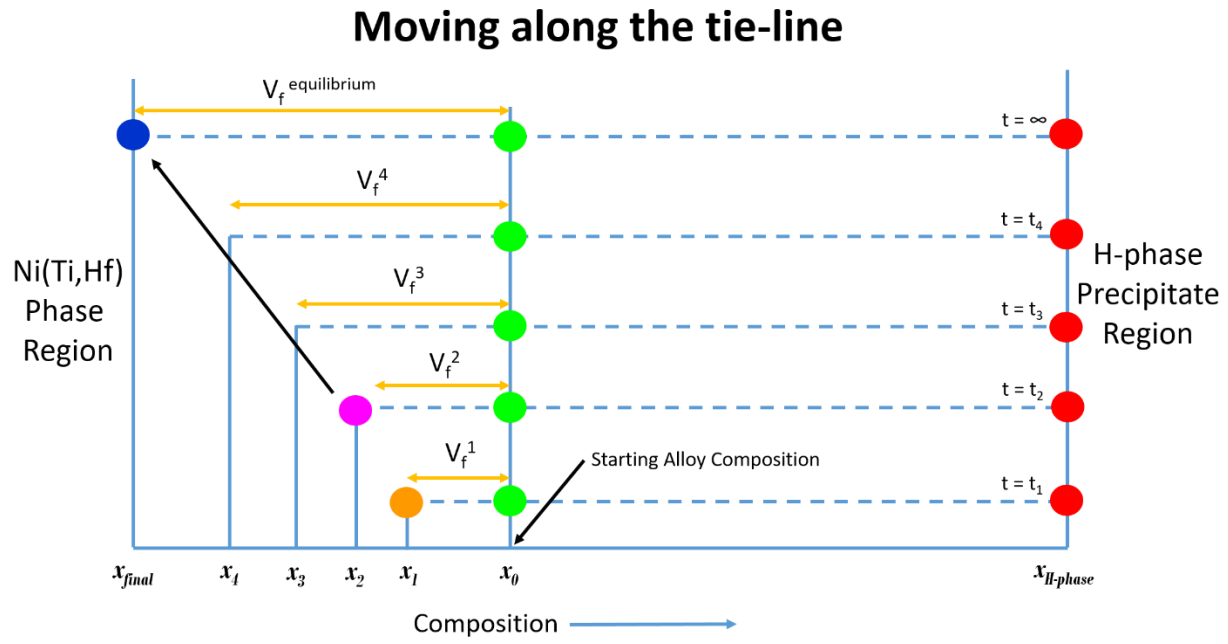

Figure 5.15 Schematic representing the change in matrix composition along the equilibrium tie-line from the initial alloy composition to the equilibrium phase composition.

During the course of precipitation, the Ni and Hf depletion of the matrix phase does not happen in a random or unorderly manner. The journey of composition of the matrix from initial starting composition, all the way to the equilibrium composition of the matrix happens by

traversing across the tie-line. For example, in Fig. 5.11, the composition of the starting alloy composition (which is depicted by the green circular marker) upon aging heat treating at 600°C, will start traversing towards the blue circular marker in the Ni(Ti,Hf) region along the dotted tie-line. Therefore as per the kinetics of the nucleation, growth and coarsening of the H-phase precipitates, the change in the matrix composition will occur accordingly. Since, this is a very crucial concept and will form the basis of performing alloy designing using phase diagram, the above analogy is elaborated in Fig. 5.12 with the help of a schematic representation of the change in matrix composition. Fig. 5.12 shows a schematic with a composition 'x_0' on the X-axis and the evolution of composition as a function of time increasing vertically. In Fig. 5.12, the composition values (in terms of 'x') on the X-axis, are a representation of the equivalent Ni, Ti and Hf composition in the phase diagram. The X-axis is scaled to composition in such a way that the endpoints on X-axis represents the end point compositions of a tie-line (in our case it is the tie-line that is marked with several colored circular markers in Fig. 5.11). Now consider an alloy in the SHT condition (shown by the green circular marker in Fig. 5.11 and Fig. 5.12), which will undergo aging heat treatment at 600°C. Therefore at t = 0, the alloy is homogenous and contains only the Ni(Ti,Hf) phase with a composition of 'x_0'. Upon subjecting this alloy to heat treatment at 600°C, the alloy will start precipitating out H-phase and the volume of H-phase precipitated will increase with increasing heat treatment time. From Fig. 5.12 consider the micro-structure of the alloy at the instance of $t = t_1$, where the alloy has precipitated out 'V_f^1' amount of volume fraction of H-phase precipitates with a composition of $x_{H\text{-}phase}$. During this precipitation process the Ni and Hf is depleted from the matrix and hence, their value in the matrix would decrease from x_0 to x_1. The composition of the H-phase precipitated out ($x_{H\text{-}phase}$) is marked by the red circular marker and the corresponding

new matrix composition (x_1) is marked by the orange circular marker as shown in in Fig. 5.12. The value of the composition of the matrix at $t = t_1$ instance is also marked by an orange circular marker in Fig. 5.11. Therefore during time interval of $t = 0$ to $t = t_1$, the matrix alloy composition has gradually changed from the green marker to the orange marker along the black color dotted tie-line in the phase-diagram.

With continuation of further precipitation, at instance $t = t_2$, the alloy has now precipitated out 'V_f^2' amount volume fraction of H-phase precipitates whose composition is $x_{H\text{-}phase}$ and is marked by a red marker, where $V_f^2 > V_f^1$. Since the volume fraction of H-phase precipitated out is more than in previous case, the matrix is further depleted with Ni and Hf and the corresponding new matrix composition is x_2 and is marked by a pink circular marker in Fig. 5.12. The corresponding new matrix composition is also marked with a pink circular marker in Fig. 5.11 along the tie-line. Hence during the time interval of $t = t_1$ to $t = t_2$, the matrix alloy composition has gradually changed from x_1 to x_2 or from the orange marker to the pink marker along the black color dotted tie-line in the phase-diagram. Such a continuous change of matrix composition ($x_0 \rightarrow x_1 \rightarrow x_2 \rightarrow x_3 \rightarrow x_4$) keeps occurring along the tie-line with further increase in heat treatment time ($t_1 < t_2 < t_3 < t_4$) and the corresponding volume fraction of the H-phase also keeps increasing ($V_f^1 < V_f^2 < V_f^3 < V_f^4$). This process will continue until the alloy x_0 is heat treated for infinite time to each a thermal equilibrium between the H-phase precipitates with composition of $x_{H\text{-}phase}$ and the matrix Ni(Ti,Hf) phase with a composition of x_{final}, and are marked by red and blue circular marker respectively in Fig. 5.11 and 5.12. The knowledge of such an evolving matrix composition with increase in heat treatment time, can be highly resourceful in designing a new alloy with required

transformation composition. By controlling the heat treatment time, we can control the volume fraction of the H-phase precipitates and hence control the corresponding matrix composition and thus can control the transformation characteristics. A choice of initial alloy composition can be made such that heat treating the alloy for a particular time will yield required amount of volume fraction of H-phase precipitate and matrix composition, best suitable for the required application. The required matrix composition (or the corresponding TTs) can be estimated from our previous of compositional dependence of TTs of NiTiHf HTSMAs [176].

Now, as the compositional path traversed by any NiTiHf alloy during aging heat treatment is known, the volume fraction of H-phase precipitates will keep increases as the alloy is traversing its path towards the equilibrium composition. In order to design a new alloy based on this approach, a correct heat treatment time is supposed to be determined at particular temperature that will impart the right amount of volume fraction of precipitates into the system. Such an estimate of the volume fraction of precipitation with heat treatment time can be accurately estimated by the knowledge of the kinetics of precipitation at that temperature. There has been very few studies that have made efforts to understand the kinetics of the H-phase precipitation [59, 169]. Prasher et al, studied the H-phase precipitation using Small Angle Neutron Scattering and have marked the different regimes or stages of precipitation kinetics in the aging heat treatment time Vs temperature plot. The authors have used ex-situ heat treated samples and conducted the Small Angle Neutron Scattering analysis on them in order to predict the size and volume fraction of the H-phase precipitates. Still a study that gives real time (or *in-situ)* evolution of precipitate length, width and volume fraction with heat treatment time is missing. Based on kinetic studies by Prasher et al, an estimate of heat treatment time can be estimated to yield a certain amount of volume fraction of H-phase precipitates in the material. Hence, after performing a few iterations based on

aforementioned approach, the targeted TTs can be achieved. Therefore such a powerful approach that utilizes the thermodynamics and kinetics of the H-phase precipitates can be employed to design alloys with a required transformation temperatures and other transformation characteristics.

5.5. Summary

In order to summarize, the thermodynamic study of the H-phase precipitation in the NiTiHf system, efforts have been made to explore the phase equilibrium in the Ni-Ti-Hf material system as such by employing the high throughput diffusion multiple experiments. Such robust experimental design have helped us yield all the equilibrium transformation phases present at 600°C. The major findings of the present work is stated as follows:

(1) The aging heat treatment studies have shown that the TTs tend to increase drastically upon H-phase precipitation. The aging treatment also decreases tends to stabilize the thermal cyclic response of the material, so that the TTs of any aged NiTiHf SMA component in application do not change with consecutive number of thermal cycling.

(2) The STEM micro-structural analysis of $Ni_{50.3}Ti_{29.7}Hf_{20}$ alloy, shows that upon aging the alloy at 600°C for 10 hours followed by WQ, yields a micro-structure with a uniform distribution of H-phase precipitates with average length of 36.2± 9.4nm and width of 16.7 ± 3.1 nm respectively. On heat treating the same alloy at 650°C for 10 hours followed by WQ produces H-phase precipitates with average length of 91.2± 18.0 nm and width of 30.8± 10.3nm respectively, with non-uniform distribution in the micro-structure.

(3) The EDX maps obtained from STEM shows that the H-precipitates are slightly Ni-rich but extremely Hf-rich and Ti-lean as compared to the matrix phase. The quantitative results obtained from them also show similar trends.

(4) The X-ray maps obtained from the diffusion multiple assembly after heat treatment at 600°C for 5000 hours and WQ, show that the Ni diffuses the fastest among all the three elements. Following Ni, Hf diffuses the second fastest as a significant amount of Hf-diffuses in the Ni-Ti side of the diffusion multiple. This also shows that Hf has higher solubility in the all the binary phases present in the Ni-Ti binary phase diagram and hence these phases will occupy larger area in the Ni-Ti-Hf ternary phase diagram. Among all the three elements, Ti diffuses the slowest as it does not diffuse on the Ni-Hf side of the diffusion multiple and also exhibits very limited solubility in the binary phases present in the Ni-Hf binary phase diagrams.

(5) The WDS analysis of the phases and phase boundaries gives an estimate of their respective span in the ternary phase diagram. All the phases found in the respective binaries (i.e., Ni-Ti, Ni-Hf and Ti-Hf) were found to be present in the diffusion multiple assembly. Along with all respective binary phases, a new phase that is not found in any of the binary phase diagram was found in between the NiHf and NiTi region of the diffusion multiple. As the new phase was Ni-rich, Ti-lean and Hf-rich as compared to the Ni(Ti,Hf) phase and hence was characterized to be H-phase based on its compositional contrast with respect to the Ni(Ti,Hf) phase.

(6) Existence of H-phase in the equilibrium phase diagram, exhibits that it is not an Ni_4Ti_3 like intermetallic phase which exists as a line compound in the phase diagram, but on the contrary is stable at equilibrium. The H-phase is a solid solution phase and occupies a region in the phase diagram with Ni content ranging from 51.13 at.% to 54 at.%, whereas Hf ranging from 7 at.% to 34 at.%, as shown in Fig. 5.6, Fig. 5.8 and Fig. 5.9.

(7) Along with H-phase precipitates, the Ni_4Ti_3 precipitate phase was also extends inside the ternary phase diagram, with certain Hf solubility. The Ni_4Ti_3 precipitate phase was found to grow inside the equilibrium NiTi phase region at 600°C and showed a maximum Hf solubility of approximately 15 at.% with Hf replacing Ti.

(8) Analysis of DM assembly heat treated at 800°C also showed all the binary phases present in individual binary phase diagrams with higher solubility of the third element as compared to that at 600°C. No evidence of H-phase and Ni_4Ti_3 precipitate phase was found. The Ni-Ti-Hf phase diagram at 700°C and 900°C was observed to be similar to that at 800°C, with distinct phase solubility's.

(9) Finally, by utilizing the newly explored equilibrium between the H-phase and the Ni(Ti,Hf) B2 martensitically transforming phase at 600°C, a novel approach can be developed that can be used to design novel NiTiHf alloys for high temperature actuation based applications with targeted TTs.

CHAPTER VI

IN-SITU SYNCOTRON BASED STUDIES FOR H-PHASE VOLUME FRACTION ESTIMATION IN NITIHF HIGH TEMPERATURE SHAPE MEMORY ALLOYS

This chapter encloses the detailed study of kinetics of H-phase precipitation performed using the SAXS experiments. SAXS, as a global technique that provide average information on a large population of precipitates, was originally developed over 60 years ago to quantify the microstructure of precipitates. In-situ monitoring of evolution of size and volume fraction of H-phase precipitates was performed at 550°C for 12 hours. The results shown in the present chapter can be used in combination with results from Chapter V, in order to design alloys with the required TTs and volume fraction of the H-phase precipitates.

6.1 Differential Scanning Calorimetry

Fig. 6.1 shows the DSC plots from a SHT and HT550°C sample with red and blue curve respectively. DSC results indicate that the TTs tend to enhance with HT. The martensitic start temperature (M_s) tend to increase from 91°C for SHT material to 144°C for HT550°C material. Also, the austenite finish temperature (A_f) increases from 124°C for SHT material to 171°C for HT550°C material. With heat treatment, the thermal hysteresis (A_f-M_s) decreases drastically from 33°C for SHT material to 27°C for HT550°C material. Also, the material tends to become more thermally stable with precipitation, as the difference between Ms1-Ms3 tends to decrease from 10°C for SHT to less than 2°C for the HT550°C sample.

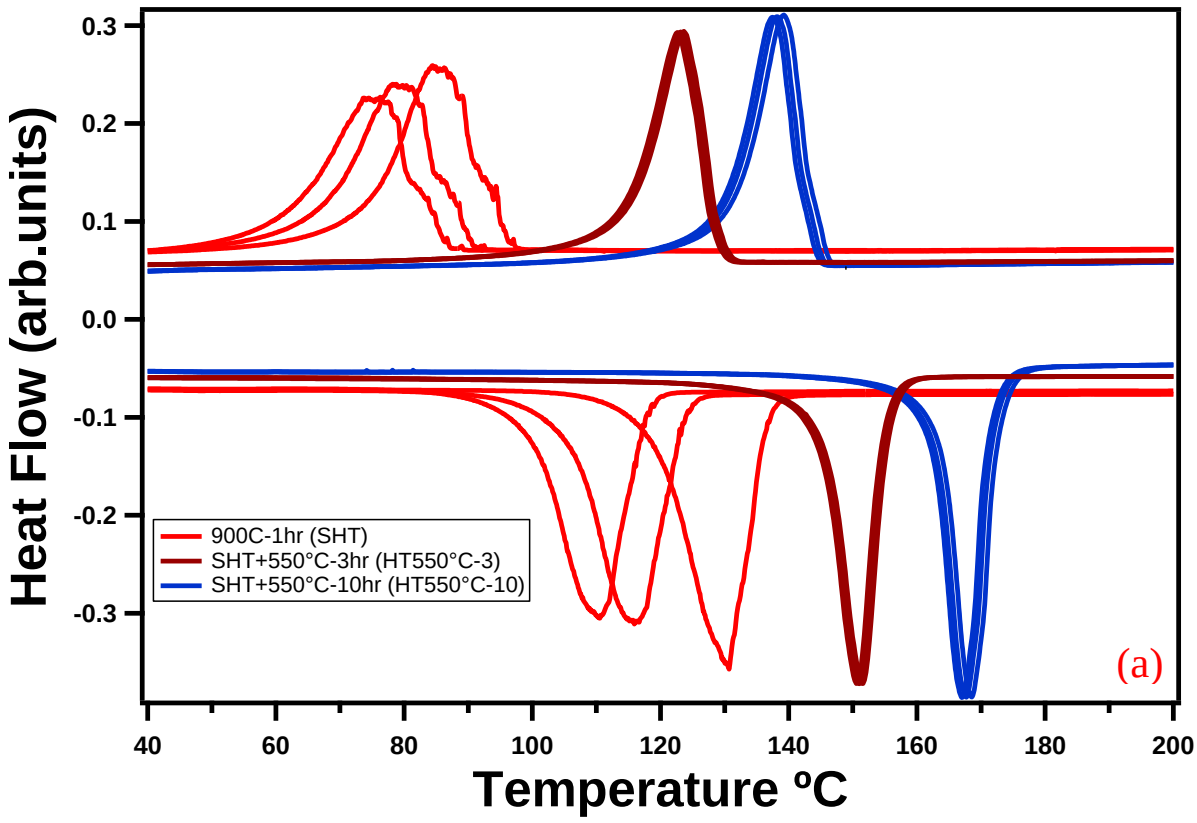

Figure 6.1 Differential Scanning Calorimetry results of the Ni50.3TiHf20 alloy after SHT and heat treatment at 550°C for 3 hrs and 10 hrs.

6.2 Transmission Electron Microscopy

Fig. 6.2a and Fig. 6.2b shows a bright field and dark field Scanning Transmission Electron Microscopy (STEM) image of the HT550°C microstructure with martensitic matrix and H-phase precipitates with an average length of 16.6 ± 3 nm and thickness of 8.67 ± 1.27 nm, respectively. The composition of the H-phase precipitate and the matrix phase measured by generating EDX X-ray maps and then taking the average composition of the square area from the center of H-phase precipitates and in the matrix phase as well. Obtained results show that the H-phase has an average composition of Ni=51.8 at.%; Ti=22.03 at.% and Hf= 26.17 at.%. On the other hand, the matrix composition was found to be Ni=50.8 at.%; Ti=25.23 at.% and Hf= 23.97 at.%. The H-phase

precipitates are found to be rich in Hf, slightly rich in Ni and poor in Ti as compared to that of the martensitic matrix after aging at 550°C for 10 hours [67]. Above DSC and TEM results hence reflect that, H-phase precipitation at 550°C for 10 hours increases the TTs, thermal stability and reduces the thermal hysteresis as compared to SHT material.

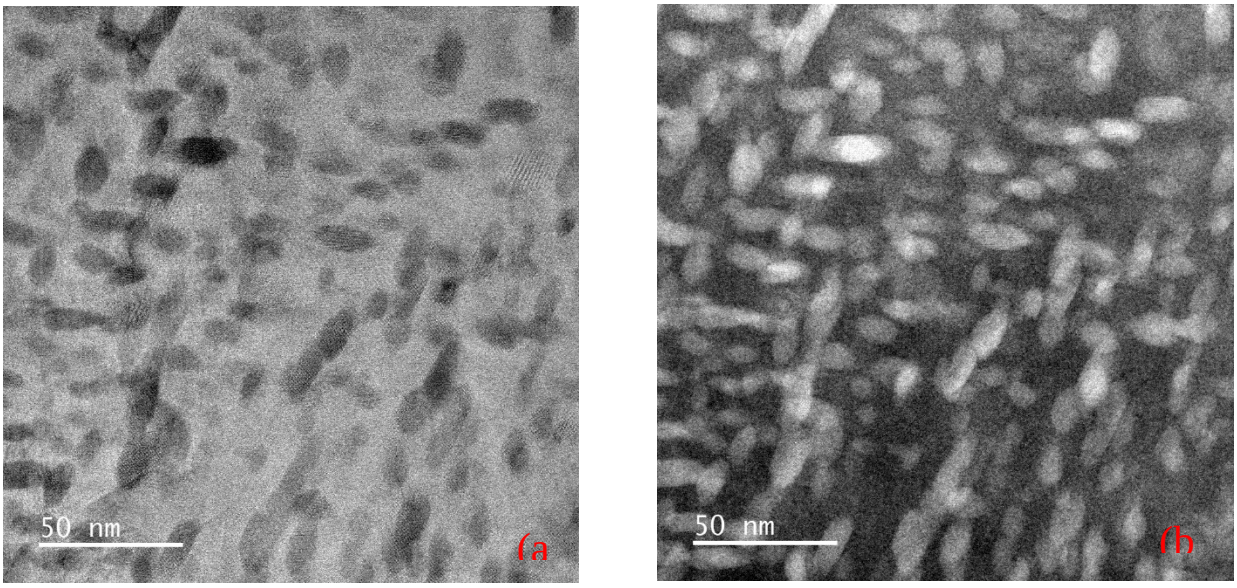

Figure 6.2 The HAADF (a) bright field and (b) dark field Scanning Transmission Electron Microscope (STEM) image of the $Ni_{50.3}TiHf_{20}$ alloy after heat treating at 550°C for 10 hours followed by water quenching. The image shows a distribution of H-phase precipitates with average length of 16.6 ± 3 nm and thickness of 8.67 ± 1.27 nm.

6.3 Small Scattering X-ray Scattering

Fig. 6.3 shows the complete set of SAXS data acquired from the $Ni_{50.3}Ti_{29.7}Hf_{20}$ sample during the *in-situ* experiments, with slit-smeared scattering intensity on Y-axis and the scattering vector *q* on the X-axis (here slit smeared refers to line shaped collimated incident electron beam instead of point electron beam). The color scale indicated by the arrow shows the acquisition time, starting from the time when the *in-situ* sample reached a temperature of 550°C. Similar SAXS

experiments have also been conducted at 600°C and 650°C, but only data from 550°C is shown in order to demonstrate the proficiency of the SAXS technique. It is worth

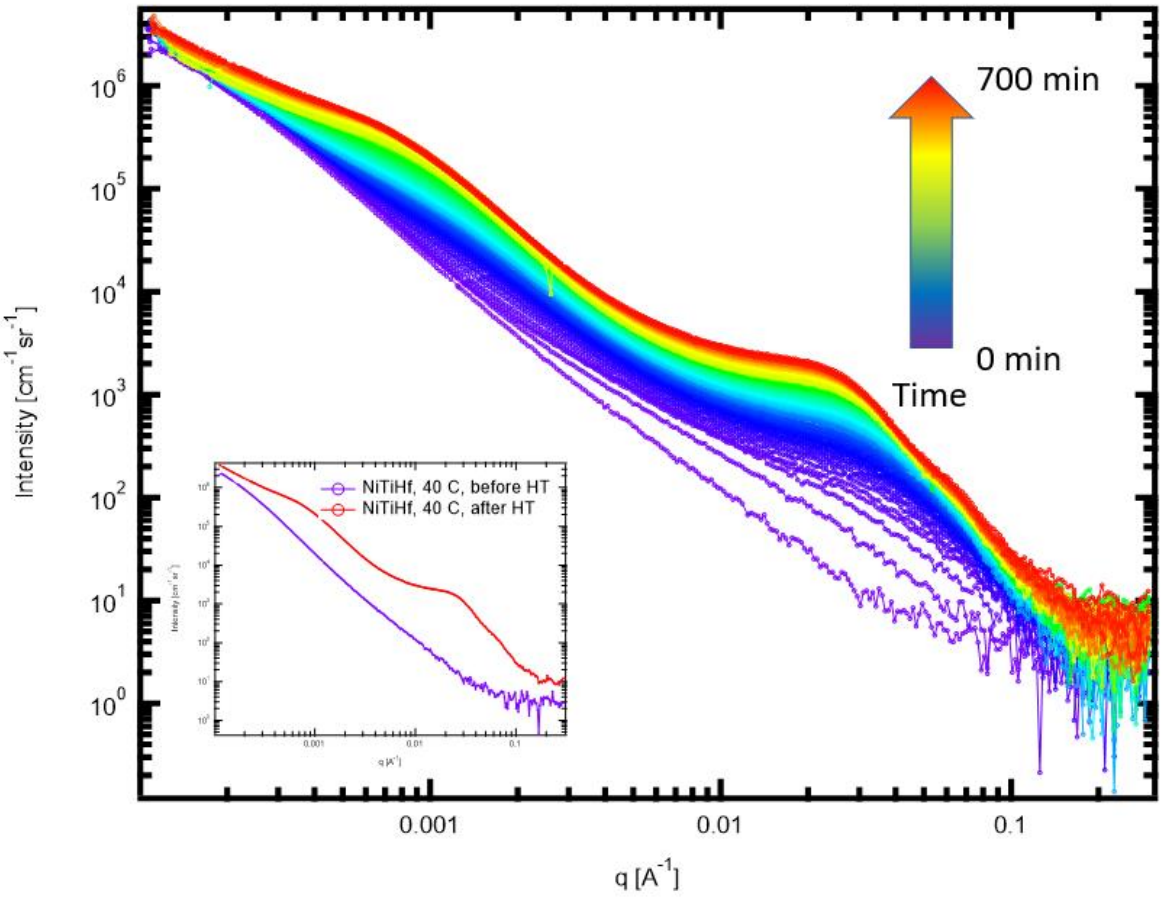

Figure 6.3 In situ SAXS data acquired at 550 °C. The acquisition time is color-coded, with purple indicating early and red indicating late during the isothermal heat treatment, respectively.

mentioning here that as SAXS measurements are performed in reciprocal space, implying that scattering contributions from lower value of *q* will be caused by larger dimension of chemical inhomogeneity in the material, and vice versa. The Fig. 6.3 demonstrates a few characteristics of the microstructural evolution. Prior to heating, the scattering profile displays a power-law behavior, typical of grain scattering. During the heat treatment, the scattering intensity increases

across the entire observable q range, indicating the formation of microstructures within the corresponding size range. Notably, three Guinier plateaus emerge during the SAXS experiments. The plateaus of the data acquired at 700 min are approximately positioned at 0.001 $Å^{-1}$, 0.03 $Å^{-1}$, and 0.06 $Å^{-1}$, respectively. These distinctive plateaus represented the nominal sizes of the microstructural features. The correct interpretation, however, requires careful modeling constructed with microscopic evidence.

From Fig. 6.3, the obtained SAXS data has the following common features. First, the presence of low-q power-law scattering indicates scattering in-homogeneities greater than the detection limit (several micrometers), often associated with grain scattering [177, 178]. Second, two Guinier-type scattering features were observed in Guinier plot, which is obtained by plotting log(Scattering Intensity) Vs q^2, strongly indicating that the precipitates have two different characteristic length scales. Third, the scattering intensity demonstrates monotonic increase within the observed q range as time increases, which is known to be associated with nucleation and growth of precipitates in alloys. Interestingly, the data also suggests that the monotonic increase in the scattering intensity was initially rapid for the first ~60 minutes, followed by a gradual decrease in rate of increase, implying a change in rate. Therefore, from above observations it can be said that, there is a continuous nucleation and growth of H-phase precipitates during heat treating the material at 550°C upto 12 hours. The thermodynamic driving force for precipitation of H-phase at 550°C is very high initially and decreases eventually with increase in time corresponding to the rate of change of scattering intensity. Therefore, the rate of nucleation and growth is initially very high, followed by gradual decrease with increasing time.

Based on the Guinier plateaus emergence, at a value of q of 0.001 $Å^{-1}$, 0.03 $Å^{-1}$, and 0.06 $Å^{-1}$, respectively corresponds to the evolution of micro-structural features in the material during

the *in-situ* SAXS experiment. Based on the TEM evidence for the $Ni_{50.3}TiHf_{20}$ alloy after heat treating at 550°C for 10 hours shows precipitates with average length of 16.6 ± 3 nm and thickness of 8.67 ± 1.27 nm, as shown in Fig. 6.2. The Guinier plateau at q value of 0.03 $Å^{-1}$, and 0.06 $Å^{-1}$ depicts the scattering associated with the increasing length and width of the H-phase precipitates respectively, during the *in-situ* SXAS experiments. The scattering intensity feature (Guinier plateau) associated with enhanced scattering intensity at q value of 0.001 $Å^{-1}$ signifies scattering occurring from a relatively large feature as compared to that of the dimension of the H-phase precipitates. Such scattering associated with a large micro-structural feature might be occurring from the movement of dislocations associated at high temperature from grain boundary movement, growth of martensite laths or movements of defects generated during the martensitic phase transformation.

From a phase transformation point of view, the transformation sequence is known. The solutionized martensite has a B19' structure (monoclinic, $P112_1/m$ space group). Upon heating to aging temperature, the matrix transforms to a B2 structure (cubic, Pm3m space group). Aging promotes the formation of H-phase precipitates (orthorhombic structure, Fddd space group). This is supported by the in situ XRD data, as shown in Fig. 6.4. For typical alloys, the growth kinetics of secondary phases can often be interrogated by the evolution of diffraction peak intensities. In our study, this is limited by the finite size of the stripe area detector, texturing of the XRD pattern, and large lattice parameter of the H-phase precipitates and their changing composition. Because of these reasons, we confine our discussion of the XRD data to the change in lattice constants.

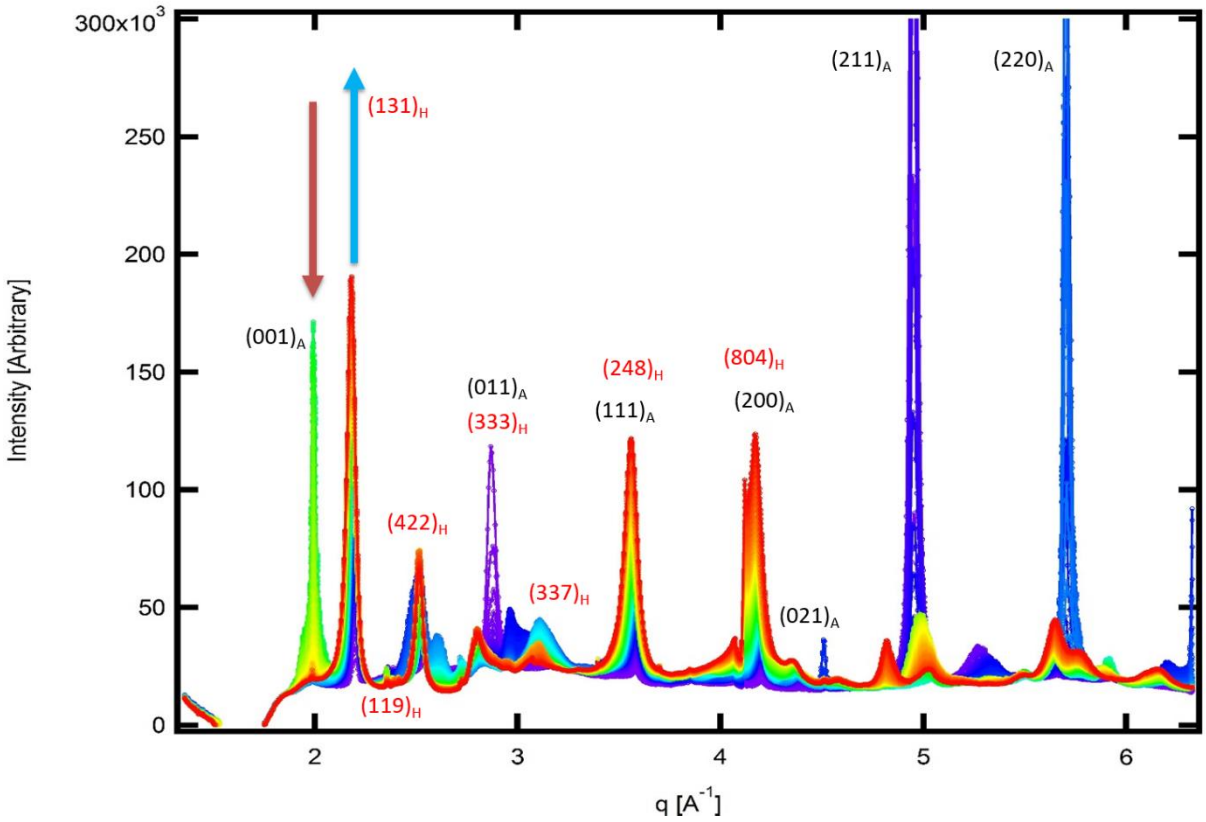

Figure 6.4 In situ XRD data acquired at 550 °C. The acquisition time is color-coded, with purple indicating early and red indicating late during the isothermal heat treatment, respectively.

The SAXS model is constructed based on TEM evidences, as shown in Fig. 6.2. Two characteristics identified from TEM are considered for the SAXS model. The first is the shape of the precipitates. TEM data clearly demonstrate that the H precipitates are anisotropic in shape with nm-scale long and short dimensions, suggesting that the precipitates are spheroid in shape. Based on this, we assigned a spheroid scattering form factor to an individual precipitate. The second is that the precipitates are densely yet almost uniformly distributed within the sample volume probed by TEM. This requires that the scattering structure factor be considered for the model to account for intensity modulation introduced by X-ray wave interferences. In this case, we assumed a Percus-Yevick structure factor, a model that is developed for liquid and finds applications in the

interpretation of scattering profiles of complex fluids [179] but also used in precipitate scattering in alloys [180].

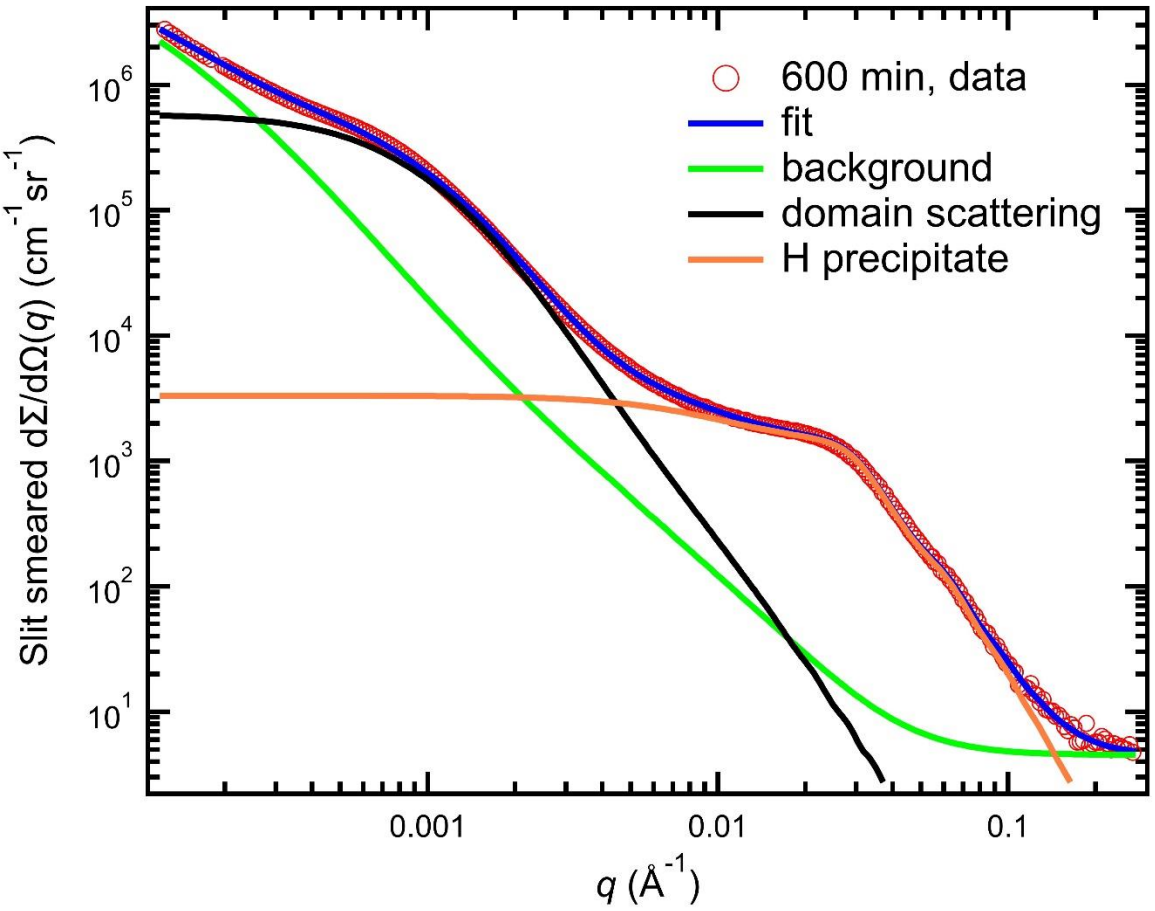

Figure 6.5 SAXS data acquired at 600 min into the heat treatment and its model fit.

Based on these observations, we constructed a quantitative model to investigate the morphological evolution of the H-phase precipitates. The data analyses were conducted using small angle scattering (SAS) analysis software *Irena* [181]. Extensive TEM work demonstrates that the H-phase precipitates exhibit preferred orientations, localized number density, and spatial non-uniformity [67]. Because of this, we adopted a data-analysis approach analogous to the unified SAS analysis method [182, 183]. Using this approach, characteristic length scales of different

scattering in-homogeneities in a complex scattering system can be reliably extracted. Fig. 6.5 uses the SAXS data acquired at 600 min into the heat treatment to illustrate the quality of the model. The green curve represents the scattering background, acquired from the solutionized specimen of the same sample volume. The orange line shows the scattering from the H precipitates. The model dictated ratio of the long-to-short dimension of the spheroid is 2. Using this scattering form factor, the Guinier regions at 0.03 $Å^{-1}$ and 0.06 $Å^{-1}$ are both well accounted for. The black line represents a scattering feature on the length scale of 250 nm. As mentioned before such scattering can be related to the growth of martensitic laths or movements of dislocations. The combination of these scattering components (background, H-phase precipitates, and domain), as the solid blue line shows, fits the data well.

For the H phase precipitates, the volume fraction evolution is shown in Fig. 6.6. We observe a continuous increase of the volume fraction of the H phase precipitates, qualitatively consistent with ex situ TEM and in situ XRD observations. The volume fraction is described by a simple exponential decay function, with a decay time scale of 385 min and model-predicted maximum volume fraction of 0.23 ± 0.01. It, however, must be noted that the volume fraction analysis assumes constant scattering contrast. In reality, as the in situ XRD data suggest, the lattice parameters of H phase precipitates increase as a function of time, indicating a gradual enrichment of Hf and subsequence increase in the scattering contrast. For the DSC plots shown in Fig. 6.1, the volume fraction of H-phase present in the samples heat treated at 550°C for 3 hrs and 10 hrs is 9.18 ± 1.24% and 18.04 ± 0.73%, respectively. There is a very limited literature data available that utilized advanced techniques such as Atom Probe Tomography and Small Angle Neutron Scattering experiments, in order to calculate the volume fraction of H-phase present in a particular alloy. Hornbuckle et al, performed Atom Probe Tomography on a $Ni_{50.3}TiHf_{20}$ nominal

composition alloy heat treated at 550°C for 3, 30 and 300 hours and estimated the volume fraction of the H-phase to be 15.6 ± 1.6%, 14.8 ± 1.5% and 22.2 ± 2.2% respectively [123]. The results from Hornbuckle et al seems to be within permissible degree of agreement with that found in the present work. The alloy used in the study by Hornbuckle et al was prepared by induction melting and hot extruded at 900°C and reports M_s temperature of the same alloy in SHT condition to be 104°C.

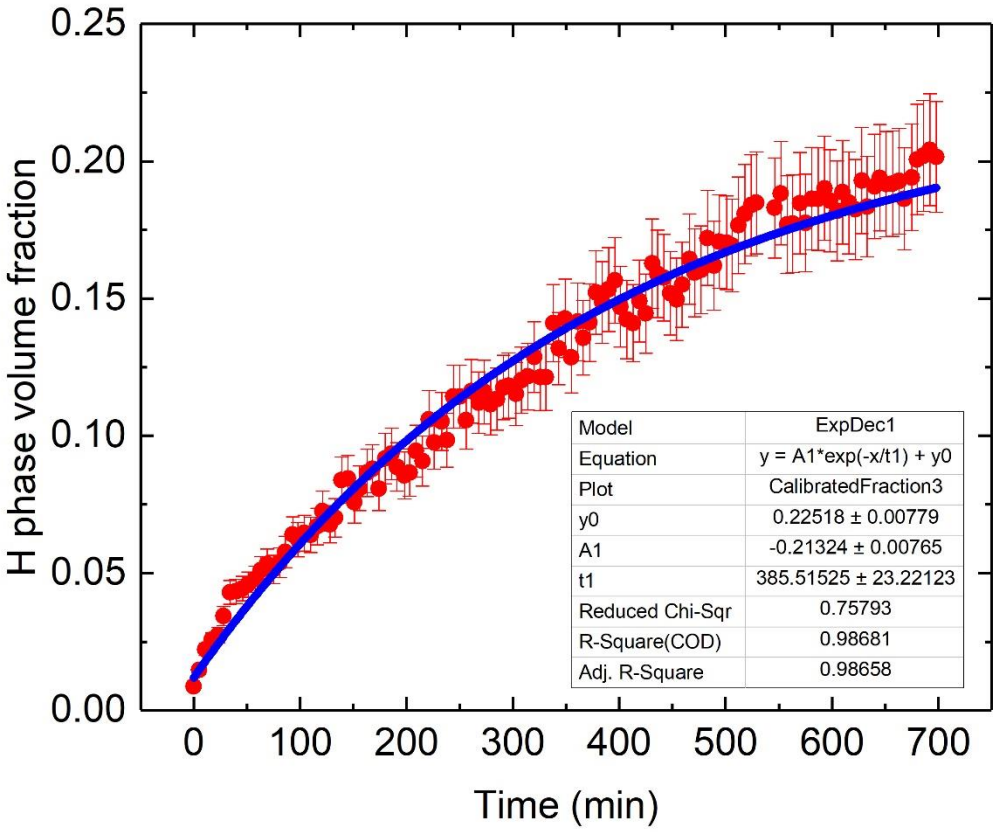

Figure 6.6 Evolution of volume fraction of H-phase precipitates at 550°C during the *in-situ* SAXS experiment.

On the other hand another work by Prasher et al on the same nominal composition $Ni_{50.3}TiHf_{20}$ alloy, shows the H-phase volume fraction measurements acquired using the Small Angle Neutron Scattering experiments [169]. Prasher et al fabricated the alloy using vacuum arc-melting and no post mechanical work was conducted and reported the SHT Ms temperature to be approximately around 180°C. Prasher et al conducted *ex-situ* measurements on the alloy with different heat treatment time and temperatures. The authors conducted heat treatment at 550°C for 96 hours and reported the volume fraction of H-phase to be 2.29 ± 0.63%. For all other heat treatment temperatures ranging from 550°C to 650°C and heat treatment ranging from 48 hours to 144 hours, the authors (Prasher et al) reported the value of volume fraction of H-phase ranges from 1.59 to 3.33 %. The values reported by Prasher et al are very different then what is found by Hornbuckle et al and in the present work. This disparity in value of volume fraction of the H-phase precipitates can be attributed to the difference in the actual compositions of all the alloys used. Results shown in Fig. 4.5 and 4.6 of the present work in Chapter 4 indicates that the Ni content of the material plays a very significant role in controlling the TTs. The higher the Ni content of the material, lower is the TTs. Santamarta et al also pointed out that the H-phase precipitation kinetics in enhanced when the initial Ni content of the alloy is higher [67]. Therefore, assuming that the Hf content of the alloys is more or less the same, based on the value of M_s temperature in SHT condition, it can be said that the alloy used in present work and by Hornbuckle et al has the actual Ni content very close to each other, whereas that used by Prasher et al has a Ni content much less than the aforementioned counterparts. As the alloy used by Prasher et al is less Ni-rich as compared to that used in the present study and Hornbuckle et al, and hence the alloy exhibit lower H-phase precipitation kinetics and shows a very low values of volume fraction of H-phase precipitates, even after heat treating the alloy at 550°C for 96 hours.

Aforementioned SAXS results lead us to unveil some interesting phenomenon regarding nucleation and growth kinetics of the H-phase precipitates in NiTiHf system. A continuous increase in scattering intensity with time as shown in Fig. 6.3, indicates that the H-phase precipitates tends to nucleate and grow continuously with time at 550°C. Interestingly, though the precipitation is continuous over the entire time span of *in-situ* SAXS experiment, the rate of increase of scattering intensity is very high initially followed by gradual decrease. This change of rate of scattering intensities indicates that the rate of H-phase precipitation is very high in the beginning, followed by a gradual decrease in rate with time. Classical precipitation theory also suggests that when enough thermal energy is provided to a super-saturated solid solution, the thermodynamic driving force for precipitation is very high and hence precipitates tends to nucleate and grow with a larger rate. But, with increasing time, the thermodynamic force (usually caused by concentration gradient across precipitate/matric interface) reduces and the rate of precipitation eventually decreases ultimately saturating to a constant value. Hence looking at the microstructure from Fig. 6.2 it can be said that the precipitates grow more or less homogenously inside the grain. Fig. 6.4 shows the *in-situ* XRD data acquired at 550°C. Here the acquisition time of the data was color-coded using the same scale as in Fig. 3a. The atomic structure transformation is notably more complex. Nevertheless, a continuous growth of diffraction peaks that can be attributed to the H-phase precipitates is evident. An example, highlighted by the arrow, shows the growth of {131} and {248} characteristic reflection of the H-phase, where the Miller indices were determined by a Fddd symmetry (orthorhombic) and lattice parameters of a = 12.34 Å, b = 9.00 Å, and c = 25.62 Å.

6.4 Alloy Designing using H-phase kinetics

From the above data shown in Fig. 6.6 for the evolution of volume fraction of H-phase precipitate with increasing heat treatment time, can be utilized to design novel NiTiHf alloys with required transformation characteristics. Evirgen et al has successfully demonstrated that the volume fraction of the H-phase precipitates tends to control the TTs and thermal hysteresis and recovery strains [57]. By controlling the heat treatment time and temperature the TTs can be changed over a range of 120˚C within the same alloy. Depending on the volume fraction, size and morphology of precipitates, they ca either suppress TTs because of 'size effect' phenomenon, in which as the precipitates are too small and the interparticle distance is very less, the austenitic matrix trapped in between the two precipitates cannot transform. A higher undercooling is required in order to reduce the critical radius of martensite nucleation and thus in this fashion the material undergoes the MT, which results in decrease in TTs below the SHTed TTs. When the precipitates grow fairly large and the interparticle distance is increased, the austenitic matrix can transform freely to martensite back and forth. Also, as now the precipitates are fairly apart, the 'size effect' vanishes and the 'compositional effect' emerges as now the TTs increases because of Ni and Hf depletion from the matrix. Therefore, by varying the volume fraction of the H-phase precipitates, the TTs can be tailored very precisely.

As mentioned in the previous chapter (section 5.4) that the thermodynamic phase diagram information can be used to design alloys with required MT characteristics. From Fig. 5.15 it can be seen as the volume fraction of the H-phase precipitates increases, the matrix composition is been modifying accordingly. Therefore, depending on the required TTs, the initial composition of the alloy can be chosen such that after heat treating, the alloy will achieve the matrix composition which will correspond to the required TTs. As the matrix composition and original alloy

composition lie on the same tie line in the ternary phase isotherm, hence after precipitating out a known amount of volume fraction of H-phase precipitate, the required matrix composition can be achieved. This known amount of volume fraction of H-phase precipitates can be estimated from the Fig. 6.6, thus the kinetic study will provide with the required recipe of heat treatment of the alloy. By combining the thermodynamic and kinetic aspects of the H-phase precipitation, choice of initial alloy composition and the heat treatment time and temperature can be chosen to acquire required transformation temperatures. By using this approach, a wide variety of NiTiHf HTSMAs can be designed to meet the required TTs.

6.5 Summary

From the above study the results are summarized as follows:

(1) The DSC results indicate that the TTs tend to increase after the precipitation of H-phase via short term aging heat treatments. Along with increase in TTs, the aging heat treatments also enhances the thermal stability of the material and reduces the thermal hysteresis. The TEM images show the uniform distribution of H-phase precipitates after heat treating the sample at 550˚C for 10 hours with average length of 16.6 ± 3 nm and thickness of 8.67 ± 1.27 nm.

(2) The SAXS experiments show a continuous increase in scattering intensity at all length scales, indicate that the Ni-Ti-Hf system is evolving continuously. The H-phase precipitates are formed and with increase in heat treatment time, the precipitation occurs continuously.

(3) The rate of increase of scattering intensity with experiment time, suggests that the precipitation kinetics is very high initially and after certain time, the precipitation occurs at a much steady rate.

(4) From the XRD two dimensional data, it is also seen that the intensity of the characteristic peaks of the H-phase precipitates (131) and (248) increases continuously with increasing time.

(5) After analyzing the SAXS data, the evolution of H-phase precipitates with increasing time was revealed. It can be seen that initially the kinetics of the H-phase precipitates increasing rapidly with increase in time, followed by a much steady state precipitation kinetics.

CHAPTER VII

A STATISTICAL MACHINE LEARNING APPROACH FOR DISCOVERY OF NOVEL Ni-Ti-Hf HIGH TEMPERATURE SHAPE MEMORY ALLOYS WITH REQUIRED MARTENSITIC TRANSFORMATION CHARACTERISTICS

This chapter demonstrates a framework that can be implemented to accelerate the discovery of novel materials with required material properties. In this study the machine learning based framework is used to design a NiTiHf HTSMA with an M_s temperature in between 200°C to 300°C with a minimum value of thermal hysteresis. It is a universal approach and can be extended to any material system and can be used to optimize or achieve any targeted material property value. In order to implement the machine learning based adaptive framework, a reliable and accurate initial dataset is needed. Using this dataset, the required properties can be pin-pointed with a high accuracy. In the following sections, a brief introduction is given regarding the importance of reliable dataset, followed by a detailed explanation of the iterative machine learning implemented and lastly the results obtained by implementing the framework.

7.1. Initial Dataset

In order to understand the material system and implement reliable machine learning approaches for designing novel alloys, an initial accurate and reliable dataset is needed in order to minimize the total effort involved in exploring the materials design space. Such an accurate diversified dataset was not available for NiTiHf system as the compositional space has not been explored extensively. Early studies performed by Abu Jodam et al [158], Angst et al [45] and Thoma et al [47] explored a very limited composition space mostly focusing on Ni-lean (Ni < 50

at.%) systems. Those studies found that Ni-lean systems possessed high transformation temperatures, but also exhibited high thermal hysteresis and poor thermal and dimensional stability [4, 100]. On the other hand, Ni-rich compositions show lower transformation temperature but displayed high strength, thermal and dimensional stability [42, 58, 70]. Ni-rich compositions also display excellent H-phase precipitation kinetics compared to their Ni-lean counterparts [53, 109]. H-phase precipitates tend to strengthen the material, lower the thermal hysteresis and enhance the cyclic stability and fatigue life further [41, 42, 57, 111]. Despite the fact that it has been shown to have promising transformation characteristics, the Ni-rich NiTiHf compositional space has not been extensively explored, until recently. Very few selected compositions such as $Ni_{50.3}Ti_{29.7}Hf_{20}$, $Ni_{50.3}Ti_{34.3}Hf_{15}$, $Ni_{50}Ti_{30}Hf_{20}$ have been investigated, but not enough literature data is available to generate a reliable dataset to implement the machine learning-based alloy design framework. Fig. 1 shows the variation of thermal hysteresis A_f-M_s vs the M_s temperature for all SHT NiTiHf alloys reported in literature, so far. The red circles indicated the literature reported transformation temperature data for all SHT Ni_xTiHf_y alloys reported in literature. It can be seen that most of the red circles lie between M_s temperature values of 0°C to 220°C, indicating that a very limited compositional space of these alloys has been explored.

Moreover, the limited literature data at our disposal has discrepancies, as the actual composition of the material tends to be far from the targeted or nominal composition due to oxidation, carbide formation and partial evaporation losses during melting process. Also, for the same nominal composition and processing conditions, the literature-reported values of transformation temperatures vary over a very large range. For example, the blue markers in Fig. 1 shows the variation of thermal hysteresis A_f-M_s vs M_s temperature for SHT $Ni_{50.3}Ti_{29.7}Hf_{20}$ alloy

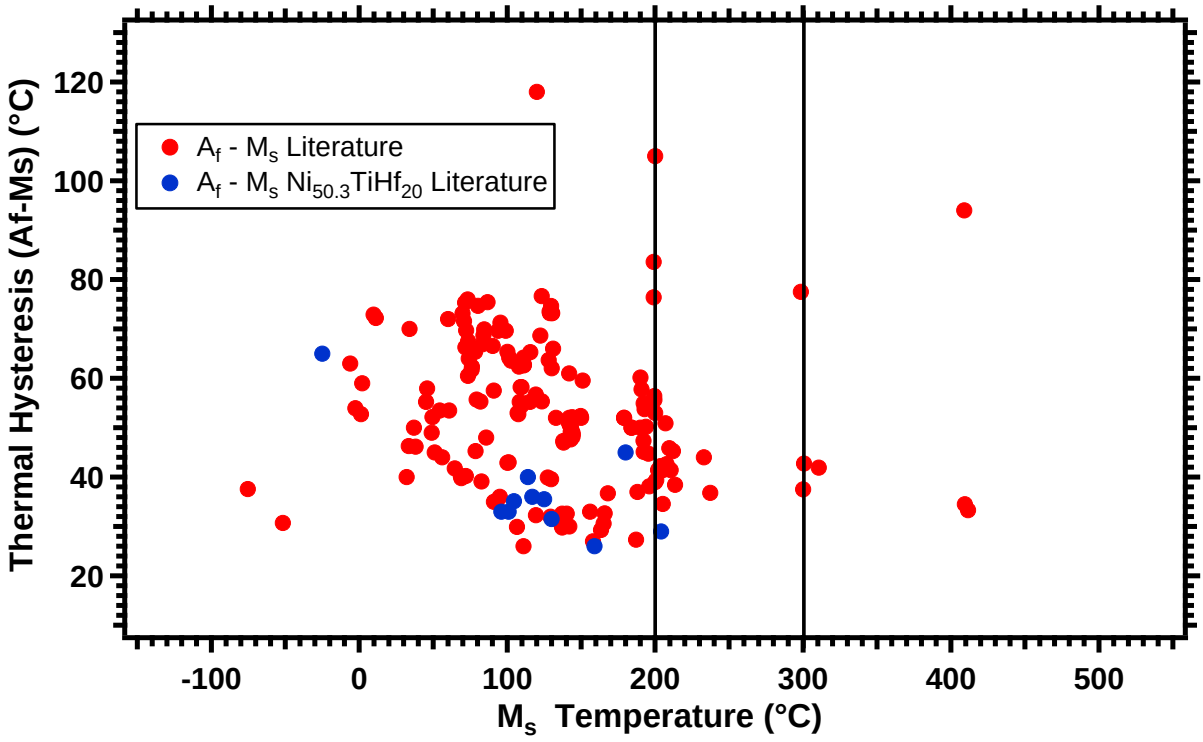

Figure 7.1 Literature data available for solution heat treated material for various NiTiHf compositions. Plot shows variation of thermal hysteresis A_f-M_s (°C) versus the M_s temperature (°C) as red markers. The blue markers indicate variation of thermal hysteresis A_f-M_s (°C) versus the M_s temperature (°C) for $Ni_{50.3}Ti_{29.7}Hf_{20}$ alone, which shows huge variation in M_s temperature (>225°C) for the nominal composition. [35, 41, 42, 45-47, 49, 53, 57-60, 69, 99, 109, 112, 123, 124, 136, 184-204].

only. It can be seen from Fig. 1 that for the same reported nominal composition of $Ni_{50.3}Ti_{29.7}Hf_{20}$ in SHT condition, the M_s temperature can vary from -25°C to 204°C. If a data point with such high discrepancies were to be used as an input for the alloy designing models using machine learning, it would incorporate a very high amount of error in the predictions. As seen from Fig. 1, there are very fewer data-points, with M_s values between 200°C to 300°C and above. Hence, a model trained on the data-points that have high variation, may be biased and not robust.

In order to get rid of all these discrepancies, we constructed our own dataset by systematically exploring the entire transforming regime in the NiTiHf alloy system, with Ni

ranging from 49.8 at.% to 51.5 at.% and Hf ranging from 0 at.% to 30 at.% [176]. More than 42 different Ni_xTiHf_y alloy compositions were fabricated and their transformation temperatures were measured in order to generate the reliable database. We would like to note that while 42 alloys may seem to be a large number already, the exceedingly large sensitivity of SMAs to composition render even this relatively large dataset essentially sparse: minute changes in alloying additions can result in extremely large changes in both transformation temperatures and hysteresis.

Similar processing was performed on all the samples, in order to avoid discrepancies arising from microstructure and heat treatment. Compositional analysis on all the alloys was performed using the EPMA equipment with mean atomic corrections for more accurate quantification. Fig. 2 shows the TTs data obtained from our work as green dots, along with literature reported data from Fig. 1. The spread of our data encompasses M_s values ranging from -125°C to 520°C. It is evident from Fig. 2 that data generated in the present work, is more widely spread with homogenous distribution of data points across the transformation regime as compared to that of literature reported data. Therefore, a dataset with such a widespread TTs data, with evenly distributed data points and the actual composition of alloy being extremely close to the targeted value, helps in generating more accurate models for predictions.

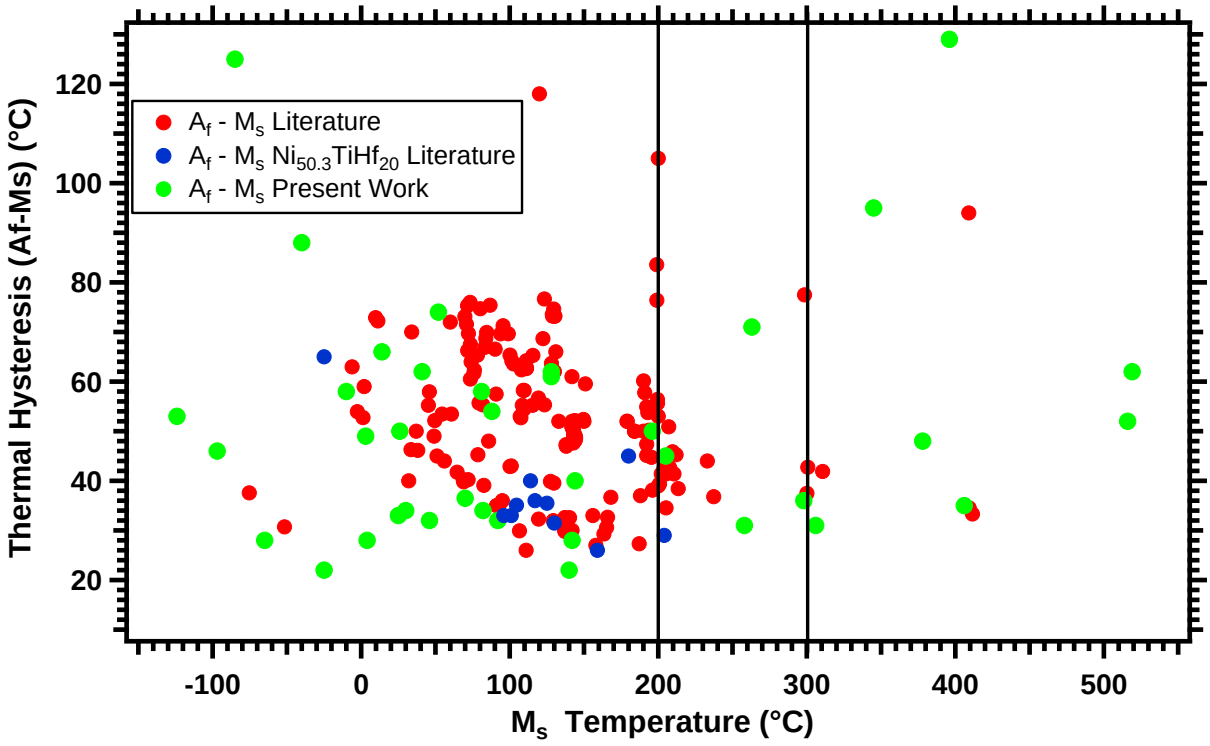

Figure 7.2 Variation of thermal hysteresis A_f-M_s (°C) versus the M_s temperature (°C) for various Ni_xTiHf_y compositions generated in this work as green markers along with the literature available data. The wide spread of the green markers along with extremely low weight loss percentage after melting (<0.1 wt.%) indicate the huge spread and accuracy of the initial dataset, which is more reliable to generate models for alloy design predictions.

7.2 Framework for Alloy Design

Fig. 4 shows the framework implemented, in order to design the new NiTiHf SMA with M_s value in between 200°C to 300°C along with minimum possible hysteresis. As with typical BO/BED frameworks for materials design, our proposed framework works in an iterative fashion. After running all the steps i.e., from step 0 to step 3 as shown in Fig. 4, the new results obtained at the end of the step 3 are included in step 1. This process of finishing execution of step 0 to step 3, for the first time is called as "iteration 1", from here on in the rest of the manuscript. Now this newly obtained result at the end of iteration 1 will be added to the initial dataset (that was generated from step 1), and step 2 to step 4 will be executed again. The process of running step 1 to step 3

with the modified dataset (initial dataset + iteration 1 results) will now be identified as iteration 2, and so on. This iteration loop will be executed in a repetitive fashion until saturation of the results (i.e., we are not being able to minimize the value of hysteresis any further while still keeping the M_s value in between 200°C and 300°C) is achieved or we started diverging from the optimal results (i.e., we minimize hysteresis with initial consecutive number of iterations and then start increasing hysteresis with further iterations, still keeping the M_s value in between 200°C and 300°C). Once one of the above conditions are met, the iteration loop is terminated, and we can conclude that the given experimental design problem is optimized in this sequential manner. In the following section, each of these steps mentioned in Fig. 4 are explained in detail.

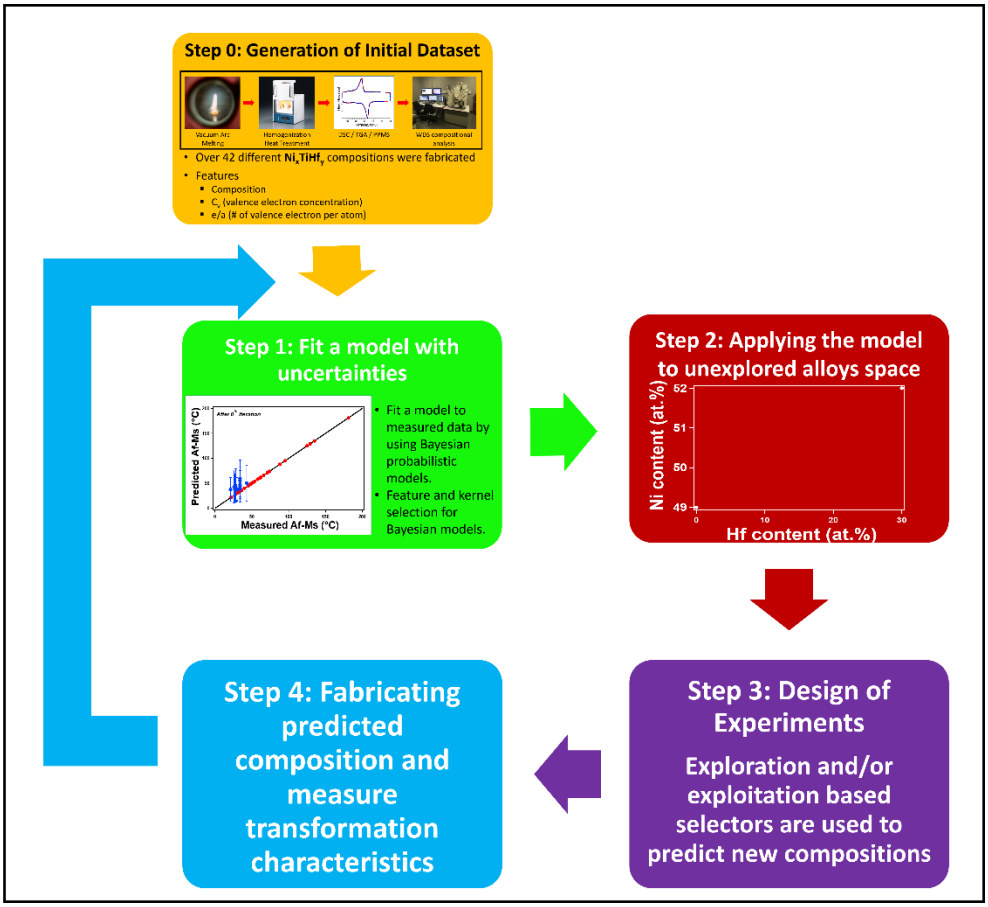

Figure 7.3 The iterative Bayesian experimental design framework for alloy designing. In step 0, the initial dataset with more than 42 different compositions of Ni_xTiHf_y were fabricated using vacuum arc melting, followed by solution heat treatment, DSC/ TGA/ PPMS measurements and WDS compositional analysis. In Step 1, the data generated in step 0 is utilized to train a model with some uncertainties, using some data points and then testing the model with the remaining data points. Then in step 2 the models are applied to the unexplored alloy design space and based on required objective functions, in step 3 different selectors are used to predict the next composition. Different selectors tend to offer different proportion of trade-off between exploration and exploitation within the alloy design space to make their predictions. In step 4 the predicted alloy composition is fabricated using procedure mentioned in step 0. Then the newly generated data is added to the initial data and Step 1, 2, 3 and 4 are repeated until we have achieved our required objective functions.

7.2.1 Step 0: Generation of Initial Dataset

We generated more than 42 NiTiHf alloys with Ni content varying from 49.8 at.% to 51.5 at.% and Hf varying from 0 at.% to 30 at.%. The initial weight of individual Ni, Ti and Hf elements

was recorded accurate up to 4 decimal places in grams, depending on individual alloy compositions. As the weight loss for all alloys used was less than 0.1 wt.%, the maximum expected variation from the nominal composition was estimated to be less than 0.02 at.%, which in turn makes the present dataset considerably more reliable than the data available from the literature.

After considering only those alloys with weight loss of <0.1 wt.%, these alloys were wrapped in Ta foil and sealed in quartz tube under high purity Ar atmosphere. These alloys were then SHT at 1050°C for 2 hours followed by water quenching. DSC samples were cut from them and tested for TTs. Another piece of SHT sample, was subjected to electron microscopy and EPMA analysis. Results obtained from EPMA analysis also depict that the measured compositions of almost all alloys are very close to their respective nominal composition. The TTs and compositional data obtained from above steps in order to generate the initial dataset is shown in Fig. 4. Fig. 4a shows the variation of M_s temperature with respect to measured Ni content for a fixed amount of Hf content. It can be seen that as the measured composition increases above 50 at.%, the M_s temperature starts to decrease rapidly. Fig. 4b shows the variation of thermal hysteresis A_f-M_s with respect to Ni content for fixed amount of Hf contents. The numerical data is given in Table 6.1. For Hf=0 at.% it can be seen that the hysteresis tends to decrease with increasing Ni content. For all Hf > 0 at.% except for Hf = 30 at.%, the general trend is that hysteresis either doesn't change much at all or starts to increase after a certain Ni content. Whereas for Hf=30 at.%, the hysteresis tends to increase drastically with increasing measured Ni content of up to 50.8 at.% followed by drastic decrease up to 51.6 at.%. Similar plots can be generated for M_s temperature and thermal hysteresis Vs measured Hf content for a fixed amount of Ni contents. But as the measured Hf content is so close to the nominal composition and the standard deviation on measurements is so low, that the plots

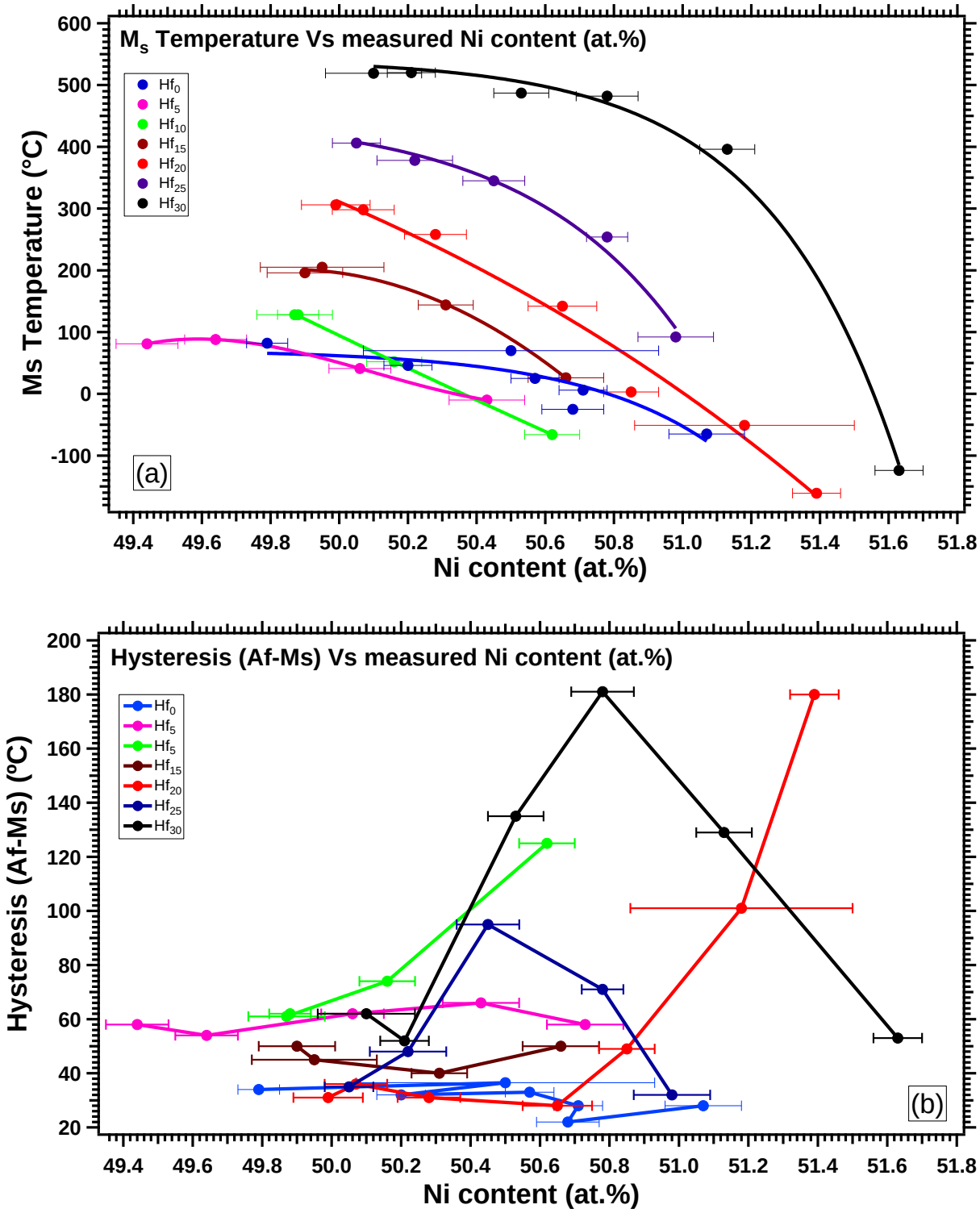

Figure 7.4 (a) Ms Vs measured composition and (b) Thermal Hysteresis (Af-Ms) Vs Hf content for respective different Ni contents, which is used as the input to the model generated in step 1 of Fig. 3.

Nominal Composition			Measured Composition			Transformation temperatures	
Ni	Ti	Hf	Ni	Ti	Hf	Ms	Af-Ms
49.8	50.2	0	49.79±0.06	50.21±0.06	-	82	34
49.8	45.2	5	49.44±0.09	45.55±0.1	5.01±0.07	81	58
49.8	40.2	10	49.88±0.06	40.03±0.16	10.09±0.14	128	62
49.8	35.2	15	49.9±0.11	29.97±0.1	15.1±0.21	196	50
49.8	30.2	20	49.99±0.1	29.97±0.1	20.04±0.07	306	31
49.8	25.2	25	50.05±0.07	24.9±0.05	25.06±0.08	406	35
49.8	20.2	30	50.1±0.14	19.92±0.37	29.99±0.45	519	62
50	50	0	50.5±0.43	49.5±0.43	-	70	36.5
50	45	5	49.64±0.09	45.39±0.09	4.98±0.06	88	54
50	40	10	49.87±0.11	40.12±0.15	10.01±0.12	128	61
50	35	15	49.95±0.18	34.81±0.15	15.24±0.2	205	45
50	30	20	50.07±0.09	29.75±0.19	20.18±0.2	298	36
50	25	25	50.22±0.11	24.83±0.09	24.95±0.1	378	48
50	20	30	50.16±0.07	19.99±0.1	29.84±0.12	516	52
50.3	49.7	0	50.2±0.07	49.8±0.07	-	46	32
50.3	44.7	5	50.06±0.09	44.92±0.1	5.03±0.06	41	62
50.3	39.7	10	50.16±0.08	39.83±0.08	10.01±0.04	52	74
50.3	34.7	15	50.31±0.08	34.61±0.08	15.08±0.06	144	40
50.3	29.7	20	50.28±0.09	29.66±0.2	20.07±0.21	258	31
50.3	24.7	25	50.45±0.09	24.47±0.12	25.07±0.15	345	95
50.3	19.7	30	50.53±0.08	19.01±1	30.46±1.02	487	135
50.4	44.6	5	50.19±0.06	44.79±0.07	5.02±0.05	14	66
50.5	49.5	0	50.57±0.07	49.43±0.07	-	25	33
50.7	49.3	0	50.71±0.07	49.29±0.07	-	4	28
50.7	44.3	5	50.43±0.11	44.6±0.13	4.98±0.06	-10	58
50.7	39.3	10	50.62±0.08	39.37±0.08	10.01±0.07	-85	125
50.7	34.3	15	50.66±0.11	34.31±0.11	15.03±0.06	26	50
50.7	29.3	20	50.65±0.1	29.31±0.16	20.04±0.19	142	28
50.7	24.3	25	50.78±0.06	24.25±0.09	24.98±0.1	263	71
50.7	19.3	30	50.78±0.09	19.23±0.09	29.99±0.1	439	181
51	49	0	50.68±0.09	49.32±0.09	-	-25	22
51	47.5	1.5	50.92±0.08	47.78±.23	1.31±0.19	-97	46
51	44	5	50.73±0.11	44.1±0.09	5.17±0.06	-	-
51	39	10	50.79±0.09	39.21±0.08	10.01±0.05	-	-
51	34	15	50.83±0.09	34.1±0.1	15.07±0.09	-	-
51	29	20	50.85±0.08	29.07±0.06	20.08±0.09	3	49
51	24	25	50.98±0.11	23.9±0.09	25.12±0.1	92	32

Table 7.1 continued…

Nominal Composition			Measured Composition			Transformation temperatures	
Ni	Ti	Hf	Ni	Ti	Hf	Ms	Af-Ms
51	19	30	51.13±0.08	18.79±0.22	30.08±0.25	396	129
51.1	48.9	0	51.07±0.11	48.93±0.11	-	-65	28
51.2	18.8	30				140	22
51.3	18.7	30	51.59±0.07	18.43±0.08	29.99±0.11	-124	53

Table 7.1 Initial reliable dataset generated in step 0 of Fig. 3.

look exactly like the ones from our previous work [176]. Data plotted in Fig 3a & Fig. 3b was then used as an input data to generate a prediction model. This step of generation of reliable data is named as "Step 0" in the iterative design framework as shown in Fig. 4.

In addition to acquiring the initial data necessary to inform the ML models used in BO/BED-based materials design, it is also important to determine the features that should be used as input parameters to the framework. Features can be any chemical or physical parameters associated with the alloy system such as atomic composition, valence electron ratio, electronegativity, atomic radius, ionic radius, melting point, Mendeleev number etc. Xue et al [145] used a Pearson correlation map to find out correlation coefficients between different features and selected those features which are not correlated with each other. Correlated features tend to add the same information to the model and hence using highly correlated features not only makes the model more complex but also provides little new knowledge to the model. Zarinejad et al [113, 166] showed that the TTs are highly correlated with the valence electron number (C_v) and number of valence electrons per atom (e/a). Equations 1 and 2 show the empirical formula to calculate C_v and e/a ratio, where f^{Ni}, f^{Ti}, f^{Hf} represent the atomic fraction of Ni, Ti and Hf present, respectively, whereas e_v^{Ni}, e_v^{Ti}, e_v^{Hf} represent the valence electrons and e_v^{Ni}, e_v^{Ti}, e_v^{Hf} represent the total electrons present in Ni, Ti and Hf atoms, respectively.

$$C_v = \frac{\#\ of\ valence\ electrons}{\#\ of\ total\ electrons} = \frac{f^{Ni}e_v^{Ni} + f^{Ti}e_v^{Ti} + f^{Hf}e_v^{Hf}}{f^{Ni}e_t^{Ni} + f^{Ti}e_t^{Ti} + f^{Hf}e_t^{Hf}}$$

$$e/a = f^{Ni}e_v^{Ni} + f^{Ti}e_v^{Ti} + f^{Hf}e_v^{Hf}$$

In the present study as only the solution heat treated samples are considered as inputs in the framework, we choose only compositional features in order to describe the system. For the Bayesian framework implemented in this work, we chose the EPMA measured Ni at.%, Ti at.%, Hf at.%, C_v and e/a ratio as our features.

7.2.2 Step1: Fitting a model with uncertainties

Once we have defined the features or input parameters, we can use them to build a model for making predictions. As described above, a model relates the property as a function of input parameters, which can be used to make predictions for the rest of the un-explored input parameter space. In our case, we have defined $M_s = g$(Ni, Ti, Hf, Cv, e/a) and also Hysteresis A_f-$M_s = f$(Ni, Ti, Hf, Cv, e/a). We model Ms and Af-Ms with nonparametric statistical approaches, namely Gaussian process regression (GPR). Nonparametric approaches rely on fewer assumptions than parametric models and are usually more robust, provided their underlying assumptions hold. More details about the models are provided in Section 6. Here, we describe some properties of these models.

The assumption for GPR is that the property being modeled is relatively smooth and continuous. In other words, the more similar the features (composition, C_v, …) of two alloys are, the closer their properties should be. Also, we know from experiments that both Ms and Af-Ms

are continuous, at least over a non-negligible composition range. Thus, the assumptions of GPR are valid here. Given the observed data, GPR predicts a Gaussian distribution for Ms and Af-Ms for each possible compound, which is characterized by a (posterior) mean and a standard deviation. The standard deviation quantifies the uncertainty corresponding to the prediction. Since GPR belongs to the class of kernel-based models—i.e. models based on a similarity measure in a dot product space—we do not need to directly include higher order degree terms of primary features. Recalling from the objective of the study, we want to find an alloy with Ms temperature between 200°C and 300°C, along with minimum thermal hysteresis. Since the surrogate model is not 100% accurate, in order to guide an efficient exploration of the compositional space to reach the goal, the quality of the predicted uncertainty from the models is as important as the (mean) prediction itself. In order to prevent the models from overfitting the observed data and limiting their predictive capacity, we consider additive Gaussian noise in our models. Intuitively, the models are more certain in neighborhoods of the already observed data in the feature space. In other words, the predicted uncertainty is lower the closer the features are to the features of previously measured compounds.

The choice of the features and kernel function for GPR specifies the properties of the models (more explanation about the kernels are included in Section 6). Choosing the features and kernel corresponds to the model selection in GPR. Generally, there are two main approaches for model selection. In the first approach, the observed data are split into training and validation sets, possibly multiple times, where the training set is larger than the validation set. Different models (here, GPR models with different features and kernels) use only the training set to make predictions for the validation set. The model (feature set and kernel) with the highest likelihood on the validation set is picked and trained using all the observed data to later make predictions for the

whole compositional space. Although this approach to model selection is commonly used, it is not applicable in cases with very small samples sizes, such as our case, due to high variation in the estimate of the likelihood because of the very small validation set size. The second approach is Bayesian model selection that translates to using a metric that considers both the likelihood (data fitting term) and also a penalty term for increasing the complexity of the model and using all the observed data for model (features and kernel) selection. Using all the available data can be very helpful when the sample size is small. The penalty term discourages more complex models that only slightly improve the likelihood to avoid overfitting and improve model generalizability. Here, we employ Bayesian information criterion (BIC) for selecting the kernels for the GPR models. BIC of model M is equal to $BIC(M) = -2L(M) + k(M)\log n$, where $L(M)$ is the likelihood of the model (the lower the error of the predictions of the model is, the higher the likelihood is), $k(M)$ is the number of the parameters of the model and n is the number of data points.

To further validate the suitability of our models, we have provided true measured Hysteresis vs predicted Hysteresis by the selected model for our data in Fig. 7 and 8. The closer the points are to the diagonal line, the better the model predictions are. The error bars indicate the 95% confidence interval of the predictions., i.e. the range with 95% predicted probability to contain the true values. In Fig. 8, we show how the predictions of the model evolve for all the initial plus iterations data using only initial data for training, and then adding each iterations data to the training set. In Fig. 9, the same progression is shown for only the iterations data. At each iteration, the selected models are trained on all the available data (up to that iteration) to be used for prediction on the rest of the compositional space in the next step.

7.2.3 Step 2: Applying the model to unexplored composition space

The model created in the step 4.2, will now be applied to all the compositional space of interest in order to make predictions of transformation temperatures and thermal hysteresis. We created a pseudo compositional space with Ni varying from 49 at.% to 52 at.% with a step size of 0.1 at.% increment and Hf varying from 0 at.% to 35 at.% with an increment of 0.05 at.%, the remaining was balanced by Ti. We used this range of compositions in our search space because in the Ti rich alloys the TTs dependence on composition is negligible and they also suffer from poor thermal and dimensional stability and hence their use in practical applications as HTSMA is insignificant [4]. Also, from our initial dataset it was also evident that for any composition with Ni>52at.% and Hf content up to 30 at.%, no martensitic transformation was observed upto -260°C. Using the above-mentioned composition range and step size, we created a pseudo compositional space of ~20000 potential alloys that were then subject to the selection procedure described below.

7.2.4 Step 3: Selection of composition to be melted from pseudo composition space

At this point, once the prediction for the ~20000 alloys is made, it is crucial to choose the correct compositions to be fabricated, such that TTs information obtained from them will give the targeted transformation properties or lead us in the direction of discovering the alloy with desired transformation properties. Since the entire exercise of implementing the BED framework is to obtain the target properties in minimum number of attempts, it will be pointless to randomly choose alloys for next iteration and hence specialized algorithms are used to choose the next candidate alloys to melted, which will either hit the target values of transformation temperatures or add the maximum information to the model so that its prediction power for further iterations is enhanced. An algorithm which will choose only those compositions which are predicted to satisfy the objective function based on the current model are called “pure exploitation selectors”. While using

a pure exploitation-based selector, it is possible that the model can get stuck in local minima or maxima and hence we will not be able to achieve a substantial improvement in the targeted properties, especially when the prediction uncertainty is large. On the other hand, if we choose a model which will only choose those compositions that help us make the future predictions better by reducing the uncertainties or inaccuracies in the model, then such algorithms are called "pure exploration selectors". Such pure exploration-based selectors are only useful to enhance the predictive power of the model, but would not necessarily be useful to identify potential compositions with optimal properties. In order to make the predictions help us achieve our target values of TTs, we implemented selector algorithms which provide a trade-off between exploration and exploitation, leveraging the knowledge gained from existing data while at the same time seeking to leverage (and reduce) the uncertainty in the model predictions for regions yet to be explored experimentally.

The acquisition function in the selector algorithm has to perform a dual function here: First, it has to guide the search towards alloy compositions with 200°C<M_s<300°C, that is, constrain its search of alloys to given desired M_s value. Secondly, it has to direct the search to minimize the thermal hysteresis A_f-M_s as much as possible. Hence, it also has to find a global minimum for the A_f-M_s value in the given space. Therefore, our problem can be considered as a constrained BO or BED. Specifically, it is a multi-objective BO or BED, where one objective is constraint satisfaction—to the best of our knowledge, no work has tackled this problem before in the context of materials discovery and/or design.

By leveraging the probabilistic modeling and the predictions based on it for the compositional space, we write the objective function as:

$$min_{x \in X}\left[\left(A_f - M_s\right)\left(1 - \mathrm{P}(200 < M_s < 300)\right)\right]$$

which encourages both constraint satisfaction and minimization of the hysteresis. Here, P denotes probability. In other words, the designed objective function is lower when the hysteresis is smaller and the probability of satisfying the constraint is larger. Although writing the objective function in this way is intuitive, we provide a mathematical justification in Section 6.

This constraint in the optimization introduces computational challenges in the selector step of the experiment design, and makes direct application of well-known algorithms, widely used in the materials community, like EGO (using EI) and KG impossible. In this work we developed an entirely new set of acquisition functions based on MOCU and show the connection with existing methods based on EI for the constrained optimization with GPR models.

The mathematical details are provided in Section 6, but here we briefly summarize the idea of each method in selecting the next experiment. The EI score as the name suggests, gives information about the expected improvement in the objective, i.e. expected difference between the previously observed lowest hysteresis among the alloys satisfying the constraint and the hysteresis of the potential next alloy that is expected to satisfy the constraint with high probability. A MOCU-based acquisition function, on the other hand, quantifies the expected reduction in the objective cost of uncertainty considering the information that can be achieved if the potential next alloy composition is added to the current dataset and the model is updated accordingly. The objective cost of uncertainty for our problem is the lowest expected hysteresis among the alloys that have higher probability of satisfying the constraints. In Section 6 we show that under the assumption that at each iteration, if we stop the experiment design loop, the final solution can only be chosen from the set of previously observed alloys, a MOCU-based acquisition function reduces to the

constrained EI. Compositions that reflect the maximum acquisition function (selector scores) are chosen to be fabricated.

The concept of exploration, exploitation and EI will be demonstrated with a toy example in Section 5 in order to explain the concepts better. By using such trade-off-based selectors, we were able to explore and exploit the composition space simultaneously with each iteration and therefore achieved our targeted TTs with very few numbers of iterative experiments.

7.2.5 Step 4: Fabrication of predicted compositions

The final step includes to actually manufacture the predicted compositions, solution heat treat them and characterize them to obtain transformation temperatures. The procedure followed to fabricate and process the newly melted iteration compositions is exactly the same as that conducted to obtain the initial dataset and hence no bias error from manufacturing, processing and characterization is affecting the TTs data obtained from the iteration compositions. The data obtained from the iteration compositions is added to the initial dataset and step 1 through step 4 in the framework is executed again. Such an iterative Bayesian framework was executed with newly obtained results from respective iterations.

7.3 Toy Example to demonstrate the Bayesian Framework

In order to demonstrate the functionality of the above-mentioned framework, we have chosen a simple function $y = x.\sin(x)$, our objective being to find a maximum value of this function within the limits of x ranging from 0 to 10. So, the example demonstrated here is similar to the original SMA objective of this paper, but without any constraints on a function of x. This helps to simplify the toy example presentation. In the example problem, we want to find a

maximum for the $y = x \cdot \sin(x)$ function and in our original SMA objective we want to find a minimum of thermal hysteresis (A_f-M_s). In the example problem, we restrict our search space within $0 \leq x \leq 10$ and in our original SMA objective we have constrained the compositions within pre-specified ranges. The difference between these two scenarios is that in the example problem, there is no

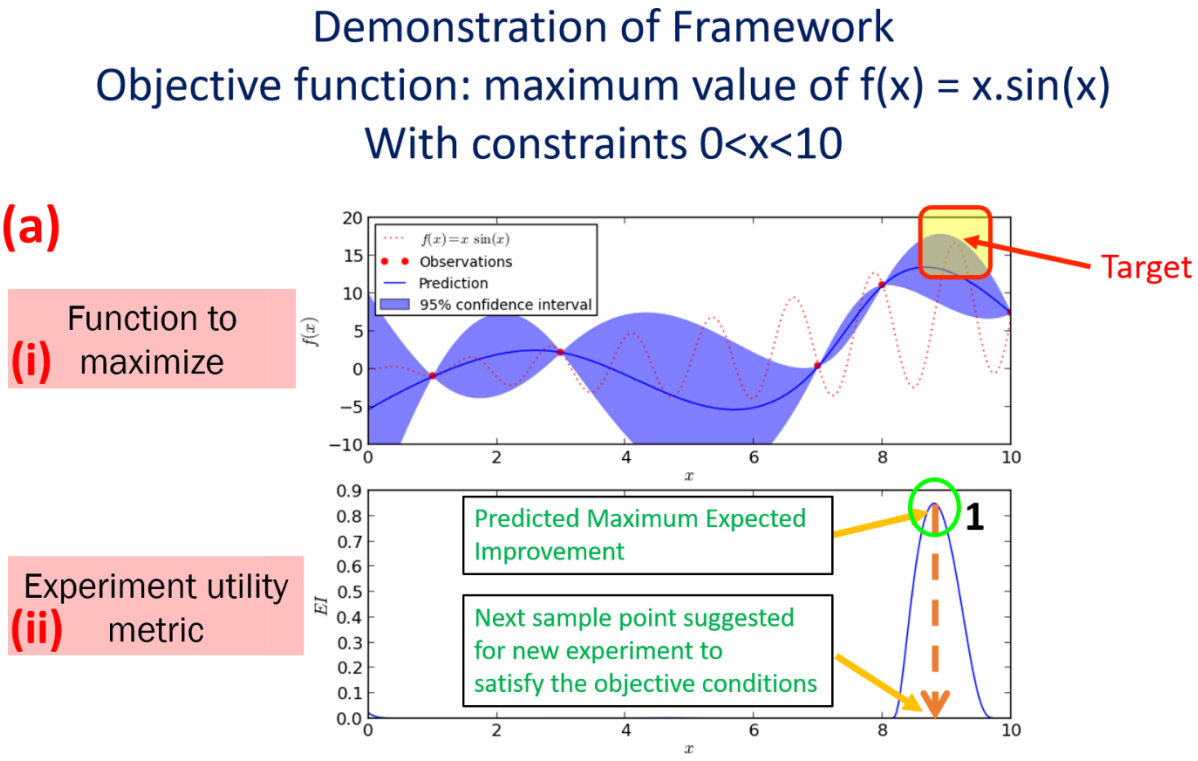

(b)

(i) Function to maximize

(ii) Experiment utility metric

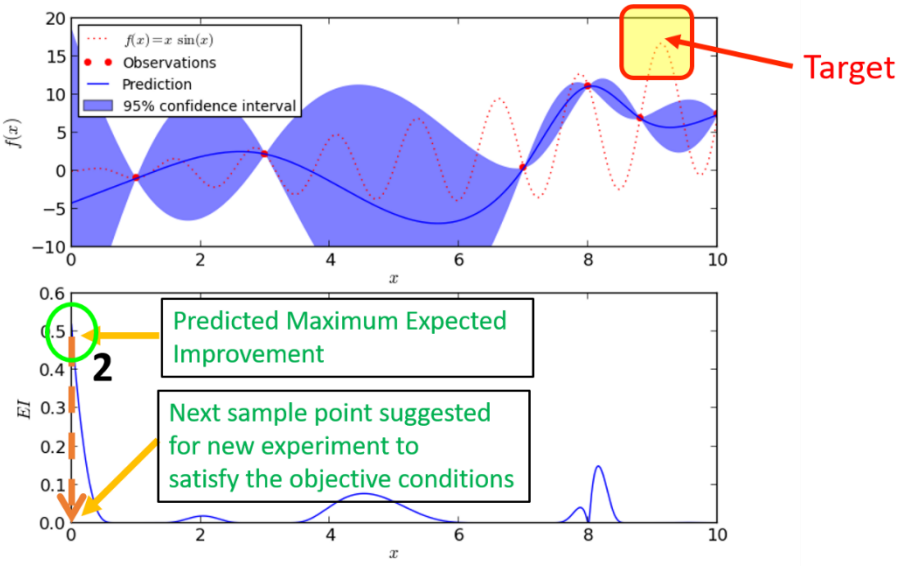

(c)

(i) Function to maximize

(ii) Experiment utility metric

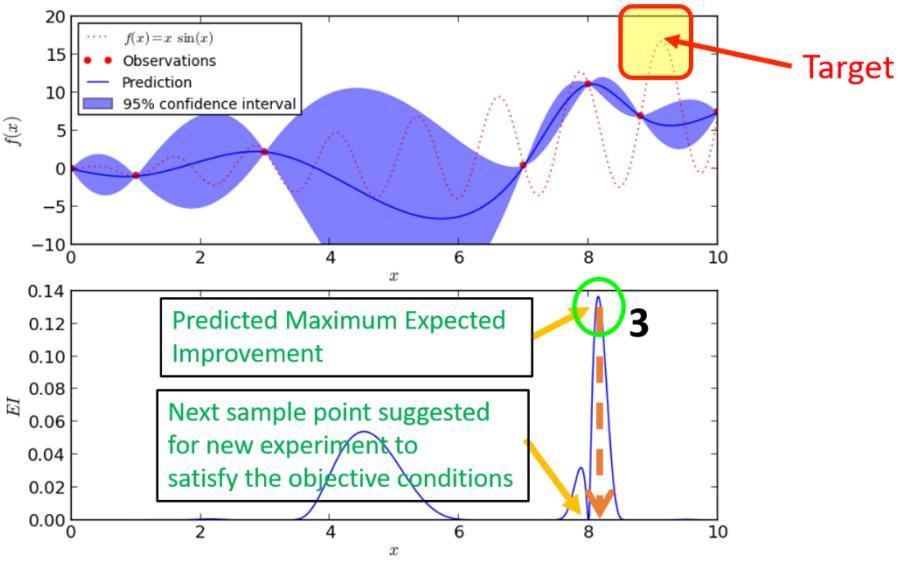

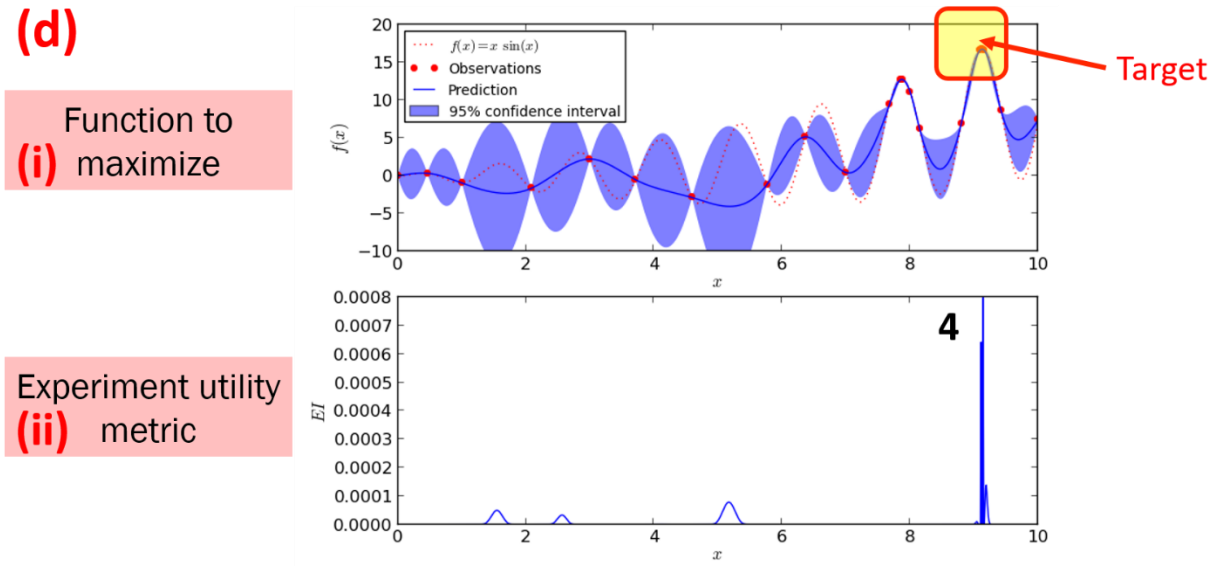

Figure 7.5 Schematics above displays a demonstration of implementation of the framework shown in Fig. 5, where (a-(i)) shows the *f(x)* Vs x plot with 5 initial data-points as red circles, which can be considered as the initial reliable dataset as shown in Step 0 of Fig. 5. The dotted curve shows the actual *f*(x) response which is unknown, and the target is to find the maximum of this *f*(x) which is highlighted by the yellow box, within an interval of 0≤x≤10. The blue solid curve fitted to the initial data-points, is the model used to make the predictions. The purple shaded region depicts the 95% confidence interval for the predictions made using the current model. (a-(ii)) shows the experiment utility metric with expected improvement (EI) corresponding the model in a-(i) on Y-axis and the variable 'x' on the x-axis. The EI is an indicator of choosing the next experiment to be conducted, in order to make highest improvement in the present model. Based on EI value, the next suggested experiment should be conducted at x≈8.7 in order to achieve the maximum improvement in the model. After conducting the experiment at x=8.7 (as suggested in step 3 of Fig.5), results from this experiment (which is referenced as 1st iteration) is used with initial dataset and a new model is generated as shown in b-(i). The corresponding EI is shown in b-(ii), and the next suggested experiment is suggested to be conducted at x=0. Results obtained from conducting experiments at x=0 (referenced as results from 2nd iteration) was used along with initial dataset and results from 1st iteration to generate new model shown in 6c-(i), with the corresponding EI in 6c-(ii). After conducting certain number of iterations and consecutively updating the model after every iteration the targeted value is achieved in 6d-(i) with the corresponding EI in 6d-(ii).

additional constraint on a function of x, and the equation $(y = x \cdot \sin(x))$ is much simpler and requires little computational power, but on the other hand in our actual SMA problem, there is a constraint on a target property which is a function of the features, and the feature set is vast and

requires heavy computational power. Nevertheless, the general idea of the approach can be demonstrated more simplistically here.

Given few reliable initial data-points, we can use the BO framework to make initial predictions (with the corresponding uncertainties) and find candidates suitable to satisfy the required criteria or candidates which provide the most information about finding suitable candidates for our goal. Suppose we have only 5 starting data-points, shown by red circles in Fig. 5a. The plot on the top in Fig. 5a (labelled as (i), which will be referred to as Fig. 5a-(i)) shows the value of variable 'x' on the x-axis and the corresponding functional value $f(x) = x \cdot \sin(x)$ on the y-axis. The red dotted line is the actual function $y = x \cdot \sin(x)$ which is not known. The only prior knowledge we have is the 5 data-points shown in red color. With the help of these 5 initial data points we explore this system from $0 \leq x \leq 10$ and find out the maximum value of $f(x)$ as marked by the yellow box and labelled as 'target' in Fig. 5a-(i). Using the initial 5 data points we fit a curve, shown by the blue solid line in Fig. 5a-(i). The equation of the fitted curve will now serve as a model to make predictions, as annotated in Fig. 5a-(i). When we utilize this equation to make predictions, there is some degree of uncertainty, or error, associated with the predictions. This error is higher in areas where the model has no or little knowledge about the nature of the data. Hence, the constructed model for making predictions provides a 'confidence interval' indicating belief about the accuracy of prediction by the current model with varying x, as shown by the blue shaded region in Fig. 5a-(i). The number associated with the confidence interval indicates the probability of the prediction lying in the blue shaded region. In Fig. 5a-(i), there is a probability of 95% that predictions made from the current model will lie in the shaded blue region. The closer to the actual data-point from initial reliable dataset, the less uncertainty, and the model can predict with 95% confidence in a narrow range, and vice versa for points far from the initial dataset. For example,

as seen from Fig. 5a-(i), at x=3 or x=7, where we have initial reliable data-points, the prediction uncertainty is low depicted by a narrow shaded blue region. On the other hand, at about x=5 we do not have any initial data-point and hence the uncertainty and error in prediction at x=5 are large comparatively, as shown by a wide spread of blue shaded region.

Based on the implemented model, which is the blue solid curve in Fig 5a-(i), we can get predictions for all the remaining values of x, for which the value of response $f(x)$ is not known. From these predicted values of y, we have to choose a value of x for which we will conduct an experiment. We can select a different value of x, for which the experiment is to be conducted, based on either exploration or exploitation perspectives, or both simultaneously as described in section 4.4. These experiment-selection algorithms are called 'selectors'. For example, the selector algorithms calculate an expected improvement (EI) value based on the present model and suggest the next experiment to make the maximum improvement in the reaching the goal. The bottom plot in Fig. 5a (labelled as (ii), which will is referred as Fig. 5a-(ii)) shows the value of x on the x-axis and the EI on the y-axis. One important thing to note here is that based on different selector algorithms, which might be pure exploration based, pure exploitation based, or serve different trade-off between exploration and exploitation based can either suggest the same or different next experiments to be conducted depending on the model and number of initial data-points. For the sake of demonstration, we have chosen a metric, EI, based on a trade-off between exploration and exploitation, and as seen from Fig. 5a-(ii), the selector suggests conducting the next experiment at $x \approx 8.7$, where the peak in EI occurs as marked by a green circle. As our target is to find the maximum, the selector is suggesting the experiment, where the maximum value of the present model (blue solid curve) is occurring. Although we are using a trade-off-based selector, the suggestions are more inclined towards exploitation than exploration. To an extent, this makes sense

because, if we do not know the maximum value, and based on curve or model fitting we observe a maximum which is not one of the initial data-points (red circles), we will tend to believe that it is the maximum. From here we can have two scenarios: the value of the response for the suggested experiment is either higher or lower than other data-points from the initial dataset. If the value of response is higher, then it suggests that the model predictions are moving in the right direction towards our objective of maximizing and the model will keep exploring this space further. On the other hand, if the value of the response for the suggested experiment is lower than any of the data-points from the initial dataset (which is in our case as shown in Fig. 5b-(i)), then it indicates that the suggested value is definitely not the maximum, but the positive side is we have a new data-point addition to the initial dataset which will help us improve the predictive capabilities of the model.

Now based on selector suggestions, we will conduct an experiment at x=8.7 and obtain the value of response $f(x)$. From Fig. 5b-(i), it can be seen that the value of response $f(x)$ for x=8.7 is lower than other data points in the initial dataset and hence it is not the maximum. This newly generated experimental data will be used along with the initial dataset, and a new model will be constructed for predictions. This entire loop of making predictions, selecting next candidate for experiments and performing experiment to obtain the value of response $f(x)$ is referred to as the 1^{st} iteration. Fig. 5b-(i) shows the new model generated with 95% confidence interval. When the model in Fig. 5b-(i) is used to make predictions and the selector is employed to pick the next experiment to be conducted, based on EI value it is suggested to conduct the next experiment at x=0 as seen from Fig. 5b-(ii). It is evident from Fig. 5b-(i), that the maximum of EI has now shifted to a data-point far from the maximum observed function value among the initial dataset at x=8. This suggests that the selector will try to reduce the uncertainty of the model in that region for

further predictions in the 2nd iteration. That is why the selectors suggest conducting an experiment at x=0 as the uncertainty in this region is high. In the 2nd iteration, the selector is more inclined towards exploration and wants to reduce the uncertainty for further predictions. After conducting the experiment at x=0, the value of response *f*(x) will be obtained and used along with initial dataset and results from 1st iteration to generate a new model.

As shown in Fig. 5c-(i), the uncertainty around x=0 region has reduced drastically, and the newly fitted model tends to show a new maximum around x=8.1. The highest EI can be achieved by conducting an experiment at x=8.1 as seen in Fig. 5c-(ii). Now according to selectors suggestion, a new experiment at x=8.1 will be conducted and the response from this experiment will be used along initial dataset and results from 1st and 2nd iteration to generate a new model. Hence, in such an iterative fashion the Bayesian global optimization framework is implemented and with consecutive certain number of iterations, the global maxima was found and the target was achieved as seen in Fig. 5d-(i). Also, from Fig. 5d-(i), it can be seen that based on the model, the selector has predicted a rather sharp utility peak (sharp peak in EI) at around x= 9.15 which is close to the previously observed points with negligible EI value elsewhere. This is also an indication that the experiment design loop might be saturated and already has found the maximum value, as it is only suggesting conducting experiments at the same value of (or very close to) the initial observations.

Similar to the example in this section, we follow the same general idea, albeit with all the challenging differences mentioned at the outset of this section, to model the NiTiHf SMA system and find out the alloy candidate which has lowest hysteresis, while constraining the Ms value between 200°C to 300°C.

7.4. Framework Implementation and Composition Selection

7.4.1 Regression Models

As mentioned in Section 5, we model Ms and the hysteresis Af-Ms with GPR, with the model selection strategy summarized there. Given the observed dataset, the GPR model predicts a Gaussian distribution for the property of interest for each potential alloy in the compositional space. A GPR is defined by the choice of the mean function $m(\cdot)$, and the kernel function $K(\cdot,\cdot)$. For the mean function, a common choice is the constant function $m(x) = w$. The kernel function characterizes the correlation between two points in the compositional space. Intuitively, the closer they are, the higher the correlation is expected to be. In this work, we consider different automatic relevance determination (ARD) kernels which can automatically determine the relevance of the features to some extent in the fitting step to further help construct better models. Here, we denote an alloy with its corresponding vector of features $x^i = [x_1^i, \dots, x_D^i]$, its output properties as $y^i = [y_1^i, \dots, y_l^i]$, the hyperparameters of the GPR model (hyper-parameters of the mean and kernel functions) as θ.

We include three ARD kernels for model selection, the ARD squared exponential kernel (ARD SE), ARD Matern 3/2, and ARD Matern 5/2. The functional forms of the kernels are provided in the appendix.

Each kernel $K(x^i, x^j|\theta)$ defines the relationship between two alloys (vector of features), i.e. a scalar quantifying the covariance between the output property of x^i and x^j. The SE kernel is more appropriate for approximating functions with higher smoothness. Matern 3/2 has a once differentiable assumption on the function to approximate, and Matern 5/2 has a twice differentiable

assumption. Therefore, considering these kernels in model selection covers a wide range of smoothness assumption over the target property behavior.

We can denote the observed data as $D_{obs} = \{X_o, Y_o\}$, where $X_o = \begin{bmatrix} x_o^1 \\ x_o^2 \\ \dots \\ x_o^n \end{bmatrix}$ and $Y_o = \begin{bmatrix} y_o^1 \\ y_o^2 \\ \dots \\ y_o^n \end{bmatrix}$ are the matrix collections of observed alloys' features and properties, respectively. We use $Y_{o,u}$ to represent the u^{th} column of Y_o, i.e. the vector containing all the u^{th} output properties (e.g. Ms) of the measured alloys. $K(X_o, X_o|\theta)$ is a symmetric matrix, where the ij element is equal to the ji element and contains the covariance of x^i and x^j. Similarly, for the remaining compositional space (test set) we have the features matrix $X_t = \begin{bmatrix} x_t^1 \\ x_t^2 \\ \dots \\ x_t^m \end{bmatrix}$ and the covariance matrix $K(X_t, X_t|\theta)$. $K(x_t^i, X_o|\theta)$ is a vector quantifying the covariance between a test point (an unobserved point in the compositional space) and all the observed points (alloys).

Given the observed data and fixing a model (feature set and kernel function), we fit the GPR model separately for each output property of interest by following the maximum-likelihood (ML-II) estimation, and find the hyper-parameters θ_u for the u^{th} output property by maximizing the marginal log-likelihood of the data as follows:

$$\log \mathrm{P}(D_{obs}|\theta, M) = -\frac{1}{2}\left[Y_{o,u} - m_u(X_o)\right]^T K(X_o, X_o|\theta_\mathrm{u})^{-1}[Y_{o,u} - m_u(X_o)] - \frac{1}{2}|K(X_o, X_o|\theta_\mathrm{u})| - \frac{n}{2}\log 2\pi,$$

where $|\cdot|$ is the matrix determinant and $m_u(\cdot)$ is the mean function for the u^{th} output property. The above optimization is performed by a quasi-Newton method.

After training the GPR, for a point in the compositional space, the predicted distribution of the property of interest y_u^i is Gaussian, $\mathrm{P}\left(y_u^i \middle| x_t^i, M, D_{obs}\right) = N\left(\mu_u\left(x_t^i\right), \sigma_u^2 \quad \left(x_t^i\right)\right)$, with the following mean and variance:

$$\mu_u\left(x_t^i\right) = m_u\left(x_t^i\right) + K\left(x_t^i, X_o \middle| \theta_u\right)^{-1} K(X_o, X_o|\theta_u)^{-1}\left[Y_{o,u} - m_u(X_o)\right]$$

$$\sigma_u^2 \quad \left(x_t^i\right) = \; K\left(x_t^i, x_t^i \middle| \theta_u\right) - K\left(x_t^i, X_o \middle| \theta_u\right) K(X_o, X_o|\theta_u)^{-1} K\left(X_o, x_t^i \middle| \theta_u\right)$$

Note that in the model selection stage described in Section 5, one feature set and kernel function is chosen based on the available data for the downstream analysis.

7.4.2 Selectors

In this section we describe the different selectors used in our approach. Let us assume that the function to optimize is $f(x)$ and the constraint is over $g(x)$. Without loss of generality we consider minimization and find the optimal point in the compositional space: $x^{\mathrm{opt}} = \arg min_{x \in X} f(x)$ subject to $c(g(x))$, where $c(\cdot)$ is a set of inequality constraints. In this paper, $f(x)$ is the hysteresis Af-Ms, and $g(x)$ is Ms, and the inequality constraint is 200°C <Ms<300°C. If $f(x)$ and $g(x)$ are each modeled by a GPR, we denote the predicted joint Gaussian distribution over $f(X_t)$ based on the trained GPR model on the training (observed) data D_{obs} containing n points as $N(\mu_f^n, \Sigma_f^n)$. The superscript n shows the dependence of the predicted mean and covariance matrix on the observed dataset after performing n measurements. Similarly, there is a joint Gaussian distribution over the $g(X_t)$, denoted as $N(\mu_g^n, \Sigma_g^n)$.

We formulate the constrained optimization problem in the following form:

$$min_{x\in X}[f(x)(1-\mathrm{P}(c(g(x))))].$$

For our specific materials problem we have:

$$min_{x\in X}\left[\left(A_f - M_s\right)(1-\mathrm{P}(200 < M_s < 300))\right].$$

We now derive the MOCU-based experiment design policy for this problem. Hereafter in this section, an *action* refers to any possible experiment. The cost of an action x is $C(x) = f(x)(1-\mathrm{P}(c(g(x))))$. Note that $f(x)$ and $g(x)$ are unknown and modeled probabilistically; otherwise, we could easily select the action with the lowest cost. After n observations, the intrinsically Bayesian robust (IBR) action [138] is the one that minimizes the average (expected) cost:

$$x_{IBR}^n = \arg min_{x\in X}\,\mathrm{E}^n[C(x)] = \arg min_{x\in X}\quad \mathrm{E}^n[f(x)(1-$$

$$\mathrm{P}^n(c(g(x))))] = \arg min_{x\in X}\,\mathrm{E}^n[f(x)](1-\mathrm{P}^n(c(g(x)))),$$

where E^n and P^n denote the conditional expectation and probability given D_{obs} containing the n observations. The optimal experiment based on the MOCU policy given n data points, x_*^n, is observing the outputs of the action that minimizes the difference between the expected remaining MOCU after the observation is added to the current set of observed data and the current MOCU [138]:

$$x_*^n = \arg min_{x\in X}\,\mathrm{E}^n_{y^{n+1}|x}\left[\mathrm{E}^{n+1}[C(x_{IBR}^{n+1})]\right] - \mathrm{E}^n[C(x_{IBR}^n)] =$$

$$\arg min_{x\in X}\,\mathrm{E}^n_{y^{n+1}|x}[min_{x'\in X}\mathrm{E}^{n+1}[C(x')]] - \ min_{x'\in X}\mathrm{E}^n[C(x')],$$

where E^{n+1} denotes the conditional expectation given the concatenation of D_{obs} containing the n observations and the new experiment result y^{n+1} of x. For our cost function we have

$$x_*^n = \arg min_{x\in X}\,\mathrm{E}^n_{y^{n+1}|x}\left[min_{x'\in X}\,\mathrm{E}^{n+1}[f(x')]\left(1-\mathrm{P}^{n+1}\left(c\left(g(x')\right)\right)\right)\right] -$$

$$min_{x'\in X}\,\mathrm{E}^n[f(x')](1-\mathrm{P}^n(c(g(x')))).$$

The first term in the equation above can be calculated with Monte Carlo (MC) sampling. When the predicted joint distribution over $f(X_t)$ and $g(X_t)$ are each a Gaussian distribution, as is the case given by the trained GPR models, the recursion for the updates of the mean and covariance can be written as the following [63] for both $f(X_t)$ and $g(X_t)$, where to simplify notation we have dropped the f and g subscripts:

$$\mu^{n+1} = \mu^n + \frac{y^{n+1} - \mu^n_{x^n}}{\Sigma^n_{x^n x^n} + \beta} \Sigma^n_{x^n x^n} e_{x^n}$$

$$\Sigma^{n+1} = \Sigma^n + \frac{\Sigma^n e_{x^n} e'_{x^n} \Sigma^n}{\Sigma^n_{x^n x^n} + \beta}$$

Here, x^n represents the selected experiment, β is the noise variance, and e_{x^n} is a vector of length m with all 0s except for the index corresponding to x^n which is 1. Note that these updates are exact when assuming that the hyper-parameters of the GPR model do not change after the addition of the new experiment result. Although, we in fact update the hyper-parameters for calculating the acquisition function, we make this assumption for approximation to keep the computations tractable. In this case, $\mathrm{E}^{n+1}[f(x')]$ and $\mathrm{E}^n[f(x')]$ are equal to $\mu^{n+1}_{x'}$ and $\mu^n_{x'}$, respectively. $\mathrm{P}^{n+1}(c(g(x')))$ and $\mathrm{P}^n(c(g(x')))$ can also be calculated based on the Gaussian CDF given $(\mu_g^{n+1}, \Sigma_g^{n+1})$ and (μ_g^n, Σ_g^n).

One of the strategies that can be used for selecting the next experiment is the pure exploitation policy. In effect, by following this policy's suggestion we are assuming that the models trained on the current available data are accurate enough, so we do not need to explore the space other than where the models predict the optimal point to be. This is an optimistic view about the accuracy of the models, especially when fewer observed data points are available. The pure

exploitation selects the next point that minimizes the expected immediate cost, which is x_{IBR}^n. In other words, selecting the IBR action (alloy) at each iteration as the next experiment is equivalent to the pure exploitation policy. On the other hand, the MOCU-based policy selects the experiment that is expected to reduce the average cost of the next IBR action, the IBR action selected at the next iteration after incorporating the selected experiment result, the most compared with the average cost of the current IBR action.

Constrained expected improvement (EI_c) in [205, 206] is another acquisition function that can be used. EI_c is equal to the usual expected improvement (EI) multiplied by the probability of satisfying the constraint:

$$x_*^n = \arg max_{x \in X} \mathrm{EI}^n(x)\, \mathrm{P}^n\left(c\left(g(x)\right)\right) = \arg max_{x \in X} \mathrm{EI}_c^n(x),$$

where $\mathrm{EI}^n(x)$ denotes the usual EI given D_{obs} containing the n observations (more details in the Appendix).

In the Appendix we show how the derived MOCU policy reduces to the constrained expected improvement (EI_c). Specifically, under the GPR modeling and Gaussian distributions over $f(x)$ and $g(x)$, if we restrict the selection of IBR action to the set of actions with observed outputs, we recover the constrained expected improvement acquisition function. Note that since MOCU-based policy is one-step look ahead, compared with EI_c, it can potentially better balance the trade-off between exploitation and exploration and select the most informative experiment in this regard.

7.4.3 Alloy Selection Criteria

From the aforementioned selectors, a list of compositions was obtained in a descendant order from the top ranked one based on the acquisition function (for trade-off-based approaches) or probability

of the composition to meet the targeted properties (for pure exploitation). The selectors and their corresponding policies are summarized in Table 1. The first ranked alloy composition on the list of MOCU-based selector is expected to provide the most information regarding finding the composition that achieves the targeted properties in the next iteration, followed by rank 2 and so on. For pure exploitation, the first ranked alloy composition has the highest probability of achieving the targeted composition based on the trained models on the available training data in that iteration, followed by rank 2 and so on. We also observed that some consecutive compositions in the list of selectors were very close to each other, within experiment precision, e.g. differed from each other by 0.05 at.% of Hf replacing Ti. We performed a filtering step to only include one composition from these sets of very close alloys to have more diversity in the top ranks in the aggregated ranking table. We continued the experiment design iterations until we saw no improvement achieved by the alloys selected and measured, which happened after the 4th iteration, and stopped the procedure for cost effectiveness. This is similar in effect to a greedy mindset that stops further experiments as soon as no improvement is achieved in one iteration.

Selector	**Policy**
Pure Exploitation	$x_*^n = \arg min_{x \in X} \mathrm{E}^n[f(x)](1 - \mathrm{P}^n(c(g(x))))$
$\mathrm{EI_C}$	$x_*^n = \arg max_{x \in X} \mathrm{E}^n_{y^{n+1}\|x}[\max(y_{o,f}^{\mathrm{opt},n} - y_f^{n+1}, 0)]\ \mathrm{P}^n\left(c\left(g(x)\right)\right)$

MOCU-based	$x_*^n = \arg min_{x \in X} \mathrm{E}^n_{y^{n+1}\|x} \left[min_{x' \in X} \mathrm{E}^{n+1}[f(x')] \left(1 - \mathrm{P}^{n+1}\left(c\left(g(x')\right)\right)\right)\right]$

Table 0.2 Different selectors used for experiment design.

Due to taking a greedy approach in deciding on when to stop the experiments, we used all three selectors in choosing the experiments at all the experimental iterations, since they provide different exploitation-exploration balances. For example, if we want to stop at any of the experimental iterations, we should select the IBR action as the final suggestion, which is equivalent to pure exploitation. But if we want to select an experiment that provides the most information about selecting the optimal alloy at the next iteration, we should use MOCU for experiment selection. At each iteration, we selected at least one experiment by MOCU, and one from pure exploitation. If the top suggestion from EI_c was different from the top one from MOCU, but still in the top 20 from MOCU, that would also be selected. The remaining experiments (the number being different at each iteration since it depended on whether the selections from pure exploitation and EI_c were actually different from MOCU) were selected by MOCU.

7.5 Results and Discussion:

Implementing the preceding Bayesian experimental design framework to the NiTiHf HTSMA system led to discovery of a novel NiTiHf composition having the lowest value of thermal hysteresis reported so far in the literature in solution heat treated conditions. Based on the compositional dependence on TTs data of SHT Ni_xTiHf_y as shown in Table 2, was considered to be the initial reliable dataset to generate the model for making predictions towards discovering the lowest possible thermal hysteresis (A_f-M_s) and having an value of M_s in between 200°C to 300°C.

Fig. 2 shows the plot with M_s temperature and the corresponding thermal hysteresis for the initial dataset as green circles. From the initial dataset it can be seen that the lowest thermal hysteresis in the range of 200°C < M_s < 300°C is 31°C for $Ni_{50.3}TiHf_{20}$ composition. On implementing the framework with the initial dataset, it suggested making $Ni_{49.9}TiHf_{18.1}$ and $Ni_{50}TiHf_{19}$. All the

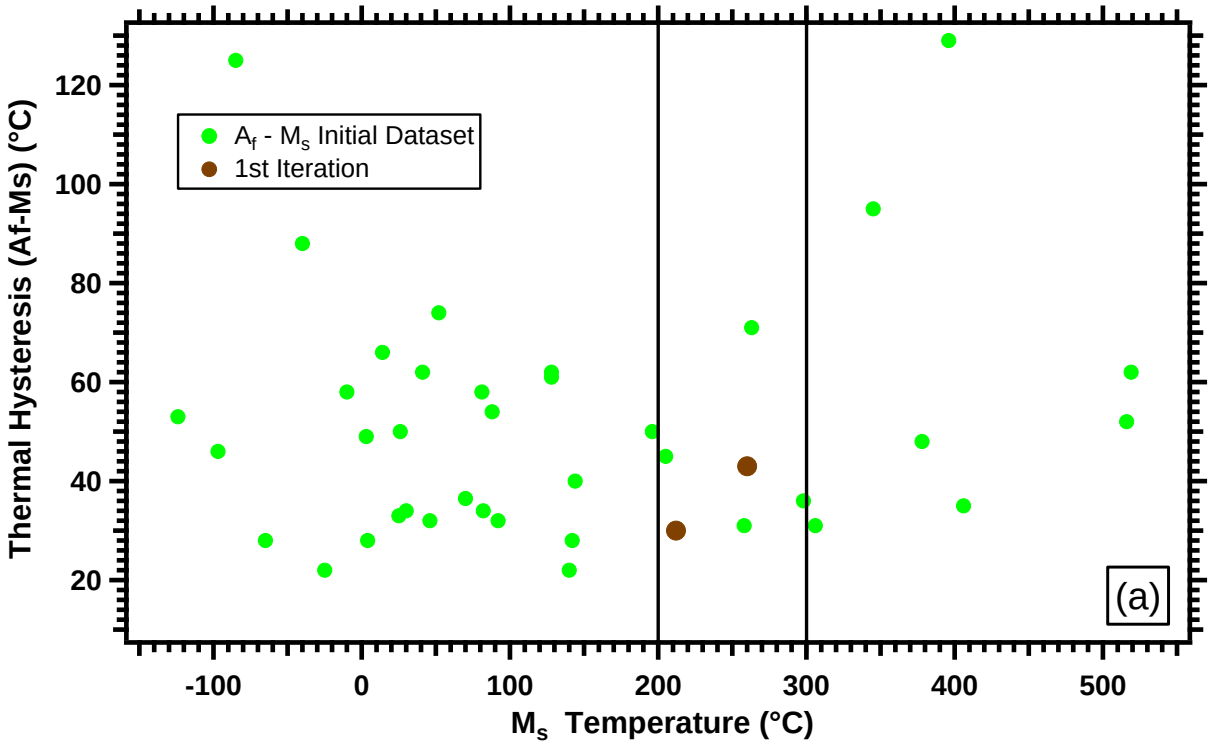

Fig. 7.6 continued…

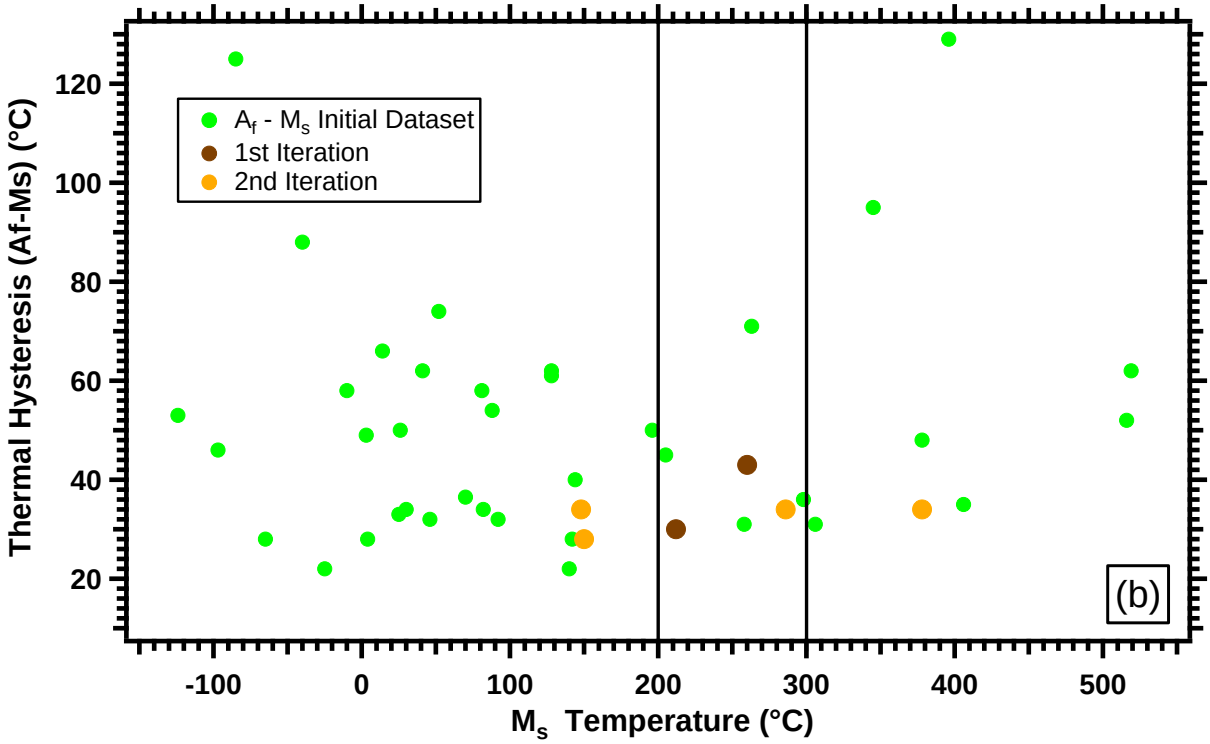

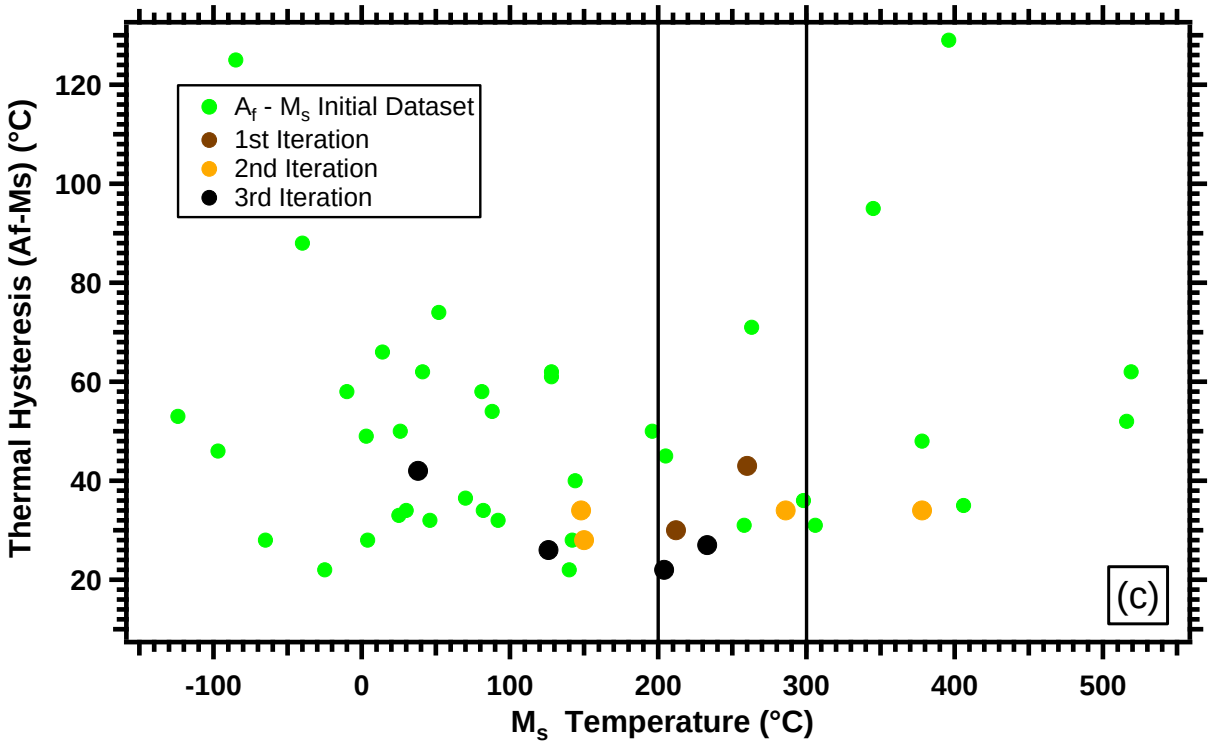

Fig. 7.6 continued…

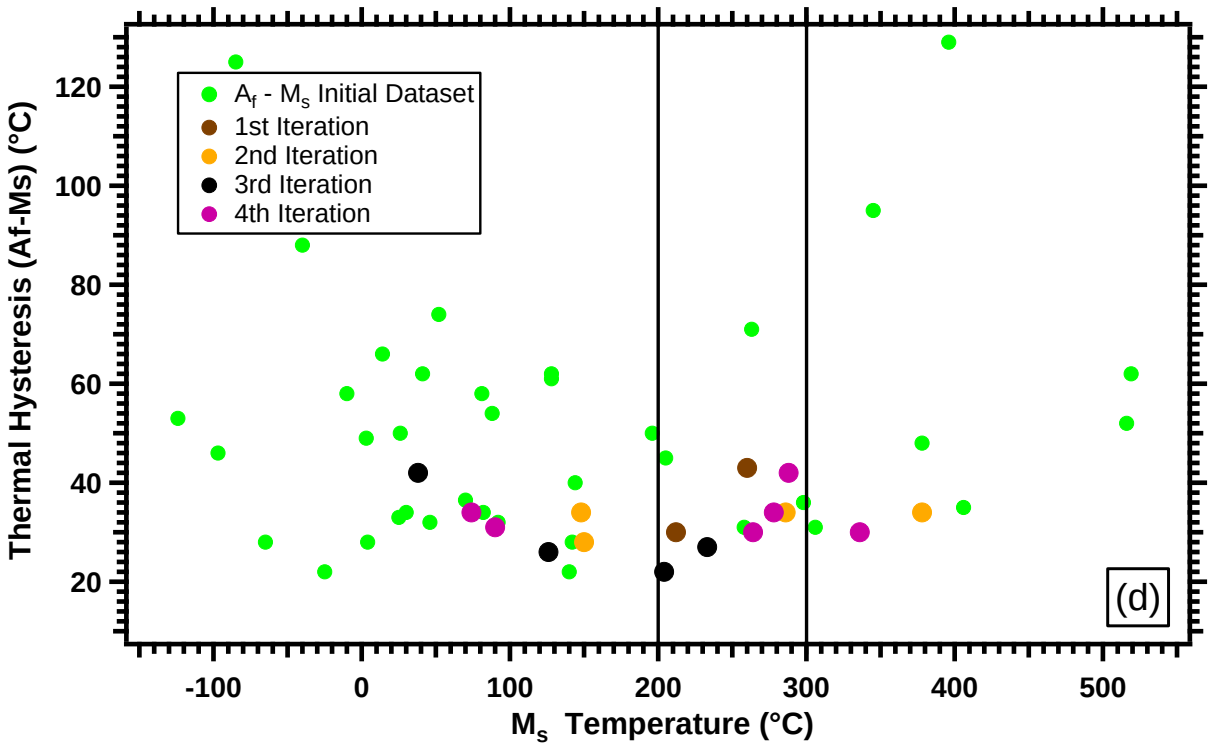

Figure 7.6 Thermal Hysteresis (A_f-M_s) Vs M_s temperature plots showing respective progression for initial dataset and with respective number of iterations. (a) shows the initial data (green markers) alonng with 1st iteration results (brown markers), depictig the a lower hysteresis was achieved in the desired range of Ms temperature. (b) shows results from initial dataset and 1st and 2nd (orange markers) iteration. Results from 2nd iteration doesn't show any minimum in hystesis as compared to results from 1st iteration, but is actually trying to explore the compositional space more in order to increase the predicting power of the model. (c) shows results from initial dataset along with 1st, 2nd and 3rd (black markers) iteration and a minimum in thermal hysteresis is again observed in desired temperature range. This mimimum is achieved because the model used 2nd iteration results to enhance its prediction power. (d) represents results from initial dataset along with 1st, 2nd, 3rd and 4th (pink markers) iteration. In the 4th iteration the model again is exploring the material space to enhance its prediction power further, in order to make the 5th iteration more accurate.

Nominal Composition			Measured Composition			Transformation temperatures	
Ni	Ti	Hf	Ni	Ti	Hf	Ms	Af-Ms
49.9	32	18.1	49.69±0.16	31.95±0.24	18.34±0.2	260	43
50	31	19	50.4±0.1	20.92±0.11	18.72±0.13	212	30

Table 7.3 1st Iteration results

Nominal Composition			Measured Composition			Transformation temperatures	
Ni	Ti	Hf	Ni	Ti	Hf	Ms	Af-Ms
50.4	28.2	21.4	50.6±0.09	27.9±0.11	21.51±0.09	150	28
50.2	27.3	22.5	50.55±0.83	26.34±0.34	23.07±0.68	378	34
50.3	31.5	18.2	50.37±0.15	31.24±0.21	18.42±0.24	148	34
50.5	27.4	22.1	50.53±0.28	27.17±0.17	22.36±0.28	286	34

Table 7.4 2nd Iteration Results

Nominal Composition			Measured Composition			Transformation temperatures	
Ni	Ti	Hf	Ni	Ti	Hf	Ms	Af-Ms
50.1	30.4	19.5	50.13±0.1	30.42±0.14	19.47±0.13	233	27
50.3	28.9	20.8	50.22±0.09	28.83±0.12	20.97±0.14	204	21
50.6	28.1	21.3	50.54±0.07	28.13±0.1	21.36±0.11	126	26
50.8	27.8	21.4	50.73±0.09	27.7±0.16	21.6±0.14	38	42

Table 7.5 3rd Iteration Results

Nominal Composition			Measured Composition			Transformation temperatures	
Ni	Ti	Hf	Ni	Ti	Hf	Ms	Af-Ms
49.8	29.4	20.8	49.74±0.09	29.19±0.47	21.11±0.54	336	30
49.9	31.4	18.7	49.93±0.13	31.15±0.24	18.93±0.23	278	34
50.2	29.1	20.7	50.23±0.1	28.98±0.19	20.82±0.22	264	30
51	24.7	24.3	51.09±0.11	24.52±0.09	24.45±0.1	74	34

Table 7.6 4th Iteration Results

selectors mentioned in Section 6.2, especially the pure exploitation-based and MOCU-based selectors, suggested the above compositions. Table 3 shows the measured EPMA compositions and transformation temperatures from the suggested compositions. These results were referenced as 'Iteration 1' in Fig. 6a and marked by brown circles. Results indicate that the value of M_s for both compositions is within the boundaries of 200°C and 300°C. The thermal hysteresis values for $Ni_{49.9}TiHf_{18.1}$ and $Ni_{50}TiHf_{19}$ are 43°C and 30°C, respectively. The results indicate that we

achieved a slightly lower value of thermal hysteresis than the lowest reported in the initial dataset. This indicates that the framework employed for alloy discovery is working towards the target.

In order to check the prediction performance of the model after execution of step 3 (of Fig. 4) in every iteration loop, we conducted an exercise of training and testing the model by splitting the available data we have at the end of every of step 3 after every iteration loop. At this point, we have data from initial dataset and 1st iteration. An algorithm was employed to randomly sample the data and divide the total available data-points into a training dataset and a testing dataset. As mentioned in section 4.2, the training data were used to generate the model for M_s and A_f-M_s and predictions were made for the compositions in the testing data using this trained model. These predicted values of A_f-M_s values were then compared with their corresponding actual values. From Fig. 7a it can be seen that all the data-points that lie on the 45° black line are the data-points from the training dataset and the data-points scattered around the 45° black line are from the testing dataset. As clearly seen that the predicted value does not match closely with the actual value and hence the model has some inaccuracies in making predictions at this stage. Also, the standard deviation errors associated with the predictions are also relatively high.

Now the data from the initial dataset and 1st iteration form our new initial data-set. We generate a model as shown in step 1 of Fig. 4 and the entire framework is implemented again. The predictions obtained as a result of the 2nd iteration is shown in Table 4 and shown in Fig. 6b as orange circles. The predictions are scattered over a wide range of Ms and only one composition of $Ni_{50.5}TiHf_{22.1}$ satisfies the criteria of 200°C < M_s < 300°C and has a thermal hysteresis of 34°C. Among the other selected compositions in this iteration, we obtained one of the lowest hysteresis of 28°C for $Ni_{50.4}TiHf_{21.4}$ composition, but it did not satisfy the constraint with M_s = 150°C. After performing the training and testing of the available data, it can be seen from Fig. 7b that the standard deviation

on the testing dataset is much lesser as compared to that observed after 1st iteration in Fig. 7a. Also, the testing data mean is much closer to the 45° line, indicating that the predicting power of the model is much improved as compared to that at the end of the 1st iteration. Clearly, the model was trying to minimize the thermal hysteresis, but couldn't satisfy the M_s criteria. One reason for this can be that the selectors in step 3 are more inclined towards the exploration and that's why it wants to reduce the uncertainties for future predictions which is supported by testing data in Fig. 7b. When all the initial data along with results from the 1st and 2nd iterations are utilized to generate the model and implement the experimental design framework, the results obtained at the end of step 4 of Fig. 4 are referenced as 'iteration 3.' These are shown in Table 5 and depicted by black colored circles in Fig. 6c. Results from the 3rd iteration show a drastic drop in hysteresis 21°C for $Ni_{50.3}TiHf_{20.8}$ composition, while still having the M_s value between 200°C and 300°C. These

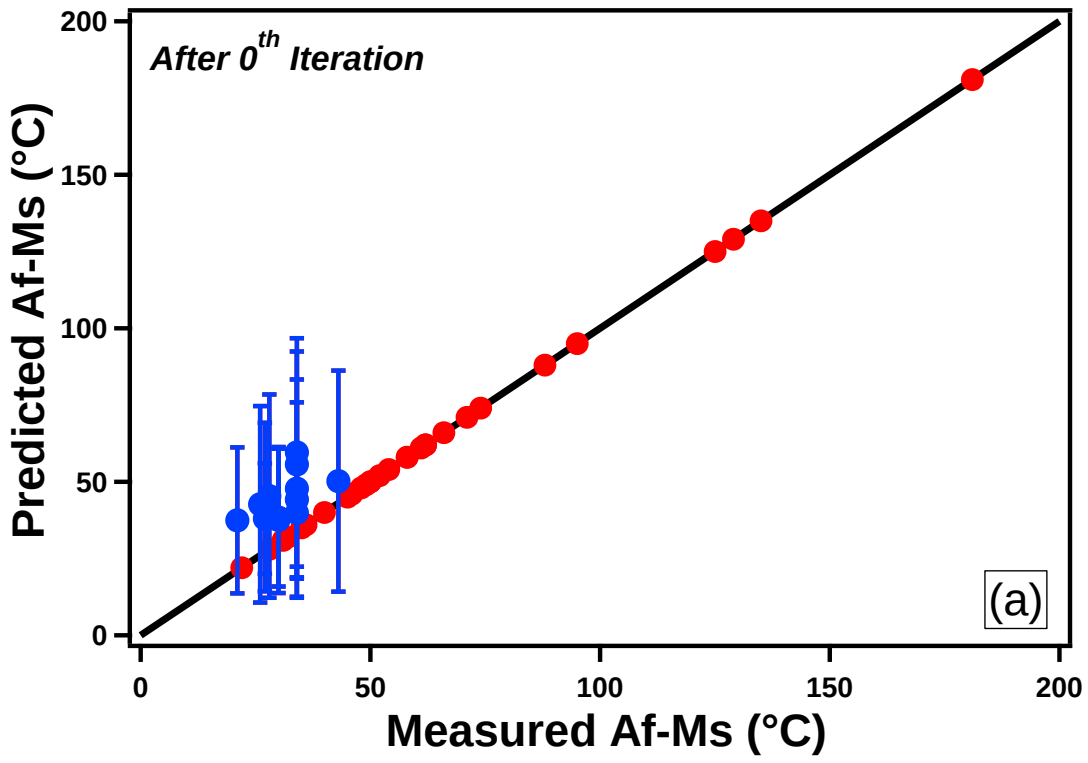

Fig. 7.7 continued…

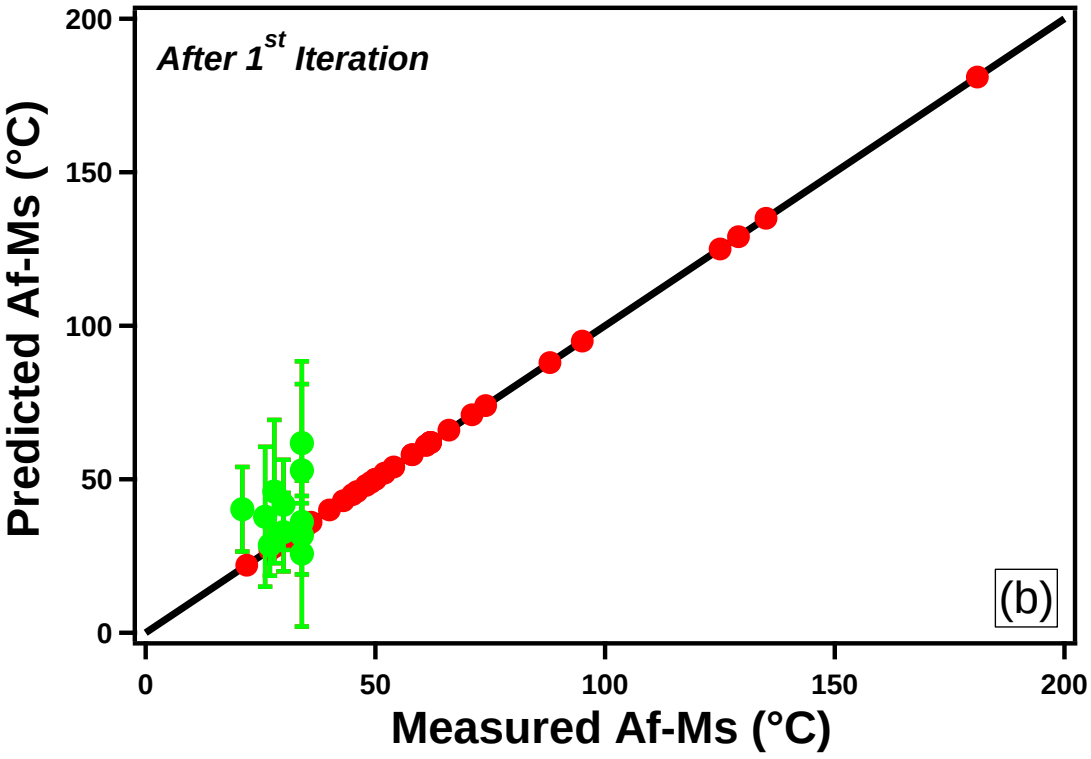

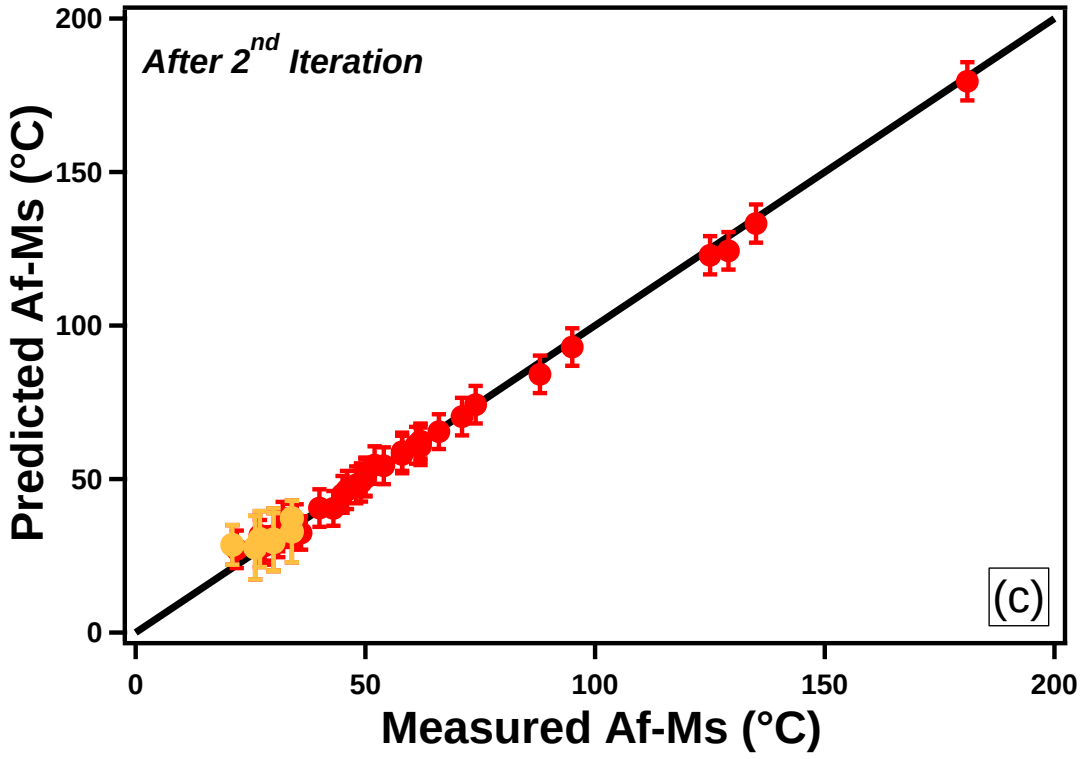

Fig. 7.7 continued…

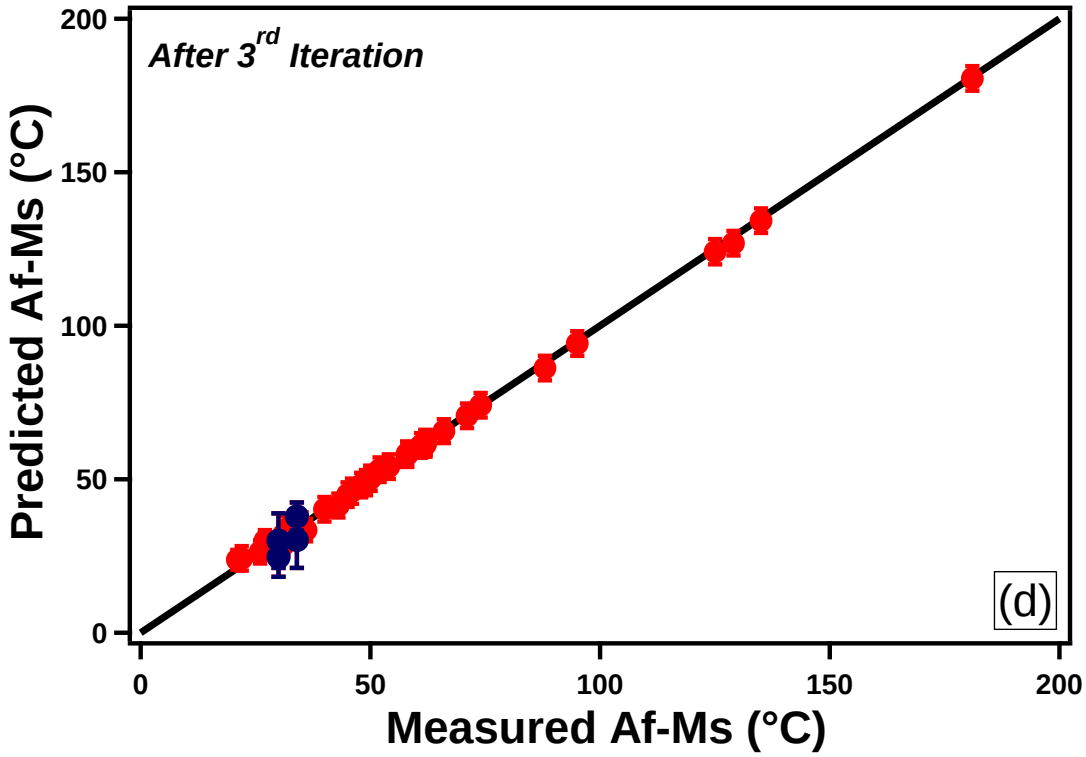

Figure 7.7 Predicted thermal hysteresis (A_f-M_s) Vs Measured thermal hysteresis (A_f-M_s) plots showing that with increasing number of iterations, the model prediction power has increased drastically. In all sub-figures above, red dot markers show the training data with assoicated standard deviation, while the colored dot markers in each each figure show the testing data results. (a) shows the predcition power of the model with initial dataset only. The testing data (blue dot markers) lies far from the 45° line with a higher assocaited standard deviation and hence the model prediction accuracy is low. (b) depicts the prediction power of the model with initial dataset and results from the first iteration. From the testing data (green dor markers) shown by green markers, it can be seen that the mean predicted value has moved much closer to the actual values, but with higher degree of standard deviation. (c) shows that the model performance after utilizing initial dataset and results from 1st and 2nd iteration. The testing data (orange dot markers) is very close to the 45° line with very less std deviation, which suggestes that the model has got much accurate with prediction. (d) depicts the model's prediction capability when the model was constructed using initial dataset and results from 1st, 2nd and 3rd iteration. The model is still very accurate as the testing data (purple markers) lies very close to the 45° line along with very neglible standard deviation.

results further support the reason that results from the 2nd iteration did not hit the targeted objectives but were able to help enhance the prediction power of the model. Along with $Ni_{50.3}TiHf_{20.8}$, another composition from the 3rd iteration predictions, Ni50.1TiHf19.5, showed a

second lowest value for thermal hysteresis of 27°C with the M_s value between 200°C and 300°C. Fig. 7c further shows that the model prediction power, after including results from 3rd iteration, is much higher than before. The standard deviation on the testing data after 3rd iteration is extremely small and all the data-points from the testing dataset lie very close to the 45° line. This suggests that the model is very accurate in making the predictions and the standard deviation associated with the prediction is also reduced drastically.

Again, the framework above was implemented with initial data along with accumulated data from 1st, 2nd, 3rd iterations to make predictions for 4th iteration . Results from 4th iteration show that two compositions from the predicted values, $Ni_{49.9}TiHf_{18.7}$ and $Ni_{50.2}TiHf_{20.7}$, satisfy the M_s criterion with thermal hysteresis of 34°C and 30°C as shown in Table 6 and in Fig. 6d by pink circles. Though the framework was able to suggest compositions which satisfy the M_s criterion, it could not minimize the thermal hysteresis below 21°C as observed in 3rd iteration. On testing the model's prediction performance after 4th iteration, the model is still accurate as the mean of the predicted value of the testing data is very close to the actual values along with extremely small standard deviation as shown in Fig. 7d. Thus, following the greedy strategy in terms of cost effectiveness, we stopped the experiment design loop after the 4th iteration.

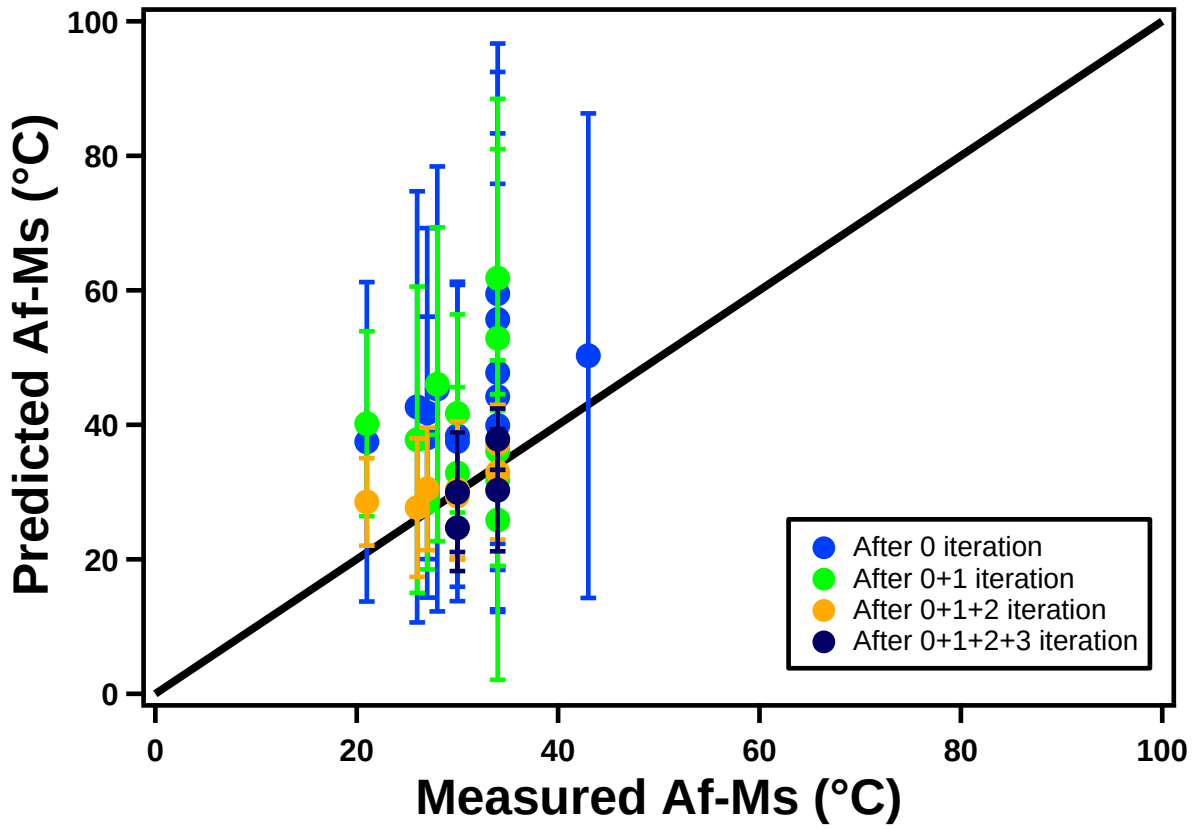

Figure 7.8 Shows a cumulative predicted hysteresis vs measured hysteresis plot for all testing data results after 0^{th}, 1^{st}, 2^{nd} and 3^{rd} iteration respectively. The summarized plot gives a detailed picture of the prediction power of the model with increasing number of iterations. With increasing number of iterations, the predicted values lie much closer to the actual value (as seen that the predictions moves closer to the 45° line) and the standard deviation assosciated with the predictions also reduces.

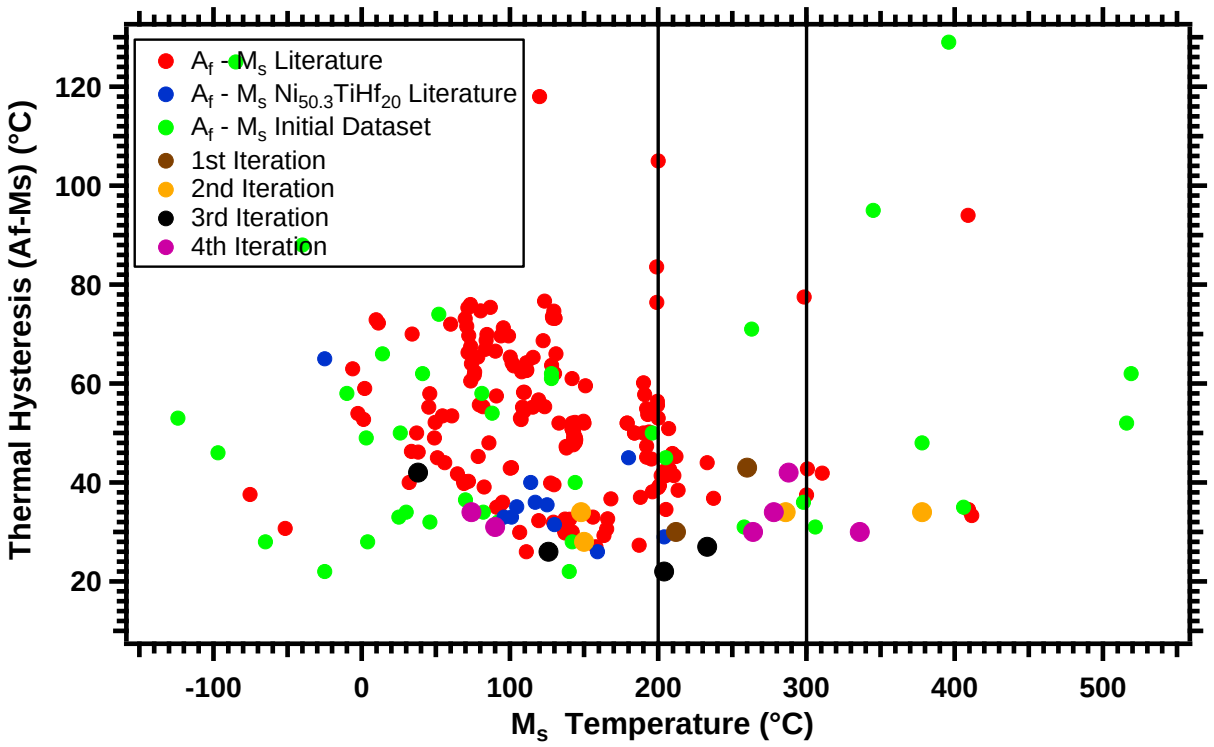

Figure 7.9 Shows a summarized plots for thermal hysteresis (A_f-M_s) Vs M_s temperature plots for all the solution heat treated literature data, initial dataset used in this study and iteration results. Iteration 3 yields the lowest hysteresis value reported so far in literature (to the best of author's knowledge) in the required range of Ms temperature.

Fig. 8 collectively shows a plot of predicted thermal hysteresis (A_f-M_s) value vs measured hysteresis value for the testing datasets after each iteration. Cumulatively, it can be clearly seen that with number of increasing iterations, the model's predicted value gets closer and closer to the actual measured value of thermal hysteresis. This tells us that with addition of new information (or highly selected datapoints) the model is becoming increasingly accurate in predicting the hysteresis. Also, the standard deviation associated with prediction also decreases with increasing number of iterations. This also indicates that the model accuracy is enhancing with increasing number of iterations. Fig. 9 shows a plot of thermal hysteresis (A_f-M_s) Vs M_s temperature for the experimentally measured values in literature and in this work combined. Clearly, the results for

alloy compositions fabricated in 3rd iterations, shows the minimum value of hysteresis ever reported in the literature so far, with the Ms temperature window of 200˚C to 300˚C.

7.6. Summary:

In order to summarize this work,

i. We have successfully demonstrated the implementation of machine learning-based iterative design framework to discover novel NiTiHf alloys with high transformation temperatures and lowest reported thermal hysteresis (Af-Ms) value in solution heat treated conditions.

ii. The similar framework can also be implemented to design H-phase precipitated NiTiHf alloys with desired transformation characteristics, provided we a reliable initial database to train the model and adding heat treatment temperature and time as addition features along with the compositional based features used in this study.

iii. Such an iterative design framework is very universal and can also be implemented to discover other material systems with desired properties.

CHAPTER VIII

CONCLUSIONS and FUTURE WORK

The study focuses on developing different methods to design novel NiTiHf alloys by exploring the Ni-Ti-Hf system with respect to the chemistry, thermodynamics and machine learning approaches. The Ni-lean side of the NiTiHf alloys have been explored systematically but as Ni-lean NiTiHf alloys exhibit lower strength and poor thermal stability along with higher thermal hysteresis which makes them impractical for modern high temperature aerospace and automobile applications. On the other hand, the Ni-rich side of the NiTiHf alloys show a higher strength, lower thermal hysteresis, high recoverable transformation strain and tunable transformation temperatures via H-phase precipitation. However, the Ni-rich side was not explored systematically and the variation of TTs with changing Ni and Hf content was not known. Over 42 different Ni_xTiHf_y compositions were fabricated and tested for their TTs using the DSC, TGA and PPMS. Also, hardness measurements were performed to have an insight about their strength. In order to understand the underlying physics of nature of compositional dependence on TTs, TEM was performed on selected compositions. In order to understand the dependence of thermal hysteresis on composition, high and room temperature XRD studies were performed to understand the phase compatibility between the austenite and martensite phase.

Also, as mentioned tunable transformation characteristics can be achieved by utilizing the H-phase precipitation phenomenon, but no study was is yet performed to understand the thermal equilibrium between the H-phase precipitate and the martensitically transforming phase. The present study also explores the thermodynamic equilibrium between the two and suggests a

methodology to design new alloys using phase diagram. Along with the equilibrium phases present the study also found new phase which doesn't exist in any of the individual binary phase diagrams.

Also, a new enterprise was ventured towards designing new NiTiHf SMAs with required TTs using artificial intelligence based machine learning approach. A systematic framework was developed using Bayesian modelling with certain uncertainties associated and the frame work was used to make prediction for a NiTiHf alloy with M_s temperature in between 200°C and 300°C and minimum possible hysteresis. Therefore, based on the results presented in Chapter IV, V and VI the results can be summarized, and the following conclusions can be drawn.

(1) The TTs in the NiTiHf system are highly dependent on the composition of individual elements. For the Ni-lean and equiatomic compositions, the TTs doesn't change much until 10 at.% Hf addition, but beyond 10 at.% Hf addition the TTs increases monotonically very drastically. However, for the Ni-rich NiTiHf compositions a different trend is observed. For Ni=50.3 at.%, the TTs initially decrease up to 5 at.% Hf addition followed by continuous increase in TTs with respect to Hf addition. For Ni=50.7 at.%, the TTs start to decrease with initial Hf addition to the binary $Ni_{50.7}Ti$ alloy composition until 10% Hf addition and achieves a minimum around Hf=10 at.%. For Ni=50.7 at.%, with further increase in Hf content beyond 10 at.%, the TTs again increases with increasing Hf content. For Ni = 51 at.%, the TTs decreases again very drastically and is completely suppressed for mere Hf=2.5 at.% addition. No reversible martensitic transformation was observed in alloys with composition ranging from $Ni_{51}TiHf_{(x=5,\ 10,\ 15)}$ even up to -260°C. The TTs however jumped back up with increase in Hf content of 20 at.% and above for Ni=51 at.% content.

(2) The TTs variation with respect to the Ni content is much similar to that observed in the binary NiTi alloy. The for all Hf contents except Hf=30 at.%, the TTs didn't change until Ni=50 at.%, but with further increase in Ni content all the TTs tend to decrease very drastically. For a fixed Hf=30 at.% alloys, The TTs didn't change much until Ni=50.7 at.% content, but beyond 50.7 at.% decreased very drastically.

(3) The reason for the initial drop in TTs with respect to the Hf content can be attributed to the enhanced local lattice distortions generated by the Ni anti-site defects and the Hf substitutional defects. Such high local lattice strains promotes the stabilization of austenite and tend to form frozen strain nano-domains in the B2 austenitic matrix. Such a dynamic system needs a higher degree of under cooling to provide the material with enough driving force in order to facilitate the martensitic transformation and hence decreases the TTs. Also based on TEM evidence, the occurrence of diffuse scattering indicates the short range ordering between the Hf and Ti in the Ti-sub-lattice, which can promote to formation of H-phase precursors and result in decrease in TTs

(4) The thermal hysteresis (A_f - M_s) with respect to the Hf content showed a very peculiar trend for all fixed Ni contents. The thermal hysteresis initially tends to increase with increasing Hf content and attain a local maximum at around Hf=10 at.%. With further increase in Hf content beyond 10 at.%, the thermal hysteresis decreases and achieves a local minimum at around Hf = 20 at.%. With further increase in Hf content, the thermal hysteresis is found to increase monotonically upto Hf = 30 at.%.

(5) The hardness values were found to increase subsequently with in Ni and Hf content of the material.

(6) The enthalpy variation with respect to Hf content revealed a similar trend to that of the TTs variation with Hf content. The initial decrease in enthalpy with increasing of Hf content can be attributed to the local lattice strains due to Ni anti-site defects and Hf substitutional defects in Ni-rich NiTiHf alloys up to Hf=20 at.%. Beyond 20 at.% Hf addition, the enthalpy decreases due to presence of H'-phase and increases because of the presence of H-phase particles.

(7) The enthalpy is found to decrease continuously with increasing Ni content, for all fixed values of Hf content except Hf=30 at.%. For 30 at.% Hf addition the behavior of enthalpy can again be explained based on formation of H' and H-phase particles.

(8) The phase compatibility study between the austenite and martensite conducted on $Ni_{50.3}TiHf_{(x)}$ alloys indicate that the thermal hysteresis does not depend on the middle eigenvalue (λ_2). The NiTiHf alloys lie on the shallow slope curve in the thermal hysteresis Vs λ_2 value and hence the thermal hysteresis shows very less or almost no dependency on λ_2 values. Instead of λ_2 value, the co-factor conditions might provide a better insight in the hysteresis variation with composition.

(9) Considering the thermodynamic studies of the Ni-Ti-Hf as such, from the $Ni_{50.3}TiHf_{20}$ bulk alloy study we can conclude the H-phase precipitates increases the TTs and the thermal stability of the material. STEM EDX maps acquired from the H-phase region, indicates that the H-phase is Ni and Hf rich and Ti lean as compared to the neighboring matrix phase.

(10) X-rays maps from the tri-junctional diffusion region show that at all temperatures of study, the Ni diffuses the fastest followed by Hf and Ti. Also, Hf exhibits a very high

solubility in the binary Ni-Ti phases, but Ti exhibits very less solubility in the Ni-Hf binary phases.

(11) All the phases that exist in the respective binary phase diagrams exist in the Ni-Ti-Hf phase diagram at 600°C, 700°C, 800°C and 900°C. Along with binary derived phases, the H-phase was found to exist at 600°C, but not at 700°C, 800°C or 900°C. At 600°C, the H-phase exists from Ni ranging from 51.13 at.% to 54 at.% , whereas Hf ranging from 7 at.% to 34 at.%. The Ni_4Ti_3 phase also found to exist at 600°C only with certain Hf solubility in the ternary phase diagram.

(12) Based on the evolution of matrix composition, which moves along the tie-line with increasing the heat treatment time can be utilized to design new NiTiHf alloys with required TTs by controlling the initial starting composition and the volume fraction of the H-phase formed.

(13) The SAXS experiments show a continuous increase in scattering intensity at all length scales, indicate that the Ni-Ti-Hf system is evolving continuously. The H-phase precipitates are formed and with increase in heat treatment time, the precipitation occurs continuously. The rate of increase of scattering intensity with experiment time, suggests that the precipitation kinetics is very high initially and after certain time, the precipitation occurs at a much steady rate.

(14) After analyzing the SAXS data, the evolution of H-phase precipitates with increasing time was revealed. It can be seen that initially the kinetics of the H-phase precipitates increasing rapidly with increase in time, followed by a much steady state precipitation kinetics.

(15) Along with thermodynamic and kinetic approach, an iterative machine learning based approach can also be used to design novel NiTiHf alloys. In our study we have generated a framework which helped us in designing novel NiTiHf alloys with a Ms temperature in between 200°C to 300°C and minimum thermal hysteresis possible. By implementing such framework, we have discovered a NiTiHf alloy with the 200°C<Ms<300°C and lowest thermal hysteresis so far ever reported in the literature in SHT condition.

The present reveal the various aspects explored in The Ni-Ti-Hf system with respect to chemistry, thermodynamics and machine learning based approaches to design novel alloys. The compositions dependence on TTs data will serve as the composition map for any NiTiHf with known transformation temperatures and unknown composition. The contour plots presented in Chapter IV can be used to pinpoint the actual composition of the alloy. Even, various bulk alloy manufacturing techniques suffer with production accuracy and there is always a discrepancy between the actual composition of the manufactured alloy to the targeted composition. The composition dependence of the TTs can be used solve this discrepancy. In order to understand the underlying physics behind the behavior of TTs and thermal hysteresis with respect to composition, sufficient proofs have been provided with plausible explanations, to explain such compositional dependence of TTs. Still in order to find out the concrete reasons for such behavior, in future a detailed High Resolution TEM study should be performed in order to identify the presence of the H-phase precursors in $Ni_{50.7}TiHf_{10}$ and $Ni_{51}TiHf_{(5.10,15)}$ alloy and also to identify the reason for occurrence of diffuse scattering. Also, Dynamic Mechanical Analysis should be formed on the aforementioned alloys in order to identify presence of strain glass in the system.

Also carrying forward with the thermodynamic work, an almost complete thermodynamic assessment of the Ni-Ti-Hf system has been provided. All the single phase regions that exist are shown on their respective ternary isotherms. Among all the phases present, the equilibrium between the H-phase and the B2 martensitically transforming phase can be used to design novel NiTiHf alloys with required transformation characteristics. Therefore, in future, several point compositions of NiTiHf alloys within the two phase equilibrium region of the H-phase and the austenite phase should be heat treated at respective temperatures in order to mark the H-phase boundary more precisely. Also, the proposed methodology towards designing new alloys should be tested to solve a real time actuator problem in order to verify the proposed method. This will aid us in developing the NiTiHf alloys with higher accuracy and a smaller number of attempts to achieve the targeted value.

Lastly, the iterative machine learning based framework has aided us in developing the novel NiTiHf alloy with lowest reported thermal hysteresis value in the SHT condition. Such a powerful framework should be extended and applied to the heat treat alloys and transformation strain values at different stress levels should also be used as an input to the model, which can further help us designing alloys with high transformation characteristics and further lower thermal hysteresis. Such a model will be indigenously capable itself to suggest the initial composition and the heat treatment needed in order to obtain a particular set of transformation characteristics.

REFERENCES

[1] K Otsuka, X Ren. Physical metallurgy of Ti–Ni-based shape memory alloys. Progress in Materials Science 2005;50:511-678.

[2] K Otsuka, CM Wayman. Shape Memory Materials: Cambridge University Press; 1999.

[3] DJ Hartl, DC Lagoudas. Aerospace applications of shape memory alloys. Proceedings of the Institution of Mechanical Engineers, Part G: Journal of Aerospace Engineering 2007;221:535-552.

[4] J Ma, I Karaman, RD Noebe. High temperature shape memory alloys. International Materials Reviews 2010;55:257-315.

[5] J. Mohd Jani, M. Leary, A. Subic, M. A. Gibson. A review of shape memory alloy research, applications and opportunities. Materials & Design (1980-2015) 2014;56:1078-1113.

[6] PK Kumar, DC Lagoudas. Introduction to Shape Memory Alloys. Shape Memory Alloys: Modeling and Engineering Applications. Boston, MA: Springer US; 2008. p. 1-51.

[7] I Suorsa, E Pagounis, K Ullakko. Magnetization dependence on strain in the Ni–Mn–Ga magnetic shape memory material. Applied Physics Letters 2004;84:4658-4660.

[8] LC Chang, TA Read. Plastic Deformation and Diffusionless Phase Changes in Metals — the Gold-Cadmium Beta Phase. JOM 1951;3:47-52.

[9] ZS Basinski, JW Christian. Experiments on the martensitic transformation in single crystals of indium-thallium alloys. Acta Metallurgica 1954;2:148-166.

[10] Z S. Basinski, JW Christian. Crystallography of deformation by twin boundary movements in indium-thallium alloys. Acta Metallurgica 1954;2:101-116.

[11] WJ Buehler, JV Gilfrich, RC Wiley. Effect of Low-Temperature Phase Changes on the Mechanical Properties of Alloys near Composition TiNi. Journal of Applied Physics 1963;34:1475-1477.

[12] M Geetha, AK Singh, R Asokamani, AK Gogia. Ti based biomaterials, the ultimate choice for orthopaedic implants – A review. Progress in Materials Science 2009;54:397-425.

[13] J Frenzel, EP George, A Dlouhy, C Somsen, MFX Wagner, G Eggeler. Influence of Ni on martensitic phase transformations in NiTi shape memory alloys. Acta Materialia 2010;58:3444-3458.

[14] BE Franco. Engineering the Martensitic Transformation Hysteresis of Ni-Rich NiTi Alloys: Texas A&M Univeristy; 2014.

[15] J Khalil-Allafi, A Dlouhy, G Eggeler. Ni4Ti3-precipitation during aging of NiTi shape memory alloys and its influence on martensitic phase transformations. Acta Materialia 2002;50:4255-4274.

[16] E Gunther, K-A Jafar, G Susanne, S Christoph, S Wolfgang, S Denis. On the effect of aging on martensitic transformations in Ni-rich NiTi shape memory alloys. Smart Materials and Structures 2005;14:S186.

[17] A Ahadi, Q Sun. Stress hysteresis and temperature dependence of phase transition stress in nanostructured NiTi—Effects of grain size. Applied Physics Letters 2013;103:021902.

[18] A Ahadi, Q Sun. Stress-induced nanoscale phase transition in superelastic NiTi by in situ X-ray diffraction. Acta Materialia 2015;90:272-281.

[19] B Chad Hornbuckle, XX Yu, RD Noebe, R Martens, ML Weaver, GB Thompson. Hardening behavior and phase decomposition in very Ni-rich Nitinol alloys. Materials Science and Engineering: A 2015;639:336-344.

[20] GS Firstov, J Van Humbeeck, YN Koval. High Temperature Shape Memory Alloys Problems and Prospects. Journal of Intelligent Material Systems and Structures 2006;17:1041-1047.

[21] RA Vandermeer, JC Ogle, WG Northcutt. A phenomenological study of the shape memory effect in polycrystalline uranium-niobium alloys. Metallurgical Transactions A 1981;12:733-741.

[22] HM Volz, RE Hackenberg, AM Kelly, WL Hults, AC Lawson, RD Field, DF Teter, DJ Thoma. X-ray diffraction analyses of aged U–Nb alloys. Journal of Alloys and Compounds 2007;444-445:217-225.

[23] RA Vandermeer, JC Ogle, WB Snyder, Jr. Shape memory effects in a uranium + 14 at % niobium alloy. Scripta Metallurgica 1978;12:243-248.

[24] RW Fonda, RA Vandermeer. Crystallography and microstructure of TaRu. Philosophical Magazine A 1997;76:119-133.

[25] RW Fonda, HN Jones, RA Vandermeer. The shape memory effect in equiatomic TaRu and NbRu alloys. Scripta Materialia 1998;39:1031-1037.

[26] K Chastaing, A Denquin, R Portier, P Vermaut. High-temperature shape memory alloys based on the RuNb system. Materials Science and Engineering: A 2008;481-482:702-706.

[27] Z-r He, J-e Zhou, Y Furuya. Effect of Ta content on martensitic transformation behavior of RuTa ultrahigh temperature shape memory alloys. Materials Science and Engineering: A 2003;348:36-40.

[28] J Sato, T Omori, K Oikawa, I Ohnuma, R Kainuma, K Ishida. Cobalt-Base High-Temperature Alloys. Science 2006;312:90-91.

[29] K Oikawa, T Ota, Y Imano, T Omori, R Kainuma, K Ishida. Phase equilibria and phase transformation of Co−Ni−Ga ferromagnetic shape memory alloy system. Journal of Phase Equilibria and Diffusion 2006;27:75-82.

[30] K Otsuka, H Sakamoto, K Shimizu. Successive stress-induced martensitic transformations and associated transformation pseudoelasticity in Cu-Al-Ni alloys. Acta Metallurgica 1979;27:585-601.

[31] J Pons, E Cesari. Martensitic transformation cycling in a β Cu□Zn□Al alloy containing γ-precipitates. Acta Metallurgica et Materialia 1993;41:2547-2555.

[32] Y Sutou, T Omori, K Yamauchi, N Ono, R Kainuma, K Ishida. Effect of grain size and texture on pseudoelasticity in Cu–Al–Mn-based shape memory wire. Acta Materialia 2005;53:4121-4133.

[33] DD C., M Peter. Size Effects on Magnetic Actuation in Ni-Mn-Ga Shape-Memory Alloys. Advanced Materials 2011;23:216-232.

[34] R Santamarta, A Evirgen, AM Perez-Sierra, J Pons, E Cesari, I Karaman, RD Noebe. Effect of Thermal Treatments on Ni–Mn–Ga and Ni-Rich Ni–Ti–Hf/Zr High-Temperature Shape Memory Alloys. Shape Memory and Superelasticity 2015;1:418-428.

[35] J Frenzel, A Wieczorek, I Opahle, B Maaß, R Drautz, G Eggeler. On the effect of alloy composition on martensite start temperatures and latent heats in Ni–Ti-based shape memory alloys. Acta Materialia 2015;90:213-231.

[36] GS Bigelow, SA Padula, A Garg, D Gaydosh, RD Noebe. Characterization of Ternary NiTiPd High-Temperature Shape-Memory Alloys under Load-Biased Thermal Cycling. Metallurgical and Materials Transactions A 2010;41:3065-3079.

[37] F Yang, L Kovarik, PJ Phillips, RD Noebe, MJ Mills. Characterizations of precipitate phases in a Ti–Ni–Pd alloy. Scripta Materialia 2012;67:145-148.

[38] F Yang, RD Noebe, MJ Mills. Precipitates in a near-equiatomic (Ni+Pt)-rich TiNiPt alloy. Scripta Materialia 2013;69:713-715.

[39] PK Kumar, DC Lagoudas. Experimental and microstructural characterization of simultaneous creep, plasticity and phase transformation in Ti50Pd40Ni10 high-temperature shape memory alloy. Acta Materialia 2010;58:1618-1628.

[40] S Besseghini, E Villa, A Tuissi. Ni□Ti□Hf shape memory alloy: effect of aging and thermal cycling. Materials Science and Engineering: A 1999;273-275:390-394.

[41] HE Karaca, E Acar, H Tobe, SM Saghaian. NiTiHf-based shape memory alloys. Materials Science and Technology 2014;30:1530-1544.

[42] HE Karaca, SM Saghaian, G Ded, H Tobe, B Basaran, HJ Maier, RD Noebe, YI Chumlyakov. Effects of nanoprecipitation on the shape memory and material properties of an Ni-rich NiTiHf high temperature shape memory alloy. Acta Materialia 2013;61:7422-7431.

[43] AP Stebner, GS Bigelow, J Yang, DP Shukla, SM Saghaian, R Rogers, A Garg, HE Karaca, Y Chumlyakov, K Bhattacharya, RD Noebe. Transformation strains and temperatures of a nickel–titanium–hafnium high temperature shape memory alloy. Acta Materialia 2014;76:40-53.

[44] DN AbuJodam, PE Thoma, MY Kao, DR Angst, High Transformation Temperature Shape Memory Alloy, In: Patent US, editor. US Johnson Service Company, Milwaukee, WI (1992).

[45] DR Angst, PE Thoma, MY Kao. The Effect of Hafnium Content on the Transformation Temperatures of Ni49Ti51-xHfx. Shape Memory Alloys. J. Phys. IV France 1995;05:C8-747-C748-752.

[46] P Olier, JC Brachet, JL Bechade, C Foucher, G Guénin. Investigation of Transformation Temperatures, Microstructure and Shape Memory Properties of NiTi, NiTiZr and NiTiHf Alloys. J. Phys. IV France 1995;05:C8-741-C748-746.

[47] PE Thoma, JJ Boehm. Effect of composition on the amount of second phase and transformation temperatures of NixTi90−xHf10 shape memory alloys. Materials Science and Engineering: A 1999;273-275:385-389.

[48] PL Potapov, AV Shelyakov, AA Gulyaev, EL Svistunov, NM Matveeva, D Hodgson. Effect of Hf on the structure of Ni-Ti martensitic alloys. Materials Letters 1997;32:247-250.

[49] Y Tong, F Chen, B Tian, L Li, Y Zheng. Microstructure and martensitic transformation of Ti49Ni51−xHfx high temperature shape memory alloys. Materials Letters 2009;63:1869-1871.

[50] GS Firstov, J Van Humbeeck, YN Koval. Comparison of high temperature shape memory behaviour for ZrCu-based, Ti–Ni–Zr and Ti–Ni–Hf alloys. Scripta Materialia 2004;50:243-248.

[51] G Airoldi, S Piredda, M Pozzi, AV Shelyakov. The Electrical Resistance of Ni50Ti30Hf20 and Ni50Ti40.5Hf9.5 Melt-Spun Ribbons during Current-Driven Thermal Cycles. Materials Science Forum 2000;327-329:135-138.

[52] XD Han, R Wang, Z Zhang, DZ Yang. A new precipitate phase in a TiNiHf high temperature shape memory alloy. Acta Materialia 1998;46:273-281.

[53] XL Meng, W Cai, F Chen, LC Zhao. Effect of aging on martensitic transformation and microstructure in Ni-rich TiNiHf shape memory alloy. Scripta Materialia 2006;54:1599-1604.

[54] XL Meng, W Cai, YF Zheng, LC Zhao. Phase transformation and precipitation in aged Ti–Ni–Hf high-temperature shape memory alloys. Materials Science and Engineering: A 2006;438-440:666-670.

[55] XL Meng, W Cai, YD Fu, QF Li, JX Zhang, LC Zhao. Shape-memory behaviors in an aged Ni-rich TiNiHf high temperature shape-memory alloy. Intermetallics 2008;16:698-705.

[56] A Evirgen, F Basner, I Karaman, R D. Noebe, J Pons, R Santamarta. Effect of aging on the martensitic transformation characteristics of a Ni-Rich NiTiHf high temperature shape memory alloy2012.

[57] A Evirgen, I Karaman, R Santamarta, J Pons, RD Noebe. Microstructural characterization and shape memory characteristics of the Ni50.3Ti34.7Hf15 shape memory alloy. Acta Materialia 2015;83:48-60.

[58] SM Saghaian, HE Karaca, H Tobe, J Pons, R Santamarta, YI Chumlyakov, RD Noebe. Effects of Ni content on the shape memory properties and microstructure of Ni-rich NiTi-20Hf alloys. Smart Materials and Structures 2016;25:095029.

[59] M Prasher, D Sen. Influence of aging on phase transformation and microstructure of Ni50.3Ti29.7Hf20 high temperature shape memory alloy. Journal of Alloys and Compounds 2014;615:469-474.

[60] O Benafan, GS Bigelow, DA Scheiman. Transformation behavior in NiTi-20Hf shape memory alloys – Transformation temperatures and hardness. Scripta Materialia 2018;146:251-254.

[61] GS Bigelow, A Garg, SA Padula, DJ Gaydosh, RD Noebe. Load-biased shape-memory and superelastic properties of a precipitation strengthened high-temperature Ni50.3Ti29.7Hf20 alloy. Scripta Materialia 2011;64:725-728.

[62] A Evirgen, J Pons, I Karaman, R Santamarta, RD Noebe. H-Phase Precipitation and Martensitic Transformation in Ni-rich Ni–Ti–Hf and Ni–Ti-Zr High-Temperature Shape Memory Alloys. Shape Memory and Superelasticity 2018;4:85-92.

[63] O Karakoc, C Hayrettin, A Evirgen, R Santamarta, D Canadinc, RW Wheeler, SJ Wang, DC Lagoudas, I Karaman. Role of microstructure on the actuation fatigue performance of Ni-Rich NiTiHf high temperature shape memory alloys. Acta Materialia 2019;175:107-120.

[64] KC Atli, I Karaman, RD Noebe, D Gaydosh. The effect of training on two-way shape memory effect of binary NiTi and NiTi based ternary high temperature shape memory alloys. Materials Science and Engineering: A 2013;560:653-666.

[65] A Cox, T Baxevanis, D Lagoudas. Numerical Evaluation of the Effect of Ni4Ti3 Precipitates on the Overall Thermo-Mechanical Response of NiTi Shape Memory Alloys. 2013:V002T002A012.

[66] T Waitz, V Kazykhanov, HP Karnthaler. Martensitic phase transformations in nanocrystalline NiTi studied by TEM. Acta Materialia 2004;52:137-147.

[67] R Santamarta, R Arróyave, J Pons, A Evirgen, I Karaman, HE Karaca, RD Noebe. TEM study of structural and microstructural characteristics of a precipitate phase in Ni-rich Ni–Ti–Hf and Ni–Ti–Zr shape memory alloys. Acta Materialia 2013;61:6191-6206.

[68] F Yang, DR Coughlin, PJ Phillips, L Yang, A Devaraj, L Kovarik, RD Noebe, MJ Mills. Structure analysis of a precipitate phase in an Ni-rich high-temperature NiTiHf shape memory alloy. Acta Materialia 2013;61:3335-3346.

[69] DR Coughlin, L Casalena, F Yang, RD Noebe, MJ Mills. Microstructure–property relationships in a high-strength 51Ni–29Ti–20Hf shape memory alloy. Journal of Materials Science 2016;51:766-778.

[70] SM Saghaian, HE Karaca, H Tobe, AS Turabi, S Saedi, SE Saghaian, YI Chumlyakov, RD Noebe. High strength NiTiHf shape memory alloys with tailorable properties. Acta Materialia 2017;134:211-220.

[71] O Karakoc, C Hayrettin, M Bass, SJ Wang, D Canadinc, JH Mabe, DC Lagoudas, I Karaman. Effects of upper cycle temperature on the actuation fatigue response of NiTiHf high temperature shape memory alloys. Acta Materialia 2017;138:185-197.

[72] AM Pérez-Sierra, J Pons, R Santamarta, I Karaman, RD Noebe. Stability of a Ni-rich Ni-Ti-Zr high temperature shape memory alloy upon low temperature aging and thermal cycling. Scripta Materialia 2016;124:47-50.

[73] BPJ S., Z Robert, K Dennis, S Alan, T Sigurd, L Alfred. A New Prototype Two-Phase (TiNi)–(β-W) SMA System with Tailorable Thermal Hysteresis. Advanced Functional Materials 2011;21:113-118.

[74] Z Robert, T Ryota, YM L., S Alan, F Yasubumi, T Sigurd, M Burkhard, R Mustafa, F Jan, B Hayo, CY S., S Vijay, JR D., T Ichiro, E Gunther, L Alfred. Identification of Quaternary Shape Memory Alloys with Near-Zero Thermal Hysteresis and Unprecedented Functional Stability. Advanced Functional Materials 2010;20:1917-1923.

[75] J Cui, YS Chu, OO Famodu, Y Furuya, J Hattrick-Simpers, RD James, A Ludwig, S Thienhaus, M Wuttig, Z Zhang, I Takeuchi. Combinatorial search of thermoelastic shape-memory alloys with extremely small hysteresis width. Nature Materials 2006;5:286.

[76] D Xue, R Yuan, Y Zhou, D Xue, T Lookman, G Zhang, X Ding, J Sun. Design of High Temperature Ti-Pd-Cr Shape Memory Alloys with Small Thermal Hysteresis. Scientific Reports 2016;6:28244.

[77] A Evirgen, I Karaman, R Santamarta, J Pons, C Hayrettin, RD Noebe. Relationship between crystallographic compatibility and thermal hysteresis in Ni-rich NiTiHf and NiTiZr high temperature shape memory alloys. Acta Materialia 2016;121:374-383.

[78] D Xue, PV Balachandran, J Hogden, J Theiler, D Xue, T Lookman. Accelerated search for materials with targeted properties by adaptive design. Nature Communications 2016;7:11241.

[79] PV Balachandran, D Xue, J Theiler, J Hogden, T Lookman. Adaptive strategies for materials design using uncertainties. Scientific reports 2016;6:19660.

[80] K Shimizu, T Tadaki. Shape Memory Alloys, ed H. Funakubo. Gordon and Breach Science Publishers 1987:1.

[81] T Tadaki, a K Otsuka, K Shimizu. Shape Memory Alloys. Annual Review of Materials Science 1988;18:25-45.

[82] Z Nishiyama. Martensitic Transformations. New York: Academic Press; 1978.

[83] L Kaufman, M Cohen. Thermodynamics and kinetics of martensitic transformations. Progress in Metal Physics 1958;7:165-246.

[84] RW Cahn. Plastic deformation of alpha-uranium; twinning and slip. Acta Metallurgica 1953;1:49-70.

[85] JW Christian, S Mahajan. Deformation twinning. Progress in Materials Science 1995;39:1-157.

[86] JK Mackenzie, JS Bowles. The crystallography of martensite transformations—IV body-centred cubic to orthorhombic transformations. Acta Metallurgica 1957;5:137-149.

[87] H Sehitoglu, I Karaman, R Anderson, X Zhang, K Gall, HJ Maier, Y Chumlyakov. Compressive response of NiTi single crystals. Acta Materialia 2000;48:3311-3326.

[88] P Chowdhury, H Sehitoglu. Deformation physics of shape memory alloys – Fundamentals at atomistic frontier. Progress in Materials Science 2017;88:49-88.

[89] T Saburi, S Nenno, Shape memory effect and related phenomena, In: Aaronson HI, Laughlin DE, Sekerka RF, Wayman C, editors. Proc Int Conf on Solid–Solid Phase Transformations, The Metallurgical Society of AIME Warrendale, PA (1982) p. 1455-1279.

[90] T Saburi, CM Wayman. Crystallographic similarities in shape memory martensites. Acta Metallurgica 1979;27:979-995.

[91] S Miyazaki, K Otsuka, CM Wayman. The shape memory mechanism associated with the martensitic transformation in Ti□Ni alloys—I. Self-accommodation. Acta Metallurgica 1989;37:1873-1884.

[92] JM Ball, RD James. Fine Phase Mixtures as Minimizers of Energy. Analysis and Continuum Mechanics: A Collection of Papers Dedicated to J. Serrin on His Sixtieth Birthday. Berlin, Heidelberg: Springer Berlin Heidelberg; 1989. p. 647-686.

[93] K Madangopal. The self accommodating martensitic microstructure of NiTi shape memory alloys. Acta Materialia 1997;45:5347-5365.

[94] P Chowdhury. Frontiers of Theoretical Research on Shape Memory Alloys: A General Overview. Shape Memory and Superelasticity 2018;4:26-40.

[95] RD Widdle, Jr., MT Grimshaw, M Shome, Optimal design of a shape memory alloy actuated composite structure with iterative finite element analysis, Society of Photo-Optical Instrumentation Engineers (SPIE) Conference Series (2009) p. 728818.

[96] JH Mabe, RT Ruggeri, E Rosenzweig, CJ Yu, NiTinol performance characterization and rotary actuator design, In: Anderson EH, editor. SPIE 5388, Smart Structures and Materials 2004: Industrial and Commercial Applications of Smart Structures Technologies (2004).

[97] RD Noebe, TA Biles, SA Padula. NiTi-Based High-Temperature Shape-Memory Alloys: Properties, Prospects, and Potential Applications. In: Soboyejo WO, Srivatsan TS, editors.

Advanced Structural Materials: Properties, Design Optimization, and Applications. Boca Raton, FL: CRC Press Taylor & Francis Group; 2006.

[98] SF Hsieh, SK Wu. A Study on Ternary Ti-rich TiNiZr Shape Memory Alloys. Materials Characterization 1998;41:151-162.

[99] XL Meng, YX Tong, KT Lau, W Cai, LM Zhou, LC Zhao. Effect of Cu addition on phase transformation of Ti–Ni–Hf high-temperature shape memory alloys. Materials Letters 2002;57:452-456.

[100] B Kockar, I Karaman, JI Kim, YI Chumlyakov, J Sharp, CJ Yu. Thermomechanical cyclic response of an ultrafine-grained NiTi shape memory alloy. Acta Materialia 2008;56:3630-3646.

[101] DR Coughlin, PJ Phillips, GS Bigelow, A Garg, RD Noebe, MJ Mills. Characterization of the microstructure and mechanical properties of a 50.3Ni–29.7Ti–20Hf shape memory alloy. Scripta Materialia 2012;67:112-115.

[102] A Evirgen, J Pons, I Karaman, R Santamarta, RD Noebe. H-Phase Precipitation and Martensitic Transformation in Ni-rich Ni–Ti–Hf and Ni–Ti-Zr High-Temperature Shape Memory Alloys. Shape Memory and Superelasticity 2018.

[103] M Kamlet, NASA Tests New Alloy to Fold Wings in Flight, nasa.gov (2018).

[104] J Russell, Metal with Memory: F-18 Wing Fold, nasa.gov (2018).

[105] D Canadinc, W Trehern, H Ozcan, C Hayrettin, O Karakoc, I Karaman, F Sun, Z Chaudhry. On the deformation response and cyclic stability of Ni50Ti35Hf15 high temperature shape memory alloy wires. Scripta Materialia 2017;135:92-96.

[106] XL Meng, W Cai, YF Zheng, YX Tong, LC Zhao, LM Zhou. Stress-induced martensitic transformation behavior of a Ti–Ni–Hf high temperature shape memory alloy. Materials Letters 2002;55:111-115.

[107] XL Meng, C Wei, KT Lau, LM Zhou, LC Zhao. Phase Transformation and Thermal Stability of Aged Ti-Ni-Hf High Temperature Shape Memory Alloys. J. Mater. Sci. Technol 2006;22:691-695.

[108] SM Saghaian, HE Karaca, M Souri, AS Turabi, RD Noebe. Tensile shape memory behavior of Ni50.3Ti29.7Hf20 high temperature shape memory alloys. Materials & Design 2016;101:340-345.

[109] XL Meng, YF Zheng, Z Wang, LC Zhao. Effect of aging on the phase transformation and mechanical behavior of Ti36Ni49Hf15 high temperature shape memory alloy. Scripta Materialia 2000;42:341-348.

[110] A Ahadi, Q Sun. Effects of grain size on the rate-dependent thermomechanical responses of nanostructured superelastic NiTi. Acta Materialia 2014;76:186-197.

[111] O Karakoc, C Hayrettin, D Canadinc, I Karaman. Role of applied stress level on the actuation fatigue behavior of NiTiHf high temperature shape memory alloys. Acta Materialia 2018;153:156-168.

[112] KS Suresh, DI Kim, SK Bhaumik, S Suwas. Evolution of microstructure and texture in Ni49.4Ti38.6Hf12 shape memory alloy during hot rolling. Intermetallics 2013;42:1-8.

[113] M Zarinejad, Y Liu, Y Tong. Transformation temperature changes due to second phase precipitation in NiTi-based shape memory alloys. Intermetallics 2009;17:914-919.

[114] EL Semenova. The Solidus Surface in the Ti — Ni — Hf System in the Ti — TiNi — HfNi — Hf Region. Powder Metallurgy and Metal Ceramics 2001;40:414-425.

[115] OL Semenova, LO Tret'yachenko, VM Petyukh. Ti-TiNi-HfNi-Hf Liquidus surface. Powder Metallurgy and Metal Ceramics 2007;46:556-564.

[116] JL Liu, LL Zhu, XM Huang, GM Cai, ZP Jin. Investigation of the phase equilibria in Ti-Ni-Hf system using diffusion triples and equilibrated alloys. Calphad 2017;58:160-168.

[117] T Baxevanis, A Cox, DC Lagoudas. Micromechanics of precipitated near-equiatomic Ni-rich NiTi shape memory alloys. Acta Mechanica 2014;225:1167-1185.

[118] A Solomou, G Zhao, S Boluki, JK Joy, X Qian, I Karaman, R Arróyave, DC Lagoudas. Multi-objective bayesian materials discovery: Application on the discovery of precipitation strengthened niti shape memory alloys through micromechanical modeling. Materials & Design 2018;160:810-827.

[119] J-C Zhao. Combinatorial approaches as effective tools in the study of phase diagrams and composition–structure–property relationships. Progress in Materials Science 2006;51:557-631.

[120] J-C Zhao. A Combinatorial Approach for Structural Materials. Advanced Engineering Materials 2001;3:143-147.

[121] J-C Zhao. Reliability of the diffusion-multiple approach for phase diagram mapping. Journal of Materials Science 2004;39:3913-3925.

[122] BC Hornbuckle, M Kapoor, GB Thompson. A procedure to create isoconcentration surfaces in low-chemical-partitioning, high-solute alloys. Ultramicroscopy 2015;159:346-353.

[123] BC Hornbuckle, TT Sasaki, GS Bigelow, RD Noebe, ML Weaver, GB Thompson. Structure–property relationships in a precipitation strengthened Ni–29.7Ti–20Hf (at%) shape memory alloy. Materials Science and Engineering: A 2015;637:63-69.

[124] SM Saghaian, HE Karaca, H Tobe, AS Turabi, S Saedi, SE Saghaian, YI Chumlyakov, RD Noebe. High strength NiTiHf shape memory alloys with tailorable properties. Acta Materialia 2017;134:211-220.

[125] A Guinier, G Fournet, KL Yudowitch. Small-angle scattering of X-rays. 1955.

[126] F De Geuser, A Deschamps. Precipitate characterisation in metallic systems by small-angle X-ray or neutron scattering. Comptes Rendus Physique 2012;13:246-256.

[127] F Zhang, LE Levine, AJ Allen, CE Campbell, AA Creuziger, N Kazantseva, J Ilavsky. In situ structural characterization of ageing kinetics in aluminum alloy 2024 across angstrom-to-micrometer length scales. Acta Materialia 2016;111:385-398.

[128] P Fratzl. Small-angle scattering in materials science - a short review of applications in alloys, ceramics and composite materials. Journal of Applied Crystallography 2003;36:397-404.

[129] A Deschamps, M Militzer. Precipitation kinetics and strengthening of a Fe–0.8 wt% Cu alloy. ISIJ international 2001;41:196-205.

[130] A Deschamps, L Lae, P Guyot. In situ small-angle scattering study of the precipitation kinetics in an Al–Zr–Sc alloy. Acta Materialia 2007;55:2775-2783.

[131] CS Tsao, US Jeng, CY Chen, TY Kuo. Small-angle X-ray scattering study of nanostructure evolution of β″ precipitates in Al–Mg–Si alloy. Scripta Materialia 2005;53:1241-1245.

[132] M Nicolas, A Deschamps. Characterisation and modelling of precipitate evolution in an Al–Zn–Mg alloy during non-isothermal heat treatments. Acta Materialia 2003;51:6077-6094.

[133] Y-C Huang, C-S Tsao, S-K Wu. A Study on the Nanoparticles Evolution in Isothermally Aged Strain Glass of Ti48.7Ni51.3 Shape Memory Alloy by In Situ Small-Angle X-ray Scattering. Metals 2018;8:352.

[134] I Jan, Z Fan, AR N., K Ivan, JP R., LL E., AA J. Development of combined microstructure and structure characterization facility for in situ and operando studies at the Advanced Photon Source. Journal of Applied Crystallography 2018;51:867-882.

[135] CA Biffi, A Figini, A Tuissi. Influence of compositional ratio on microstructure and martensitic transformation of CuZr shape memory alloys. Intermetallics 2014;46:4-11.

[136] WH Gao, XL Meng, GB Song, W Cai, LC Zhao. Effect of Hf content on martensitic transformation, microstructure, and mechanical properties of Cu50Zr50−xHfx alloys. Journal of Alloys and Compounds 2016;662:578-582.

[137] W Ito, Y Imano, R Kainuma, Y Sutou, K Oikawa, K Ishida. Martensitic and Magnetic Transformation Behaviors in Heusler-Type NiMnIn and NiCoMnIn Metamagnetic Shape Memory Alloys. Metallurgical and Materials Transactions A 2007;38:759-766.

[138] S Boluki, X Qian, ER Dougherty. Experimental design via generalized mean objective cost of uncertainty. IEEE Access 2018;7:2223-2230.

[139] B-J Yoon, X Qian, ER Dougherty. Quantifying the objective cost of uncertainty in complex dynamical systems. IEEE Transactions on Signal Processing 2013;61:2256-2266.

[140] PI Frazier, J Wang. Bayesian Optimization for Materials Design. In: Lookman T, Alexander FJ, Rajan K, editors. Information Science for Materials Discovery and Design. Cham: Springer International Publishing; 2016. p. 45-75.

[141] A Seko, A Togo, H Hayashi, K Tsuda, L Chaput, I Tanaka. Prediction of low-thermal-conductivity compounds with first-principles anharmonic lattice-dynamics calculations and Bayesian optimization. Physical review letters 2015;115:205901.

[142] LM Ghiringhelli, J Vybiral, SV Levchenko, C Draxl, M Scheffler. Big Data of Materials Science: Critical Role of the Descriptor. Physical Review Letters 2015;114:105503.

[143] K Rajan. Materials Informatics: The Materials “Gene” and Big Data. Annual Review of Materials Research 2015;45:153-169.

[144] A Agrawal, A Choudhary. Perspective: Materials informatics and big data: Realization of the “fourth paradigm” of science in materials science. APL Materials 2016;4:053208.

[145] D Xue, D Xue, R Yuan, Y Zhou, PV Balachandran, X Ding, J Sun, T Lookman. An informatics approach to transformation temperatures of NiTi-based shape memory alloys. Acta Materialia 2017;125:532-541.

[146] B Shahriari, K Swersky, Z Wang, RP Adams, N De Freitas. Taking the human out of the loop: A review of Bayesian optimization. Proceedings of the IEEE 2015;104:148-175.

[147] EG Ryan, CC Drovandi, JM McGree, AN Pettitt. A review of modern computational algorithms for Bayesian optimal design. International Statistical Review 2016;84:128-154.

[148] CE Rasmussen, CK Williams. Gaussian Processes for Machine Learning. Gaussian Processes for Machine Learning, by CE Rasmussen and CKI Williams. ISBN-13 978-0-262-18253-9 2006.

[149] A Seko, T Maekawa, K Tsuda, I Tanaka. Machine learning with systematic density-functional theory calculations: Application to melting temperatures of single-and binary-component solids. Physical Review B 2014;89:054303.

[150] D Basak, S Pal, DC Patranabis. Support vector regression. Neural Information Processing-Letters and Reviews 2007;11:203-224.

[151] !!! INVALID CITATION !!! [57-60].

[152] A Talapatra, S Boluki, T Duong, X Qian, E Dougherty, R Arróyave. Autonomous efficient experiment design for materials discovery with Bayesian model averaging. Physical Review Materials 2018;2:113803.

[153] R Dehghannasiri, D Xue, PV Balachandran, MR Yousefi, LA Dalton, T Lookman, ER Dougherty. Optimal experimental design for materials discovery. Computational Materials Science 2017;129:311-322.

[154] DR Jones, M Schonlau, WJ Welch. Efficient global optimization of expensive black-box functions. Journal of Global optimization 1998;13:455-492.

[155] P Frazier, W Powell, S Dayanik. The knowledge-gradient policy for correlated normal beliefs. INFORMS journal on Computing 2009;21:599-613.

[156] D Xue, PV Balachandran, R Yuan, T Hu, X Qian, ER Dougherty, T Lookman. Accelerated search for BaTiO3-based piezoelectrics with vertical morphotropic phase boundary using Bayesian learning. Proceedings of the National Academy of Sciences 2016;113:13301-13306.

[157] MT Emmerich, AH Deutz, JW Klinkenberg, Hypervolume-based expected improvement: Monotonicity properties and exact computation, 2011 IEEE Congress of Evolutionary Computation (CEC) IEEE (2011) p. 2147-2154.

[158] D. Abu Jodam, P. Thoma, M. Kao, D Angst, High Transformation Temperature Shape Memory Alloy, U.S Johnson Service Company (1992).

[159] P Antoni, V Eduard. Avalanche criticality in thermal-driven martensitic transitions: the asymmetry of the forward and reverse transitions in shape-memory materials. Journal of Physics: Condensed Matter 2017;29:334001.

[160] DL Beke, MK Bolgár, LZ Tóth, L Daróczi. On the asymmetry of the forward and reverse martensitic transformations in shape memory alloys. Journal of Alloys and Compounds 2018;741:106-115.

[161] J Khalil-Allafi, B Amin-Ahmadi. The effect of chemical composition on enthalpy and entropy changes of martensitic transformations in binary NiTi shape memory alloys. Journal of Alloys and Compounds 2009;487:363-366.

[162] KF Hane, TW Shield. Microstructure in the cubic to monoclinic transition in titanium–nickel shape memory alloys. Acta Materialia 1999;47:2603-2617.

[163] K Bhattacharya. Microstructure of martensite: why it forms and how it gives rise to the shape-memory effect: Oxford University Press; 2003.

[164] N Singh, A Talapatra, A Junkaew, T Duong, S Gibbons, S Li, H Thawabi, E Olivos, R Arróyave. Effect of ternary additions to structural properties of NiTi alloys. Computational Materials Science 2016;112:347-355.

[165] Z Zhang, Y Wang, D Wang, Y Zhou, K Otsuka, X Ren. Phase diagram of ${\text{Ti}}_{50\ensuremath{-}x}{\text{Ni}}_{50+x}$: Crossover from martensite to strain glass. Physical Review B 2010;81:224102.

[166] M Zarinejad, Y Liu, TJ White. The crystal chemistry of martensite in NiTiHf shape memory alloys. Intermetallics 2008;16:876-883.

[167] AM Sandu, K Tsuchiya, M Tabuchi, S Yamamoto, Y Todaka, M Umemoto. Microstructural Evolution during Isothermal Aging in Ni-Rich Ti-Zr-Ni Shape Memory Alloys. Materials Transcations 2007;48:432-438.

[168] AM Sandu, S Yamamoto, Y Todaka, M Umemoto, K Tsuchiya, M Saito, T Hara, Y Matsui, Precipitation in Ni-rich Ti-Zr-Ni Shape Memory Alloys by Isothermal Aging, In: Berg B, Mitchell MR, Proft J, editors. Proceedings of the International Conference on Shape Memory and Superelastic Technologies Tsukuba, Japan (2007) p. 101-108.

[169] M Prasher, D Sen, J Bahadur, R Tewari, M Krishnan. Correlative SANS and TEM investigation on precipitation kinetics of H-phase in Ni50.3Ti29.7Hf20 high temperature shape memory alloy. Journal of Alloys and Compounds 2019;779:630-642.

[170] BC Hornbuckle, RD Noebe, GB Thompson. Influence of Hf solute additions on the precipitation and hardenability in Ni-rich NiTi alloys. Journal of Alloys and Compounds 2015;640:449-454.

[171] T Wang, ZP Jin, JC Zhao. Experimental study and reassessment of the Ni-Hf binary system. Zeitschrift für Metallkunde 2001;92:441-446.

[172] Y Yang, BP Bewlay, YA Chang. Thermodynamic modeling of the Hf–Ti–Si ternary system. Intermetallics 2007;15:168-176.

[173] FJJ van Loo, GD Rieck. Diffusion in the titanium-aluminium system—I. Interdiffusion between solid Al and Ti or Ti-Al alloys. Acta Metallurgica 1973;21:61-71.

[174] FJJ van Loo, GD Rieck. Diffusion in the titanium-aluminium system—II. Interdiffusion in the composition range between 25 and 100 at.% Ti. Acta Metallurgica 1973;21:73-84.

[175] J-C Zhao. A combinatorial approach for efficient mapping of phase diagrams and properties. Journal of Materials Research 2001;16:1565-1578.

[176] T Umale, D Salas, B Tomes, R Arroyave, I Karaman. The effects of wide range of compositional changes on the martensitic transformation characteristics of NiTiHf shape memory alloys. Scripta Materialia 2019;161:78-83.

[177] RN Andrews, J Serio, G Muralidharan, J Ilavsky. An in situ USAXS–SAXS–WAXS study of precipitate size distribution evolution in a model Ni-based alloy. Journal of applied crystallography 2017;50:734-740.

[178] F Zhang, LE Levine, AJ Allen, MR Stoudt, G Lindwall, EA Lass, ME Williams, Y Idell, CE Campbell. Effect of heat treatment on the microstructural evolution of a nickel-based superalloy additive-manufactured by laser powder bed fusion. Acta Materialia 2018;152:200-214.

[179] F Zhang, AJ Allen, LE Levine, D-H Tsai, J Ilavsky. Structure and dynamics of bimodal colloidal dispersions in a low-molecular-weight polymer solution. Langmuir 2017;33:2817-2828.

[180] R Triolo, E Caponetti, S Spooner. Analysis of small-angle scattering patterns from precipitating alloys. Physical Review B 1989;39:4588.

[181] J Ilavsky, PR Jemian. Irena: tool suite for modeling and analysis of small-angle scattering. J. Appl. Crystallogr. 2009;42:347-353.

[182] G Beaucage. Approximations leading to a unified exponential/power-law approach to small-angle scattering. J. Appl. Crystallogr. 1995;28:717-728.

[183] G Beaucage, D Schaefer. Structural studies of complex systems using small-angle scattering: a unified Guinier/power-law approach. J. Non-Cryst. Solids 1994;172:797-805.

[184] Y Wu, L Patriarca, H Sehitoglu, Y Chumlyakov. Ultrahigh tensile transformation strains in new Ni50.5Ti36.2Hf13.3 shape memory alloy. Scripta Materialia 2016;118:51-54.

[185] B Kockar, I Karaman, JI Kim, Y Chumlyakov. A method to enhance cyclic reversibility of NiTiHf high temperature shape memory alloys. Scripta Materialia 2006;54:2203-2208.

[186] SM Saghaian, HE Karaca, H Tobe, M Souri, R Noebe, YI Chumlyakov. Effects of aging on the shape memory behavior of Ni-rich Ni50.3Ti29.7Hf20 single crystals. Acta Materialia 2015;87:128-141.

[187] M Moshref-Javadi, SH Seyedein, MT Salehi, MR Aboutalebi. Age-induced multi-stage transformation in a Ni-rich NiTiHf alloy. Acta Materialia 2013;61:2583-2594.

[188] AA Simon. Shape memory response and microstructural evolution of a severe plastically deformed high temperature shape memory alloy (NiTiHf): Texas A&M University; 2004.

[189] MA Azeem, D Dye. In situ evaluation of the transformation behaviour of NiTi-based high temperature shape memory alloys. Intermetallics 2014;46:222-230.

[190] C Zhang, PE Thoma, R Zee. High Hf Content NITIHF Shape Memory Films. MRS Proceedings 2011;604:129.

[191] S Saghaian. Shape memory behavior of single crystal and polycrystalline Ni-rich NiTiHf high temperature shape memory alloys: University of Kentucky; 2015.

[192] G Ded. Characterization of Ni-rich NiTiHf based high temperature shape memory alloys: University of Kentucky; 2010.

[193] S Kornegay. Influence of zirconium additions on nitinol shape memory phase stability, transformation temperatures, and thermo-mechanical properties 2016.

[194] L Patriarca, H Sehitoglu. High-temperature superelasticity of Ni50.6Ti24.4Hf25.0 shape memory alloy. Scripta Materialia 2015;101:12-15.

[195] S Besseghini, E Villa, A Tuissi. Ni□Ti□Hf shape memory alloy: effect of aging and thermal cycling. Materials Science and Engineering: A 1999;273:390-394.

[196] X Yi, W Gao, X Meng, Z Gao, W Cai, L Zhao. Martensitic transformation behaviors and mechanical properties of (Ti36Ni49Hf15)100-xYx high temperature shape memory alloys. Journal of Alloys and Compounds 2017;705:98-104.

[197] CC Wojcik. Properties and Heat Treatment of High Transition Temperature Ni-Ti-Hf Alloys. Journal of Materials Engineering and Performance 2009;18:511-516.

[198] DHD Hsu, B Hornbuckle, B Valderrama, F Barrie, H B. Henderson, G Thompson, M Manuel. The Effect of Aluminum Additions on the Thermal, Microstructural, and Mechanical Behavior of NiTiHf Shape Memory Alloys. Journal of Alloys and Compounds 2015;638.

[199] NAI David, PE Thoma, M-Y Kao, DR Angst, High transformation temperature shape memory alloy, Google Patents (1992).

[200] KM Kim, J Keun Hong, CH Park, J-T Yeom. Comparative study of the thermocyclic behavior of Ti-Ni-Hf and Ti-Ni-Hf-Ta shape memory alloys. Journal of Nanoscience and Nanotechnology 2016;16:11775-11778.

[201] XL Meng, W Cai, YF Zheng, YB Rao, LC Zhao. Two-way shape memory effect induced by martensite deformation and stabilization of martensite in Ti36Ni49Hf15 high temperature shape memory alloy. Materials Letters 2003;57:4206-4211.

[202] XD Han, WH Zou, R Wang, Z Zhang, DZ Yang. Structure and substructure of martensite in a Ti36.5Ni48.5Hf15 high temperature shape memory alloy. Acta Materialia 1996;44:3711-3721.

[203] ZJ Pu, H-K Tseng, K-H Wu. Innovative system of high-temperature shape memory alloys: SPIE; 1994.

[204] BX Wang, R Bhagat, XZ Lan, RJ Dashwood. Production of Ni-35Ti-15Hf Alloy via the FFC Cambridge Process. Journal of The Electrochemical Society 2011;158:D595.

[205] P Feliot, J Bect, E Vazquez. A Bayesian approach to constrained single- and multi-objective optimization. J. of Global Optimization 2017;67:97-133.

[206] JR Gardner, MJ Kusner, Z Xu, KQ Weinberger, JP Cunningham, Bayesian optimization with inequality constraints, Proceedings of the 31st International Conference on International Conference on Machine Learning - Volume 32 Beijing, China JMLR.org (2014) p. II-937-II-945.

APPENDIX

A.1 Functional forms of the GPR kernels

The functional forms of the kernels in Section 6 are as follows:

ARD SE: $K\left(x^i, x^j\middle|\theta\right) = \theta_0^2 \exp\left[-\frac{1}{2}\sum_{d=1}^{D}\frac{(x_d^i - x_d^j)^2}{\theta_d^2}\right]$

ARD Matern 3/2: $K\left(x^i, x^j\middle|\theta\right) = \theta_0^2\left(1+\sqrt{3}\sqrt{\sum_{d=1}^{D}\frac{(x_d^i - x_d^j)^2}{\theta_d^2}}\right)\exp\left(-\sqrt{3}\sum_{d=1}^{D}\frac{(x_d^i - x_d^j)^2}{\theta_d^2}\right)$

ARD Matern 5/2: $K(x^i, x^j|\theta) = \theta_0^2\left(1+\sqrt{5}\sqrt{\sum_{d=1}^{D}\frac{(x_d^i - x_d^j)^2}{\theta_d^2}}+\frac{5}{3}\sum_{d=1}^{D}\frac{(x_d^i - x_d^j)^2}{\theta_d^2}\right)\exp\left(-\sqrt{5}\sum_{d=1}^{D}\frac{(x_d^i - x_d^j)^2}{\theta_d^2}\right)$

A.2 Connection of MOCU policy with constrained expected improvement

In this section we show how the derived MOCU policy reduces to the constrained expected improvement (EI_c) in [205, 206]. Specifically, under the GPR modeling and Gaussian distributions over $f(x)$ and $g(x)$, if we restrict the selection of IBR action to the set of actions with observed outputs, we recover the constrained expected improvement acquisition function. The (restricted) IBR action in this case is

$$x_{IBR}^n = \arg min_{x\in X_o^n} \mathrm{E}^n[C(x)] = \arg min_{x\in X_{o,s}^n} y_{o,f}^x,$$

where $y_{o,f}^x$ denotes the output of x corresponding to $f(x)$, and $X_{o,n}^n = \{x \in X_o^n | c(y_{o,g}^x)\}$ represents the set of actions in X_o^n (the set of actions with observed outputs at iteration n) that satisfy the constraints. The expectation is dropped since the output values are observed and known for X_o. Denoting $min_{x\in X_{o,s}^n} y_{o,f}^x$ as $y_{o,f}^{\mathrm{opt},n}$, the optimal experiment based on the MOCU policy given n data points is

$$x_*^n = \arg min_{x\in X}\, \mathrm{E}^n_{y^{n+1}|x}\left[\mathrm{E}^{n+1}[C(x_{IBR}^{n+1})]\right] - \mathrm{E}^n[C(x_{IBR}^n)]$$

$$= \arg min_{x\in X}\, \mathrm{E}^n_{y^{n+1}|x}[\min(y_f^{n+1}, y_{o,f}^{\mathrm{opt},n})1_{c(g(x))} + y_{o,f}^{\mathrm{opt},n}1_{1-c(g(x))}] - y_{o,f}^{\mathrm{opt},n}$$

$$= \arg min_{x\in X}\, \mathrm{E}^n_{y^{n+1}|x}[\min(y_f^{n+1} - y_{o,f}^{\mathrm{opt},n}, 0)1_{c(g(x))}]$$

$$= \arg max_{x\in X}\ \mathrm{E}^n_{y^{n+1}|x}[\max(y_{o,f}^{\mathrm{opt},n} - y_f^{n+1}, 0)1_{c(g(x))}]$$

$$= \arg max_{x\in X}\, \mathrm{E}^n_{y^{n+1}|x}[\max(y_{o,f}^{\mathrm{opt},n} - y_f^{n+1}, 0)]\ \mathrm{P}^n\left(c\big(g(x)\big)\right)$$

$$= \arg max_{x\in X}\, \mathrm{EI}^n\,(x)\ \mathrm{P}^n\left(c\big(g(x)\big)\right) = \arg max_{x\in X}\, \mathrm{EI}_{\mathrm{c}}^n(x),$$

which is the same as the selection based on the constrained expected improvement acquisition function.